

UNIVERSIDAD DE NAVARRA  
ESCUELA SUPERIOR DE INGENIEROS  
SAN SEBASTIÁN



*Design and Implementation of Subcutaneous  
UHF Band Antennas for  
Smart Implants using a  
Novel Characterization Procedure*

THESIS

A dissertation submitted for the degree of Doctor of Philosophy by

**Christoph Schmidt**

Under the supervision of:

**Daniel Valderas Gazquez, Ph.D.  
Beatriz Sedano García, Ph.D.**

Donostia-San Sebastián, February 2016



**DECLARATION**

I hereby declare that this thesis is my own work and effort and that it has not been submitted anywhere for any award. Where other sources of information have been used, they have been acknowledged.

Signature:.....





*To my family*



*I keep six honest serving-men:*

*(They taught me all I knew);*

*Their names are What and Why and When*

*And How and Where and Who.*

*- Joseph Rudyard Kipling -  
(The Elephant's Child)*



# ***Acknowledgments***

---

I would like to express my genuine gratitude and recognition to my supervisors Daniel Valderas and Beatriz Sedano for the dedication, motivation and effort they have placed in me during this whole experience.

My particular appreciation goes out to Daniel, first and foremost for the trust he has placed in me and for being ever so supportive and understanding. Without his patience, expertise and unhesitant assistance during the design, manufacturing and measurements of the antenna prototypes it would have been impossible to complete this work. His continuous guidance helped me in all the time of research and writing this thesis. I could not have imagined having a better advisor and mentor for my Ph.D. study.

Most sincere thanks to Bea, who provided me with advice at times of critical need, for her assistance in writing reports, her valuable feedback and fundamental contribution regarding the design and assembly of the smart implant prototype.

My gratitude also extends to CEIT and Tecnun for supporting this research and giving me the opportunity to prepare this Ph.D. thesis. I would like to thank all colleagues, particularly the members of the Antenna Group of the Department of Electronics and Communications for receiving me so cordially and contributing to both my professional and personal development. I can't help to admire their patience to keep up conversations with me despite an initially slow improvement of my Spanish skills. I truly appreciate all the instances in which their friendly goodwill helped me along the way.

Furthermore, I would like to express my honest appreciation to Aitor Arriola for the productive exchange of ideas and, in particular, the excellent technical assistance he provided in the anechoic chamber and antenna lab at Ikerlan, Mondragón, together with Felix Casado. With his skills and broad

experience he is significantly accountable for the successful completion of the 3-D CVC antenna measurements.

My most sincere recognition also to Prof. Xiaodong Chen from Queen Mary University of London for the supportive collaboration regarding the measurements of the planar CVC antenna.

Moreover, I would like to mention the kind contribution of Jacobo Paredes, who designed the CVC sensor and helped me so much with the construction of the phantom. I honestly value the good collaboration and his technical support in the biolab.

Very special thanks go out to Maikel Alonso who gave me a helpful hand with the employment of the Application Development Kit and co-authored a paper with me.

Besides, I would like to dedicate a special reference to my partner and friend, Claudia, for whose motivation and editing assistance I am immensely grateful and, over all, for joining this journey and sharing this impressive experience with me.

Finally, my deepest acknowledgment goes to my family for being a continuous source of support and encouragement throughout my life.

Christoph Schmidt

February 2016

# ***Abstract***

---

Smart implants enable the wireless transfer of physiological parameters gathered inside the human body. In this research work two broadband antennas for implanted smart central venous catheters (SCVC) are designed, implemented and characterized using a novel characterization procedure. The design of implanted antennas involves several challenging aspects such as miniaturization because of the very limited space, high efficiency despite the highly lossy environment in the near field of the antenna, adaptability to the given shape of the implant as well as insulation from the surrounding tissue. These constraints in mind, the electromagnetic specifics of body tissues are studied. This knowledge is required for a profound simulation and analysis of antenna topologies suitable for smart implants.

According to two different scenarios for SCVC applications, two different antenna topologies are proposed. A planar round-shaped broadband UHF antenna for passive RFID is designed for mounting on the top of a smart CVC reservoir placed in a subcutaneous position in the chest. This printed monopole-strip antenna operated at 868 MHz is suitable for near field applications. Alongside a virtual body phantom of the chest, near field simulations as well as simulations in the close far field up to 1 meter distance are run. Since the actual working range turns out to be narrower than anticipated, another topology is projected answering the purpose of higher performance in the far field. This dual-band CVC antenna is 3-D conformal to a truncated cone and scheduled for 402-405 MHz MICS band and 2.4 GHz ISM band. The corresponding smart CVC is battery powered to provide a wide working range.

Measurement environments imitating the properties of the human body are prepared and the antenna prototypes are implemented in a test bed. Measurements inside a body phantom are carried out, yet, the results do not reveal conclusive data. Simulations of the antenna in the test bed detect an influence of the test bed feeding cables on the radiation properties. This observation anticipates the insight that simulation and

measurement cannot be regarded separately, but need to be interpreted in common. Only a procedure that comprehends a combination of both is a viable way to accurately characterize antenna properties for a selected application despite all manipulating factors. In order to resolve the observed mismatch, an uncertainty factor is calculated taking into account the measured and the simulated maximum gain. The obtained results, again, are used to adapt the dual-band UHF antenna to the smart implant prototype. Finally, the performance of the system is examined by running functional tests. These prove that the link budget calculation reliably enables the evaluation of possible application scenarios and, in particular, the maximum operating distance of the future system in certain positions even before a working smart implant prototype is manufactured.

The results of the study state that the presented novel characterization procedure is suitable to verify obtained property data. Consequently, the limits of measurement set ups can be compensated and realistic and comparable antenna characterization can be assured.



# ***Glossary of Acronyms***

---

ADK	Application Development Kit
ADS	Advanced Design System
AMI	Active Medical Implant
ANSI	American National Standards Institute
ARIB	Association of Radio Industries and Businesses
ARPANSA	Australian Radiation Protection And Nuclear Safety Agency
ASA	Australian Safety Approval
AUT	Antenna Under Test
AVI	Automatic Vehicle Identification
BAN	Body Area Network
BS	Base Station
CNS	Central Nervous System
CST MWS	CST Microwave Studio®
CT	Computed Tomography
CVC	Central Venous Catheter
CVCA	Central Venous Catheter Antenna
DECT	Digital Enhanced Cordless Telecommunications
DGBE	Di-ethylene Glycol Butyl Ether
DUT	Device Under Test
EAS	Electronic Article Surveillance
EIRP	Equivalent Isotropically Radiated Power
EM	Electromagnetic
EMC	Electromagnetic Compatibility

---

ERP	Effective Radiated Power
ETSI	European Telecommunications Standards Institute
FCC	Federal Communications Commission
FDA	Food and Drug Administration
FDTD	Finite-Difference Time-Domain
FEKO	FELdberechnung für Körper mit beliebiger Oberfläche
FEM	Finite Element Method
FIT	Finite Integration Technique
FPBA	Fast Perfect Boundary Approximation
HFSS	High Frequency Structural Simulator
IC	Integrated Circuit
ICNIRP	International Commission on Non-Ionizing Radiation Protection
ICU	Intensive Care Unit
IEC	International Electrotechnical Commission
IEEE	Institute of Electrical and Electronics Engineers
ISM	Industrial, Scientific and Medical
ISO	International Organization for Standardization
ITU	International Telecommunication Union
kbps	kilo bits per second
LBT	Listen Before Talk
MedRadio	Medical Device Radiocommunications Service
MEDS	MEDical Data Service
Met Aids	Meteorological Aids
MICS	Medical Implant Communication Service
MMN	Medical Micro-Power Network
MoM	Method of Moments
MR	Magnetic Resonance
MRI	Magnetic Resonance Imaging
mSRD	medical Short Range Devices
MUT	Material Under Test
NFC	Near Field Communication

---

NLM	National Library of Medicine (U.S.)
PCB	Printed Circuit Board
PDA	Personal Digital Assistant
PEC	Perfect Electric Conductor
PIFA	Planar Inverted-F Antenna
PU	Polyurethane
Q	Quality Factor
RF	Radio Frequency
RF	Radio Frequency
RFID	Radio-Frequency IDentification
RISC	Reduced Instruction Set Computing
RMS	Root Mean Square
SAM	Specific Anthropomorphic Mannequin
SAR	Specific Absorption Rate
SCVC	Smart Central Venous Catheter
SHF	Super High Frequency
SMA	Sub-Miniature-A
SMD	Surface-Mounted Device
SN	Sensor Node
SRD	Short Range Devices
TCC	Telecommunication Technology Committee
UHF	Ultra High Frequency
ULP-AMI	Ultra Low Power Active Medical Implant
VHF	Very High Frequency
VNA	Vector Network Analyzer
WAN	Wide Area Network
WLAN	Wireless Local Area Network
WSN	Wireless Sensor Network



# ***Table of Contents***

---

<b><i>Acknowledgments</i></b>	<b><i>i</i></b>
<b><i>Abstract</i></b>	<b><i>iii</i></b>
<b><i>Glossary of Acronyms</i></b>	<b><i>v</i></b>
<b><i>Table of Contents</i></b>	<b><i>ix</i></b>
<b><i>List of Figures</i></b>	<b><i>xiii</i></b>
<b><i>List of Tables</i></b>	<b><i>xix</i></b>
<b><i>1 Introduction</i></b>	<b><i>1</i></b>
<b>1.1 Background</b>	<b>2</b>
1.1.1 Remote Patient Monitoring	2
1.1.2 Monitoring Hospital Patients	3
1.1.3 Telemetric Implant Developments	5
<b>1.2 Setting of Terms</b>	<b>6</b>
<b>1.3 Wireless Communication in Body Surroundings</b>	<b>7</b>
<b>1.4 Challenging Aspects of Implanted Antenna Design</b>	<b>9</b>
<b>1.5 Structure of the Document</b>	<b>10</b>
<b><i>2 State of the Art</i></b>	<b><i>11</i></b>
<b>2.1 Dielectric Anomaly of Body Tissues</b>	<b>12</b>
2.1.1 Dielectric Properties of Tissues	12
2.1.2 Anatomical Tissue Distribution in Humans	14
2.1.3 Tissue-specific Phenomena	19
<b>2.2 Phenomena of Propagation in Dielectric Media</b>	<b>27</b>
2.2.1 Plane Wave Propagation Parameters	28
2.2.2 Dosimetry	32

<b>2.3</b>	<b>Body Phantoms</b>	<b>36</b>
2.3.1	Phantom Types for the Human Body	37
2.3.2	Measurements of the Phantom Properties	41
<b>2.4</b>	<b>Regulations of Short Distance Wireless Communication</b>	<b>42</b>
2.4.1	EM Regulation	42
2.4.2	Regulation for SAR Limits	43
2.4.3	Wireless Communication Standards	45
<b>2.5</b>	<b>Implanted Antennas</b>	<b>55</b>
2.5.1	General Integration	56
2.5.2	Miniaturization of Antennas	58
2.5.3	Traveling Wave Antennas	60
2.5.4	Linear Conformal Antennas	63
2.5.5	Microstrip Antennas	64
2.5.6	Helical Antennas	71
<b>2.6</b>	<b>Conclusion of the State of the Art</b>	<b>72</b>
<b>3</b>	<b><i>Objectives</i></b>	<b>75</b>
<b>3.1</b>	<b>Objectives of the Project</b>	<b>75</b>
<b>4</b>	<b><i>Design of UHF Antennas for Implants</i></b>	<b>77</b>
<b>4.1</b>	<b>Design of an Implanted Planar CVC Antenna</b>	<b>78</b>
4.1.1	Antenna Layout	79
4.1.2	Simulation	80
4.1.3	Impedance Matching	81
<b>4.2</b>	<b>Design of an Implanted 3-D CVC Antenna</b>	<b>83</b>
4.2.1	Antenna Layout	83
4.2.2	Simulation	84
4.2.3	Impedance Matching	90
<b>5</b>	<b><i>Implementation</i></b>	<b>93</b>
<b>5.1</b>	<b>Implementation of the Antenna Prototypes in Test Beds</b>	<b>93</b>
5.1.1	Planar CVC Antenna in Test Bed	94
5.1.2	3-D CVC Antenna in Test Bed	95
<b>5.2</b>	<b>Implementation of the 3-D CVCA Prototype in a Smart Implant</b>	<b>95</b>
5.2.1	Smart Implant Layout	96
5.2.2	Transceiver Matching	97
<b>5.3</b>	<b>Body Phantoms</b>	<b>101</b>
5.3.1	Phantom Size and Composition for Planar CVCA	101

---

5.3.2	Phantom Size and Composition for 3-D CVCA	104
<b>6</b>	<b><i>Measurements and Results</i></b>	<b>107</b>
<b>6.1</b>	<b>Antenna Characterization</b>	<b>108</b>
6.1.1	Impedance Matching in the Phantom	108
6.1.2	Gain Measurements in Skin Tissue Phantoms	111
<b>6.2</b>	<b>Link Budget Estimate</b>	<b>119</b>
6.2.1	Near Field Measurement for the Planar CVCA	120
6.2.2	Perpendicular Measurements of the Planar CVCA	127
6.2.3	Far Field Measurements of the 3-D CVCA	128
<b>6.3</b>	<b>Functional Tests of the 3-D CVCA</b>	<b>135</b>
<b>7</b>	<b><i>Conclusions and Future Work</i></b>	<b>143</b>
<b>7.1</b>	<b>Result Summary</b>	<b>144</b>
7.1.1	Design of Implanted Antennas	144
7.1.2	Measurement Methodology	147
<b>7.2</b>	<b>Conclusions</b>	<b>147</b>
<b>7.3</b>	<b>Future Work</b>	<b>148</b>
<b>7.4</b>	<b>Acknowledgment</b>	<b>149</b>
	<b><i>Bibliography</i></b>	<b>107</b>
	<b><i>Publications</i></b>	<b>169</b>
	<b><i>Patent</i></b>	<b>223</b>





# **List of Figures**

---

Fig. 1.1. Remote patient monitoring (adapted from [4]).	3
Fig. 1.2. Patient monitored by wired sensors at an Intensive Care Unit [7].	4
Fig. 1.3. Implanted antenna in pacemaker [24].	6
Fig. 1.4. Communication links in Body Area Network.	8
Fig. 1.5. Wireless Cardiac Stimulation system (WiCS) (adapted from [31]).	9
Fig. 2.1. Loss tangent (adapted from [43]).	14
Fig. 2.2. Tissue distribution in normal (a) male and (b) female human bodies [47].	15
Fig. 2.3. Dissected view of a Voxel-Man model [48].	15
Fig. 2.4. Uppermost body tissue layers (adapted from [49]).	16
Fig. 2.5. Dielectric properties of (a) skin, (b) fat and (c) muscle in the UHF band.	18
Fig. 2.6. Principal polarization types [43].	20
Fig. 2.7. Normed Debye diagram separated for $\epsilon_r'$ and $\epsilon_r''$ [59].	21
Fig. 2.8. Cole-Cole model with single relaxation frequency [59].	22
Fig. 2.9. Dielectric properties of muscle [39].	23
Fig. 2.10. Frequency dependence of relative permittivity $\epsilon(x)$ and conductivity $\sigma(o)$ with $\alpha$ , $\beta$ and $\gamma$ dispersion regions (adapted from [63]).	25
Fig. 2.11. High-frequency and low-frequency current distribution in cell suspensions [66].	26
Fig. 2.12. Idealized spectrum of the real part of the complex dielectric permittivity of cell suspensions and tissues [65].	27
Fig. 2.13. The magnetic and electric field components of a plane wave in a lossy medium [58].	29
Fig. 2.14. FDTD simulation of electric and magnetic fields of a plane wave at 403.5 MHz hitting a 1-D phantom [70].	31
Fig. 2.15. Signal reflection at muscle - fat - air boundaries [71].	31
Fig. 2.16. Two E-field probes for dosimetry demonstrating their size [74].	33
Fig. 2.17. Principal schematic of electromagnetic susceptibility of the human body [76].	35
Fig. 2.18. Family of phantoms of anthropomorphic phantoms to investigate organ dose [79].	37
Fig. 2.19. Face down liquid phantom of the SAM v6 with robotic arm [80].	38

Fig. 2.20. Thelonious: voxel model of a 6-year-old boy from the "Virtual Family" showing skin, muscle, inner organs, blood vessels and skeleton [81].	39
Fig. 2.21. Measurement set up for coaxial probe calibration [42].	41
Fig. 2.22. Measurement techniques for permittivity [43].	42
Fig. 2.23. SAR measurement using the E-field method with (a) a liquid phantom [88] and (b) TWIN-SAM liquid body and head phantom made of fiberglass by SATIMO [89].	45
Fig. 2.24. Implantable RFID dosimeter as part of a monitoring system of radiation treatments [92].	46
Fig. 2.25. ISM frequency spectrum in different world regions (only 2.4 GHz is worldwide free usable) [95].	50
Fig. 2.26. Deployable smart diagnostic skin patch GT200 for fever monitoring [96].	51
Fig. 2.27 MedRadio frequency band divided into MICS and MEDS [101].	52
Fig. 2.28. Implanted MRI compatible CVC [103].	54
Fig. 2.29. Microstrip spiral folded antenna topology with short circuit: Layout (left) and implemented design (right) [106].	57
Fig. 2.30. Lossless matching antenna network with antenna input impedance $Z_A$ , source impedance $Z_s$ and reflection coefficient $\Gamma$ [108].	58
Fig. 2.31. Example of a multilayer microstrip antenna for MedRadio frequency [109].	59
Fig. 2.32. Simulation of momentary electric field of a wire: (a) non-insulated in air (b) non-insulated in a lossy medium and (c) insulated in a lossy medium [70].	61
Fig. 2.33. Different sizes of implants with external antenna for mammals [115].	63
Fig. 2.34. Circumference antenna for a pace maker for 403 MHz [70].	64
Fig. 2.35. (a) Top view, (b) side view and (c) prototype of a microstrip dual-band antenna for ISM 2.45 GHz and 403 MHz MICS frequency [116].	67
Fig. 2.36. Dual layer stacked microstrip antenna [120].	68
Fig. 2.37. Example of a 403 MHz dualstacked microstrip antenna [121].	69
Fig. 2.38. Matching bandwidth of the dual layer microstrip antenna [121].	69
Fig. 2.40. Two PIFA topologies for the MedRadio frequency [117].	70
Fig. 2.41. Layout of a PI-shaped wideband antenna for MICS band (left) and results of the tuned wideband return loss (right) [123].	71
Fig. 2.42. Design steps of rectangular spiral antenna over a ground plane.	71
Fig. 2.43. Intermediate prototype showing helical radiator [124].	72
Fig. 4.1. Subcutaneous implanted CVC port [103].	78
Fig. 4.2. Antenna simulation model with ceramic bottom layer.	80
Fig. 4.3. Radiating structure of the antenna with geometric parameters.	80
Fig. 4.4. -10 dB matching bandwidth, simulated in big phantom.	82
Fig. 4.5. Monopole one-sided on cone.	84
Fig. 4.6. Monopole meandering on cone.	84

Fig. 4.7. Topologies used during the optimization process: (a) Short monopole. (b) Long monopole. (c) Long monopole with short circuit to ground. (d) Extended monopole with short circuit. (e) Extended monopole with short circuit and loop. ....	86
Fig. 4.8. Smith chart showing the complex impedance matching between(a) 0.3 - 0.5 GHz and (b) 2.0 - 3.0 GHz referring to the design steps towards the final antenna model. 1) Short monopole. 2) Long monopole. 3) Long monopole with short circuit to ground. 4) Extended monopole with short circuit. 5) Extended monopole with short circuits and loop. ....	87
Fig. 4.9. Top view of the final antenna simulation model without the protection layer. ....	88
Fig. 4.10. Simulated $ S_{11} _{dB}$ vs. frequency of the 3-D CVCA in a 216 cm <sup>3</sup> skin phantom. ....	89
Fig. 4.11. Simulated $ S_{11} _{dB}$ vs. frequency of the 3-D CVCA in representative skin phantom for different isolation layer thicknesses. ....	90
Fig. 4.12. Simulated $ S_{11} _{dB}$ vs. frequency of the 3-D CVCA in representative skin phantom for different functional states. ....	91
Fig. 4.13. Simulated $ S_{11} _{dB}$ vs. frequency of the 3-D CVCA in representative phantom for different tissue phantoms and in the presence of battery and electronics. ....	91
Fig. 4.14. 3-D CVCA along with metallic parts corresponding to the presence of the battery and electronics. The non-metallic elements were removed for clarity. ....	92
Fig. 5.1. Planar CVC antenna prototype with detailed assembly (test bed). ....	94
Fig. 5.2. 3-D CVC antenna prototype with detailed assembly. ....	95
Fig. 5.3. Function blocks and layout of the PCB. ....	96
Fig. 5.4. Assembled prototype showing function blocks. ....	97
Fig. 5.5. Schematic view of low pass filter (top) and high pass filter (bottom) for the matching network. ....	98
Fig. 5.6. Schematic of high pass filter in ADS. ....	98
Fig. 5.7. $S_{11}$ , $S_{21}$ , $S_{13}$ , and $S_{23}$ for the simulated results. ....	100
Fig. 5.8. Mock board to test the matching antenna network. ....	101
Fig. 5.9. Dielectric properties of skin and of tissue-simulating liquid compared. ....	102
Fig. 5.10. Dielectric properties of muscle and of tissue-simulating liquid compared. ....	102
Fig. 5.11. Human torso-size phantom and location of the implant at height $z_{block}$ [mm]. ....	103
Fig. 5.12. Simulated antenna gain patterns in the xy-plane at 866.5 MHz for three phantom heights $z$ . ....	104
Fig. 5.13. Simulated antenna gain [dBi] in relation to phantom height $z/2=z_{block}$ [mm] for 403 MHz (vertical polarization, horizontal plane). ....	105
Fig. 5.14. Comparison of dielectric properties of dry skin and of tissue-simulating liquid. ....	105
Fig. 5.15. Comparison of dielectric properties of dry skin and tissue-simulating liquid at 2.45 GHz (solid theory, dash experimental). ....	106
Fig. 6.1. Return loss for the implanted antenna in different phantoms and compared to simulation result [127]. ....	108
Fig. 6.2. (a) Measurement locations for matching robustness study on the implanted antenna in test bed. (b) Return loss of the implanted antenna for the corresponding positions in the muscle case phantom compared to the skin case. ....	109

Fig. 6.3. Comparison of the reflection coefficient $ S_{11} $ of the 3-D CVCA simulated with different isolation thicknesses and measured. ....	110
Fig. 6.4. Measured reflection coefficient $ S_{11} $ in two experimental phantoms. ....	110
Fig. 6.5. Antenna gain measurement environment showing all function blocks. ....	112
Fig. 6.6. Antenna gain simulation models depending on the measurement setup (side view). Phantom size is identical in the three cases (350 x 250 x 165 mm <sup>3</sup> ). (a) Implanted antenna (r=8mm, w=2mm, $\alpha=215^\circ$ , $\beta=50^\circ$ , a=5mm, b=2mm) (b) Implanted antenna with test bed and (c) Implanted antenna with anechoic chamber feeding cable. ....	113
Fig. 6.7. Antenna gain simulation comparison at 866.5 MHz for measurement setup (a), (b) or (c) in Fig. 6.6 in horizontal (left) and vertical polarization (right).....	114
Fig. 6.8. Visualization of current for planar CVCA model with cable in phantom. ....	114
Fig. 6.9: Antenna gain comparison simulated (case (c) of Fig. 6.6, dotted) and measured (solid) at 866.5 MHz in horizontal (left) and vertical polarization (right). ....	115
Fig. 6.10. Far field measurement in the anechoic chamber showing phantom with inserted 3-D CVCA (absorbers removed) ....	117
Fig. 6.11. Calculated vs. measured results of vertical and horizontal gain component [dBi] in the horizontal plane at 403 MHz. ....	117
Fig. 6.12. Calculated vs. measured results of vertical and horizontal gain component [dBi] in the horizontal plane at 2.45 GHz. ....	118
Fig. 6.13. Measurement setup for on-chest measurement. ....	120
Fig. 6.14. (a) PIFA probe antenna and (b) the positions for on-chest measurements on phantom (dimensions in cm). ....	120
Fig. 6.15. Return loss of the reader antenna placed on the chest phantom and in free air. ....	121
Fig. 6.16. Power received by the from a reader placed on the chest at positions given by Fig. 6.13 and Fig. 6.14 (b). ....	122
Fig. 6.17. Power received by the reader placed on the chest at positions given by Fig. 6.13 and Fig. 6.14 (b) from the backscattered signal by the implanted RFID tag. ....	122
Fig. 6.18. Simulation arrangement with long cables (main section). ....	123
Fig. 6.19. Comparison of the transmission coefficient for the same set of positions and horizontally oriented PIFA, top line. ....	123
Fig. 6.20. Simulated transmission coefficient for bottom line, measurement uncertainty included, reader antenna horizontally oriented. ....	124
Fig. 6.21. Simulated transmission coefficient for top line, measurement uncertainty included, reader antenna horizontally oriented. ....	125
Fig. 6.22. Simulated transmission coefficient for top line, measurement uncertainty included, reader antenna vertically oriented. ....	125
Fig. 6.23. Simulated transmission coefficient for bottom line, measurement uncertainty included, reader antenna vertically oriented. ....	125
Fig. 6.24. Characterization of zones with different transmission reliability, reader antenna PIFA vertically oriented. ....	126
Fig. 6.25. Characterization of zones with different transmission reliability, reader antenna PIFA horizontally oriented. ....	126
Fig. 6.26. Near field measurements setup for reader to implant communications. ....	127

---

Fig. 6.27. Power received by the implanted tag from a reader placed perpendicularly to the chest for vertical and horizontal PIFA as reader antenna (see Fig. 6.26). Point A (0.46 m, -20 dBm). .....	128
Fig. 6.28. Power received by the reader from the implanted tag backscattered signal for vertical and horizontal PIFA as reader antenna (see Fig. 6.26). Point B (0.46 m, -70 dBm).....	128
Fig. 6.29. Principal sketch of the measurement of the transmit power $P_{TX}$ of the base station. ....	129
Fig. 6.30. Principal sketch of the measurement of the maximum sensitivity $P_{RXp}$ of the SN. ....	130
Fig. 6.31: Measured radiation diagram of the helica BS antenna at 2.45 Ghz .....	131
Fig. 6.32. Measured reflection coefficient of the base station helical antenna ( $ S_{11BS} $ ).....	131
Fig. 6.33. Principal sketch of the measurement for maximum transmission range. ....	132
Fig. 6.34. Measurement setup in anechoic chamber for link budget calculation in free space. ....	132
Fig. 6.35. Output signal of the CVC-implant PCB.....	136
Fig. 6.36. Measured reflection coefficient for the mock board at port 1. ....	136
Fig. 6.37. Reflection coefficient from the antenna placed into the phantom at the defined position. .....	137
Fig. 6.38. (a) Electronics connected to (b) the 3-D CVCA placed into the phantom. (c) Laboratory environment with base station and control laptop at maximum operating distance.....	137
Fig. 6.39. Implanted 3-D CVCA setup with proprietary electronics. ....	138
Fig. 6.40. Implanted electronics transmitting for an emergency event. ....	138
Fig. 6.41. Setup of the entire implanted smart system, with base station and control unit. ....	139
Fig. 6.42. Separation of human phantom from base station while communication session is maintained (see green light on the computer screen). ....	139



# **List of Tables**

---

Tab. 2.1. Dielectric parameter overview of the outermost body tissues in the frequencies of interest 403, 868 and 2450 MHz. ....	19
Tab. 2.2. Cole-Cole model parameters for skin, fat and muscle [60].....	23
Tab. 2.3. Complex impedance for human tissues at 403 MHz [69].....	30
Tab. 2.4. Transmission factor for normal wave incidence at tissue boundaries at 403 MHz [69].....	31
Tab. 2.5. Selection of commercially available software with different EM solver. ....	40
Tab. 2.6. Comparison of numerical solver methods [83]. ....	40
Tab. 2.7. SAR limits specified by various administrations [86]. ....	44
Tab. 2.8. Frequency ranges and associated maximum allowed field strengths [90], [94]. ....	48
Tab. 2.9. Minimum required immunity levels according to IEC/EN60601-1-2 [94]. ....	49
Tab. 2.10. Recommended separation of RFID transmitter to medical devices [cm] [94]. ....	49
Tab. 2.11. Benefits and possible future scenarios based on operating modes for NFC devices [99]. ..	51
Tab. 2.12. MedRadio specific requirements for different frequency bands [100], [101]. ....	54
Tab. 2.13. Comparison of radiated power ( $P_{in}=1W$ ) and radiation efficiency between PIFA and microstrip antenna of the same size [117]. ....	70
Tab. 4.1. Final antenna parameters at 868 MHz. ....	81
Tab. 4.2. Final geometry of the 3-D CVC antenna. ....	88
Tab. 5.1. Component values of the low pass filter (left) and high pass filter (right). ....	99
Tab. 5.2. Dielectric properties of body tissue [53]. ....	102
Tab. 6.1. Link budget calculation according to the measured results for line of sight.....	133
Tab. 6.2. Resulting values of sensitivity of the electronics. ....	134
Tab. 7.7.1. Basic performance comparison of implanted antennas for MICS based on [153]. ....	145
Tab. 7.7.2. Basic performance comparison of implanted antennas for ISM 2.4 GHz based on [153]. ....	146





# *Chapter 1*

## ***Introduction***

---

This chapter gives an introduction to the topic of the Ph.D. thesis at hand. It determines the boundaries of the scope of the work, exhibits the necessity of modern implants and wireless communication in this regard, sets the context of wireless communication in body surroundings, points out major challenges of implanted antenna design and finally, summarizes the structure of the document.

Information transfer between implanted medical devices and the environment outside the body implicates, without doubt, major benefits in the area of modern health care. In the endeavor to take one step further towards autonomy and abolish connecting cables, it is essential to carry out comprehensive research on a key technology in this field of investigation: implantable antennas for smart implants.

In the extremely sensitive matter of health, smart implants (see section 1.2) can only provide confidence at the time when a long term transmission of the signals can be guaranteed.

Wireless communication of smart implants in autonomous medical systems can be established in a reliable way once the antenna has accurately been characterized in a measurement environment that meets the real circumstances of the targeted application.

In the present dissertation, essential facts are gathered throughout the design and implementation processes of two subcutaneous UHF band antennas for smart implants. In addition, the use of a novel characterization procedure marks a contribution to current knowledge about the verification of antenna property data.

While prototypes of the respective antennas were manufactured and evaluated in the design process, the fabrication of a fully assembled medical device was still pending at the time of writing this thesis.

## **1.1 BACKGROUND**

In Europe, where the average life expectancy has already reached the mark of 80 years, and almost 25% of the population will be over 65 by 2020, the over-ageing population is becoming a challenge for the social and health systems [1].

However, in nowadays' society, not only elderly people suffer chronic disorders, but the health condition of the younger generation is giving cause of major concern, too. The advance of lifestyle diseases which affect the cardiovascular system, or diabetes, reason the necessity to come up with long-sighted perspectives to improve the wellbeing of the concerned persons. Likewise keeping the health care costs within affordable limits is an ambitious enterprise.

### **1.1.1 REMOTE PATIENT MONITORING**

The concept of remote patient monitoring is on the way to find solutions for holding the personnel expenses for hospital stays down and allow the patients a convenient lifestyle in familiar surroundings at the same time.

In this context, body area networks (BAN) (see section 1.3), i.e., wireless sensor networks (WSN) optimized for physiological parameter

monitoring, are a key enabling technology [2]. In a BAN superficial sensor nodes placed around the body set up a connection among each other. A central node, the controller, is also worn on the body. Whilst external sensors, such as those for measuring vital signs, have continued to improve, it is the area of implantable sensors that has generated the greatest interest [3]. The option of embedding smart implants (see section 1.2) into a BAN significantly expands the spectrum of remote patient monitoring (see Fig. 1.1), as certain data can only be gathered from inside the body.

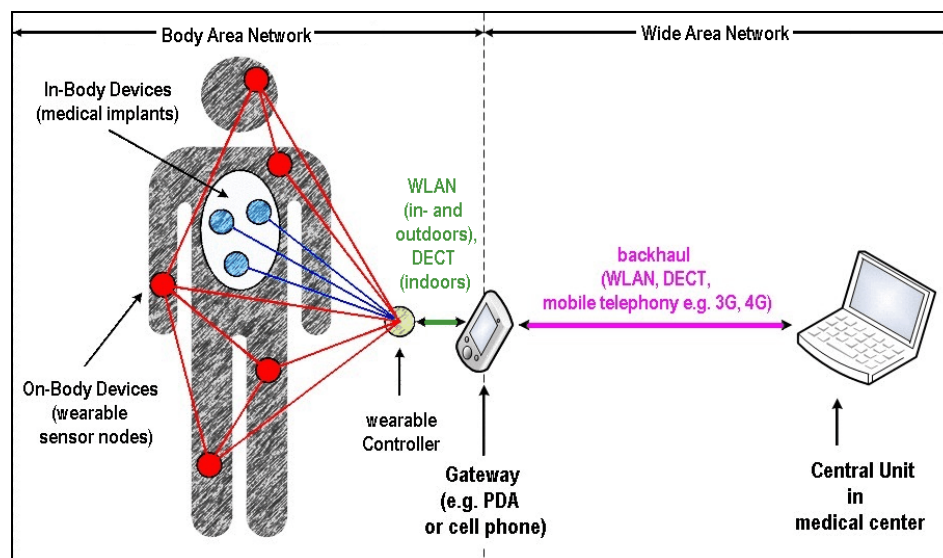


**Fig. 1.1. Remote patient monitoring (adapted from [4]).**

A gateway device may also be part of the wearable network. It could be a multifunction device, such as a personal digital assistant (PDA), mobile phone [5], or alternatively, it may be a fully proprietary telemedicine unit. As soon as the communication with the controller is initiated, the process of wireless patient monitoring or telemetry can be supervised remotely from a medical center via backhaul communication technologies [6], such as wireless local area network (WLAN), digital enhanced cordless telecommunications (DECT), or mobile telephony.

### 1.1.2 MONITORING HOSPITAL PATIENTS

Particularly with regard to patients in intensive care units (ICU), implanting medical devices capable of transmitting signals wirelessly from inside their bodies to a monitoring device outside, provides a promising perspective to those confined to bed.

A major advantage of wireless implantation technology is the possibility to reach innermost and inaccessible places in the body and perform in-vivo, in-real-time diagnosis. In the pursuit of reducing the number of cables the patient is connected to, as shown in Fig. 1.2, wireless communication of active medical implants (AMI), also known as smart implants, in autonomous systems considerably enhances the standard of health care quality. Dangerous situations due to the inadvertent dislocation of the applied sensors caused by a movement of the patient can be prevented. Furthermore, the abolition of sensor and power supply cables driven through the skin eliminates the risk of possible infections at these spots.



**Fig. 1.2. Patient monitored by wired sensors at an Intensive Care Unit [7].**

Implants like intravenous catheters, prosthetic heart valves, prosthetic joints, pacemakers, etc. are widely used in healthcare saving millions of lives. Yet, the utilization of implants involves a certain risk of infection [8]. The importance of biofilm-associated infection was estimated to represent over 80% of human microbial infections [9]. Approximately 50% of hospital-acquired infections per year in the U.S. are associated with indwelling devices [10]. The detection and diagnosis before the treatment of the infectious processes caused by microbial biofilms is an ongoing unsolved problem. The period between the infection and the detection, the task of analyzing which bacteria is growing, often is very time-consuming. In fact, an infectious process not detected on time may end up in several medical complications for which, in many cases, the only way to ensure a good outcome is to remove the device [11], [12]. Those incidents cause high expenses and, on top, jeopardize the patients' health.

A way to achieve advances on the treatment of the infection is to develop new methods to improve biofilm early detection and reliable signalization. To accomplish this purpose it would necessary to develop a new generation of intravascular catheters. Novel techniques allow in-depth in vitro study of the most important aspects of the formation of bacterial biofilms.

A recorded historic data, stored in the device, can be used as the reference value for the detection of bacterial biofilm. A new, smart device should consist of a sensor and an electronic module to control the measurement and to process the communication wirelessly to a external reader. Such a smart implant which provides continuous monitoring of, e.g., the reservoir content of central venous catheters (CVC) and send an alarm signal in case of bacterial colonization would be of high value in the clinical practice [13].

### 1.1.3 TELEMETRIC IMPLANT DEVELOPMENTS

Currently, modern applications of remotely operated wireless smart implants already include prosthesis control via myoelectric sensors [14], interaction with cochlear implants [15], artificial electrical stimulation of the surviving ganglion cells [16], automated drug delivery devices [17], etc. Apart from that, new ways to monitor parameters, such as blood pressure [18], glucose ratio for diabetes treatment [19] and intracranial pressure [20] took center stage over the last decade.

Nevertheless, there is a major trouble hard to be tackled: while in on-body WSN each sensor node has its own easily accessible energy supply, sustainable power supply still remains a challenge to overcome in smart implants. In this regard, advances in power supply miniaturization, increased battery duration, reduced energy consumption, etc. will be essential, particularly in AMIs [3]. Latest research approaches investigate the options of wireless power supply for implants from outside (e.g., via sound [21]) or by means of energy harvesting (i.e., making use of the energy produced naturally in the body, e.g., body heat [22]). Though, until these concepts are technically mature, completely battery-less solutions, e.g., radio frequency identification (RFID), may be another path to follow.

In summary, the progressive development of smart implants contributes significantly to the independence, safety and last but not least the health of the patients.

## 1.2 SETTING OF TERMS

**Smart systems** are, by definition, capable of describing and diagnosing a situation. Not only are they prognostic, but also able to make decisions or help to decide by enabling the artifact to interact with the environment. Smart systems are as small as possible, networked and energy autonomous [23]. However, these systems cover a broad field, which is why interdisciplinary investigation is a feasible option.

In the following, **smart implant** makes reference to the autonomous medical device that is to be implanted into the human body as part of such smart system. In the actual scientific literature and standards the abbreviation AMI for active medical implant has been established.

Special antennas are implemented in smart implants to enable the wireless communication in the autonomous system. Throughout this work, the term **implanted antennas** will be used to refer to antennas that are destined to be implanted into the human body as part of smart implants. The antenna performance is exclusively restricted to environments that possess the electromagnetic properties of the human body. Therefore, they cannot be operated whenever they are surrounded by air. In section 2.5 several antenna topologies that can be used in implants are addressed.

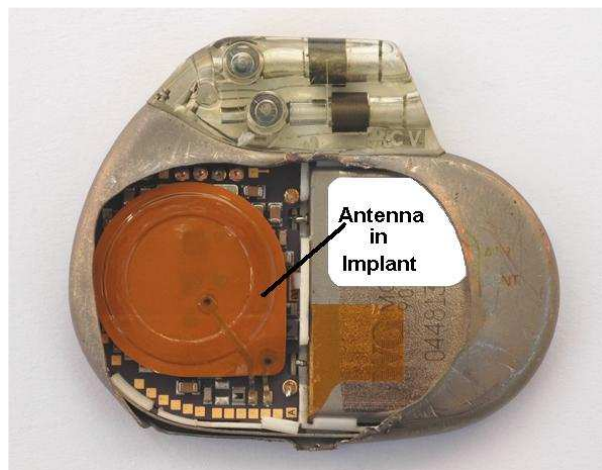


**Fig. 1.3. Implanted antenna in pacemaker [24].**

### 1.3 WIRELESS COMMUNICATION IN BODY SURROUNDINGS

The quest for imparting selected information from a human being to a base station without resorting to physical bonding is pursued in body-centric wireless communication systems [6]. In order to accomplish this mission, different ways are followed to establish the requisite communication link:

*Off-body communication:* A controller worn on the body surface contacts a wide area network (WAN) via WLAN or DECT (see Fig. 1.1). The broadcast between the controller and the gateway must be independent from the position of the body. This technique is employed whenever a considerable distance from the controller to the gateway device is to be bridged.

*On-body communication:* A BAN comprises a series of attachable miniature sensor/actuator nodes each of which is able to communicate with other sensor nodes or with the controller [25]. Low power wireless network protocols (e.g., ZigBee® [26], Bluetooth®LE [27], ANT® [28]) are used for transmitting data (see Fig. 1.4). The communication channel is shared by all nodes and the short-distance broadcast along the body alters due to clothes and movements. Such BANs are frequently employed in user monitoring (e.g., fitness training or recreational activities), specialized occupations (such as paramedics and fire fighters) and, above all, in the medical field (see section 1.1.1).

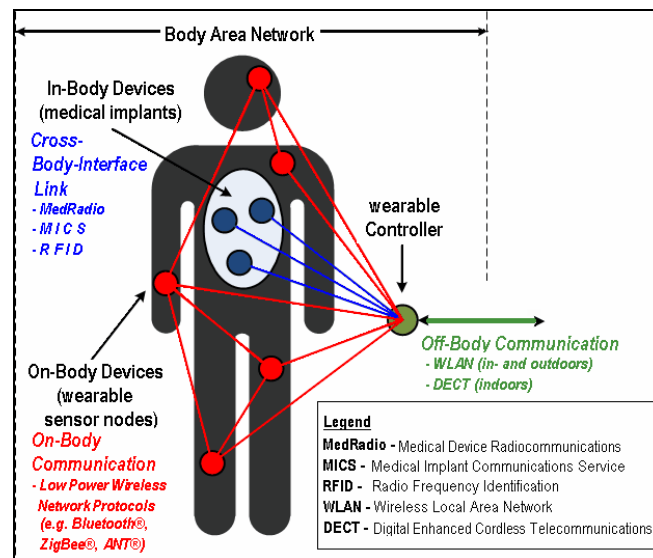


**Fig. 1.4. Communication links in Body Area Network.**

*Cross-body-interface link:* An implanted device inside the body connects with an outside controller placed on or near the body. Here, technologies like RFID, Medical Device Radiocommunications Service (MedRadio), Medical Implant Communications Service (MICS), etc., are approved for data transmission (see section 2.4). The link crosses the body-air interface and the channel harbors exclusively the communication between the implanted antenna and the controller. However, the link performance is highly dependent on the electromagnetic properties of the body tissues to cross (see section 2.1) and finding the adequate transmission frequency also requires careful consideration. After all, wireless communication in implants is designated for medical applications in which the patient carries an implant for continuously monitoring crucial physiological parameters (see section 1.1.2).

For completeness, a last vision is to be mentioned which, indeed, is most desirable, but up to now hardly viable, i.e., at the most within very short distances and frequencies below 1 MHz [29], [30].

*Inner-body link:* Implanted devices connect among each other, avoiding hereby the body-air interface. Their full adaption to the highly resistive environment in the interior of the body is considered indispensable.



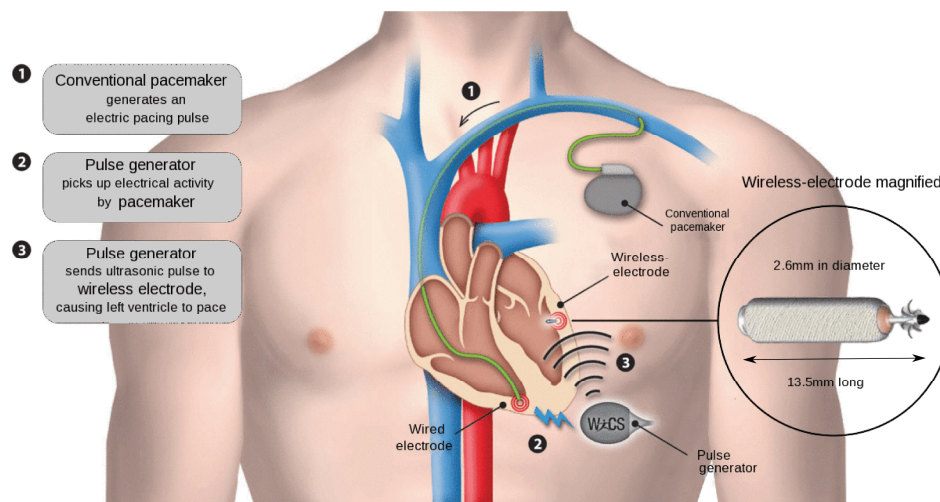


Fig. 1.5. Wireless Cardiac Stimulation system (WiCS) (adapted from [31]).

Since the present work is on implanted antennas, the cross body link interface is in the focus of attention.

#### 1.4 CHALLENGING ASPECTS OF IMPLANTED ANTENNA DESIGN

The design of implantable antennas faces, in fact, a range of challenges. Primarily, the constraints that have to be overcome derive from the demanded properties, some of which happen to be mutually exclusive. In general, implanted antennas are to be:

**Small:** In implants, the limits of space dedicated to the antenna are extremely narrow. Therefore, implanted antennas need to be preferably small in size.

**Directive:** Implanted antennas are to be highly directive in order to reach an elevated communication range. Given the required small size of the antenna, however, general matters of physics implicate difficulties in accomplishing that directivity.

**Highly efficient:** The most desirable high efficiency is undermined by the body environment, which causes high dielectric losses.

**Low frequency:** At low frequencies the dielectric losses in the body environment remain low. Nevertheless, a small-in-size antenna topology actually matches a high frequency to be operated in.

**Adjustable:** The antenna surface has to be adapted to the shape of the implant without causing malfunctions or function alterations.

**Insulated:** The metal component has to be outright covered in biocompatible material to avoid any contact and therefore reaction with the body tissue.

The dissertation at hand exhibits the design and implementation processes of two subcutaneous implanted UHF antennas for smart implants in autonomous medical systems. Suitable measurement environments are configured and most notably, a novel characterization procedure is used to allow the verification of antenna property data in a reliable way.

## 1.5 STRUCTURE OF THE DOCUMENT

The subsequent chapters of the document are structured as follows:

After having given an introduction to the subject in Chapter 1, Chapter 2 examines the issue-related state of the art providing necessary background information and laying the foundation for further investigation. Regulatory issues with the resultant standards are addressed as well as the human body structure and tissue properties, which leads to the presentation of phantoms as artificial models of the human body. Next, different antenna types used in implants are exemplified, e.g., traveling wave, microstrip and helical antennas. The state of the art report closes with essential considerations concerning the selected transmission protocol and antenna types. Chapter 3 summarizes the research goals of the project, paving the way for the practical part of the dissertation. This experimental partition starts with Chapter 4 illustrating the simulation of two novel antennas that address the specifications required in this context. Chapter 5 is entirely dedicated to the subject of implementation, that is on the one hand the description of the two antenna prototypes with their test beds assembled and on the other hand, the implementation of the dual band antenna in the smart implant for which it was designed. Chapter 6 details the measurements carried out in the selected environments and sums up the relevant results obtained. Above all, a novel characterization procedure is introduced as crucial contribution to the calculation of the discovered uncertainty factors. To close with, Chapter 7 provides a space for drawing final conclusions and gives a forecast on future lines.

## *Chapter 2*

# ***State of the Art***

---

This chapter illustrates the basic concepts and relevant terms of the dielectric spectrum of biological tissues and their distribution in the human body, with a particular focus on the frequencies of interest 403 MHz, 868 MHz as well as 2.45 GHz, explains phenomena of RF wave propagation in dielectric media and addresses the issues of the mutual influence between electromagnetic waves and the human body, whereupon, phantoms are introduced as appropriate body models. Furthermore, a summary of the currently valid regulations concerning applicable short range wireless communication protocols is given and the chapter concludes with a comprehensive state of the art review of antenna topologies suitable for implantation.

## 2.1 DIELECTRIC ANOMALY OF BODY TISSUES

This section presents a review of the dielectric (insulating) properties of body tissues, detailing the respective key parameters as well as transferring this knowledge into the anatomical distribution of tissues in the human body with a final focus on the frequencies of interest 403 MHz, 868 MHz and 2.45 GHz.

The necessity of knowing the environment in which an antenna is going to operate makes basic information about body tissues and their distribution in the human anatomy fundamental requisites in the design of implanted antennas. The interaction between materials and electric fields can be explained by the respective media's electromagnetic (EM) parameters. The electrical properties of biological tissues and cell suspensions have been of interest for over a century for many reasons. They determine the pathways of current flow through the body, which gives them fundamental importance in studies of the biologic effects of EM fields [32]. On a macroscopic level, body tissues are described by their permittivity  $\epsilon$  and conductivity  $\sigma$ . The permittivity characterizes the tissue's ability to trap or store charge or to rotate molecular dipoles, whereas the conductivity describes its ability to transport charge [33].

### 2.1.1 DIELECTRIC PROPERTIES OF TISSUES

Since biological tissues are non-magnetic, i.e., with permeability  $\mu = \mu_0$ <sup>1</sup> [34], EM field penetration and propagation in the body is a function of material properties such as electrical permittivity  $\epsilon$  and electrical conductivity  $\sigma$  [35]. The tissues of the human body feature dielectric properties, i.e., when they are placed into an electric field, electric charges do not flow through the material, as in a conductor, but only slightly shift from their average equilibrium positions causing dielectric polarization [36].

At low frequencies, the constitutive dielectric parameters of tissues are real and frequency independent. At higher frequencies, these parameters often alter with frequency and become complex. In addition to frequency dependence, the constitutive parameters may also depend on position (inhomogeneous) and direction (anisotropic) in the material, as well as on field strengths (non-linear). The complex value of permittivity also indicates that the medium is lossy (dissipates power, e.g., heat) [37], [38]. The dielectric properties are determined as  $\epsilon'$  and  $\epsilon''$  values, or  $\epsilon'$  and  $\sigma$  values, as a function of frequency [39].

---

<sup>1</sup>  $\mu_0$ : permeability of free space or magnetic constant.

### 2.1.1.1 Permittivity

From a macroscopic point of view dielectric properties of materials are quantified by their bulk complex permittivity [40]. The permittivity  $\epsilon$  of a material measures its ability to store and consume the energy of an applied electric field as it indicates the extent to which charge distribution can be polarized (see section 2.1.2). In a lossy medium, the permittivity is complex and can be expressed as:

$$\epsilon = \epsilon_0 \epsilon_r = \epsilon_0 (\epsilon_r' - j\epsilon_r'') = \epsilon' - j\epsilon'' \quad (2.1)$$

$\epsilon_0$  refers to the vacuum permittivity, i.e., the electrical energy stored in vacuum, and  $\epsilon_r$  describes the relative permittivity<sup>2</sup>. In this expression is  $\epsilon_r'$  the real part and  $\epsilon_r''$  the imaginary part of the relative permittivity. The real part of permittivity  $\epsilon'$  exhibits the storage of the electric field energy and the imaginary part  $\epsilon''$  reflects the losses in the medium [38].

### 2.1.1.2 Conductivity and Losses

The **conductivity**  $\sigma$  (S/m) describes the ease with which free charges in a material can be moved by an electric field. The moving free charges are typically electrons or in some cases ions. Tissues have finite ionic conductivities commensurate with the nature and extent of their ionic content and ionic mobility [39]. In biological tissues, an applied electric field induces ionic as well as displacement currents. Displacement currents and their losses are represented by the displacement conductivity  $\sigma_d$ , while ionic currents and the corresponding losses are expressed by the frequency-independent ionic conductivity  $\sigma_i$ . The total conductivity of a material is given by [41]:

$$\sigma = \sigma_d + \sigma_i \quad (2.2)$$

The **dielectric loss factor** is the imaginary part of relative permittivity, which represents the losses of the applied field associated with energy dissipation, i.e., the conversion of electric energy to heat energy in the material, [42] due to ionic currents and polarization. It is related to the

---

<sup>2</sup> Misleadingly, both relative permittivity and absolute permittivity, are frequently referred to by the historical term of dielectric constant. Apart from that, the real part of complex relative permittivity is often called relative permittivity or permittivity, omitting the complex nature of the quantity [32]. The complex relative permittivity, being a relative quantity, has no unit [41].

total medium conductivity  $\sigma$  and angular frequency  $\omega$  of the electric field through the expression [39]:

$$\epsilon_r'' = \frac{\sigma}{\omega\epsilon_0} \quad (2.3)$$

Equation (1.3) implies that at a certain frequency, the losses increase with increasing conductivity. The dielectric loss factor is also required to calculate the **loss tangent**, a dielectric parameter that describes the ratio (or angle in a complex plane, see Fig. 2.1) between the real and imaginary parts of the relative permittivity, i.e., the resistive (lossy) component of an electromagnetic field and its reactive (lossless) counterpart:

$$\tan \delta = \frac{\sigma / \omega\epsilon_0}{\epsilon_r'} \quad (2.4)$$

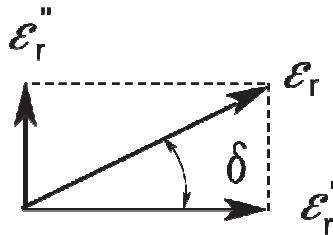


Fig. 2.1. Loss tangent (adapted from [43]).

### 2.1.2 ANATOMICAL TISSUE DISTRIBUTION IN HUMANS

For biological materials, water is one of the major constituents. The relative percentage of water in the body varies with such things as gender, age, physiologic state, and tissue type. Water content and state (free or bound [44]) of biological tissues play important roles in EM field penetration and propagation in the body [35] and the contributions of water to the dielectric properties of tissues at microwave and UHF frequencies have been studied fundamentally [45].

Groups of cells that are similar in structure and function are called tissues. The anatomical tissue distribution in humans occurs individually and in a gender- and age-specific manner [46]. For instance, females tend to accumulate excess fat in the thighs, hips and breasts, whereas men first

increase adipose in the abdomen. Visual displays of the tissue distribution inside the human body are offered by projects such as The Visible Human<sup>3</sup> Project<sup>®</sup> (see Fig. 2.2) or Voxel-Man (see Fig. 2.3).

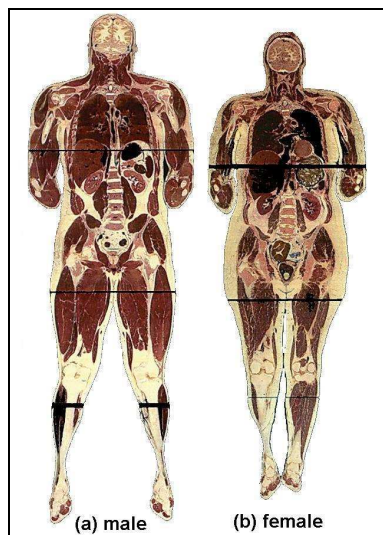


**Fig. 2.2.** Tissue distribution in normal (a) male and (b) female human bodies [47].

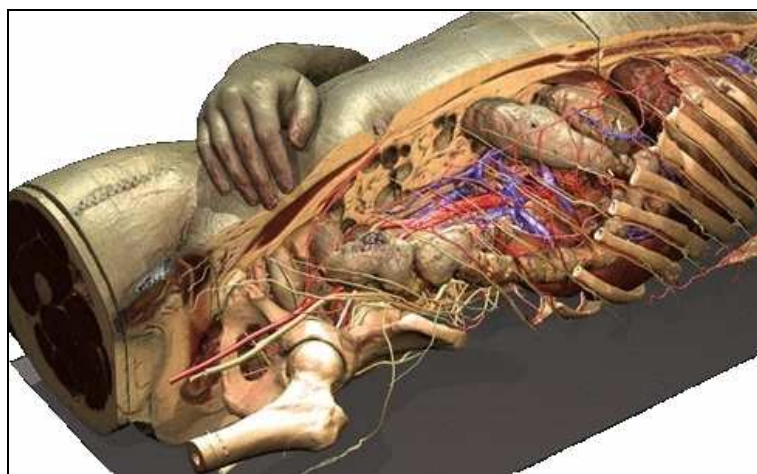


**Fig. 2.3.** Dissected view of a Voxel-Man model [48].

<sup>3</sup> The Visible Human Project<sup>®</sup> is an effort of the U.S. National Library of Medicine's (NLM) to create complete, anatomically detailed, 3-D representations of the normal male and female human bodies. The datasets comprehend Computed Tomography (CT), Magnetic Resonance (MR) and cryosection high resolution images gained from representative cadavers sectioned at intervals of one millimeter (the male) and one-third of a millimeter (the female) [47].

The scope of this section will concentrate on the three outermost tissue layers of the human body, which play a decisive role in the matter of wireless communication in implants: skin, fat and muscle (see Fig. 2.4).

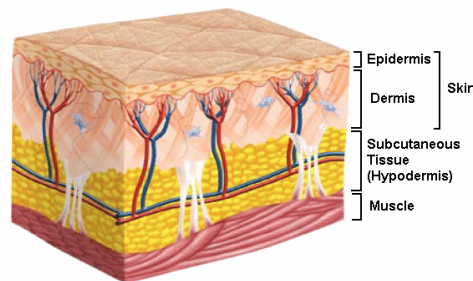


**Fig. 2.4. Uppermost body tissue layers (adapted from [49]).**

- a) **Skin:** one essential function of the skin is to form a barrier that protects the body from dehydration. The human skin is composed of two primary tissue layers: the Epidermis and the Dermis [46]. The uppermost layer of the Epidermis, the Stratum Corneum, consists of 10-15 layers of dead skin cells and comprehends a thickness of 10-15  $\mu\text{m}$  in dry state (and up to 40  $\mu\text{m}$  when hydrated). A series of lipid bilayers is incorporated and the water content of the Stratum Corneum is only around 15 to 20% of the dry weight but can vary according to humidity of the external environment [50]. It is therefore highly resistant (low conductivity). The lower part of the Epidermis is the Viable Epidermis with about 30  $\mu\text{m}$  of thickness [51]. Just like the Dermis underneath, the Viable Epidermis holds moisture in aqueous intercellular spaces and comprises a network of blood vessels. Viable Epidermis and Dermis dispose of a higher conductivity than the Stratum Corneum. The dielectric properties of composite skin fall within the bounds formed by all its components [39]. The skin's subcutaneous tissue or Hypodermis is technically no part of the skin and consists mostly of adipose (fat) and some areolar connective tissue [46].
- b) **Fat:** adipose tissue is a type of loose connective tissue designed to store fat. In the subcutaneous layer between skin and muscle it helps insulate the body from temperature changes [46]. Fat cells principally contain lipids, primarily composed of triglycerides, which are non-polar and insoluble in water, which leads to the fat layer having the least water content, compared to skin and muscle. Shielded from the water, it is thus poorly conducting at all frequencies. Fat tissue suffers a high degree of structural heterogeneity, which is being reflected in its composition and



dielectric properties. In practical applications, this translates into a source of errors, wherefore a single value cannot be chosen for the permittivity or conductivity. Instead, a range of values should be applied, unless the exact composition of the tissue is known [45]. As a result of the drastic change in medium properties compared to the surrounding skin and muscle, a standing-wave pattern is produced inside the fat layer. This may lead to an increased signal absorption when the thickness of the layer is a quarter of a wavelength in the medium [52]. This is equivalent to approximately 9 mm at 2.45 GHz, 37.7 mm at 868 MHz and 77.7 mm at 403 MHz [53].

- c) **Muscle:** muscles are composed of fibers and aligned in the direction of muscle contraction. Electrical conduction along the length of the fiber is significantly easier than between the fibers, for which reason the transverse conductivity is significantly lower than the longitudinal conductivity [33]. Apart from that, muscle tissues are not homogeneous and can have certain infiltrations of fat and vessels [36]. Muscle is therefore a very lossy medium. Muscle tissue manifests anisotropic electric properties below 10 MHz [39]. The common muscle thickness is about 30 mm [52], can amount up to 39.4 mm [54] and recent studies even reported maximum values of 47.5 mm [55].

Accordingly, from an engineering point of view, the different tissues in the human body can be classified into two basic groups: high-water-content tissues with high permittivity and losses (e.g., skin and muscle [56]) and low-water-content tissues which have lower permittivity and losses (e.g., fat). Fig. 2.5 displays the respective alterations in loss tangent and relative permittivity, the key parameters for implanted antenna design.

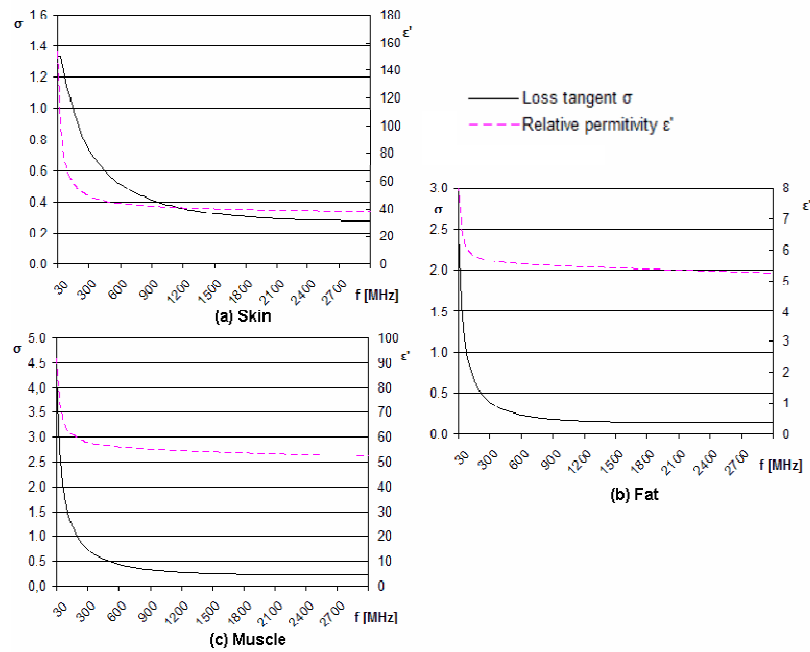


**Fig. 2.5. Dielectric properties of (a) skin, (b) fat and (c) muscle in the UHF band.**

The following table (see Tab. 2.1) displays the dielectric properties of skin, fat and muscle, the three outermost tissue layers of the human body, at frequencies of 403 MHz, 868 MHz and 2.45 GHz. Drastic changes in the values of conductivity and relative permittivity at all frequencies can be noted at the skin-fat and fat-muscle interfaces.

	Skin dry	Fat <sup>4</sup>	Muscle	Skin dry	Fat	Muscle	Skin dry	Fat	Muscle
Frequency [MHz]	403			868			2450		
Conductivity [S/m]	0.69	0.04	0.80	0.86	0.05	0.93	1.46	0.10	1.74
Relative permittivity	46.7	5.58	57.1	41.6	5.47	55.11	38.0	5.28	52.73
Loss tangent	0.66	0.33	0.62	0.43	0.19	0.35	0.28	0.15	0.24
Wavelength [mm]	103	310	94.3	52.4	147	45.9	19.7	53.1	16.7
Skin depth <sup>5</sup> [mm]	55.2	308	52.5	40.8	248	42.9	22.6	117	22.3

**Tab. 2.1. Dielectric parameter overview of the outermost body tissues in the frequencies of interest 403, 868 and 2450 MHz.**

A review of relevant literature and databases [39], [57], [53], [52] quickly reveals discrepancies in the measured values of the properties. Coupled with the effects of water content and state (free or bound) [44], the variations can account for an appreciable amount of the reported range of permittivity. However, multiple other factors such as temperature, orientation, measuring techniques, instrumentation, and tissue dissimilarities can also affect the measured permittivity of biological tissues [35].

### 2.1.3 TISSUE-SPECIFIC PHENOMENA

#### 2.1.3.1 Polarization

The concept of polarization is an important property of an EM wave and describes the various types of electric field variation and orientation. [58]. When an EM wave is propagating, the orientation of the resulting field may vary in space, depending on the type of wave and the medium [59]. Permittivity (see section 2.1.1.1) describes the polarization induced in a material and the associated losses. Dielectric materials are electrically insulative and yet susceptible to polarization in the presence of an electric field. The fundamental phenomenon behind polarization is the fact that an applied electric field affects the charged particles of a material in a manner that positive and negative charges are being attracted to opposite directions. Dielectric materials commonly exhibit not all, but at least one of the main

<sup>4</sup> In the literature conductivity and relative permittivity of fat vary about 5 - 10 % because of different measurement methodologies, inhomogeneity of the tissue and its water content [52].

<sup>5</sup> The skin depth describes the EM field's depth of penetration into tissues where the power is attenuated by 8.7 dB (see section 2.2.1).

polarization phenomena assembled in Fig. 2.6 that contribute to their overall permittivity:

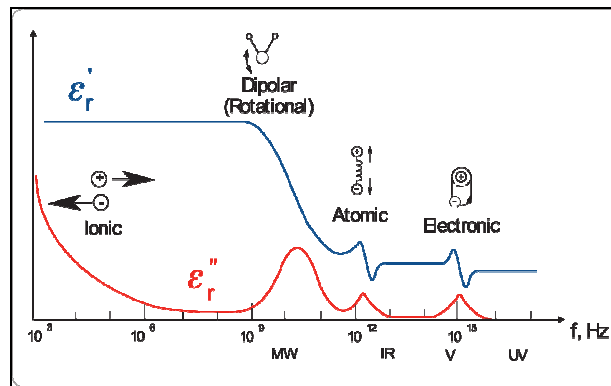


Fig. 2.6. Principal polarization types [43].

In tissues the magnitude of permittivity is mainly dependent on the polarization (see section 2.1.3.1) mechanism, which further depends on the frequency (see section 2.1.3.2). When the frequency of the applied field is increased, the dipoles tend to orient with the field every time its direction is reversed. This process requires some finite time because of the limited freedom of the molecules to move in the liquid.

The point by which the dipoles are finally too slow to orientate with the field is called the **relaxation frequency** [38].

The relaxation frequency  $f_c$  is inversely related to the relaxation time constant  $\tau$ .

$$\tau = \frac{1}{\omega_c} = \frac{1}{2\pi f_c} \quad (2.5)$$

Materials with a single relaxation time constant can be described by Debye first order equation.

$$\varepsilon(\omega) = \varepsilon' - j\varepsilon'' = \varepsilon_\infty + \frac{\varepsilon_s - \varepsilon_\infty}{1 + j\omega\tau} \quad (2.6)$$

for  $\omega = 2\pi f = 0$   $\varepsilon(0) = \varepsilon_s$ ; and for  $\omega = 2\pi f = \infty$   $\varepsilon(\infty) = \varepsilon_\infty$

$\epsilon_s$  is called the static dielectric constant and  $\epsilon_\infty$  the optical dielectric constant. They represent the real part of the permittivity at zero and infinite frequency respectively.

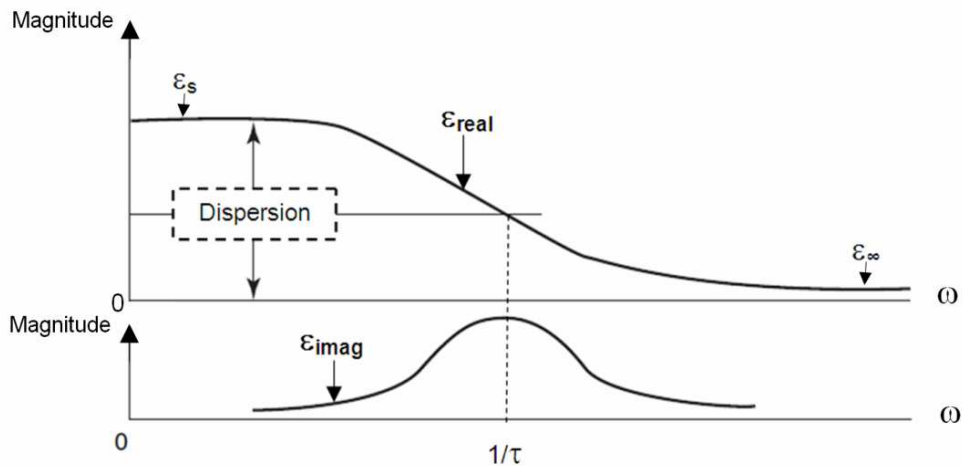


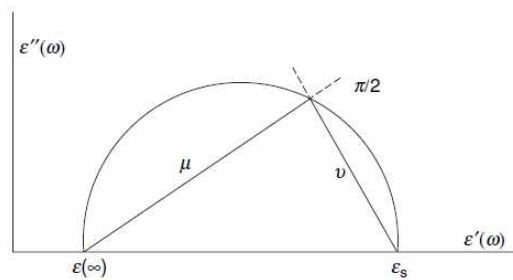
Fig. 2.7. Normed Debye diagram separated for  $\epsilon_r'$  and  $\epsilon_r''$  [59].

Fig. 2.7 illustrates the alteration of  $\epsilon_r'$  and  $\epsilon_r''$  because of the physical phenomena around the relaxation frequency  $f_c$ .

At frequencies below relaxation the dipoles are able to follow the alternating field. The electric field is slow enough so the polarization develops fully and the loss ( $\epsilon_r''$ ) raises proportional to frequency. As the frequency nears to the frequency  $f_c$   $\epsilon_r''$  continues to increase but  $\epsilon_r'$  decreases as dipoles start delaying from the electric field.  $\epsilon_r''$  peaks in the transition region at the relaxation frequency  $f_c$ , where the  $\epsilon_r'$  is already decreasing, due to the phase lag between the dipole alignment and the electric field. Above the relaxation frequency both  $\epsilon_r''$  and  $\epsilon_r'$  drop off as the electric field is too fast to influence the dipole rotation and the orientation polarization disappears.

The two diagrams in Fig. 2.7 also show, that  $\epsilon_r''$  losses are raising significantly when  $\epsilon_r'$  changes over frequency. This means that dissipation and dispersion are directly connected.

This connection is visualized by the Cole-Cole diagram where the imaginary part ( $\epsilon_r''$ ) is on the vertical axis and the real part ( $\epsilon_r'$ ) on the horizontal axis and with frequency as the independent parameter.



**Fig. 2.8. Cole-Cole model with single relaxation frequency [59].**

A material that has a single relaxation frequency as exhibited by the Debye relation will appear as a semicircle with its center lying on the horizontal  $\epsilon_r''=0$  axis and the peak of the loss factor occurring at  $1/\tau$ . The relaxation frequency  $f_c$  is material specific but biological tissues show not just one single relaxation time but a distribution over frequency behavior. A material with multiple relaxation frequencies will be a semicircle (symmetric) distribution or an arc (nonsymmetrical distribution) with its center lying below the horizontal  $\epsilon_r''=0$  axis.

As biological tissues have broader dispersions in reality, they are more closely modeled, i.e., with a 4-term Cole-Cole equation (see equation (2.7)) by adding also the ionic conductivity [39].

$$\epsilon(\omega) = \epsilon_{\infty} + \sum_{n=1}^4 \frac{\epsilon_{sn} - \epsilon_{\infty n}}{1 + (j\omega\tau_n)^{(1-\alpha_n)}} + \frac{\sigma_i}{j\omega\epsilon_0} \quad (2.7)$$

For each tissue and each dispersion region the parameters of the 4-term model have been statistically fitted. The results are shown in table Tab. 2.2. for the 3 principle human tissues skin, fat and muscle. Based on equation (2.7) the permittivity  $\epsilon_r$  and conductivity  $\sigma$  can be calculated for a broad frequency range.

The diagram in Fig. 2.9 exhibits a comparison between the modeled and measured permittivity and conductivity values of the muscle tissue. The resulting graphs indicate a good matching of the model to the measured values found in the literature.

Tissue	$\epsilon_{\infty}$	$\sigma_i$
Skin	4	$2 \cdot 10^{-4}$
Fat	2.5	0.035
Muscle	4	0.2

Tissue	$\epsilon_{S1} - \epsilon_{\infty 1}$	$\tau_1$ (ps)	$\alpha_1$	Tissue	$\epsilon_{S3} - \epsilon_{\infty 3}$	$\tau_3$ ( $\mu$ s)	$\alpha_3$
Skin	32	7.234	0	Skin	0	159.155	0.2
Fat	9	7.958	0.2	Fat	$3.3 \cdot 10^4$	159.155	0.05
Muscle	50	7.234	0.1	Muscle	$1.2 \cdot 10^6$	318.310	0.1

Tissue	$\epsilon_{S2} - \epsilon_{\infty 2}$	$\tau_2$ (ns)	$\alpha_2$	Tissue	$\epsilon_{S4} - \epsilon_{\infty 4}$	$\tau_4$ (ms)	$\alpha_4$
Skin	1100	32.481	0.2	Skin	0	15.915	0.2
Fat	35	15.915	0.1	Fat	$10^7$	15.915	0.01
Muscle	7000	353.678	0.1	Muscle	$2.5 \cdot 10^7$	2.274	0

Tab. 2.2. Cole-Cole model parameters for skin, fat and muscle [60].

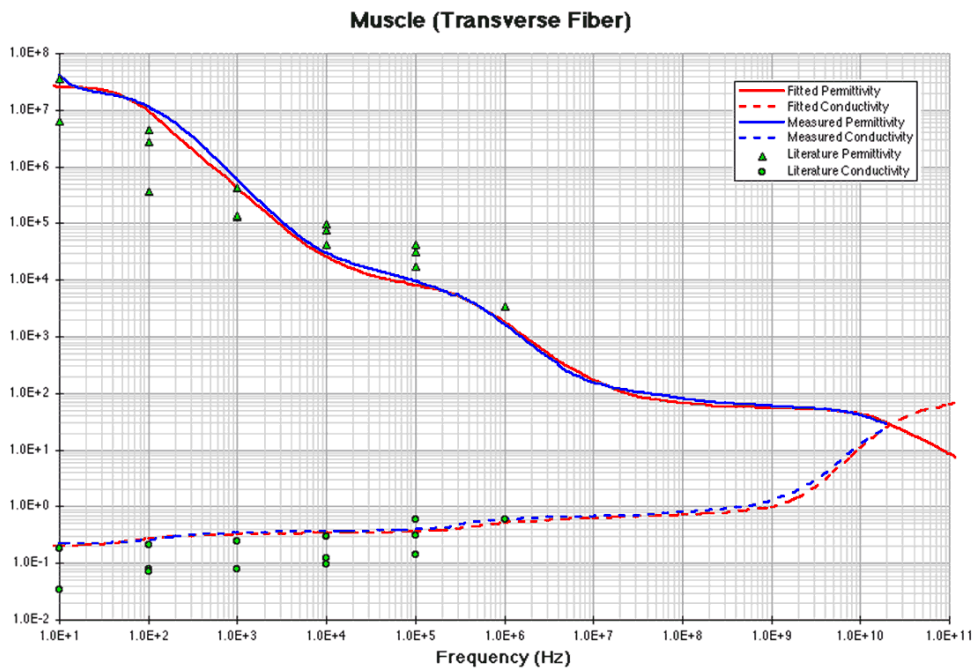


Fig. 2.9. Dielectric properties of muscle [39].

At low frequencies predominates the **ionic polarization**, but only in ionic materials, such as in water dissolved solids. Cations and anions are shifted in opposing directions, which results in a net dipole moment in the material. The imaginary part of the permittivity is inversely proportional to

the frequency. As a consequence the relative permittivity of a tissue, e.g., may reach values of up to  $10^6$  or  $10^7$  at frequencies below 100 Hz [39].

In **dipolar (orientation) polarization**, materials have permanent dipole moments which rotate in the direction of the applied field. The thermal vibrations in the material oppose the rotation, causing the dipolar polarization to decrease with increasing temperature [61].

**Atomic polarization**, appears at higher frequencies because of the relative change of the mean position of the nucleus within the molecule. It is intrinsic to the nature of the atom caused by the applied EM field.

The **electronic polarization** occurs because the center of the electron cloud is shifted away from the positive nucleus, creating an electric dipole moment. Electronic polarization is usually higher compared to atomic polarization.

Biological tissues are heterogeneous, so, another phenomenon is also of certain importance: interfacial polarization. It occurs when the dielectric properties differ at an interface within the material. Migrating charges can become trapped in between [43], resulting in a charging of the interface (Maxwell-Wagner effect) [62]. Opposite charges are gathered, e.g., at the boundaries of macromolecules and cell membranes, which makes the whole particle act as a dipole [32], [38].

Atomic and electronic mechanisms are relatively weak, usually constant over the microwave region, and only become noticeable at higher frequencies than the ones included in the scope of the present work. Dipole orientation and ionic conduction, however, strongly interact at microwave frequencies [43]. In biological tissues, the determinant factors regarding dielectric properties are water content and cell structure [34], [52]. Water molecules have high permanent dipole moments and align easily with the field. Consequently, the most decisive polarization type is the dipolar polarization.

### 2.1.3.2 Dispersion

[41] The dielectric properties of tissues are strong functions of frequency [32]. If the frequency of an externally applied EM field changes, the interaction between the field and the tissue also changes [63]. The dielectric spectrum of tissues consists of three main regions known as  $\alpha$ ,  $\beta$  and  $\gamma$  dispersions. They describe the three main steps in which the relative permittivity of a tissue decreases with rising frequency [64] due to losses caused by particular polarization processes [65]. At the same time, the conductivity increases. Consequently the EM fields of higher frequency



attenuate faster than those with lower frequency and the waves with different frequencies propagate at different speeds in the medium [38].

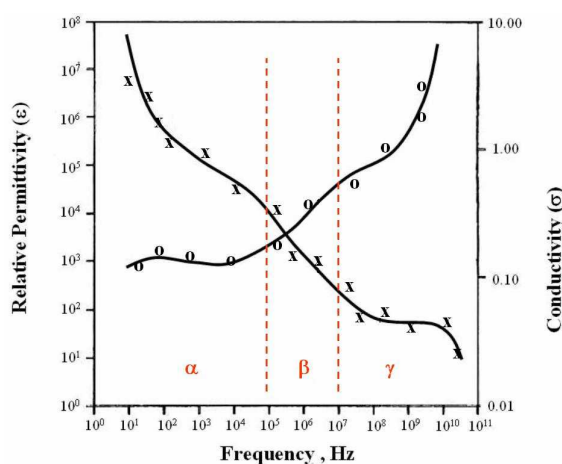


**Fig. 2.10.** Frequency dependence of relative permittivity  $\epsilon$  (x) and conductivity  $\sigma$  (o) with  $\alpha$ ,  $\beta$  and  $\gamma$  dispersion regions (adapted from [63]).

The high relative permittivity at low frequencies and the three dispersion regions (see Fig. 2.10) are common to all human tissues. At frequencies below the  $\alpha$  dispersion, the relative permittivity of tissues reaches very high values and the conductivity is relatively low [32]. The dipoles orient themselves easily in response to the change in the applied field. The charge carriers otherwise travel large distances, where trapping at an interface is more likely.

As the frequency increases, the dipoles can not follow the changes in the applied field, and the corresponding polarization disappears. In contrast, the charge carriers travel shorter distances and are less likely to be trapped. As frequency increases, the permittivity decreases and, because trapping becomes less important, the conductivity increases.

- a)  **$\alpha$  dispersion:** at low frequencies, tissues exhibit the  $\alpha$  dispersion centered in the low kilohertz range. It is associated with ionic diffusion processes at the site of the cellular membrane [41]. These include polarization of **counter ions** near charged surfaces and facilitate the polarization of large membrane-bound structures in the tissue [32]. The  $\alpha$  dispersion shows a large decrease in the permittivity graph but is very low and almost steady in the conductivity of the tissue. Thus, at low frequencies, tissues are essentially resistive despite their tremendous permittivity values [59]. The high values of permittivity reflect the

trapping of charges at internal interfaces and are not related to dipole orientation [33].

- b)  **$\beta$  dispersion:** at radiofrequencies (RF) the  $\beta$  dispersion extends over 3 - 4 frequency decades centered in the hundreds of kilohertz region. It mainly originates in the **interfacial** polarization of cellular membranes [33] which act as barriers to the flow of ions between the inner and outer cellular media and organic macromolecules [41], [64]. Additional contributions might also develop because of the dipolar orientation of tissue proteins and other organic macromolecules [59], [33]. The  $\beta$  dispersion is apparent in both the permittivity and conductivity of the tissue and represents a large decrease in permittivity (from several thousand to less than 100) and a large increase in conductivity by approximately a factor of 10.
- c)  **$\gamma$  dispersion:** at microwave frequencies, the EM field interacts only with water molecules [63] and the tissue exhibits the  $\gamma$  dispersion in the gigahertz region due to the molecular polarization of tissue water [41], [64]. This dispersion is centered at 20 GHz <sup>6</sup>and is the same as that found in pure liquid water. At high frequencies, above the  $\beta$  dispersion, the cell membranes exhibit such elevated conductivity that the current passes through both the extracellular and intracellular water compartments [32], [66] (see Fig. 2.11).

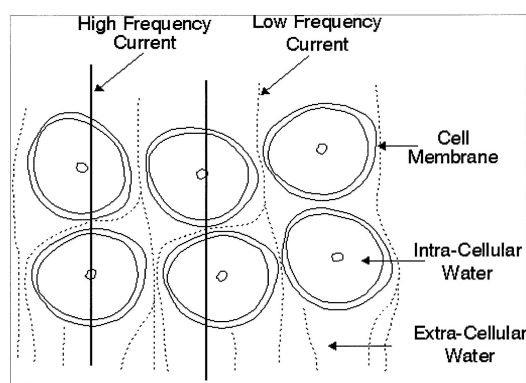


**Fig. 2.11. High-frequency and low-frequency current distribution in cell suspensions [66].**

<sup>6</sup> Pure water has a single relaxation centered at 20 GHz at room temperature and 25 GHz at 37 °C body temperature [59].

In addition to these three major dispersions, other smaller dispersions occur due to rotational relaxation of bound water ( $\delta$  dispersion) and other effects. These dispersions overlap in frequency and lead to a broad and often featureless dielectric dispersion in tissue [32].

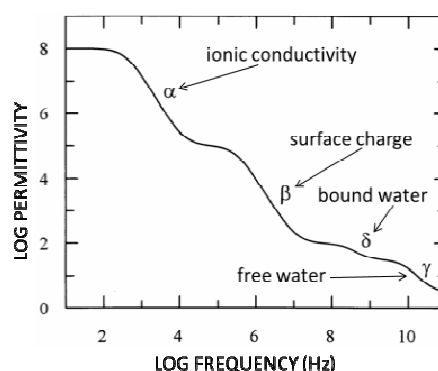


**Fig. 2.12. Idealized spectrum of the real part of the complex dielectric permittivity of cell suspensions and tissues [65].**

The phenomenon of dispersion can be described based on the orientation of the dipoles and the motion of the charge carriers [33].

The conductivity (and permittivity) of tissues, like those of many other materials, are temperature dependent. The change in parameters is highest at low radiofrequencies, about 1-2 %/°C [64]. In the temperature range 20-40 °C, the conductivity and permittivity increase with increasing temperature in most frequencies, the change being typically about 2 %/°C for the conductivity and about 1.5 %/°C for the permittivity [67]. At frequencies above 400 MHz, the permittivity starts to decline with increasing temperature and the same happens for conductivity at frequencies above 1000 MHz. The largest temperature dependent changes in conductivity are expected for tissues with a high fat content [67].

## 2.2 PHENOMENA OF PROPAGATION IN DIELECTRIC MEDIA

The concept of propagation may be regarded as a way of transferring energy or information from one point (a transmitter) to another (a receiver) by means of a traveling EM wave [58]. In body environments, the EM wave can be absorbed, reflected or transmitted when passing from one medium to another, depending on the complex conductivity of the tissue and the frequency of the source [37], [59]. In this section, the effects of the dielectric

properties presented in section 2.1 on the applied electric field, i.e., the EM wave, are explored.

### 2.2.1 PLANE WAVE PROPAGATION PARAMETERS

An EM field can be represented in a linear system by a summation of plane waves. The plane wave propagation parameters bear physically meaningful information [40]. The following equations determine different ways in which the EM plane wave is being altered when propagating through a lossy medium like the human body.

The **propagation constant** is a complex value which measures the amplitude variation of an EM wave in the medium. Equation (2.8) exhibits that the **complex propagation constant** ( $\gamma$ ) is composed of a real part ( $\alpha$ ) and an imaginary part ( $\beta$ ) [68], [58].

$$\gamma = \alpha + j\beta \quad (2.8)$$

Each of the two components has a different effect on the EM wave. The imaginary part, also called the **phase constant** ( $\beta$ ), affects the propagation of the EM field by shortening the wavelength due to high permittivity and losses in the medium (see equation (2.9)).

$$\beta = \omega \sqrt{\frac{\mu\epsilon}{2} \left[ \sqrt{1 + \left(\frac{\sigma}{\omega\epsilon}\right)^2} + 1 \right]} \quad (2.9)$$

Apart from that, the **wavelength** ( $\lambda$ ) of the signal, an essential parameter in the design process of an antenna, can be calculated on the basis of the phase constant according to equation (2.10) [58], [68].

$$\lambda = \frac{2\pi}{\beta} \quad (2.10)$$

The real part of the **complex propagation constant** is also referred to as the **attenuation constant** ( $\alpha$ ) [58] and determines the exponential damping factor of the EM wave amplitude, i.e., its rate of decay with distance [68].

$$\alpha = \omega \sqrt{\frac{\mu\epsilon}{2} \left[ \sqrt{1 + \left(\frac{\sigma}{\omega\epsilon}\right)^2} - 1 \right]} \quad (2.11)$$

As the EM wave propagates in the medium, its amplitude is attenuated according to  $e^{-\alpha z}$  (see Fig. 2.13).

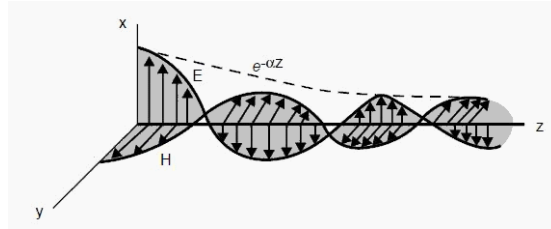


**Fig. 2.13. The magnetic and electric field components of a plane wave in a lossy medium [58].**

The distance  $\delta$  through which the wave amplitude is reduced by a factor of  $e^{-1}$  (about 37% or 8.7 dB) is called **skin depth** or **penetration depth** of the medium [58] and is represented by the inverse of attenuation [40].

$$\delta_{skin} = \frac{1}{\alpha} \quad (2.12)$$

EM waves do not necessarily penetrate the entire body. Equations (2.11) and (2.12) show the relationship between frequencies and the depth of penetration.

As for most biological materials the displacement current (i.e., due to the imaginary part of permittivity  $\epsilon''$ ) is of the order of the conduction current (i.e., due to the real part of permittivity  $\epsilon'$ ). Therefore, no approximation can be applied when skin depth is calculated based on equation (2.11) and inserted in equation (2.12) [59]. In summary can be concluded that the higher the frequency of the signal and/or the conductivity of the tissue, the smaller the skin depth, i.e., the less the EM wave penetrates the tissue.

In general, at a given frequency, the lower the water content of the tissue, the deeper an EM wave penetrates it. Also the lower the frequency,

the deeper is the penetration depth into tissues with given water content. [59].

### *HUMAN BODY INFLUENCE ON RF WAVE*

The different electromagnetic properties of air and the human body lead to a change of the propagation of the electromagnetic wave.

When the RF wave runs from free space straight to a dielectric tissue, just a fraction of it crosses the skin-air interface and enters the body. The other part is reflected. The RF wave travels from free space with a wave impedance equal to  $377 \Omega$  and hits the surface of the body tissue. The skin tissue has a much lower impedance as shown in Tab. 2.3.

Tissue	$\epsilon_r$	$\rho$	$\eta [\Omega]$
Muscle	57.6	0.85	$43.5 < 13.0^\circ$
Fat	12.1	0.07	$105.4 < 14.1^\circ$
Skin	47.6	0.71	$47.7 < 14.0^\circ$

**Tab. 2.3. Complex impedance for human tissues at 403 MHz [69].**

With the wave impedance of the skin of about  $50 \Omega$  resulted a reflection coefficient of 0.78 with respect to the  $377 \Omega$  of air at 403 MHz. This is very close to the reflection coefficient of a short-circuit. As a result the electric field is at a minimum and at a maximum of the magnetic field on the body surface. A standing-wave pattern is generated due to the combination of the incident wave and the wave reflected from the body. A quarter-wavelength away from the body opposite conditions for electric and magnetic fields can be observed. Fig. 2.14 illustrates this behavior based on a simplified air-muscle-air example with a simulation of the electric and magnetic fields of a 403.5 MHz signal hitting a one-dimensional phantom. It also shows the attenuation of the propagating wave inside the muscle tissue.

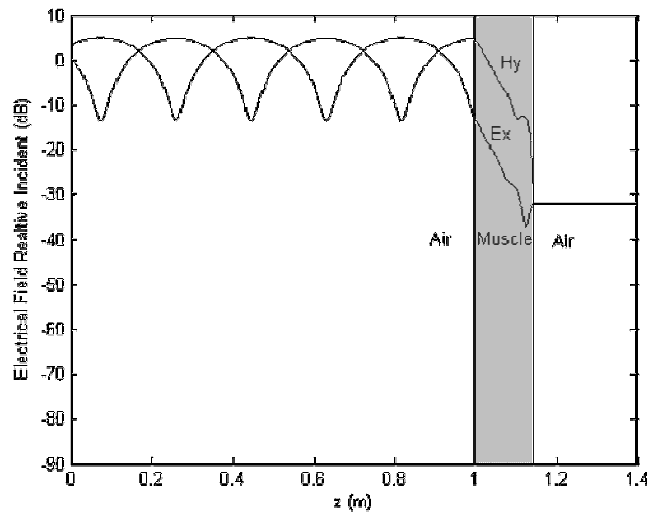


**Fig. 2.14.** FDTD simulation of electric and magnetic fields of a plane wave at 403.5 MHz hitting a 1-D phantom [70].

Interface	Field refl. coefficient. $ \Gamma $	Power transmission factor [%]
muscle to fat	0.41	83.2
fat to skin	0.37	86.3
skin to air	0.78	39.2

**Tab. 2.4.** Transmission factor for normal wave incidence at tissue boundaries at 403 MHz [69].

Based on the power transmission it can be shown how the transmitted power is attenuated by crossing the three-tissue interface. If an implant set below the muscle transmits with 1mW power, three quarters of its transmitted power is reflected at the tissue boundaries before leaving the body [71] as displayed in Fig. 2.15.

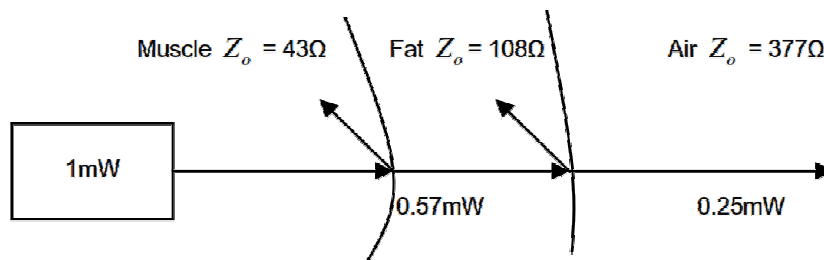


**Fig. 2.15.** Signal reflection at muscle - fat - air boundaries [71].

### 2.2.2 DOSIMETRY

The electromagnetic dosimetry is an area of scientific research, in which the EM exposure to biological tissue is examined. The analysis is divided into two areas: macroscopic and microscopic dosimetry.

*Macroscopic dosimetry:* The EM fields are determined as an average over some small volume of space. To sum up, both E-field and H-field are averaged over the volume of the cell.

*Microscopic dosimetry:* The EM fields are determined at a microscopic level, such as cellular level in biological systems.

The assessment is based not only on measurements but also on numerical calculations of the internal field within exposed structures. The interaction between the tissue and the EM field is valued and based on that defined as safe, hazardous or even effective EM field levels, e.g., for specific medical applications [64]. The latter is especially important in medical science and health risk assessment of radiology treatments. The dose is usually reported in quantities such as electric fields, current densities, specific absorption rate (SAR) and temperature increase inside the body.

The study of physiological mechanisms provoked by EM fields is a further area called bioelectromagnetic studies. Examples of this mechanisms are flashing lights in the eyes at 20 MHz and at EM field level of 50 mV/m at the retina or external muscle stimulation at 6 V/m for a skeletal muscle [72]. To achieve useful biological effects data in dosimetry studies an accurate measurement of the biological response is necessary.

It is a common technique to utilize phantoms or cadavers to measure localized and whole-body SAR with the subject in the experimental exposure position. The relation between incident EM and so called internal EM field is determined by the frequency of the incident fields, the size and shape of the body, and the electromagnetic properties of the body. As a consequence, if, e.g., a small animal is exposed to RF fields, the desired human equivalent exposure condition is to be extrapolated for the adequate frequency and RF power [73].

The basic dosimetry measurement is the differential power procedure. It is measured in a closed exposure system using two main steps:

- 1) *Accurate measurement of the incident EM-field over the exposure volume:* The actual field strength at the later measured points is



determined in absence of the test object either by measurement or a combination of measurement and simulation software.

- 2) *Accurate measurement of the EM field inside the test object:* For the measurement of the test object (human body, animal or phantom) broadband E- and H-field probes like shown in Fig. 2.16 are used.

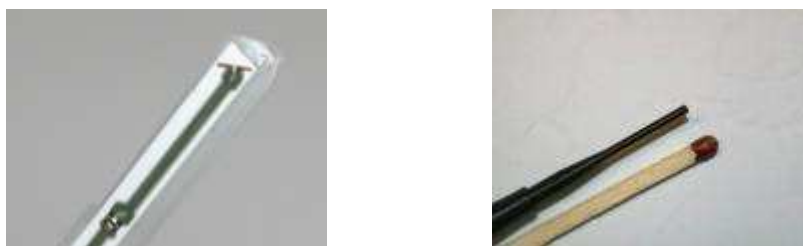


**Fig. 2.16. Two E-field probes for dosimetry demonstrating their size [74].**

This kind of dosimetry can be used when the object is far enough away from the source so that the presence of the object does not change the configuration of the source. For systems where the source is close to the object, the presence of the object changes the incident fields from the source. This coupling mechanism must be modeled within the dosimetry calculations. Most mid frequency systems require this type of dosimetry.

Other common techniques are [73]:

- Measurement of the temperature change in the biological test subject with non-interfering probes
- Calorimetric techniques
- Thermographic techniques

In cases where non-uniform exposures occur, i.e., in near field condition or where incident-power density cannot be measured, SAR is the only measurement that allows the definition of the RF exposures.

Exposure assessments using numerical simulations require detailed models of the human anatomy. These high resolution models are created by delineating various tissues from MRI scans and by using a literature database of physical tissue properties. The application of these models for EM dosimetry require that the respective dielectric properties are allocated to the various tissues and evaluated at all the frequencies to which the model is exposed.

### *SPECIFIC ABSORPTION RATE (SAR)*

Absorbed RF energy can be converted to other forms of energy and thus interfere with the normal functioning of the body. The bulk energy conversion into heat is called absorption [59], [37].

When the absorbed energy in the human body is converted into heat, thermal effects occur. There are two types of heating effects: dielectric heating at relatively low frequencies (several kHz to MHz), and inductive heating at higher frequencies from RF to microwaves.

Emission protection is regimented especially for living things in general, as high power radiation may induce into biomaterial. Radiofrequency exposure limits are given in terms of Specific Absorption Rate (SAR). It is specified as the power absorbed per mass of tissue and is quantified in watts per kilogram (W/kg) [75]. The intense and wide use of mobile wireless devices especially mobile phones has raised concerns about their influence on men's health.

The physiological effects of EM fields are divided into thermal and nonthermal causes. Moreover, there are various tissues inside the body distinctly sensitive to specific frequency ranges. The primal effect of the absorption of high-frequency radiation is the heating of the body tissue. The organs with the least blood flow are most affected, e.g., the eyes. Heart and brain are better at handling heat due to their better blood flow and the resulting heat equilibration.

On the other hand, a low-frequency field (nonthermal) can affect the sensory, nerve and muscle cells. A summary sketch of the human body's electromagnetic susceptibility and physiological effects of raising field strength is displayed in Fig. 2.17.

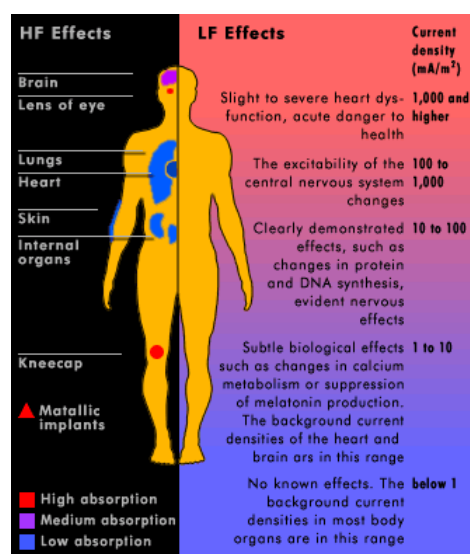


**Fig. 2.17. Principal schematic of electromagnetic susceptibility of the human body [76].**

Currently, two international standardization bodies have developed exposure guidelines [77] for workers and for the general public, except patients undergoing medical diagnosis or treatment. These guidelines are based on a detailed assessment of the available scientific evidence.

As the SAR takes into account only the absorption of the RF signal; it does not consider non-thermal effects [59]. It should be noted that the SAR limits refer to an induction of energy to a specific biomaterial. This is different to simple field strength of electric, magnetic field or radiated power.

The human body only absorbs power from the electric part of the electromagnetic wave. That is due to the fact that the human body mainly consists of water and electrolytes. The content of magnetic material is negligible. Therefore, only the electric field inside the body is considered to be evaluated. For this reason, a measurement technique, e.g., uses an E-field probe to evaluate the exposure in the near field of RF sources. SAR can be calculated from the electric field within the tissue as [78]:

$$P_g = SAR = \frac{\sigma}{2\rho} |E(r)|^2 \quad [W / kg] \quad (2.13)$$

Where

$\sigma$  is the sample electrical conductivity,

$\rho$  sample density and

$E$  electric field (averaged).

## 2.3 BODY PHANTOMS

Body phantoms are used as physical or numerical model simulating the same electrical properties as the represented biological tissues of which consists the human body. It is the most valuable tool for studying the propagation of EM waves in and around the human body.

Physical phantoms are used when a realistic environment for the measurements is essential, for instance, in SAR measurements or system evaluations. Numerical or virtual phantoms are employed in electromagnetic simulations, e.g., during the antenna design process or the verification of measurement results. According to their complexity of the composition, physical phantoms are further divided in homogenous and inhomogeneous phantoms. Depending on how precise the model has to reproduce the electromagnetic body characteristics, homogenous phantoms or inhomogeneous phantoms with a composition more complex are selected.

Homogeneous phantoms represent one single electrical property in the entire phantom. As they represent the characteristics of the outer layer of the body they exhibit skin or muscle properties, especially for higher frequencies with low skin depth. The body or body parts are represented by simple shapes like boxes or cylinders. They are easy to fabricate and EM simulations for verification are comparably fast.

In comparison, inhomogeneous phantoms are composed more detailed and represent specifics of the internal structure and the external appearance. The properties are obtained by using CT, MRI and cryogenic images [47]. Such phantoms are more expensive and complicated to build because of their higher complexity. Their simulation is more challenging, but today's EM simulation software supports the import of external detailed body models. Detailed models are required for the simulation of low-frequency communications due to the deep EM wave penetration and for implanted antennas.

### 2.3.1 PHANTOM TYPES FOR THE HUMAN BODY

Phantom types can be categorized by means of their constitution. The two most common types are liquid phantoms and solid dry phantoms.

#### *SOLID DRY PHANTOMS*

Solid phantoms are in use for thermographic measurements for, e.g., SAR evaluation or RF propagation around or on the surface of the body. As there is no outer shell necessary, no intersection effects influence the RF propagation. This is of special importance for higher frequencies as their skin depth is low.

By using precut models or multilayer variants thermographic analysis inside the phantom for dosimetry is feasible. They are comparably complicated to manufacture, but commercial models are available. They also have a good long-term chemical stability due to non degrading substances.

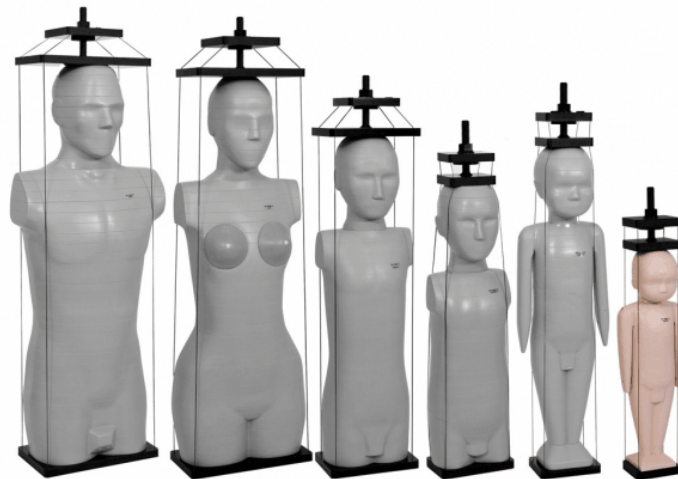


**Fig. 2.18. Family of phantoms of anthropomorphic phantoms to investigate organ dose [79].**

#### *LIQUID PHANTOMS*

Contrary to solid phantoms liquid phantoms consists of a container and a tissue simulating liquid. The container is made of a low RF propagation influential material, like fiberglass or PU. The phantom liquid consists mainly of water and additives for the control of permittivity and conductivity.

The conductivity is controlled through salt (NaCl), the permittivity on the other hand, by adding sugar for low frequencies and either Diacetin or Di-ethylene Glycol Butyl Ether (DGBE) for higher frequencies. A bactericide is also added in order to prevent the deterioration of the properties over time, otherwise the mixture ferments.

The reproduction of the EM properties of the body tissue over a broad frequency range is only possible by commercially available liquids. Simple, self made mixtures are narrow band, but can easily be adapted to the frequency range in question. A disadvantage of this type of phantom is, however, the difficulty of handling the liquid. Measurements are limited to only certain directions and mounting positions because of the spilling liquid inside the container. On the other hand, it is possible to measure directly inside the phantom by using a small probe. This type of phantom is used within this thesis including the preparation of the body tissue mimicking liquid as well as the verification of its properties.



**Fig. 2.19. Face down liquid phantom of the SAM v6 with robotic arm [80].**

### *NUMERICAL PHANTOMS*

Numerical or so-called virtual phantoms are essential during the antenna design process or SAR calculations in and around the human body, where they are used in electromagnetic simulation software.

One type called theoretical phantom is made of simple shapes or spheres. Common are cubes for the chest or cylinder for the trunk. The tissue is assumed as homogenous. The simplification allows rapid simulation but the result accuracy is limited.

The other type of virtual phantoms, in contrast, contains very detailed information about the structure and properties of the human body. The so-called voxel<sup>7</sup> phantom represents data obtained by using medical imaging technologies such as MRI- and CT scanner, or from human cadavers.

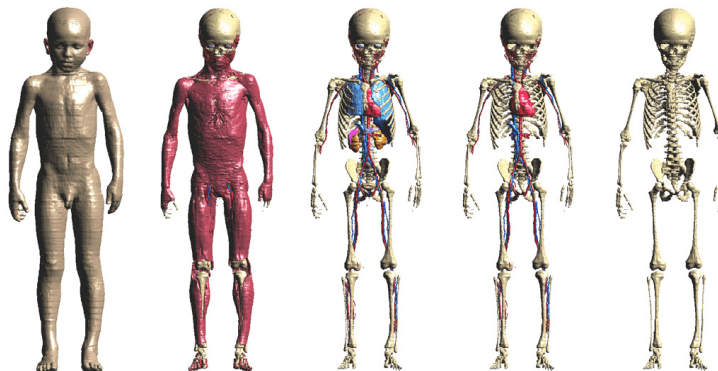


**Fig. 2.20. Thelonious: voxel model of a 6-year-old boy from the "Virtual Family" showing skin, muscle, inner organs, blood vessels and skeleton [81].**

With this immensely detailed tissue distribution information (see Fig. 2.20), the RF wave propagation inside the body can be calculated with an EM solver. This is especially important for implanted antenna design or deep low frequency EM wave penetration of the body (e.g., SAR calculation).

One recent project to obtain this detailed image of human body tissue distribution is the Voxel-Man<sup>8</sup> project of the Institute of Mathematics and Computer Science in Medicine of the University of Hamburg-Eppendorf, Germany. It comprises a diverse selection of 3-D anatomical atlases based on tomographic volume data.

<sup>7</sup> Volume piXEL=representation of a value on a regular grid in a 3-D space.

<sup>8</sup> Voxel-Man is a project of the Institute of Mathematics and Computer Science in Medicine of the University of Hamburg-Eppendorf, Germany, and comprises a diverse selection of 3-D anatomical atlases based on tomographic volume data. With newly developed methods for segmentation and visualization, it is a pioneer in surgery simulation technology providing highly realistic renderings of the human anatomy in very life-like colors [48].

In this thesis, only homogenous phantoms are used for simplicity instead of voxel based ones, because the application is subcutaneous, and therefore the antenna is only covered by skin tissue.

### *SIMULATION*

Suitable voxel model as commercial products exist for most of the EM solver software. As a consequence of this high-resolution models the simulation time with voxel phantoms is very increased.

Software	Numerical solver Type	Manufacturer
EMPIRE XCcel	FDTD	IMST GmbH
SEMCAD X	FDTD	Schmid & Partner Engineering AG (SPEAG)
HFSS	FEM	Ansoft Technologies
Microwave Studio	FIT	CST Computer Simulation Technology AG
FEKO	MoM/FEM	Altair Engineering, Inc

**Tab. 2.5. Selection of commercially available software with different EM solver.**

But simulation time is not only depending on the complexity of the model but also on the adequate EM solver method itself. The three most common EM solver methods with their specific advantages are summarized in Tab. 2.6. It compares the method of moments (MoM), finite element method (FEM) and finite-difference time-domain (FDTD) for their strengths and weaknesses. An advanced method called finite integration technique (FIT) (see Tab. 2.5 CST AG) was first proposed by Weiland [82]. It is a generalization of the FDTD method and employs the Maxwell's equation on spatial grids.

Formulation	Equation type	Domain	Radiation condition	PEC only	homogeneous penetrable	inhomogeneous penetrable
MoM	integral	frequency	yes	good	good	not optimal
FEM	differential	frequency	no	not optimal	good	good
FDTD	differential	time	no	not optimal	good	good

**Tab. 2.6. Comparison of numerical solver methods [83].**

It illustrates that FEM and FDTD are the most suitable methods for problems involving inhomogeneous objects, as is the case of voxel phantoms [83]. They can efficiently model the heterogeneity of the human body with high resolution and frequency-dependent properties. In this work CST MWS was used as the appropriate simulation tool for the assigned problem.



### 2.3.2 MEASUREMENTS OF THE PHANTOM PROPERTIES

The characterization of the EM properties of the used phantom material is an essential step during the fabrication and verification of the final model. The used techniques are common for the determination of material properties. Different characterization techniques are applied depending on material properties and studied frequency.

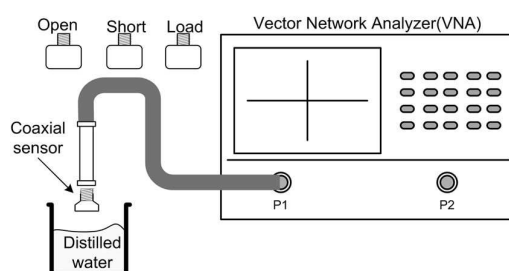


**Fig. 2.21. Measurement set up for coaxial probe calibration [42].**

Most common technique is the measurement with an open-ended coaxial probe. The open-ended coaxial probe is a cut off section of a transmission line. The probe is slightly immersed in to a liquid material or requires to touch the flat surface of solid or powder material. There must not be an air gap between probe and material, as it would alter the results.

A calibration measurement is mandatory for the used network analyzer and also for the coaxial probe by using pre-qualified material, e.g., distilled water. The fields at the probe-end penetrate slightly into the investigated material, so that a measurement of the reflection coefficient will provide information on its complex permittivity.

This method is suitable for liquid or semi-solid material characterization. For solid materials without a flat surface the results are uncertain because of the high influence of the air in between probe and material.

A benefit of the coaxial probe is its broadband property and the simplicity of the measurement but the accuracy of the results is limited in comparison to other methods. With its characteristics this method has been widely used for the characterization of human tissues and it was also applied in the thesis for verifying the dielectric properties of the used phantom liquids.

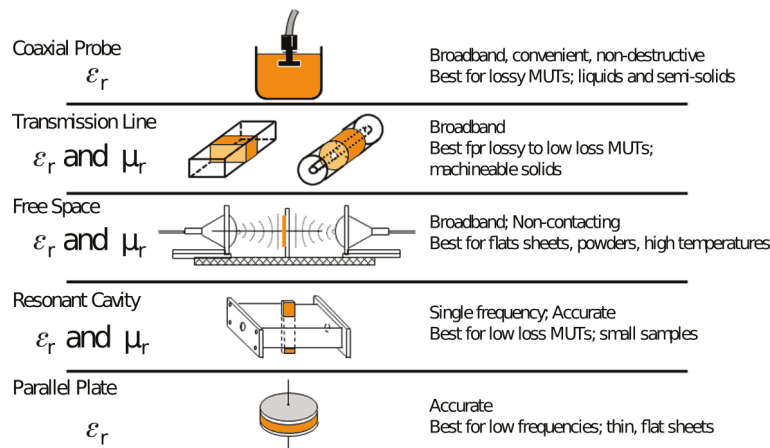


**Fig. 2.22. Measurement techniques for permittivity [43].**

Using discrete results of dielectric tissue measurements, i.e., in a EM simulation software, the calculation of the continuous progression of these values for a wide range of frequencies by using an arithmetical model is necessary.

## 2.4 REGULATIONS OF SHORT DISTANCE WIRELESS COMMUNICATION

The selection of the appropriate wireless technology is necessary during first design steps of a wireless implant. The application and its special communication demands are decisive factors in this process.

The factors cost-efficiency, flexibility and interoperation demand standardized wireless technology to be the basis of a body centric communication, even if proprietary technical approaches might be superior for specific applications. A classification of the different regulation rules is given in the next section.

### 2.4.1 EM REGULATION

Regulations in general provide protection and immunity to electromagnetic interference. The regulation of wireless application and the properties of the respective devices have two main objectives.

The first goal is self-protection against unwanted interference from other devices, also called electromagnetic immunity or susceptibility. In the case of biological tissue, these limits are defined by SAR.

The second objective is electromagnetic compatibility (EMC) including the protection of other devices in order to prevent influences in their functioning. The emission of EM energy by any source is covered by guidelines, including the instruction of taking countermeasures, in an effort to reduce such radiation.

In a medical environment the application of the guidelines has to address all potential risks associated to EM interference with medical devices. The regulatory framework, as a result, facilitates the market access and allows putting radio devices into service in that respective region.

The main international organizations for standards of EMC are the International Organization for Standardization (ISO) and the International Electrotechnical Commission (IEC), which dispose of several committees working full time on EMC issues. Regulation authority of the United States is the Federal Communications Commission (FCC), which sets the limits of permitted radiation.

Harmonization is promoted through international collaboration of the regional standardization bodies. Standards are often adopted with little or no change by others. In Europe the European Telecommunications Standards Institute (ETSI) is in charge of the EMC guidelines with the main standard EN 301 489 [84].

#### **2.4.2 REGULATION FOR SAR LIMITS**

SAR is measured as power absorbed per mass of a tissue. It is usually stated in units of watts per kilogram. SAR is averaged either over the whole body or over a small sample volume with a reference weight of typically 1 g or 10 g of the tissue in question. The value, then, expresses the maximum SAR level measured or permitted for this respective body part. The small sample volumes are selected to prevent high local peaks, which otherwise may be equalized in a larger volume.

On a worldwide level, SAR regulation is established based on different limits and verification procedures. In Europe, e.g., the SAR limits follow [75] and are restricted to a maximum absorption rate of 2W/kg, measured as an average over a 10 g volume. In the U.S., the limits are based on [85], where a maximum SAR of 1.6W/kg (RMS on 1g volume) is established. This stricter U.S. standard is taken as reference in this study.

The main worldwide SAR regulations are summarized in Tab. 2.7.

	Australia	Europe	USA	Japan	Taiwan	China
Measurement method	ASA ARPANSA	(ICNIRP) EN 50360	ANSI C95.1b:2004	TTC/MPTC ARIB		
Whole body [W/kg]	0.08	0.08	0.08	0.04	0.08	
Spatial peak [W/kg]	2.0	2.0	1.6	2.0	1.6	1.0
Averaged over	10g cube	10g cube	1g cube	10g cube	1g cube	10g
Averaged for	6 min.	6 min.	30 min.	6 min.	30 min.	

**Tab. 2.7. SAR limits specified by various administrations [86].**

#### **2.4.2.1 SAR Measurement**

SAR levels are evaluated either by using solid or liquid body phantoms or by electromagnetic simulations. Measurement methods for SAR evaluation are the E-field method [78] for liquid phantoms and the thermographic method for solid phantoms [87]. To obtain SAR data, common EM simulation software provides integrated SAR limit calculations, but verification measurements are still necessary.

A common phantom model for SAR is the Specific Anthropomorphic Mannequin (SAM). It consists of a homogeneous head and body phantom (e.g., Fig. 2.23 (b)), which is specified by the harmonized standards IEEE 1528-2003, IEC/EN 62209-2:2010 and EN 50566:2013 for worldwide compliance tests.

By using small probes, the E-field inside a liquid phantom can be measured directly and the SAR values can be calculated (see section 2.2.2). The advantages of this method are, on the one hand, the option of direct three-dimensional SAR measurement and, on the other hand, the possibility to employ the actual RF device in the measurements. A limiting factor is the size of the E-field probe in matters of 3-D resolution. Apart from that, the range of possible phantom shapes is limited as well as SAR measurements on the surface or at high frequencies due to the influence of the container material.

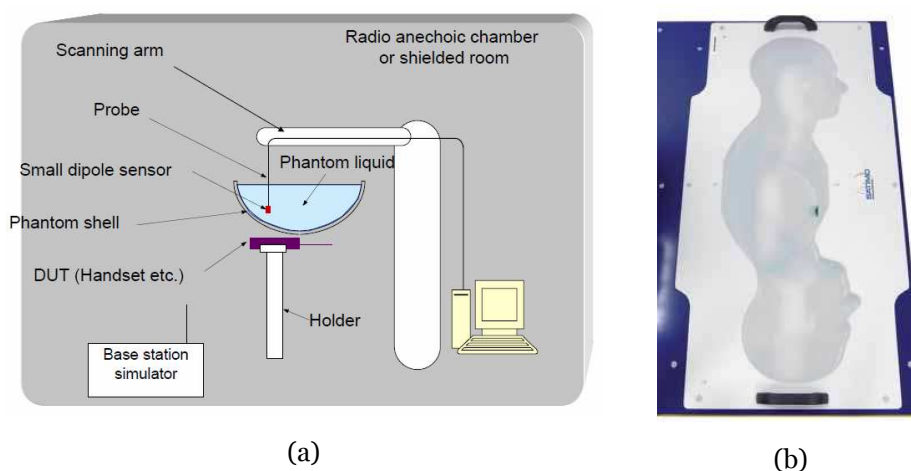


**Fig. 2.23. SAR measurement using the E-field method with (a) a liquid phantom [88] and (b) TWIN-SAM liquid body and head phantom made of fiberglass by SATIMO [89].**

For solid or semi-solid phantoms the thermographic method is applied. It consists of a predefined high-power RF source which provokes a rise in temperature. This change is recorded by an infrared thermographic camera, and a thermal profile of the phantom is generated.

An important advantage of this method is, that it allows SAR measurements on the surface of a phantom. Complex, multi-layered phantoms can also be evaluated. However, an external RF source is necessary, as the original device usually radiates too weakly to be detectable by the thermographic cameras.

### 2.4.3 WIRELESS COMMUNICATION STANDARDS

In this section, three short range wireless technologies are presented. The selected RFID- and near field communication (NFC) standards are already in use in a broad range of applications, also compatible to a hospital environment. The MedRadio standard originally is an U.S. standard, though, lately harmonized with the European EM regulation. The Short Range Device (SRD) standardization in the EU is recognized to be a key aspect in the future vision of the "internet of things", which incorporates medical SRD (mSRD) regulation. The harmonization of SRD also covers the European UHF-RFID frequencies in the SRD g1 band from 865 -868 MHz [90]. Key properties of the RFID, NFC and MedRadio technologies are presented and advantages and disadvantages are discussed.

One basic requirement of any wireless system in the medical environment is reliability. In this context, RF immunity is an essential requirement here. In the European Union this issue is harmonized in standard EN60601-1-2:2007. In the U.S., the Food and Drugs Administration (FDA) regulates all medical equipment. Concerned about the non-existence of appropriate standards, it recommends in its guidelines the use of the international version of IEC/EN60601-1-2:2007 [91].

#### 2.4.3.1 *RFID Regulation*



**Fig. 2.24. Implantable RFID dosimeter as part of a monitoring system of radiation treatments [92].**

RFID is a technology which uses electromagnetic coupling to uniquely identify an object, product, animal or person. It can remotely store and retrieve data by employing devices called RFID tags.

A RFID system consists of two elements:

- a) A *reader*, which acts as a transceiver, initiates the communication and retrieves the answer from the tag. It mainly consists of a power amplifier, an antenna and a computer interface for managing the received data.
- b) A *RFID tag* is a transponder, which is fixed on or within the object. It consists of a low power integrated circuit (IC) together with an antenna.

#### *GENERAL ADVANTAGES OF RFID:*

RFID does not require direct line of sight and therefore, the tags can be inserted in non-metallic media. Depending on the used technology and the frequency range, tags can be read from longer distances (passive UHF up to 10m, active tags up to 100 m) [93].

The read rates of RFID tags can be much higher for higher frequencies. RFID tags have read/write capabilities and can store additional

information. Extensions of the RFID protocol provide the ability of securing sensitive data through encryption of the data transmission.

RFID enables retrieving information from inside the body without the need of active devices within certain limits. The permitted transmit power in connection with the working frequency limits the penetration depth of the RF wave (skin depth). The lossy properties of body tissue attenuate twice for passive RFID tags in the transmission power budget. Therefore, only subcutaneous application of RFID technology is promising.

Studies on radiators based on electromagnetic coupling are conducted for subcutaneous wireless biosensors, where the distance between the implant and the interface body-air is below a few millimeters. This would be the case of certain applications such as glucose analysis for diabetes treatment, intracranial pressure characterization etc. The combination of biosensors with RFID, a well developed EM coupling technology, can offer a platform for a smart implants.

This technology has been chosen using the European frequency bands g1 for SRD taken into account the transmission losses in the body tissue and having no assisting battery in the smart implant.

Although several advantages arrive with the introduction of such a technology in healthcare, risks of electro-magnetic interference with medical devices exist, since RFID systems emit considerable electromagnetic power.

RFID operates in unlicensed frequency spectrum, which is referred as ISM (Industrial, Scientific and Medical). Depending on the local regulations these frequencies vary in different countries. Tab. 2.8 [90] shows maximum transmission power for the corresponding frequency ranges for Europe and USA. Electromagnetic compatibility of RFID is regulated by three ETSI standards and is covering a frequency range from 9 kHz to 40 GHz ETSI EN 300-220-1; EN 300-330-2; EN 300-440. The FCC also regulates the power restrictions, emission limits and the use of certain frequencies in Part 15 of Title 47 of the RFID Regulation extension for Medical Devices.

Frequency range	Comment	Allowed field strength/ transmission power
< 135 kHz	low frequency, inductive coupling	72 dB $\mu$ A/m max
3.155 - 3.400 MHz	EAS (electronic article surveillance)	13.5 dB $\mu$ A/m
6.765 - 6.795 MHz	medium frequency (ISM), inductive coupling	42 dB $\mu$ A/m
7.400 - 8.800 MHz	EAS (electronic article surveillance) only	9 dB $\mu$ A/m
13.553 - 13.567 MHz	medium frequency (13.56 MHz, ISM), inductive coupling, contactless smartcards, smartlabels, item management	60 dB $\mu$ A/m
26.957 - 27.283 MHz	medium frequency (ISM), inductive coupling, special applications only	42 dB $\mu$ A/m
433 MHz	UHF (ISM), backscatter coupling, rarely used for RFID	10 - 100 mW
865 - 868 MHz	UHF (RFID only), LBT (listen before talk)	100 mW ERP Europe only
865.6 - 867.6 MHz	UHF (RFID only), LBT (listen before talk)	2W ERP (=3.8W EIRP) Europe only
865.6 - 868 MHz	UHF (SRD), backscatter coupling, new frequency, systems under development	500 mW ERP, Europe only
902 - 928 MHz	UHF (SRD), backscatter coupling, several systems	4 W EIRP – spread spectrum, USA/Canada only
2.400 - 2.483 GHz	SHF (ISM), backscatter coupling, several systems	4 W – spread spectrum, USA/Canada only
2.446 - 2.454 GHz	SHF (RFID and AVI (automatic vehicle identification))	0.5 W EIRP outdoor 4 W EIRP indoor
5.725 - 5.875 GHz	SHF (ISM), backscatter coupling, rarely used for RFID	4 W USA/Canada 500 mW Europe

**Tab. 2.8. Frequency ranges and associated maximum allowed field strengths [90], [94].**

RFID readers operated in hospital environments have to be considered as portable RF communication equipment. In order to guarantee the normal functioning of medical devices, a certain distance to from the RFID system needs to be maintained. The EM interference depends on the



distance, the frequency of the RFID reader and the immunity of the medical device.

Frequency range	Immunity level	
	Life-supporting device	Not life-supporting device
Conducted RF (150 kHz – 80 MHz)	10 V (rms)	3 V (rms)
Radiated RF (80 MHz – 2.5 GHz)	10 V/m	3 V/m

**Tab. 2.9. Minimum required immunity levels according to IEC/EN60601-1-2 [94].**

Considering the minimum required immunity, e.g., a life supporting device according to IEC/EN 60601-1-2:2007, a minimum distance is required. Tab. 2.10 lists the recommended separation respective to frequencies and transmitted power. The standard does not consider RFID systems below 150 kHz and above 2.5 GHz.

Rated maximum output power of transmitter [W]	Separation to RFID transmitter [cm]	
	865 – 956 MHz	2.45 GHz
0.01	23	23
0.1	73	73
0.2	103	103
0.5	163	163
1	230	230
2	325	325
4 (USA, CANADA)	-	460 (USA, CANADA)

**Tab. 2.10. Recommended separation of RFID transmitter to medical devices [cm] [94].**

### *INTERNATIONAL REGULATION OF ISM BANDS*

National radio regulations differ in the assignment of the frequency region and specific requirements. The ISM ranges in the frequency spectrum below 1 GHz are not synchronized in different parts of the world, shown in Fig. 2.25. The use of RFID at this frequency range would result in better range and building penetration with the same output power as for ISM 2.4 GHz band.

Therefore, RFID equipment has to be adapted and authorized separately in every region. Limitations vary a lot from region to region. Especially passive low price tags and responder cannot be commercialized

and used worldwide. The only worldwide validated frequency is ISM 2.4 GHz. The International Telecommunication Union (ITU) has specified in ITU-R 5.137, 5.150 and 5.280 of the radio regulations the ISM frequency bands. Due to the fact that many communication standards are using the same unlicensed ISM bands, they need to be tolerant towards any interference from other ISM equipment.

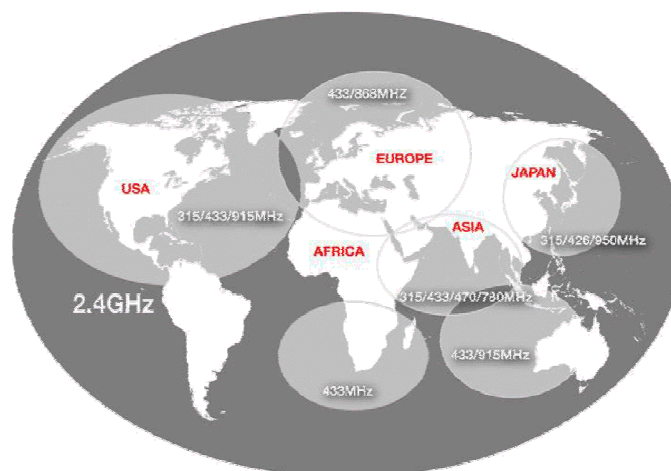


**Fig. 2.25. ISM frequency spectrum in different world regions (only 2.4 GHz is worldwide free usable) [95].**

In this study the ISM 2.4 GHz was used in combination with the MICS band for taking full advantage of the specification of the applied transceiver in the implant (see section 5.2.1).

#### **2.4.3.2 NFC Regulation**

NFC is a wireless connectivity standard (Ecma-340, ISO/IEC 18092) for short-ranges up to about 20 cm. It extends the application capabilities of RFID technology by introducing new communication modes but remains backward compatible. It allows communication to non self powered devices in the so-called passive NFC mode. In the active NFC mode both partners generate their own RF field

The communication is initiated by simply holding two devices close to each other. NFC communication is based on inductive RF Technology at 13,56 MHz. Active and passive NFC mode can reach speeds until 424 kbps with the actual specification. For higher data rates NFC can be used as a

secure way for identification and initiation of other wireless communication, e.g., WLAN.



**Fig. 2.26. Deployable smart diagnostic skin patch GT200 for fever monitoring [96].**

As NFC enables new applications in medical environments, the EMC regulations also apply in this area. An example of a new medical application is a wireless diagnostic skin patch that can be read directly by NFC enabled cell phones. In this manner, home or remote diagnostics can be applied. Parameters like skin temperature, moisture, surface tension or glucose level are monitored with a disposable skin patch sensor system [97]. Another proposed application is a medication tracking system to minimize erroneous drug administration [98].

	Benefits	Future Scenarios
Card Emulation Mode	1. Physical object elimination	1. Integration of ID-cards, passports, fingerprints, driver-licenses
	2. Access control	2. Storage area for critical information to provide user privacy and authorizing people to access those information
Reader/Writer Mode	1. Increases mobility	Many real-life scenarios can be adapted to NFC in this mode. In all of the scenarios, some data need to be read from an NFC tag, and additional jobs need to be done by NFC-enabled mobile phone.
	2. Decreases physical effort	
	3. Ability to be adapted by many scenarios	
	4. Easy to implement	
Peer-to-Peer Mode	1. Easy data exchange between devices	1. Secure exchange of critical data
	2. Device pairing	2. Gossiping

**Tab. 2.11. Benefits and possible future scenarios based on operating modes for NFC devices [99].**

In Tab. 2.11 the different operating modes of NFC devices are explained together with their advantages in future applications. Although this technology is promising, it is not further considered in this study because of the very limited NFC working range, which fails meeting the core requirement of the intended application scenario.

### 2.4.3.3 MedRadio Regulation

The MedRadio standard is defined by the FCC to regulate wireless communication with medical implants. FCC service rules for the MedRadio can be consulted in [94]. The U.S. MedRadio band comprises the frequencies (401-406 MHz). The MedRadio core band, however, coincides with the international MICS frequency of 402 - 405 MHz (see Fig. 2.27). The MICS adjacent spectrum with the two wing bands (401-402 MHz and 405-406 MHz) [100] are also known as Medical Data Service (MEDS) (see Fig. 2.27). In Europe it is regulated by the ETSI standard ETSI EN 302 537-1.

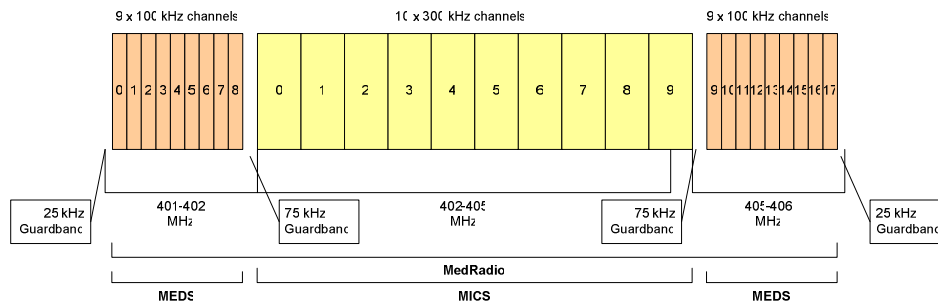


**Fig. 2.27 MedRadio frequency band divided into MICS and MEDS [101].**

The spectrum allocation 401-406 MHz is also in use for meteorological services (Met Aids) as weather, water and climate monitoring and prediction. An interference analysis by the ITU concludes that there is very low probability of interference between these two services (ITU-R RS.1263 and ITU-R SA.1346) [102]. The MedRadio spectrum, however, is used for diagnostic and therapeutic purposes in implanted and on-body medical devices. MedRadio devices, for example, include implanted cardiac pacemakers and defibrillators as well as neuromuscular stimulators that help restore sensation, mobility and other functions to limbs and organs. Only authorized health care providers are allowed to operate MedRadio devices. Manufacturers of MedRadio devices are authorized to demonstrate, install and maintain the equipment.

The MedRadio standard allows bi-directional radio communication with a pacemaker or other electronic implants. The maximum transmit power is very low with equivalent isotropically radiated power (EIRP) is  $25 \mu\text{W}$ . The maximum used bandwidth at any time is 300 kHz (see Tab. 2.12), which makes it a low bit rate system compared to WiFi or Bluetooth. The main advantage is the additional flexibility compared to previously used inductive technologies, which required the external transceiver to touch the skin of the patient. MedRadio allows a range of several meters. To ensure the communication, the LBT principle is obligatory for devices using the entire band of 401-406 MHz when transmitting with a maximum power of  $\text{EIRP}=25\mu\text{W}$ . With this Busy-Channel-Detection technology, the transmitter verifies the absence of other traffic on the shared RF channel before it starts its own transmission. It answers the purpose of preventing collisions or interferences on a shared RF channel and maintaining a high level of transmission safety.

In the wing bands, implant as well as body-worn transmitters using non-LBT spectrum access methods (with reduced EIRP and duty cycle limits) will also be permitted. In the core band, non-LBT operation is limited to medical implant devices operating with a total channel emission bandwidth of up to 300 kilohertz, centered in 403.65 MHz.

In this thesis, the MICS standard is the one being referred to, as this regulation is internationally harmonized, unlike MedRadio. As MICS, in general, is covered by the MedRadio standard, all MICS references in this work also apply to the MedRadio regulation, if not stated otherwise.

	Frequency band [MHz]	Single channel width [kHz]	Requirements for 25 $\mu$ W EIRP	EIRP Power Levels without LBT
MedRadio/MEDS	401 – 401.85	100	LBT	250nW; Duty cycle 0.1%
MedRadio/MEDS	401.85 – 402	150		25 $\mu$ W; Duty cycle 0.1%
MedRadio/MICS	402 – 405	300	LBT	100nW; Duty cycle 0.01%, only permitted from 403.5-403.8MHz
MedRadio/MEDS	405 – 406	100	LBT	250nW; Duty cycle 0.1%
Medical Micro-Power Networks (MMN)(U.S. only)	413 - 419 426 - 432 438 - 444 451 - 457	Max 6000	1mW with LBT	/

**Tab. 2.12. MedRadio specific requirements for different frequency bands [100], [101].**

LBT-enabled body-worn devices will, with one exception, be permitted to operate only in the new wing bands at 401-402 MHz and 405-406 MHz. Temporary body-worn transmitters can be used in the 402-405 MHz core band solely during a limited patient evaluation period in order to determine the suitability of a fully implanted device, provided a full compliance with all other MedRadio rules applicable to the band. The FCC encourages the usage of the MedRadio core band, the band, predominantly for life-critical applications, such as pacemakers and defibrillators. The MICS band harmonizes worldwide the wireless communication of mSRD for its application for implants. That is why the study at hand evaluates its implementation in a CVC (see Fig. 2.28).



**Fig. 2.28. Implanted MRI compatible CVC [103].**

## 2.5 IMPLANTED ANTENNAS

An antenna, set into a different dielectric medium than air, changes its electromagnetic properties considerably. This is especially true for implanted antennas. The human body, for instance, consists of about 60% water on average. It consists of highly lossy matter and therefore, its dielectric properties are different compared to air ( $\epsilon_r=1$  vs.  $\epsilon_r\approx 80$ ). As a consequence, an implanted antenna placed in a human body requires a different design approach than antennas operated through air, commonly used in communication devices.

An antenna cannot be treated separately from the surrounding medium whenever the influence on the radiation properties is that fundamental. The tissue in the closest environment has a high influence on the antenna by changing its near field properties. This situation deteriorates as every patient's tissue properties (thickness, distribution) as well as his constitution are subject to changes. The same applies to the position of an antenna inside the body or in relation to the body skin.

With this characteristics in mind can be claimed, that the radiation properties of the implanted antenna are a result of three factors:

- the implanted antenna structure
- the implant itself and
- the specific constitution of the body.

From outside the body the resulting properties cannot simply be attributed separately to these structures, that means, the measured "antenna gain" and "antenna efficiency" derive from them altogether.

Furthermore, when compiling a link analysis three transmission segments are to be considered:

- the propagation inside the body,
- the transition between body surface and air and finally,
- the transmission in free space to the receiver.

A characterization of the propagation, for each segment separately, is difficult as the radiation pattern of the antenna together with the implant is hard to determine inside the body. This raises the question whether the

body is part of the “radiation structure” or not. Its influence on the radiation properties is of such high significance that it is debatable what exactly constitutes the “antenna” in reality.

Due to the considerable variations depending on the patients, a standardization of the measurement setup is necessary to reach comparable results that can be used as reference. This incorporates, for example, relevant factors like the antenna placement inside the body, especially the distance to the body-air interface, or the body size. The efficiency of an implanted antenna is difficult to quantify as, on the one hand, it is affected by the amount of tissue and, on the other hand, by the reflection of the walls depending on the phantom dimensions. It generates standing waves depending on the implant position and affects the radiation efficiency [104], [105].

In practice, this uncertainty is to be taken into account even during the planning phase for the system design, including an additional margin in the link budget calculations.

In general, many antenna topologies can be used for smart implants., but in reality, only a few have reached importance. The reasons for that are illuminated in the following section.

### **2.5.1 GENERAL INTEGRATION**

Implanted antennas can be implemented as either integrated or externally attached to the implant, sticking out from the outer shape of the enclosure.

If antennas are not integrated directly in the implant, wire antennas are used. These externally attached antennas act as large monopoles. Due to their size they need to be flexible. Dipoles, in contrast, are not suitable for external layouts, as they always entail a feeding cable, located perpendicularly towards the two antenna branches. This extending shape implies that the pointy edges of the antenna would harm the surrounding tissue [60].

By now, the main group among the suitable topologies is an antenna layout that conforms to the outer implant shape. In other words, the antenna is mounted flush with the implant shell or at the most scarcely stepping up the surface. The principal advantage of this antenna layout is the fact that it does not take up room inside the implant itself. However, small antenna dimensions are preferred here, as the choices are limited to layouts that match the implant surface. In most instances, patch or



microstrip antennas are chosen when the implant has a rather flat appearance and so the main radiation is perpendicular (Fig. 2.29).



**Fig. 2.29. Microstrip spiral folded antenna topology with short circuit: Layout (left) and implemented design (right) [106].**

For mobile devices a common design decision is to embed the antenna itself on the printed circuit board (PCB). On PCBs, large metal components (e.g., ground planes) are situated in the near field of the antenna. The directivity may benefit as they act as coupled radiators. Profiting from the larger aperture or effective area, it increases and enhances thereby the bandwidth and radiation efficiency of the antenna.

Placing an antenna inside a smart implant always presupposes the availability of vacant room, which is a scarce resource in implants. A preferred antenna topology constitutes a separate component inside the enclosure, e.g., short loop- or wire strip topologies. They permit easy matching with dedicated components and free placement inside with a high level of freedom of the position. This antenna type meets the basic demands of the design problem and therefore, promised a viable solution. The adoption and modification of that basic topology is described in the practical part of this thesis.

Integrated types mentioned above are best applicable at high frequencies, which allow the antenna to be very small. Investigations about tradeoffs of using higher frequencies have been carried out by Ahmed et al. [107].

In the following sections a selected variety of implanted antenna topologies is discussed. Each of them involves certain advantages for particular applications and yet, microstrip antennas are the most common ones in implants [60].

### 2.5.2 MINIATURIZATION OF ANTENNAS

Today, common handheld devices often integrate not just one antenna. Engineers face the problem of integrating them occupying as little room as possible but providing multiple frequency band capabilities. In the design process of antennas used in free space, miscellaneous miniaturization techniques are common. This knowledge can be translated for topologies of implanted antennas. The absorbing properties of the body have to be preconceived advisedly due to the fact that, after implantation, this lossy medium is going to be the wireless communication environment of the antenna.

Besides, antennas cannot be built arbitrarily small while remaining efficient for the fact that, as soon as antenna miniaturization techniques are applied, the antenna performance is affected by major implications. The dimension of an electrical small antenna in relation to its lowest resonating frequency (in case of multiband capabilities) is commonly assumed as

$$ka = \frac{2\pi}{\lambda} a < 1 \quad (2.14)$$

where  $k$  is the wave number  $2\pi/\lambda$ , and  $a$  is of the minimum radius of a sphere that encloses the antenna structure [108].

Assuming matched antenna input impedance, the radiation efficiency factor  $\eta$  is stated as the ratio between the power radiated and the power accepted by the antenna. Expressing the additional losses through a series loss resistor  $R_{\text{loss}}$ ,  $\eta$  can be represented as:

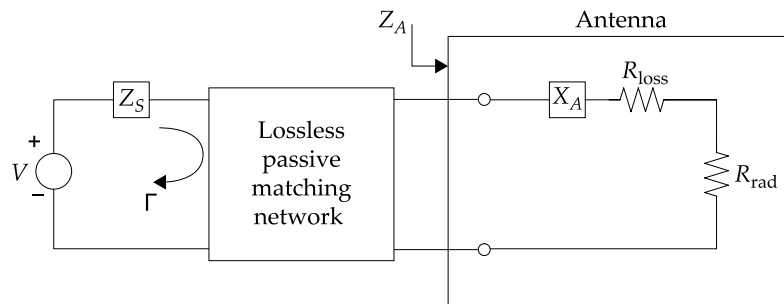


**Fig. 2.30. Lossless matching antenna network with antenna input impedance  $Z_A$ , source impedance  $Z_S$  and reflection coefficient  $\Gamma$  [108].**

$$\eta = \frac{R_{Rad}}{R_{Rad} + R_{Loss}} = \frac{R_{Rad}}{R_A} \quad (2.15)$$

where  $R_A$  is the total antenna input resistance  $R_{Rad}+R_{Loss}$ .

As electrical antenna size ( $ka$ ) further decreases, it is stated that the radiation resistance  $R_{Rad}$  of the antenna decreases as well and as a result, most of the RF power destined for radiation is commuted to resistive losses  $R_{Loss}$  in the antenna structure itself.  $R_{Loss}$  dominates the efficiency expression of the equation (2.15). This decrease in efficiency is primarily due to frequency-dependent conduction and dielectric losses within the antenna [108].



**Fig. 2.31. Example of a multilayer microstrip antenna for MedRadio frequency [109].**

As another consequence of miniaturization, the quality factor ( $Q$ ), increases, i.e., a higher amount of energy is retained inside the antenna, which severely sets limits to its broadband performance.

The radiation efficiency of an antenna always depends on choosing the right antenna topology for the application in the first place and cannot be raised artificially afterwards. In order to increase the bandwidth of a small antenna, resistive losses can be added to its structure or feeding setup (e.g., thicker dielectric covering to insulate the radiating element), although, this leads to a decrease of the radiation efficiency at the same time [110].

On the bottom line can be confirmed, that there are feasible miniaturization techniques for antennas, yet, in implants additional

complicating factors have to be considered. An example of the design of a very small antenna for MedRadio frequency is demonstrated by Skrivervik [109], shown in Fig. 2.31.

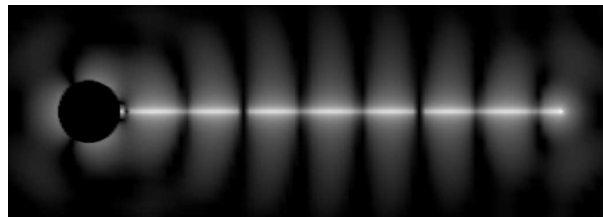
### 2.5.3 TRAVELING WAVE ANTENNAS

Wire antennas are a simple type of implanted antennas. Today they are primarily employed in implants for animals, particularly for tracking purposes and health monitoring of fish swarms or herds of animals, or subcutaneous implanted in birds for population monitoring.

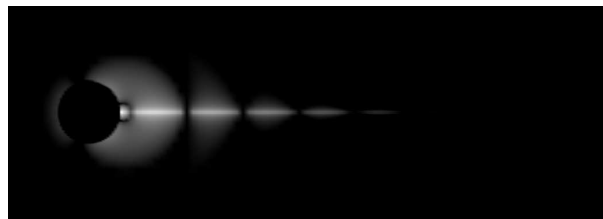
For people this topology proved to be problematic because of coupling effects in medical MRI examinations. The high energy magnitude raises the possibility of interference with the connected implant and may cause malfunctions, or exceed locally the permitted SAR limits. Especially for live supporting or actuating implants this is not acceptable. The impact of MRI and electromagnetic radiation on implants has been studied by Schenke [111] and Geisbusch [112].

#### 2.5.3.1 *Mode of operation*

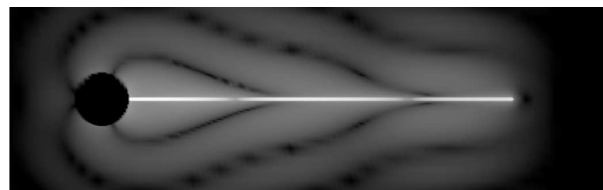
A traveling wave antenna topology basically operates like a single long wire antenna [113]. The input impedance depends on the length of the wire, i.e., if the wire is extended for the specific frequency it changes its input impedance. [114]. This is caused by the electromagnetic wave traveling along the wire, which is reflected at its end, and propagates back to the feed point. If the antenna is placed in a lossy medium, the magnitude of the traveling wave declines [60]. Fig. 2.32 illustrates the electromagnetic influence of the environment in the nearfield range of the wire antenna.



(a)



(b)



(c)

**Fig. 2.32. Simulation of momentary electric field of a wire: (a) non-insulated in air (b) non-insulated in a lossy medium and (c) insulated in a lossy medium [70].**

In free space the wavefronts are circular (side view) and meet the wire at  $90^\circ$ , as shown in Fig. 2.32 (a). The momentary electric field is uniformly distributed. For- and backwards traveling waves around the wire are superposing and therefore establish a standing wave pattern. In Fig. 2.32 the minimum and maximum (gray) can be identified.

If a lossy medium is located directly around the un-insulated wire, i.e., the implanted wire is in direct contact to it, the traveling wave is attenuated and thus the impedance at the feed point changes.

In that situation the antenna is described as “slow wave structure” (b). The reflected wave magnitude is much lower compared to free air conditions (Fig. 2.32 (a) vs. Fig. 2.32 (b)). The attenuation of the momentary electric

field along the wire is clearly visible in Fig. 2.32 (b) [60]. Therefore, the input impedance of a long wire antenna is independent from its exact length, but depend on dielectric properties of the surrounding medium.

If the wire is surrounded by an insulation material with much lower permittivity than the surrounding tissue, the loss per unit length is lower due to the removal of the lossy matter from the region with the strongest near field (see Fig. 2.32 (c)). Consequently, the reflection on the wire end has as impact of the input impedance of the antenna.

The phase velocity is also changed in the wire. Then, the structure is called a fast wave structure, with a phase velocity relation  $V_{in\_wire} > V_{surr\_medium}$ . Fig. 2.32 (c) shows the instantaneous electric field where the wavefronts meet the wire at an angle of less than  $90^\circ$ , because the phase front moves faster in the wire than in the lossy matter. A standing wave pattern over the whole length of the wire is visible. The input impedance depends on the length of the wire, the permittivity and the dimension of the surrounding medium. The reflected wave is less attenuated compared to the case of a non-isolated wire. In a lossy matter the insulated wire antenna can be treated as a coaxial wave guide. The lossy matter acts, thus, as the outer conductor.

### ***2.5.3.2 Applications and Specifics***

The long wire antenna topology is not common for application in human body implants. Integrated antennas are less susceptible to interference of the high magnitude EM fields of MRI scans.

The simple design and manufacturing make it convenient for its application in temporal implants for animals. Even semi-implantable applications, where part of the antenna is located outside the animal, are applied. The antenna is easily tuneable to the application specific surrounding tissue and its permittivity.

Common frequencies are in the lower very high frequency (VHF) band, for instance, animal implants transmitting in the frequency band of 140 - 220 MHz from Telonics Inc. [115]. They are used for health monitoring and tracking animal populations.

By reason of the implications for human health stated above, this type of antennas has not been further pursued in this work.

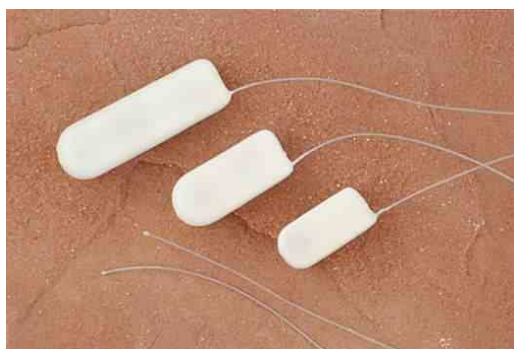


**Fig. 2.33. Different sizes of implants with external antenna for mammals [115].**

#### **2.5.4 LINEAR CONFORMAL ANTENNAS**

Linear conformal antennas are wire or narrow strip-like antennas which are mounted outside and around an implant casing, e.g. a pacemaker. It is a versatile antenna layout option as it requires minor effort to adapt the structure to the specific outer shape of an existing implant casing. It can largely be developed independently from the implant itself and a simplification of the case can be used during the design process. Even mechanically it can be designed with little demands for additional space, i.e., it requires only a small step-up of the implant volume.

Making use of a meander layout, it is easily adaptable to frequency bands. The following analysis describes a monopole quarter wave antenna in air [60]. The bandwidth can be increased by using a strip instead of a wire.

A drawback of the antenna topology is its low input impedance of about  $5\text{-}10\ \Omega$ . A matching circuit might be necessary to match it to the common  $50\ \Omega$  impedance. Another way of matching the input impedance is to modify the design with a short circuit near the feeding point. The short circuit acts like a geometric inductance, hence, giving the option to match the input impedance to  $50\ \Omega$ . This design is then closely related to a planar inverted-F antenna (PIFA) adapted to the casing of the implant.

In this configuration the bandwidth is higher compared to the linear antenna. Nevertheless, the literature is not elaborate in this subject. One example design was proposed by [70]. The prototype is shown in Fig. 2.34.



**Fig. 2.34. Circumference antenna for a pace maker for 403 MHz [70].**

## 2.5.5 MICROSTRIP ANTENNAS

This antenna type is a common conformal antenna topology. The radiating structure can be placed on a large flat surface of a typical implant, like a pacemaker.

Several studies investigated various microstrip antenna topologies like spirals and serpentines for MICS band operation, e.g., [116]. In free space most conventional designs for low-frequency operation have narrow bandwidth and substantial volume. Although microstrip antennas are relatively easy to design and fabricate for free-space applications, in a lossy medium some particularities have to be kept in mind.

### 2.5.5.1 *Microstrip Patch Antennas*

Patch antennas are considered to be compact and small compared to their wavelength and are among the basic topologies of microstrip antennas. They are also referred to as square microstrip patch antennas. Their topology is beneficial for flat implants with a usable surface as the main radiation direction is perpendicular to it. Due to their favorable shape they are used for pacemakers.

Several designs have shown that it is a challenging task to make them work properly inside a lossy medium [117].

In general a patch antenna can be described as a resonant structure consisting of a ground plane, over which another metallic plate is situated. This is the plate the topology owes its name to. A dielectric isolating sheet, or air, resides between these two metallic sheets. The upper plate is electromagnetically excited with a feeding line on one or more feed points. The position of the feeding points determines the input impedance and the



resonating modes, which can be excited. The type of resonating modes can be controlled by using slots. The size of this patch determines the resonance frequency of the antenna, by which a standing wave is formed on its surface.

When the antenna is placed in a lossy medium, the reflection of a surface wave is mitigated at the edges of the patch. The impedance change at the edge of the patch is much lower, so that the wave continues to propagate attenuatedly in the lossy medium. On that account, the resonating property weakens and, as a consequence, lowers the radiation efficiency.

Embedding the antenna in a dielectric medium offers a solution here. A high dielectric constant and a low loss factor are the basic requirements to the material as otherwise, the resonating size of the patch enlarges too much.

Consequently, layouts for higher frequencies are also investigated, taking advantage of a smaller resonating size. With miniaturization techniques the needed antenna size can be further adapted to the provided area.

#### *APPLICATIONS AND SPECIFICS*

The opportunities of using a high frequency of 31.5 GHz are investigated in the following study [107]. The antenna was placed subcutaneous beneath a 4 mm skin and 4 mm fat layer. With a patch size of  $L=2.66\text{mm}$  and  $W=3.39\text{mm}$ . A return loss of more than 30 dB and directivity of 9.32 dBi in the air cavity is reported. As an embedded result, including the losses of the surrounding tissues, a gain of -46.5 dB was calculated.

The results show, that the favorable antenna properties cannot compensate the transmission losses at 31.5 GHz. With a power loss of around 52.4 dBm inside the body only a limited short range application (closer than 1m) is a viable option.

##### *2.5.5.2 Folded Microstrip Antennas*

The folded microstrip antenna is another special type of microstrip antenna. It has a similar layer assembly, but the upper layer has a geometric structure, like a flat spiral or meander-like stripe with alternating width. This layout often integrated directly on PCBs, because with its strip-like structure it is well adaptable to the constraints of the PCB layout. This makes this topology an economical solution for an integrated antenna.

On the basis of the same principle layer setup this antenna topology is subject to the same constraints as the patch antenna. When the upper patch

is in direct contact with the lossy medium a very low efficiency is achieved. Therefore, with this antenna type For this reason, a second, additional dielectric layer is applied on the microstrip layer.

Adding a superstrate of high permittivity is a standard technique in antenna design. Due to the fact that the human tissue in general possesses an elevated permittivity, with an additional dielectric layer on the top, the electrical size of the antenna increases for the same frequency but the efficiency is higher, too. In other words, the loading of the superstrate elevates the resonant frequency and narrows the impedance bandwidth of the antenna.

Another technique is placing a shorting pin from the radiator to the ground plane. This procedure typically produces the same frequency response at less than half the size of a similar antenna without the shorting pin albeit lowers the resonant bandwidth.

Compared to other antenna types (e.g., monopoles), folded microstrip antennas in general provide a smaller bandwidth and, apart from that, only offer 2-D solutions, which needs to be considered by the time of selecting an antenna topology suitable for the final SCVC.

#### *APPLICATIONS AND SPECIFICS*

An optimized folded microstrip antenna is proposed in [116]. The optimization is based on a particle swarm algorithm varying antenna layout parameters like width and length of several strips along the meander layout as well as the position of the feed and the ground point. All vertical layer thicknesses are kept, like shown in Fig. 2.35 (a) and (b). An optimized size of 22.5mm x 22.5mm x 2.5mm for a dual resonating design is indicated. Measurements show a -10 dB bandwidth in the MICS region of 35.3% while 7.1% in the 2.4 GHz ISM-band. A slight disadvantage is the 90° offset of the main radiation direction of the two frequency bands.

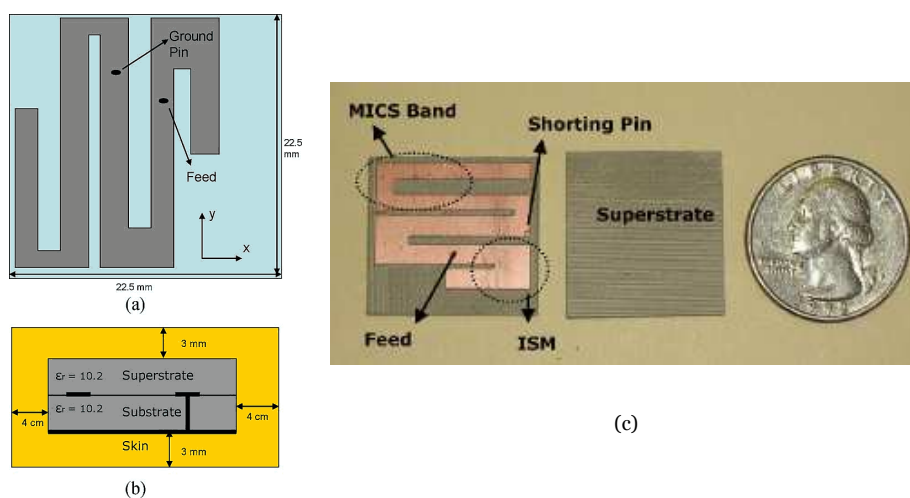


**Fig. 2.35.** (a) Top view, (b) side view and (c) prototype of a microstrip dual-band antenna for ISM 2.45 GHz and 403 MHz MICS frequency [116].

### 2.5.5.3 Stacked Microstrip Antennas

This design consists of several microstrip layers, which are piled over each other and share a common ground plane. In between it is placed a isolating dielectric layer. The patches can be stimulated using a shared feed line, but also a parasitic stimulation of the upper metal structure using near field coupling is possible. Using different topologies and feed positions additional optimization of the radiation properties can be achieved. An additional patch or microstrip layer gives the designer freedom to adapt the properties of the antenna to the specific application.

Stacked designs are typical to stimulate dual or multi frequency resonances. Moreover, they can be used to lower the required resonating footprint of the patch [118]. It can be used to improve the broad band properties or polarization purity [119]. By varying the dielectric properties of the dielectric layers and their thickness the radiation distribution can be shaped [68].

### APPLICATIONS AND SPECIFICS

An example for a circular stacked microstrip design for the MICS frequency band is demonstrated by [120]. The stacked approach was selected to enhance resonating bandwidth. The design consists of a disc with a diameter of 15 mm and a height of 1.9 mm integrating two strip layers.

The size and 10 dB bandwidth is optimized by the length of the microstrips on the two conducting layers ( $r$  and  $L_C$ ) and the position of the feed and shorting pin ( $d$ ) as well as the strip width ( $w$ ) (see Fig. 2.36). Furthermore, the influence of the thickness of the dielectric superstrate layer was investigated, which shows a detuning of the resonance frequency.

Simulations show a radiation efficiency of 0.31% and a maximum gain value of -26 dB when the antenna is placed in a subcutaneous position 4 mm beneath the skin. The antennas demonstrate very stable properties towards different body tissues, but results of fat tissue influence are not demonstrated.

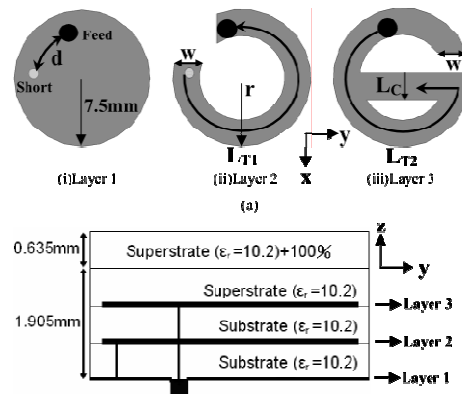


**Fig. 2.36. Dual layer stacked microstrip antenna [120].**

A slotted patch design is introduced by [121]. The two rectangular layers are intended for bandwidth enhancement and for a more environment independent radiation properties. The compact size of the ground layer is  $10 \times 10 \times 1.9 \text{ mm}^3$ . The antenna is placed 5 mm subcutaneous and is optimized for skin tissue. A radiation efficiency of 0.61 % is reported as well as a measured 10 dB bandwidth of 50 MHz.

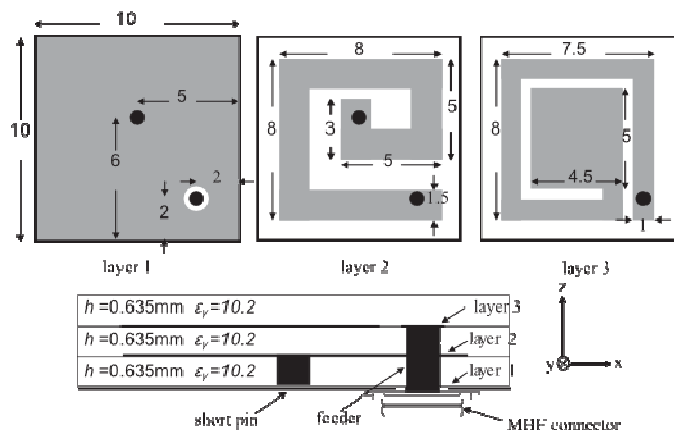


Fig. 2.37. Example of a 403 MHz dualstacked microstrip antenna [121].

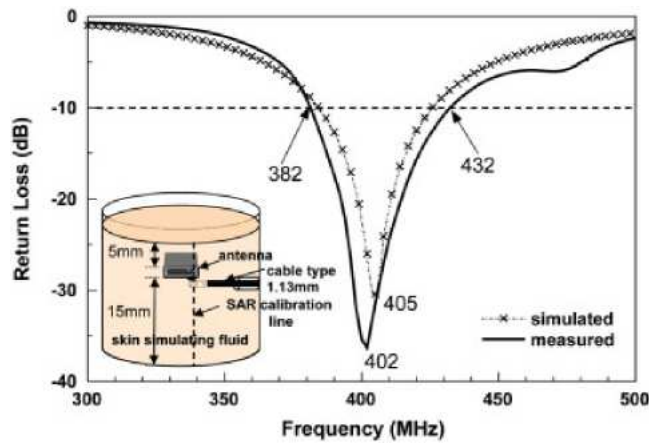


Fig. 2.38. Matching bandwidth of the dual layer microstrip antenna [121].

#### 2.5.5.4 Planar Inverted-F Antennas

The Planar Inverted-F antenna (PIFA) is another variant of the microstrip antenna. A grounding pin is used as an effective way of reducing the dimensions of the antenna, while maintaining adequate electromagnetic performance [106], [122].

The requirements are the same as for patch antennas. The antenna consists of a ground plane and a minimum distance to the metallic layer, which has to be constant and must not be discontinuous.

In a study of a PIFA and a patch antenna [117] with a comparable planar spiral radiator and footprint it was shown that, although the

radiation patterns are similar to each other, the PIFA has a higher radiation efficiency in an implanted environment (see Tab. 2.13). This can be explained by the use of the grounding pin which builds up a loop with high currents. In this manner, half of the antenna works as a magnetic antenna. These have lower losses in comparison to an electrical monopole, explaining the higher efficiency.

Return loss measurements were conducted with the antennas placed in a liquid tank, 4 mm separated from the front. With a PIFA design of a 4 mm thick dielectric superstrate layer was demonstrated that the isolation of its radiating patch was high enough and, that the resonant frequencies in air and tissue simulating liquid were close, however, to expense of a total thickness of the antenna of 8 mm. Otherwise, the thick superstrate assisted the antenna to be well matched to  $50 \Omega$  by decreasing effects of the surrounding high conductive biological tissues.

Antenna Type	Radiated Power	Radiation Efficiency
Microstrip Antenna	0.0016 W	0.16 %
PIFA	0.0025 W	0.25 %

**Tab. 2.13. Comparison of radiated power ( $P_{in}=1W$ ) and radiation efficiency between PIFA and microstrip antenna of the same size [117]**

The detuning effect was also demonstrated by slimming the dielectric layer from 4 mm each to 2 mm thickness.

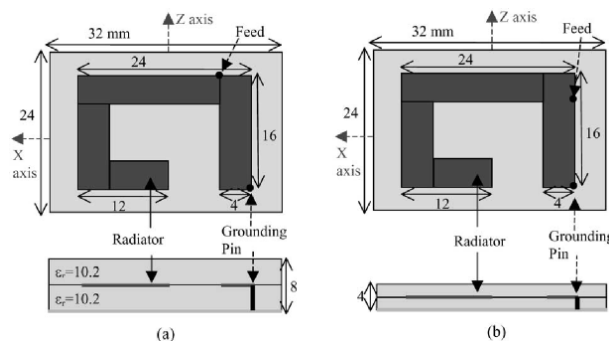


**Fig. 2.39. Two PIFA topologies for the MedRadio frequency [117].**

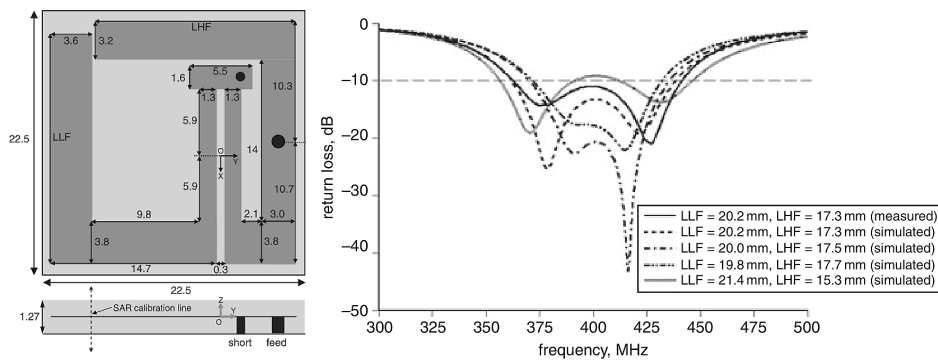


**Fig. 2.40. Layout of a PI-shaped wideband antenna for MICS band (left) and results of the tuned wideband return loss (right) [123].**

A compact design is proposed for a  $\Pi$ -shape PIFA antenna by Lee [123] (see Fig. 2.40). By exciting dual-resonant frequencies around the MICS frequency band a wideband input matching is accomplished. The two frequencies are tuned by varying the two L-strip lengths. The final antenna reaches a 80 MHz 10 dB bandwidth, as shown in the diagram. Three dimensional simulation revealed a -25 dB gain if the antenna is placed 4 mm subcutaneous in a skin tissue mimicking phantom.

### 2.5.6 HELICAL ANTENNAS

A helical antenna is a rather less common design for implanted antennas, but it delivers interesting results and permits a straight forward tuning with few geometric parameters.

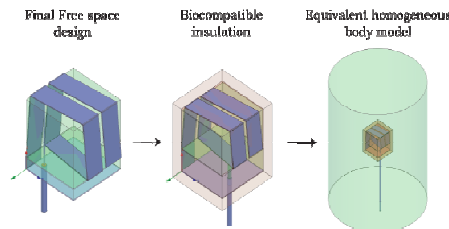


**Fig. 2.41. Design steps of rectangular spiral antenna over a ground plane.**

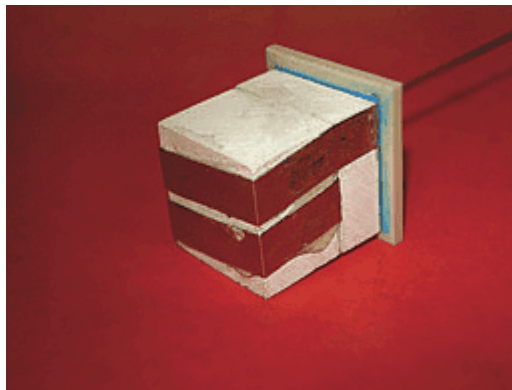


**Fig. 2.42. Intermediate prototype showing helical radiator [124].**

Adabia [124] proposed a rectangular, horizontally over ground plane mounted normal-mode helical antenna. This antenna occupies a volume of about  $3 \text{ cm}^3$  with a final size of  $14 \times 14 \times 15 \text{ mm}^3$ . It consists of two rectangular loops over a ground plane with a coaxial feed. It builds around a ceramic core (HIK500  $\epsilon_r=11$ ) and it is enclosed by a teflon substrate of  $1.5 \text{ mm}$  with  $\epsilon_r=3$ . As a consequence, the lateral substrate faces (lower  $\epsilon_r$ ) provide extra surfaces for the design of a three-dimensional radiator.

The antenna is matched for the insertion in muscle tissue. Simulation results show a gain of  $-28.5 \text{ dB}$  and a  $10 \text{ dB}$  bandwidth of  $225 \text{ MHz}$  ( $55.7\%$ ).

Varying the geometric parameter of the rectangular helix reveals that, with a higher diameter of the helix, the gain raises and the  $10 \text{ dB}$  bandwidth stays constant. Further simulations show, that the extension of the spiral lowers the  $10 \text{ dB}$  bandwidth, but elevates the gain. Furthermore, the radiation pattern as well as the main direction completely change from free-space to in-body simulations, even if the matching does not alter.

This antenna topology poses a solution close to the desired: a 3-D antenna, conformal to the CVC. The helical radiator serves as an inspiration for monopoles or wire antennas conformal to the implant and will set the basis for the main designs in the present work.

## 2.6 CONCLUSION OF THE STATE OF THE ART

The preceding state of the art report delivers an insight into the present situation of implanted antenna design and wireless communication in smart systems. The key aspects to face future trends cover the indispensable conformability of the antenna to the implant surface, the



combined utilization of multiple frequency bands and, above all, an advanced procedure of antenna characterization that responds to the mismatches between simulation and measurement.

In the area of implanted antennas, research tends to focus on flat topologies with a ground plane. Since every attached structure eventually adds to the outline of an implant, planar topologies are limited to implants with flat surfaces. Patch-like antennas, often stacked, allow miniaturization by means of shorting pins, but their integration is also restricted to certain implant shapes. Monopoles, for instance, are flexible towards a huge number of objects, and therefore meet the demand of 3-D conformability for implanted antennas. Furthermore, most state-of-the-art designs are confined to monofrequency topologies while multifrequency designs would offer enhanced functionality and provide new visions of potential application scenarios. Latest developments in the field of transceivers for smart implants support the dual-band operation, which expands the options for future applications. Apart from that, a conclusive comparison of results can be difficult due to the wide range of phantom types, shapes and sizes and the alternating position of the antenna in the body, respectively in the phantom. In addition, the vast variety of antennas and the array of essential considerations to bear in mind make the elaboration of an overall characterization method a critical endeavor.

The approach to combine simulation and measurement analysis and the integrated contemplation of 3-D implants together with their projected antennas imply promising future perspectives towards a reliable establishment and maintenance of wireless communication in smart systems and finally, leave room for an outlook on the tasks that lie ahead.



## *Chapter 3*

# **Objectives**

---

In Chapter 3 the research goals of the study are exposed in preparation for the forthcoming chapters.

### **3.1 OBJECTIVES OF THE PROJECT**

The general objective of this work is to develop antennas for subcutaneous implants, meeting requirements beyond the state of the art. An optimum 3-D surface conformity of the antenna is to be considered with regard to the specified smart implant, a CVC port. Apart from that, the application is to achieve maximum efficiency. Broadband dimensioning with two frequency bands, the MICS band at 402-405 MHz and the 2.4-2.5 GHz ISM band, operating simultaneously is to be pursued to prevent the input impedance from detuning. For patient monitoring, two scenarios are conceived: an outdoor scenario, in the global RFID UHF band at 865-956 MHz and an indoor scenario, in the MICS band, as this standard is

not subject to interferences. To select the suitable scenario, the maximum operation range of the antenna is to be determined. For this purpose a characterization procedure is to be developed in order to confirm the real world antenna performance in the body tissue environment. The primary research goal is broken down into several subordinate targets:

State-of-the-art antenna topologies for implants will be studied and appropriate antenna layouts conformable to being attached to and operated in smart implants will be evaluated. Particular attention will be paid to design and specification issues for subcutaneous applications. This will include regulation matters and standard reviews.

In CST MICROWAVE STUDIO® (CST MWS), simulation environments will be developed representing the distribution of the electromagnetic field in- and outside the human body, i.e., the influence of the human body on the antenna radiation pattern and radiation efficiency.

Measurement environments imitating the properties of the human body, i.e., the future subcutaneous body tissue environment will be prepared. This will include building carefully designed phantoms while respecting suitable component ratios in the mixture of the mimicking liquid and adequate dimensions, which will be determined beforehand by means of simulation.

Antenna prototypes will be manufactured according to the simulation results and their gain distribution, i.e., radiation patterns will be measured and analyzed. Furthermore, the link budgets will be calculated based on real measurement by de-embedding the effect of cables.

A new procedure will be used as a methodology to verify the obtained property data in order to assure a realistic and comparable antenna characterization.

The measurement results will be used to adapt and optimize an UHF antenna to a smart implant and finally, the performance of the system will be examined by running functional tests.

## *Chapter 4*

# ***Design of UHF Antennas for Implants***

---

This chapter enters the practical part of the dissertation and exhibits the first experimental chapter of the document. In Chapter 4 the antenna layouts, simulation processes and results of two antennas for implants are presented. In the first section, a single-band antenna operating in the European SRD band g1 [125] of 863-870 MHz<sup>9</sup> is in the focus of attention, whereas in the second section a dual-band antenna designed for the MICS band (see section 2.4.3) and the ISM band of 2.4 GHz is introduced.

---

<sup>9</sup> including the European UHF-RFID band from 865-868MHz.

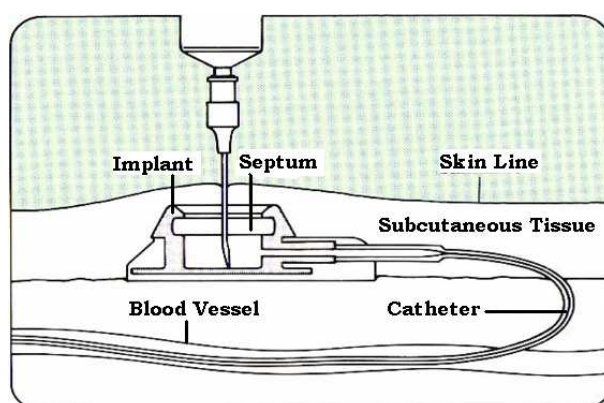


**Fig. 4.1. Subcutaneous implanted CVC port [103].**

The shape of the implant was given to be the truncated cone of a portacath or CVC port. A portacath is an implant placed beneath the skin to administer medication, connected to a large vein by means of a central venous catheter (see Fig. 4.1).

Neither was there any additional room available to store the antenna, nor was the antenna's integration inside the cone a favoured option. In addition to that, this would have implied a more complicated construction process of the portacath. Hence, a paramount demand on the antenna was to merge with the implant shell without stepping up the surface. Above all, only a partial area of the cone surface was dedicated to supporting the antenna. The first antenna design was planned to be mounted on top of the portacath as it is the closest part to the skin surface. It was intended to be placed on the thin circular edge on top of the truncated cone of the liquid reservoir. The second antenna for the SCVC implant exploited the entire outer surface of the CVC port's truncated cone shell.

To better distinguish both implanted CVC antennas (CVCA) in the thesis, the first one is referred to as planar CVCA or RFID CVCA and the second one as 3-D CVCA or dual-band CVCA.

#### **4.1 DESIGN OF AN IMPLANTED PLANAR CVC ANTENNA**

The following section displays the layout and simulation process of the single-band antenna operating in the European SRD g1 band. Unlike others, this frequency band is not subject to strict regulations of certification authorities and is therefore of free use. The antenna is planar and particularly compact. Circumferential space constraints limited the antenna

diameter to a maximum of 20 mm. The distance to the interface skin-air was fixed to 9 mm.

#### 4.1.1 ANTENNA LAYOUT

The layout of an implantable antenna is determined by several key issues:

- Protecting the body tissue from being harmed
- Compensating tissue and environment variations
- Occupying as little space as possible

To meet the first requirement, a round shape was chosen to be a suitable topology for the antenna rather than a square shape with sharp corners.

With regard to the second demand, a broad-band design was chosen in order to balance tissue properties and environment alterations provoked by gender, age or figure of a person. Disturbing influences caused by the location of the implant itself could also be compensated, as may be the case. Hence, known for its convenient broadband frequency properties, described in section 2.5.4, a monopole-like structure was adopted.

Finally, ceramic layers were applied on the top and bottom of the antenna instead of using a ground plane or short circuits to it for miniaturization purposes. This allowed maintaining the antenna at minimum size without reducing its radiation efficiency at the same time. As mentioned, the maximum dimensions of the round shaped antenna were limited to an outside diameter of 20 mm.

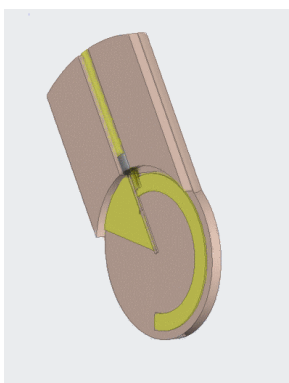


**Fig. 4.2. Antenna simulation model with ceramic bottom layer.**

Fig. 4.2 illustrates the top view of the implanted antenna along with the feeding setup. For clarity, the ceramic top layer of the antenna was removed.

#### 4.1.2 SIMULATION

The antenna model was simulated in CST MWS. A cubical single-tissue phantom (see section 2.3) with a side length of 63 mm was defined as simulation environment.

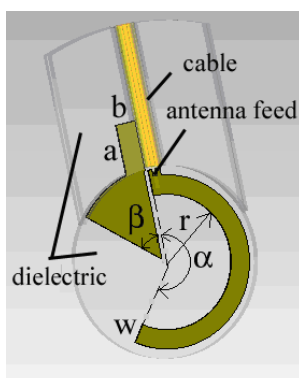


**Fig. 4.3. Radiating structure of the antenna with geometric parameters.**

As shown in Fig. 4.3 the antenna was described by two angles. The radiating element was a flat circle-shaped monopole. Its length corresponded to the resonant frequency and was defined by the angle  $\alpha$ . The angle  $\beta$  determined the size of the plane connected to the outer conductor of the coaxial cable (ground). This outer conductor was soldered to the antenna at the area defined by the two auxiliary parameters  $a=5\text{mm}$  and



$b=2\text{mm}$ . The correspondent assembled prototype is presented in Chapter 5, Fig. 5.1.

The length of the monopole was increased iteratively. Different lengths were given a trial and matched to a reference impedance of  $50\ \Omega$  by means of a corresponding capacity load. By increasing the angle  $\beta$ , the open end of the monopole gained capacity load and, as a result, the impedance was modified. By variation of the angles  $\alpha$  and  $\beta$ , the antenna could be matched to different frequencies and ceramic layer thicknesses. The antenna's final bottom and top layers were simulated to be made of a dielectric, ceramic substrate with a high permittivity of  $\epsilon_r=10$  (Rogers Ro3210). Each layer was 1.27 mm thick. The antenna was tailored to have its resonating frequency at 868 MHz. Tab. 4.1 shows the final, optimum antenna configuration based on which the prototype was built.

Parameter	Value [mm,°]
r	8
w	2
$\alpha$	215
$\beta$	50

**Tab. 4.1. Final antenna parameters at 868 MHz.**

In the following section the simulation results are displayed.

### 4.1.3 IMPEDANCE MATCHING

The antenna was simulated with skin mimicking liquid (see section 2.3.1). Not all the parts of the setup could be perfectly modeled in the simulation, especially the antenna feed and the shape of the phantom.

In order to keep the computing time short, a reduced phantom size with symmetric dimensions was selected. The simulation in a phantom smaller than the final phantom used in the measurements turned out to be a very acceptable approximation for reflection coefficient estimation, as its impact on the matching results was negligible. The accordant downsized phantom for the simulation had a side length of 6 cm and the antenna was placed at 9 mm to the phantom-air interface (subcutaneous-like position).

Moreover, a single-tissue phantom was considered satisfactory for the simulation as in the later measurements the applied mimicking liquid would also replicate the skin tissue properties in only one single average value. In addition, the antenna was projected to be implanted right beneath the skin

after all. Apart from that, the use of a more complex three-tissue phantom (skin, fat and muscle)(see section 2.3) for the measurements would not have altered significantly the return loss of the antenna, but only prolonged the simulation time.

The mimicking liquid, which later was also used to build the phantom, was mixed and the properties measured. The permittivity probe in the skin mimicking liquid did not capture the data at every single frequency, but in certain intervals. The obtained results were gathered and compiled in the dispersion list, which consequently featured data gaps between the selected frequencies. These gaps, again, were filled by importing the list into CST MWS, which in turn calculated the missing data and finally drew a continuous graph based on these parameters by a fitting process.

After optimizing the antenna in the small phantom, the graph below eventually corresponds to the simulation in the final, bigger phantom.

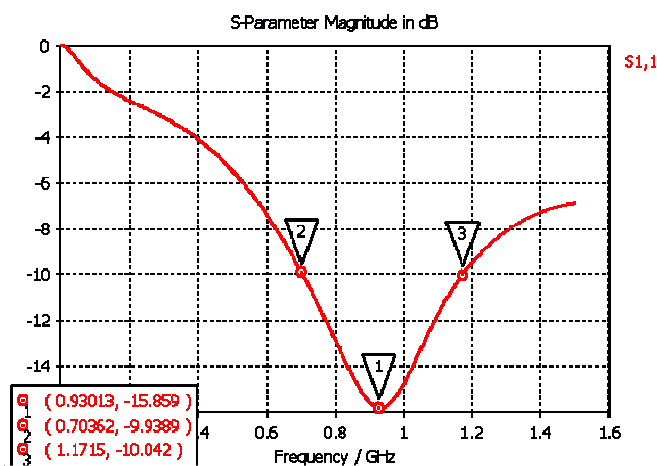


Fig. 4.4. -10 dB matching bandwidth, simulated in big phantom.

In Fig. 4.4 the reflection coefficient, (reference impedance 50  $\Omega$ ) of the antenna is represented. At the reference value of  $\Gamma_{11} < -10$  dB the frequency bandwidth lies between 704 MHz and 1.17 GHz, i.e., the antenna can be operated worldwide in all UHF-RFID bands (see section 2.4.3.1). The relative bandwidth equals 49.7%.

## 4.2 DESIGN OF AN IMPLANTED 3-D CVC ANTENNA

### 4.2.1 ANTENNA LAYOUT

The layout and simulation process of an implanted dual-band 3-D CVCA operated in the MICS frequency at 402-405 MHz as well as in the global ISM band of 2.4-2.5 GHz is displayed in the following sections. While the former was exclusively dedicated to medical applications, the latter was being used in a number of wireless communication protocols. The dual-band antenna was determined to the application on the liquid reservoir of a CVC port and therefore tailored to a prior specified, truncated cone. The framework of the project also included the development of a correspondent transceiver to sustain wireless communication with an external base station. Although system design is not in the focus of this dissertation, basic information about the used transceiver is put on record in section 5.2. The advanced dual-band capabilities of the Zarlink ZL70102 made it an ideal complement to this antenna for SCVC.

#### 4.2.1.1 Requirements

The shape of the supporting reservoir was a truncated cone with a base radius of 16 mm and a height of 16 mm. As a result, the antenna was determined to be three-dimensional, conformal to the truncated cone and low-profile, i.e., ideally with no extra volume added to the SCVC. The antenna required broad-band behaviour to avoid detuning in a changing live environment. Dual-band operation in the MICS frequency at 402-405 MHz as well as in the global 2.4 GHz ISM band was also required. As a basic principle, data is transferred in the MICS band, whereas the higher frequency was used to initiate communication and wake up the smart implant in order to enter its operating mode. A biocompatible synthetic layer made of the same material as the CVC (see Fig. 4.1) [103] prevents physiological interaction between the surrounding tissue and the antenna.

#### 4.2.1.2 Antenna Design Process

The constraints mentioned above had already been taken into account at the time when the basic antenna topology was settled. That was why a monopole-like structure was preferred as radiating element. The advantages of this antenna type (e.g., high impedance bandwidth, etc.) are illustrated in section 2.5.4).

Its broadband impedance bandwidth [126], unlike implanted microstrip antennas [116], [121], and low-profile extension were major advantages with respect to the antenna requirements. The design required a

convenient way to mount a monopole onto the cone. The constraint was to have to accommodate the radiator on the limited surface with enough length to allow the antenna to operate in the 402-405 MHz MICS band.

In the endeavor to find a convenient way to mount a monopole onto the cone, different design ideas were pooled, two of which are exemplified in Fig. 4.5 and Fig. 4.6. The difficulty was to make sure that the monopole was accommodated on the limited cone surface with sufficient length in order to allow the 3-D CVCA's functioning in the MICS band. The topology represented in Fig. 4.5 was singled out and later further developed to where the monopole extends over both sides of the cone shell, like shown in section 4.2.1.

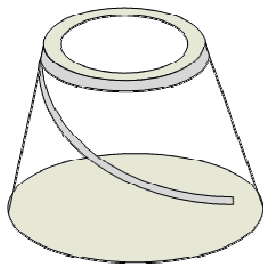


**Fig. 4.5. Monopole one-sided on cone.**

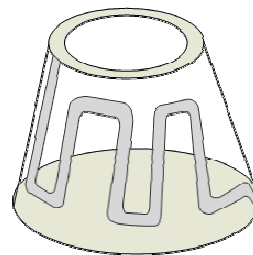


**Fig. 4.6. Monopole meandering on cone.**

#### 4.2.2 SIMULATION

In order to reduce computation time, the simulation model used a body phantom that had smaller dimensions than the phantom applied in the measurements. This was considered an acceptable approximation, as the impact of phantom size on the input impedance matching was mostly negligible within certain limits. The reduced cubical phantom for the simulation had a side length of 6 cm. The subcutaneous position of the implant in the body was replicated in the simulation by locating it at 9 mm from the phantom-air interface. The chosen antenna topology was designed with CST MWS electromagnetic simulation software.

Moreover, a single skin tissue phantom was considered to be accurate enough for the simulation for several reasons. Firstly, its properties were similar to general muscle tissue at 403 MHz ( $\epsilon_{r\_skin}=46.7$ ,  $\epsilon_{r\_muscle}=57.1$ ;  $\sigma_{skin}=0.658$ ,  $\sigma_{muscle}=0.623$ ) and secondly, it represented the volume between implant and air through which the data transmission was studied. Simulations showed that peak SAR was more critical in this area and

accordingly, material definition should be done accurately. The use of a more complex three-tissue phantom (skin, fat and muscle) would not significantly have altered the return loss of the antenna, and it would only have increased the simulation time [127], [117], [128]. The skin mimicking liquid was elaborated (according to [116]) and measured with the Agilent Technologies 85070E dielectric probe. The results were gathered and compiled in a dispersion list. Prior to simulation, the dispersion list was imported into CST MWS, which in turn calculated the missing data based on a dispersion model (2<sup>nd</sup> order Debye model).

A broadband simulation type from 0 to 4 GHz was utilized by applying a transient solver based on the Finite Integration Technique. By using the Fast Perfect Boundary Approximation (FPBA), hexahedral mesh was employed without the need to resort to the subgridding technique. The absorbing boundary condition was chosen for the computation domain around the phantom keeping a radiating space in the off-body direction of  $\lambda/8$  for a precise far field computation at 403 MHz. An increased number of 35 mesh cells per wavelength was considered for the upper frequency limit. The number of mesh cells was kept under 100 million regardless of phantom size and surrounding tissue for computational limits. The “bend sheet” feature was employed to project the antenna over the CVC port’s truncated cone. The feeding cable was included in the model. The design was optimized with respect to a reference impedance of 50  $\Omega$ .

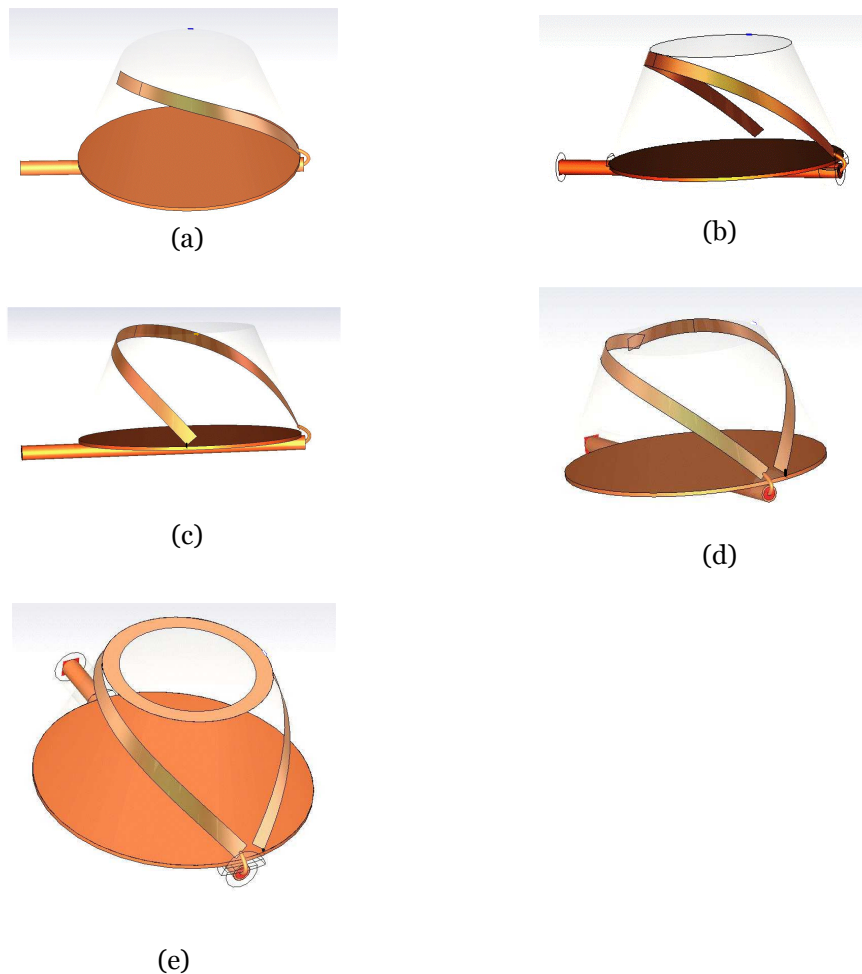
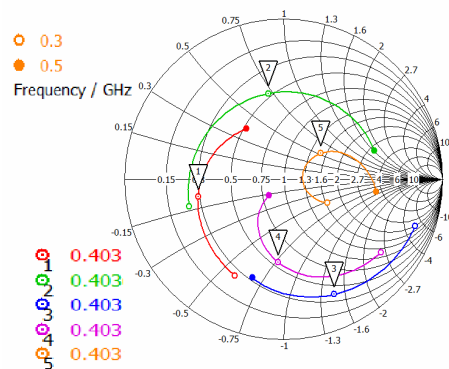
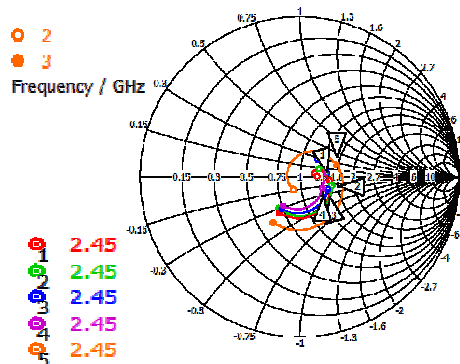


**Fig. 4.7. Topologies used during the optimization process: (a) Short monopole. (b) Long monopole. (c) Long monopole with short circuit to ground. (d) Extended monopole with short circuit. (e) Extended monopole with short circuit and loop.**

The simulation model included a round ground plane that covered the bottom side of the cone. The outer conductor of the coaxial feed cable was soldered to this implant's ground plane. The inner conductor was connected to the monopole, which, in turn, was attached to the cone shell. To describe the cone itself, the parameters of silicon rubber [103] based material were employed. Its relative permittivity was set to 3 according to [129]. The design process is illustrated in Fig. 4.7 and Fig. 4.8, where the optimization steps in Fig. 4.7 (a) through Fig. 4.7 (e) correspond to markers 1-5 shown in Fig. 4.8.



(a)



(b)

**Fig. 4.8. Smith chart showing the complex impedance matching between (a) 0.3 - 0.5 GHz and (b) 2.0 - 3.0 GHz referring to the design steps towards the final antenna model. 1) Short monopole. 2) Long monopole. 3) Long monopole with short circuit to ground. 4) Extended monopole with short circuit. 5) Extended monopole with short circuits and loop.**

The design process started with a single monopole (see Fig. 4.7 (a)). Marker 1 in the Smith chart of Fig. 4.8 (a) shows its resistive properties around 403 MHz. The monopole was too short as the resonating frequency was located above the MICS band. In this case, matching conditions were not optimal. By extending the monopole (see Fig. 4.7 (b)), the frequency point of interest in Fig. 4.8 (a), marker 2, moves clockwise towards the inductive part of the Smith chart. In order to take advantage of the cone surface, a short circuit implementation was applied as miniaturization technique. (see Fig. 4.7 (c)). By adding a short circuit to this configuration,

the graph was mirrored to the capacitive region of the diagram with respect to the center (see Fig. 4.8 (a)), marker 3. Even by adding a further extension of the monopole, as displayed in Fig. 4.7 (d), the matching left room for improvement (see Fig. 4.8 (a)), marker 4. By using a closed loop (see Fig. 4.7 (e)), which could be seen as an additional inductance, the input impedance rotated clockwise from marker 4 to 5 and almost matched the desired  $50 \Omega$  (see Fig. 4.8 (a), marker 5. This loop was narrow enough to leave the top of the implant clear.

The Smith chart in Fig. 4.8 (b) demonstrates the low influence of the abovementioned geometric changes of the antenna on the impedance matching for the 2-3 GHz range. This was due to the resistive properties of the lossy medium around the antenna. After applying further minor optimizations, the final topology was singled out, where the monopole extends over both sides of the truncated cone shell (see Fig. 4.9). The specific design parameters are displayed in Tab. 4.2.

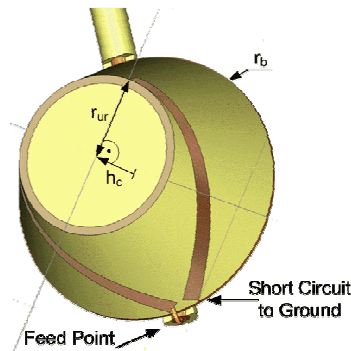


**Fig. 4.9.** Top view of the final antenna simulation model without the protection layer.

Parameter	Value [mm,°]
Base radius ( $r_b$ )	16
Upper ring outside radius ( $r_{ur}$ )	10
Cone height ( $h_c$ )	16
Copper strip length	33
Copper strip width at upper ring	1.5
Copper strip width at monopole	2
Angle between the monopole-to-ring connections	90

**Tab. 4.2.** Final geometry of the 3-D CVC antenna.



The outside metal 3-D CVCA parts had to be insulated to prevent interactions with the surrounding body tissue. As a design strategy, when the coating was made thinner, the antenna reduced its operating frequency (becoming more compact) due to the size-reduction effect introduced by the closer presence of the high permittivity medium. At the same time, a large relative frequency bandwidth was achieved. This increased the robustness against implant environment variations [60], [130] including, for example, variations in the proportion of body tissues over different patients or position variations of the implant itself. However, the radiation efficiency decreased due to the proximity of the same lossy medium and a trade-off should be struck.

For this purpose, the 3-D CVCA was coated with a 0.2 mm biocompatible synthetic film made of the same silicone rubber material as the CVC. In this way, the dual-band CVCA was fully integrated. This nonconductive coating had a major impact on the electromagnetic properties, as it was placed in the near field of the antenna. Commonly used coatings for implanted planar microstrip antennas include a ceramic layer with high permittivity ( $\epsilon_r \geq 10$ ) and low loss with at least 0.6 millimeters [116], [121], [120]. This solution was not feasible because of the 3-D cone-like conformal shape of the 3-D CVCA topology.

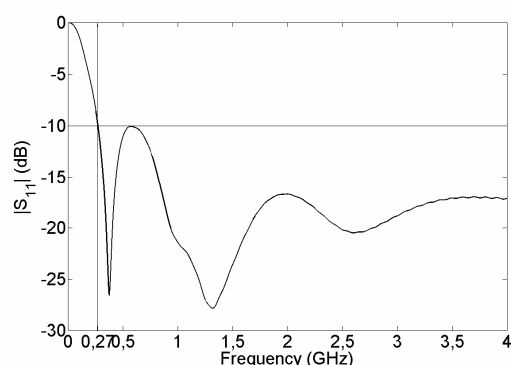


**Fig. 4.10. Simulated  $|S_{11}|_{\text{dB}}$  vs. frequency of the 3-D CVCA in a 216 cm<sup>3</sup> skin phantom.**

Fig. 4.10 depicts the simulation results of the 3-D CVCA's S-parameter  $|S_{11}|_{\text{dB}}$  (reference impedance 50  $\Omega$ ) with a 0.2 mm biocompatible synthetic film isolation within the 6 cm<sup>3</sup> cube phantom.

At the reference value of  $|S_{11}|_{\text{dB}} < -10$  dB the antenna covers the required bandwidth from 0.273 GHz to more than 4 GHz. This means that it can be operated worldwide in the MICS band as well as in the ISM 2.4 GHz band.

### 4.2.3 IMPEDANCE MATCHING

Once the basic antenna shape and an appropriate phantom size were defined a study was conducted focusing on the robustness of the matching against certain functional aspects. The investigation about the minimum height for a representative phantom size is explained in section 5.3. The study was performed in a 355 mm x 250 mm x 160 mm phantom.

#### 4.2.3.1 Biocompatible Layer Thickness

Fig. 4.11 shows the impact of the biocompatible layer thickness on the 3-D CVCA matching. The lowest  $|S_{11}|_{dB} < -10$  dB condition is given at 230 MHz, 390 MHz and 452 MHz for 0.2 mm, 0.4 mm and 0.6 mm respectively. It is observed that from a thickness of 0.6 cm, the matching is not accomplished in the MICS band. The insulation layer on the top was kept to a thickness of 1 mm and its variation did not significantly affect the performance (not shown for brevity).

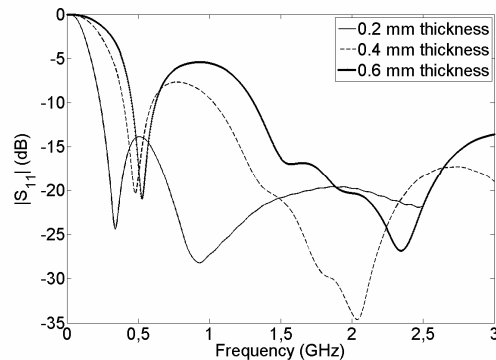


**Fig. 4.11. Simulated  $|S_{11}|_{dB}$  vs. frequency of the 3-D CVCA in representative skin phantom for different isolation layer thicknesses.**

#### 4.2.3.2 Functional Operation

Computed matching against reservoir status (not present, present but empty and filled with body liquid) was studied. The body liquid option was selected as being representative of functional operation [53], and imported in CST MWS with a 2nd order Debye model fit. Fig. 4.12 shows that the antenna is robust against the functional variations.

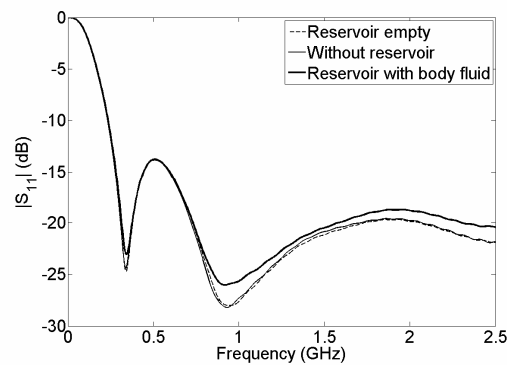


**Fig. 4.12. Simulated  $|S_{11}|_{dB}$  vs. frequency of the 3-D CVCA in representative skin phantom for different functional states.**

#### 4.2.3.3 Tissue Variation

In order to analyze the impact of the variability of the surrounding tissue on the antenna matching, a muscle and a muscle-skin bilayer phantom were considered. In the latter case, the skin was considered to be between the top antenna part and the free space interface. Muscle properties were extracted from [53] and imported by a 2nd Debye fitting into CST MWS. The selected antenna proved to be robust against tissue variability (see Fig. 4.13).

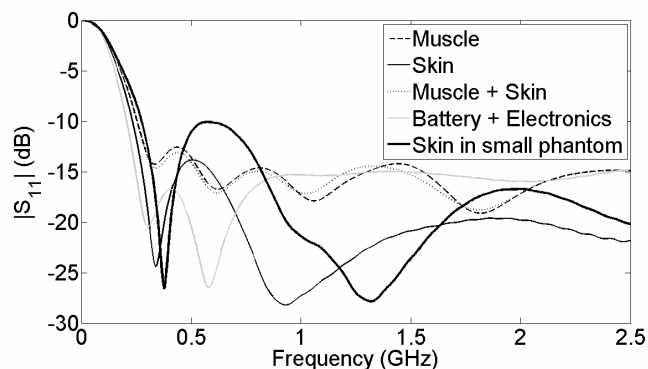


**Fig. 4.13. Simulated  $|S_{11}|_{dB}$  vs. frequency of the 3-D CVCA in representative phantom for different tissue phantoms and in the presence of battery and electronics.**

The robustness of the antenna against dielectric environment changes can be attributed to the short-circuit at one end, which gives the 3-D CVC antenna a magnetic nature.

#### 4.2.3.4 Battery and Electronics Proximity

The antenna was conceived to operate in close proximity to a biofilm sensor, electronics and implanted battery Varta LPP 402025 CE [131]. The specific battery dimensions are 25.5 mm x 20.5 mm x 4.3 mm. The electronics and battery were placed alongside the truncated cone to avoid placing them beneath it and therefore preventing excessive total implant height (see Fig. 4.14). The antenna feeding cable, previously running underneath the ground plane, was substituted by a discrete port at the antenna terminals for functionality purposes.

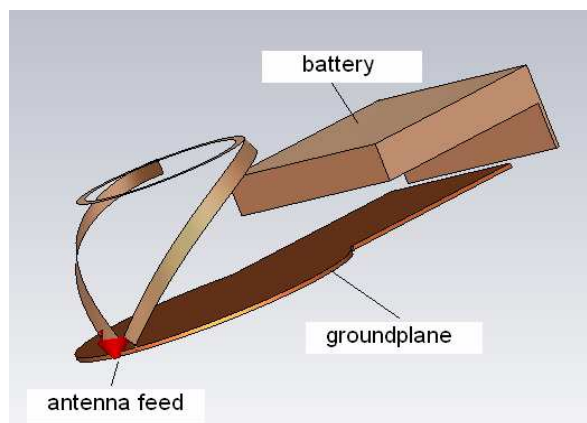


**Fig. 4.14. 3-D CVCA along with metallic parts corresponding to the presence of the battery and electronics. The non-metallic elements were removed for clarity.**

The computed 3-D CVCA's  $50\Omega$  reflection coefficient with battery and electronics displayed in Fig. 4.13. shows, that the reflection coefficient remains below -10 dB at both frequency bands.

The proper integration of the SCVC is described in Chapter 5, also introducing the two matching networks between the transceiver chip's RF ports (MICS and ISM 2.4 GHz bands) with arbitrary impedances [132], [133] as well as the antenna.

## *Chapter 5*

# ***Implementation***

---

Chapter 5 delivers an insight in the two antennas' test bed assemblies and continues with the implementation of the electronics of the dual-band 3-D CVCA in the SCVC for functionality tests. Although system design is not in the focus of this dissertation, the functional units of the smart implant are introduced briefly. Finally, simulations for defining a minimum size of the body phantom and the preparation of the phantom liquids are addressed.

### **5.1 IMPLEMENTATION OF THE ANTENNA PROTOTYPES IN TEST BEDS**

A test bed is an experimentation platform that allows transparent and replicable testing of scientific theories and new technologies. Whereas theory and simulations generally issue the resulting radiation patterns under ideal conditions (see Chapter 4), test beds are essential in order to

affirm the simulated results in the presence of implementation interferences.

The following test beds comprise the antenna prototypes together with the measurement assemblies including the coaxial feeding cables.

### 5.1.1 PLANAR CVC ANTENNA IN TEST BED

A test bed was designed to measure the impedance bandwidth in the tissue simulating liquid. The cable was covered by a plastic tube and sealed at the top and bottom parts as illustrated in Fig. 5.1.

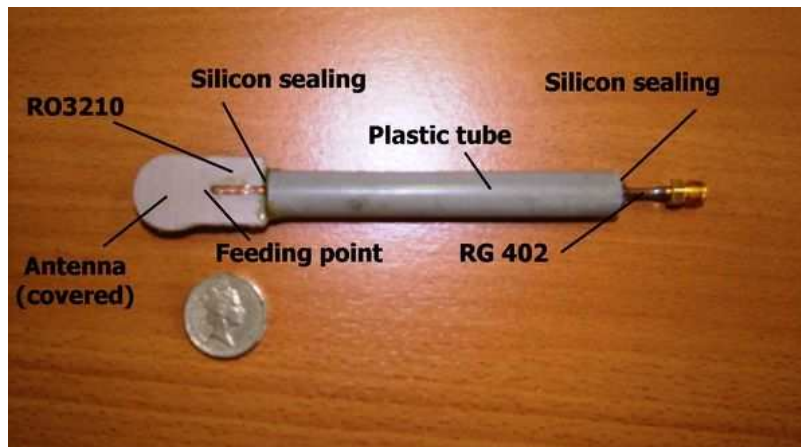


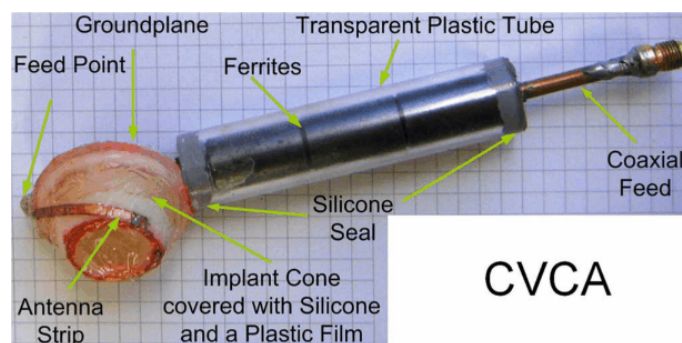
Fig. 5.1. Planar CVC antenna prototype with detailed assembly (test bed).

Fig. 5.1 shows the prototype of the RFID CVCA assembled in the test bed. The round-shaped, planar antenna structure simulated in section 4.1.2 can be seen on the left hand side, now covered by the ceramic top layer. The final antenna substrate and top layer was made of Rogers RO3210 laminate ( $\epsilon_r=10$ ). The copper antenna feeding point was supported on both sides by two ceramic pieces of the same dielectric in order to guarantee its mechanical stability. The center core wire of a thin, rigid coax cable (RG402) was inserted between the bottom and top layer and soldered to the radiating element (monopole) while the outer conductor was soldered to the ground plane. Magnetic beads were placed around the RG 402 cable inside the plastic tube to minimize undesired currents along the outer conductor. Once the antenna feed was connected to the CVCA, the junction between bottom and top layer, as well as the cable, were sealed with glue. A tubular waterproof cable connection fixture, additionally sealed with silicone, was designed as antenna feed.

### 5.1.2 3-D CVC ANTENNA IN TEST BED

During the simulations a standing wave was observed in the stretch of the cable under the liquid level, as the wave was exposed to a strong reflection due to the interface between very different permittivity media (air and skin mimicking liquid). This phenomenon is analyzed more deeply for the RFID CVCA in section 6.1.2.2 by showing its influence on the radiation pattern.

To overcome this phenomenon, inspired by [127] and [134], a test bed was considered where the cable was covered by a plastic tube and sealed at its edges with silicone as shown in Fig. 5.2. Magnetic beads were placed around the cable inside the plastic tube to minimize undesired currents along the outer conductor. The antenna structure on the truncated cone was covered with silicone and a thin plastic film protection layer. Due to prototyping limitations, the thickness was estimated to be between 0.2 mm and 0.4 mm. The core of a thin coax cable (RG402) was soldered to the radiating element (monopole) while the outer conductor was soldered to the copper ground plane of the cone. The junction at the feed point as well as the ground plane were sealed with glue.



**Fig. 5.2. 3-D CVC antenna prototype with detailed assembly.**

Once the prototype was assembled, a characterization of reflection coefficient and gain was conducted.

## 5.2 IMPLEMENTATION OF THE 3-D CVCA PROTOTYPE IN A SMART IMPLANT

In this section, the implementation of the dual-band CVCA into a ULP-AMI (see section 1.1.2) is outlined. In the present case, the smart implant is a SCVC with a portacath holding the 3-D CVCA. The functional

units of the SCVC comprise the dual-band CVCA, the electronics and the biosensor.

### 5.2.1 SMART IMPLANT LAYOUT

The electronics of the implant is designed to interact with a biosensor on the base of the liquid reservoir to monitor the state of the fluid. The 3-D CVCA is integrated with the electronic circuit. The implantable electronic circuit monitors the sensor measurements and calculates whether the measured vital parameter is within normal levels. In this manner, it sets a wireless communication with the off-body device whenever necessary. Fig. 5.3 depicts the elements that form the electronic circuit.

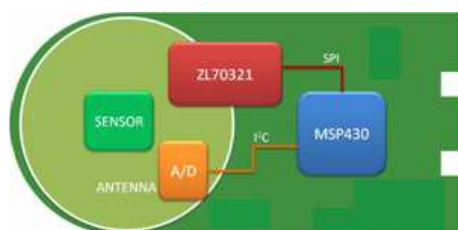


**Fig. 5.3. Function blocks and layout of the PCB.**

The sensor signal is processed by an impedance converter (Analog Devices AD5933 [135]). The sensor measurements are monitored via an I2C interface by the ultra low power MSP430F248 microcontroller [136]. Besides, the microcontroller establishes a wireless communication if the measurement is not within normal levels. It is a 16-bit RISC microcontroller with four different low power modes. Once the information is processed by the microcontroller, it is passed on to the implantable radio module, the ZL70321 by Zarlink Semiconductors [137], a complete MICS RF telemetry radio solution that meets the regulatory requirements of FDA, FCC, and ETSI. The ZL70321 implantable radio module provides high performance while consuming very little power. This RF module is based on the transceiver IC ZL70102 [138]. This transceiver operates in the MICS band at 402-405 MHz and provides an extremely low power wake-up option which is achievable using the 2.4 GHz ISM Band wake-up receiver option.



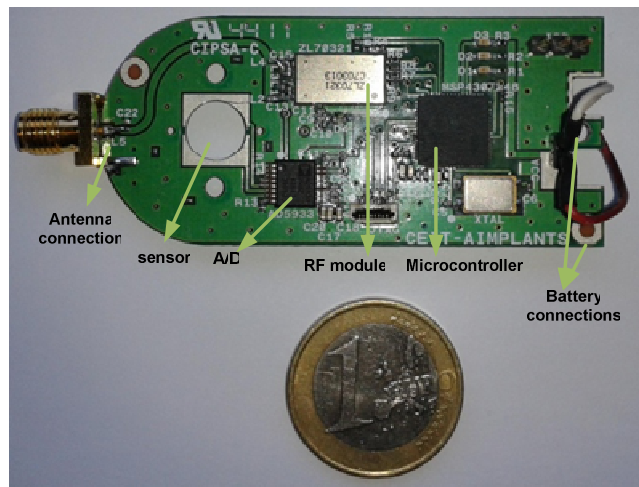


**Fig. 5.4. Assembled prototype showing function blocks.**

The electronic circuit is printed on a FR4 2-layer printed circuit board. All the components shown in Fig. 5.4 are in the top layer due to the packaging requirements.

### 5.2.2 TRANSCEIVER MATCHING

The two transceiver input ports were matched to  $50 \Omega$  at 2.4 GHz by a high pass filter and to  $100\text{-}150j \Omega$  (chip impedance) at 400 MHz by a low pass filter. The Advanced Design System (ADS) schematic model is represented in Fig. 5.5, where port 1 represents the antenna and ports 2 and 3 the 2.4 GHz and 400 MHz terminals, respectively.

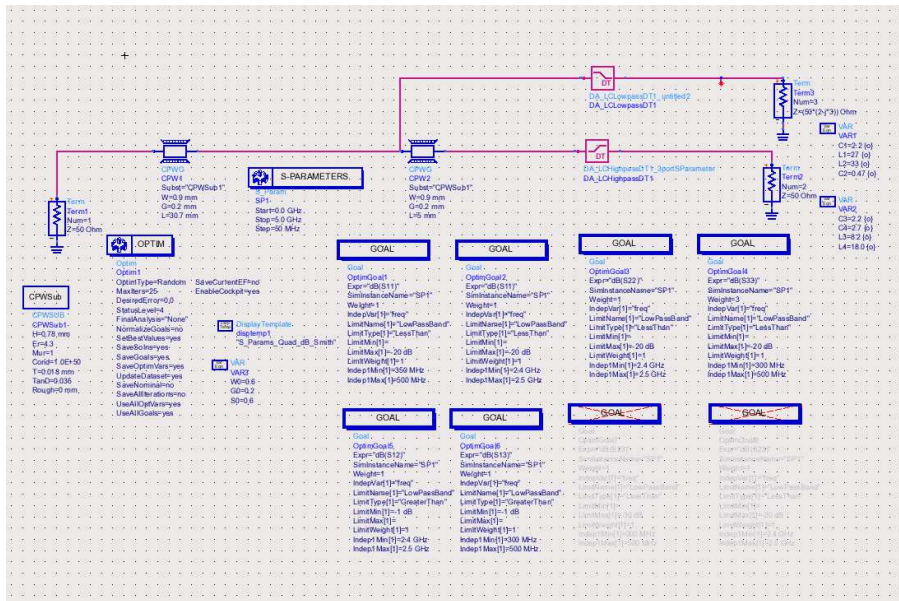


**Fig. 5.5. Schematic view of low pass filter (top) and high pass filter (bottom) for the matching network.**

The pads to accommodate both filters were adequately modeled. With parasitic elements fitting the according SMD components the final matching network was built (see example in Fig. 5.6).

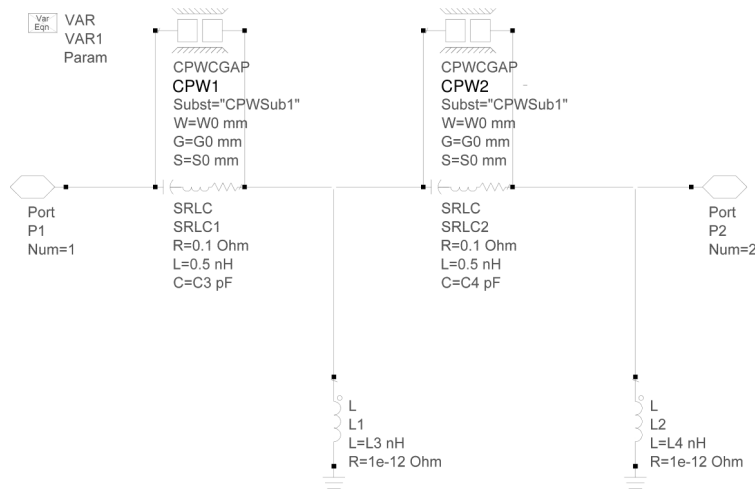


**Fig. 5.6. Schematic of high pass filter in ADS.**

The following goals were set for the optimization:

- $S_{11} < -20$  dB from 350 MHz to 500 MHz
- $S_{11} < -20$  dB from 2.4 GHz to 2.5 GHz
- $S_{33} < -20$  dB from 300 MHz to 500 MHz
- $S_{22} < -20$  dB from 2.4 GHz to 2.5 GHz
- $S_{13} < -1$  dB from 300 MHz to 500 MHz
- $S_{12} < -1$  dB from 2.4 GHz to 2.5 GHz

At the same time  $S_{32}$  at 400 MHz and 2.4 GHz are kept under -20 dB.

The final components of the filters, provided by an optimization process and rounded by the discrete available values, are presented in Tab. 5.1.

Low pass filter		High pass filter	
Component	Value (nH/pF)	Component	Value (nH/pF)
L1	27	L3	8.2
L2	33	L4	18
C1	2.2	C3	2.2
C2	0.47	C4	2.7

**Tab. 5.1. Component values of the low pass filter (left) and high pass filter (right).**

The most representative simulation results are shown in Fig. 5.7.

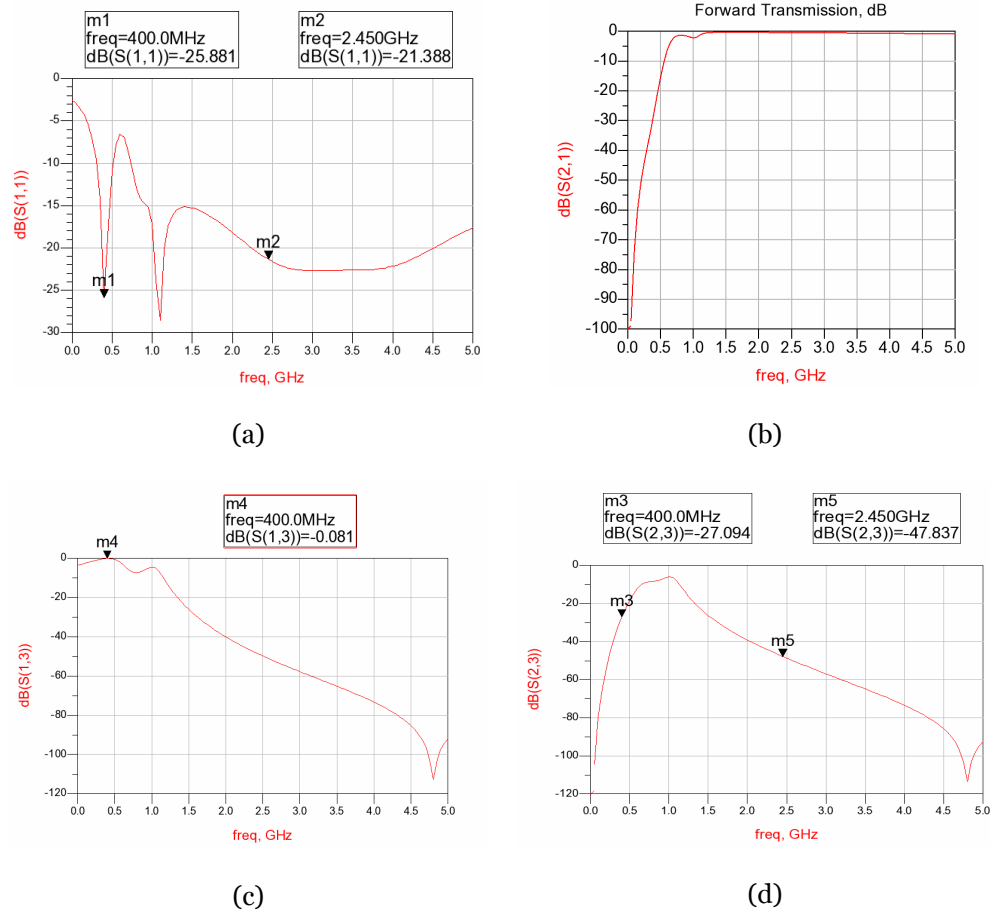


**Fig. 5.7. S<sub>11</sub>, S<sub>21</sub>, S<sub>13</sub>, and S<sub>23</sub> for the simulated results.**

The implementation of the filters were previously performed in a mock board, shown in Fig. 5.8. It served to evaluate the matching network for the two RF ports of the transceiver, implemented later on the PCB of the prototype for the functional tests. The results are shown in the next chapter.

A SMD resistance of  $47\ \Omega$  was chosen to model the chip input impedance at 2.4 GHz and a series  $100\ \Omega$  resistance with a  $2.7\ \text{pF}$  capacitance ( $-150j\ \Omega$  at 400 MHz equals to  $2.65\ \text{pF}$ ) to model the chip input impedance at 400 MHz.

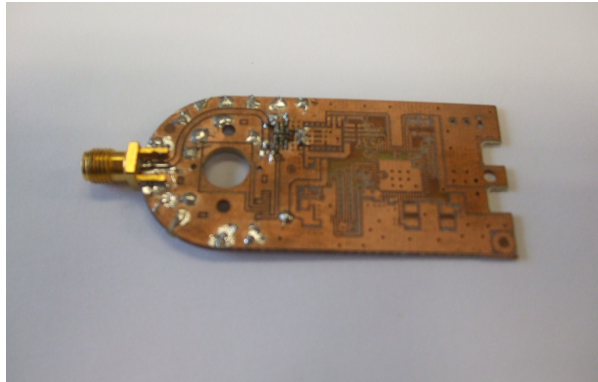


**Fig. 5.8. Mock board to test the matching antenna network.**

## 5.3 BODY PHANTOMS

Implanted antennas have to face the task of operating in the delicate environment of body tissues (see section 2.1). To imitate the dielectric properties of body surroundings, a body simulating fluid is employed in a body phantom. The most common types of mimicking liquids simulate skin, fat or muscle tissue, depending on the future location of the AMI. Apart from commercial products, the mimicking gel can also be mixed after a recipe. In this case, the body simulating liquid was mixed and its composition was measured. The phantom size, on the other hand, was simulated.

### 5.3.1 PHANTOM SIZE AND COMPOSITION FOR PLANAR CVCA

Most of the subcutaneous implanted antennas are designed in a skin simulating fluid, as they are to operate through skin [116], [123]. Sometimes, a liquid representing the average properties of the body is employed [105]. As part of the investigation of a suitable body phantom, the antenna matching was studied inside skin and muscle separately. At the frequency limits of the worldwide UHF RFID band both tissues exhibited similar electromagnetic properties (see Tab. 5.2).

Tissue	$f_u$ [MHz]	$\epsilon_r$	$\sigma$
Skin dry	865	41.6	0.855
Muscle	865	55.11	0.931
Skin dry	956	41.13	0.885
Muscle	956	54.9	0.962

**Tab. 5.2. Dielectric properties of body tissue [53].**

For the skin tissue simulating liquid, a composition of 41.49 % of deionized water, 56.18 % of sugar and 2.33 % of salt [116] was used. For muscle, the body tissue simulating liquid MSL900 by SPEAG [139] was employed in compliance with the FCC standard for SAR and radiation measurements in the body (see section 2.4.2). Fig. 5.9 and Fig. 5.10 show the real and the imaginary part of their dielectric constant measured by an open-ended coaxial dielectric probe and a computer-controlled network analyzer, compared to real tissue properties [53] in both cases.

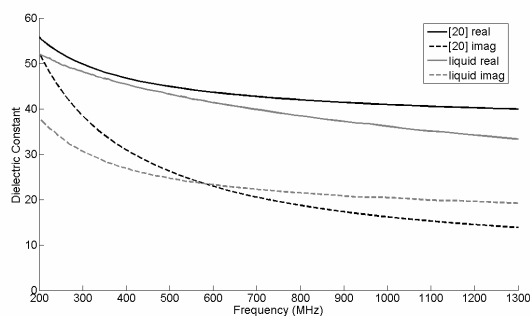


**Fig. 5.9. Dielectric properties of skin and of tissue-simulating liquid compared<sup>10</sup>.**

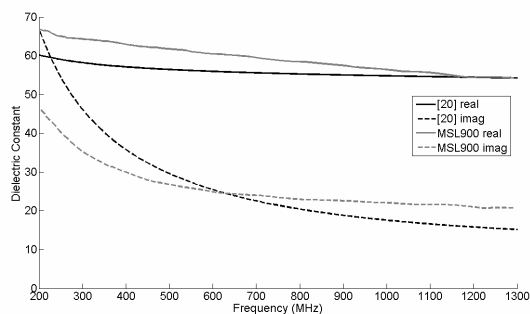


**Fig. 5.10. Dielectric properties of muscle and of tissue-simulating liquid compared.**

<sup>10</sup> In this diagram [20] refers to [39].

Both liquids represent a good approximation for subsequent experimentation in the entire 865 MHz - 956 MHz range. However, skin simulating liquid was employed to study the radio link due to the SCVC's subcutaneous position.

Since entire human phantoms are often not practical in terms of radiation measurements and simulation time, a study was to determine the minimum phantom size, which would dramatically influence the radiation properties according to the working frequency and direction of interest. In the simulation setup, the antenna was placed into a human torso at 9 mm from the interface and with an offset of 60 mm respect to the center (see Fig. 5.11) as a typical subcutaneous position for the portacath.

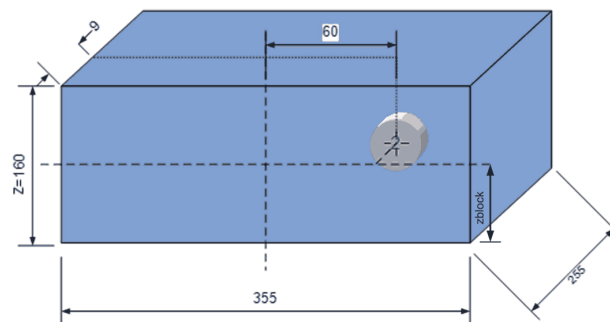


**Fig. 5.11. Human torso-size phantom and location of the implant at height  $z_{\text{block}}$  mm].**

The horizontal plane was chosen for the 866.5 MHz radio link to a base station outside the body. For that reason, the torso cross-section dimensions in this plane should be as realistic as possible in order to replicate reflections caused by the change of media. This was modeled by a polystyrene tank with a 35 cm x 25 cm base, filled with the tissue simulating liquid. Simulations were performed with CST MWS to investigate the minimum height  $z$  of the phantom (corresponding to two  $z_{\text{block}}$  in Fig. 5.11), in order to reveal its impact on the horizontal plane gain patterns. Fig. 5.12 shows the convergence of the gain patterns for different phantom heights  $z$ . A value of  $z=160\text{mm}$  was estimated to be enough to account for body effects as the simulated gain diagram converges.

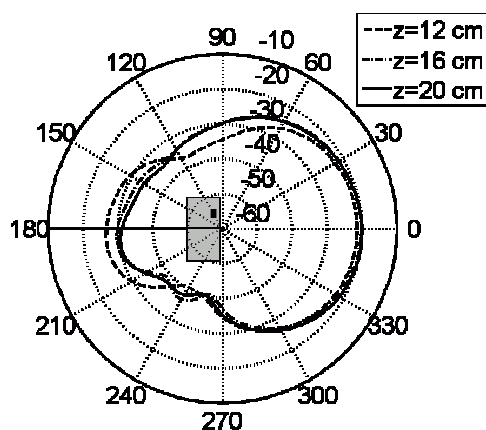


Fig. 5.12. Simulated antenna gain patterns in the  $xy$ -plane at 866.5 MHz for three phantom heights  $z$ .

### 5.3.2 PHANTOM SIZE AND COMPOSITION FOR 3-D CVCA

The amount of body tissue surrounding the implanted 3-D CVCA undermines the antenna's efficiency by absorbing the RF wave in the lossy medium and due to reflections of the wave at the body-air interface.

A study was to define the minimum phantom height, that would influence the radiation properties of the 3-D CVCA in the lower 403 MHz frequency, since the higher frequency of 2.4 GHz was less affected by the reflections coming from the phantom boundaries. A phantom representing the chest as a body part was studied, taking into account the operation frequency and direction of interest. The latter was specified to be on the horizontal plane for the communication link. The antenna was mounted in the body phantom at the same position as described in section 5.3.1.

Simulations were performed to investigate the minimum phantom height  $z$  in order to represent its impact on the gain pattern for the vertical polarization ( $\theta=90^\circ$ ) in the horizontal plane ( $\theta=90^\circ$ ). Fig. 5.13 shows the change of the gain in relation to the phantom height with  $z_{\text{block}}$  that equals  $z/2$  (see Fig. 5.11).

A value of  $z=160$  mm was estimated to be sufficient to account for body effects, as the simulated gain patterns reasonably converged at 403 MHz below 109 million mesh cells. (see Fig. 5.11). For higher frequencies, the phantom would be electrically larger and therefore representative as well.



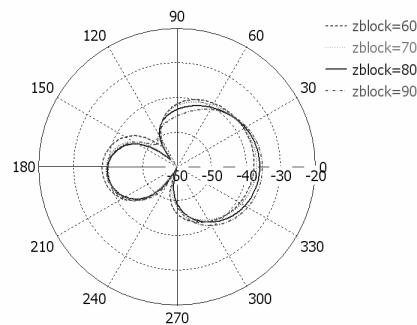


**Fig. 5.13. Simulated antenna gain [dBi] in relation to phantom height  $z/2=Z_{\text{block}}$  [mm] for 403 MHz (vertical polarization, horizontal plane).**

The cross section of the torso was modeled by a polystyrene tank of 355 mm x 255 mm filled with skin tissue mimicking liquid composed of 56.18% sugar, 41.49 % deionized water and 2.33 % NaCl salt [116]. The liquid's properties were measured by the dielectric probe. Its permittivity and loss tangent are shown in Fig. 5.14 with reference to [53]. These properties were the ones involved in the design process described in section 4.2.

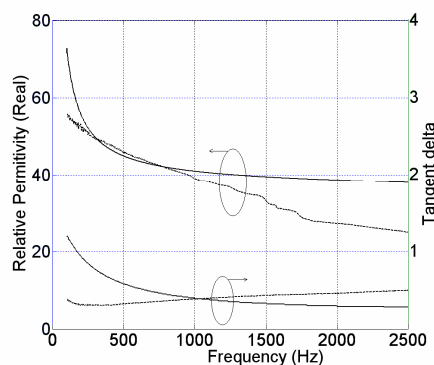


**Fig. 5.14. Comparison of dielectric properties of dry skin and of tissue-simulating liquid.**

In order not to disregard the possibility of drawing imprecise conclusions for the higher frequency, a phantom of the same size was generated for the ISM 2.4 GHz band with 53 % sugar and 47 % deionized water according to [116]. The phantom properties were verified against theoretical values taken from [53] and shown in Fig. 5.15.

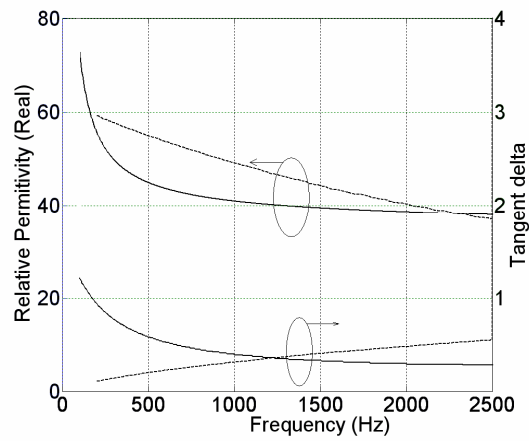


**Fig. 5.15. Comparison of dielectric properties of dry skin and tissue-simulating liquid at 2.45 GHz (solid theory, dash experimental).**

## *Chapter 6*

# ***Measurements and Results***

---

This chapter presents the methodology developed in the present study in order to measure implanted antennas. It is based on the work on the design process described in Chapter 4. The cable influences on the measurement and simulation results observed during the design and evaluation process were analyzed. Observed uncertainties were quantified with simulations. Subsequently, the results were integrated in the model for the link budget calculation in order to obtain a realistic working range. Finally, an indoor propagation model for indoor environments was applied to facilitate an accurate system design.

## 6.1 ANTENNA CHARACTERIZATION

The evaluation of the antenna parameters begins with the impedance matching measurements. The methodology of the radiation pattern measurements in the antenna test chamber is explained and the results are analyzed and compared with simulations.

### 6.1.1 IMPEDANCE MATCHING IN THE PHANTOM

The first step in the methodology was to determine the input impedance of the antenna while the antenna was immersed into to the skin mimicking gel. The impedance matching was determined in a similar way for both antenna types. In addition, the influences of phantom size, type of phantom liquid, etc., were investigated.

#### 6.1.1.1 Impedance Matching of the Planar CVCA

At first, the antenna matching was analyzed in simulations, the prototype was tested in different phantoms and the results were compared in a diagram. Fig. 6.1 shows the return loss (reference impedance  $50 \Omega$ ) of the antenna with test bed measured in two phantoms of different size: a cup and a tank of 14.5 liters, both made of polystyrene and filled with skin mimicking gel. The antenna in the tank was placed close to the interface (9 mm). It could be observed that the measurement in a phantom with reduced volume was a very acceptable approximation in terms of matching.

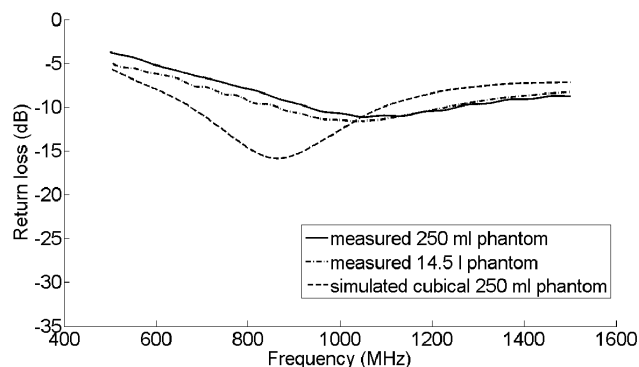


**Fig. 6.1. Return loss for the implanted antenna in different phantoms and compared to simulation result [126].**

In the simulation, neither the test bed nor the magnetic beads were included. Apart from that, the critical antenna feed point could not be

perfectly modeled. Nevertheless, even with these approximations the simulation provided the final prototype dimensions. The antenna covered the required spectrum with  $|S_{11}| < -10$  dB from 866.5 MHz to 1.2 GHz (32.3 %) and can operate in RFID bands worldwide.

Secondly, another phantom of the dimensions 220 mm x 220 mm x 110 mm with the antenna inserted deep inside was filled with muscle tissue-simulating liquid [139]. The antenna matching was evaluated at different distances to the phantom-air interface in order to stress the robustness of the matching towards various insertion locations of the implant. Tests were run against the standard reference impedance of  $50 \Omega$ . Fig. 6.2 (a) illustrates the setup and the positions where the measurements were conducted. Fig. 6.2 (b) shows that the reflection coefficient was stable in different locations.

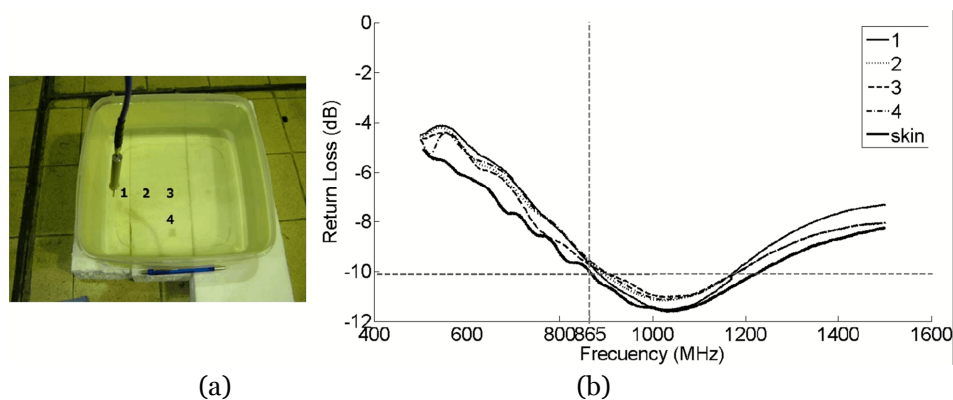


**Fig. 6.2. (a) Measurement locations for matching robustness study on the implanted antenna in test bed. (b) Return loss of the implanted antenna for the corresponding positions in the muscle case phantom compared to the skin case.**

In conclusion, the result is quite similar to the one obtained in the preceding case of skin mimicking gel [116] in the 14.5 liter tank, i.e., the implanted antenna is quite tolerant to tissue and insertion variation.

#### **6.1.1.2 Impedance Matching of the 3-D CVCA**

Beforehand, factors related to the variation of the impedance matching were investigated for the planar CVC antenna. During the design process of the 3-D CVC antenna, simulations confirmed its robustness against these influences (see section 4.2.3).

The representative phantom and the antenna position inside was set according to section 5.3.2 Fig. 5.13. The 3-D CVCA was first simulated and

then the results were compared with the prototype return loss measurements. The  $|S_{11}|$  fitted very accurately between the simulations corresponding to protection film layers of 0.2 mm and 0.4 mm (see Fig. 6.3). It was below -10 dB from 345 MHz to 555 MHz and from 965 MHz onwards. The preparation of the antenna prototype for the measurements in the phantom proved to be difficult since the thickness of the protecting layer had to be uniform over the 3-D surface and seal the implant against the liquid.

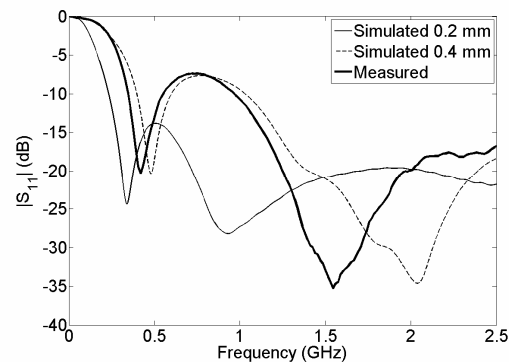


**Fig. 6.3. Comparison of the reflection coefficient  $|S_{11}|$  of the 3-D CVCA simulated with different isolation thicknesses and measured.**

A second, similar phantom, also filled with skin mimicking gel, was prepared to demonstrate the antenna broadband matching in the ISM 2.4 GHz band (see section 5.3). Fig. 6.4 displays the variation of the measured reflection coefficient due to the different dielectric properties of the skin mimicking liquid and proves that the  $|S_{11}| < -10$  dB broadband performance was kept at the band of interest.

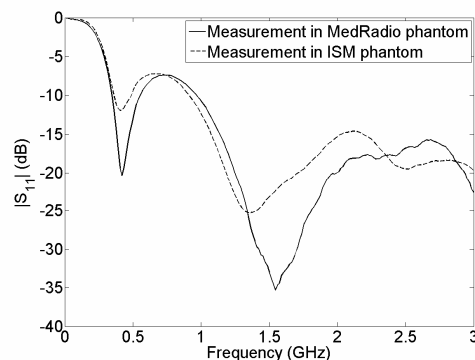


**Fig. 6.4. Measured reflection coefficient  $|S_{11}|$  in two experimental phantoms.**

## 6.1.2 GAIN MEASUREMENTS IN SKIN TISSUE PHANTOMS

As the implanted antenna was destined to work inside the body, simulations and measurements were carried out in a comparable environment. To conduct the measurements, a test bed and a measurement environment had to be set up. This section points out the consequences that need to be accepted regarding the setup.

### 6.1.2.1 Antenna Measurement Methodology

Before measuring the antenna in the anechoic chamber, the far field assumption was to be verified by equations (6.1) - (6.3) [140]. The diameter of the effective radiating part of the phantom was settled to be 2/3 of the cross section, i.e., 240 mm.

$$r_{far\_field} > \frac{2D^2}{\lambda} \quad (6.1)$$

$$r_{far\_field} > 1.6\lambda \quad (6.2)$$

$$r_{far\_field} > 5D \quad (6.3)$$

The far field zone ( $r_{far\_field}$ ), calculated by means of equations (6.1) - (6.3), respectively corresponded to 0.16 m, 1.18 m and 1.20 m for the lowest frequency ( $f=403.5$  MHz;  $\lambda =0.74$  m).

In the measurement environment of the test chamber (see Fig. 6.5) the actual measuring distance between antenna under test (AUT) and measurement antenna in an anechoic chamber was about 2.70 m and therefore assured that all measurements were carried out in the far field zone. With the measured received power, the antenna gain of the AUT could be calculated and a radiation pattern was drawn.

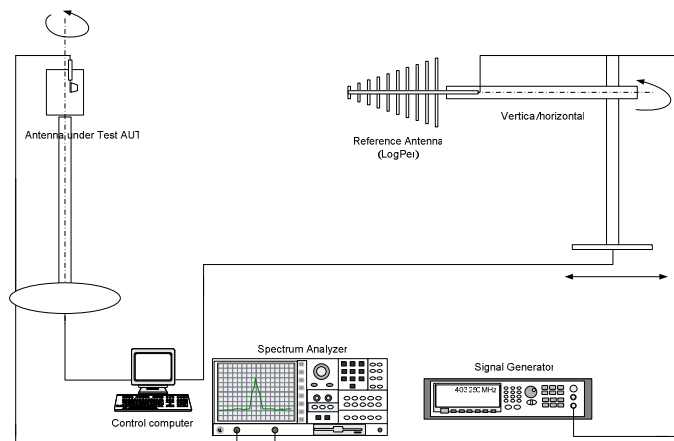


**Fig. 6.5.** Antenna gain measurement environment showing all function blocks.

### 6.1.2.2 Gain Measurement of the Planar CVCA

As the overall gain was very low, about less than  $-20$  dBi, it was advisable to further investigate the influence of the feeding cable's radiation before taking gain measurements. Three setups for simulation were considered and shown in Fig. 6.6 (a) implanted antenna, (b) antenna with test bed and (c) antenna with test bed and feeding cable placed in a similar position to the anechoic chamber's one. Fig. 6.7 shows the gain comparison for the three cases in both polarizations (vertical and horizontal).



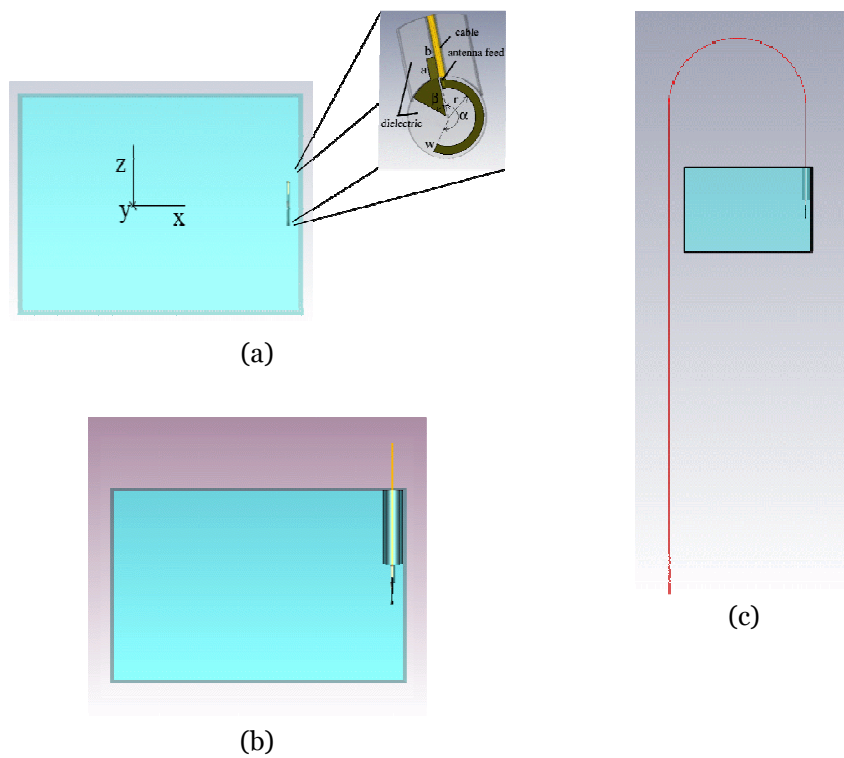


**Fig. 6.6. Antenna gain simulation models depending on the measurement setup (side view). Phantom size is identical in the three cases (350 x 250 x 165 mm<sup>3</sup>).**  
**(a) Implanted antenna ( $r=8\text{mm}$ ,  $w=2\text{mm}$ ,  $\alpha=215^\circ$ ,  $\beta=50^\circ$ ,  $a=5\text{mm}$ ,  $b=2\text{mm}$ )**  
**(b) Implanted antenna with test bed and (c) Implanted antenna with anechoic chamber feeding cable.**

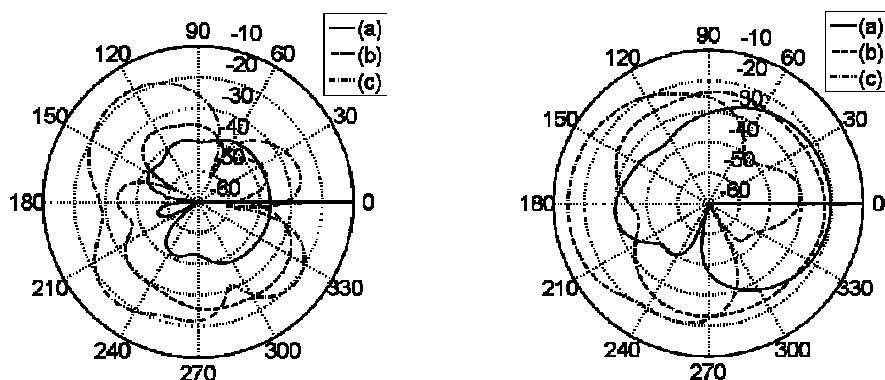


**Fig. 6.7.** Antenna gain simulation comparison at 866.5 MHz for measurement setup (a), (b) or (c) in Fig. 6.6 in horizontal (left) and vertical polarization (right).

The radiation patterns demonstrate that the chamber cable had a deep impact on both polarizations. The test bed's influence was below a reasonable threshold on vertical polarization for the main lobe direction.

Further simulations revealed, that surface current freely circulated on the outside jacket shield of the cable and its radiation was added to the antenna gain pattern. The influence was falsifying the results because of the low gain of the antenna structure.

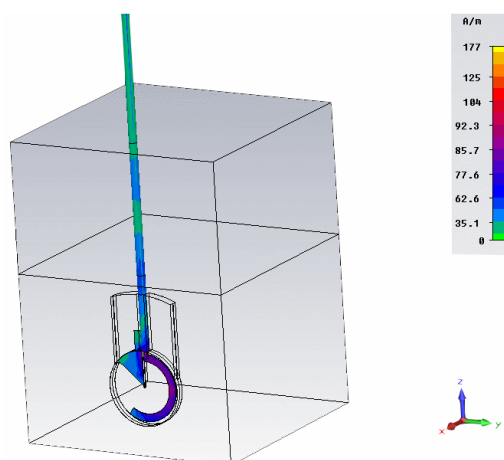


**Fig. 6.8.** Visualization of current for planar CVCA model with cable in phantom.

This simulation results were verified in the anechoic chamber. The measurements were performed in the antenna measurement laboratory at

Queen Mary University of London. A polystyrene tank was filled with 14.5 l ( $z=165\text{mm}$ ) of tissue-simulating liquid [116]. The antenna was placed 90 mm deep via the test bed and 9 mm from the interface. The implant within the phantom was placed in an anechoic chamber for gain measurements. The gain patterns of the horizontal plane over the  $180^\circ$  sweep for front radiation coming from the chest are shown in Fig. 6.7. Although the measurement and simulation results were not obtained under equal conditions (simulation with static cable versus measurement with rotating and arbitrarily positioned cable), some similarities were observed. This led to the conclusion that the impact of the radiation coming from the cable currents disguised the radiation from the implanted antenna.

According to Fig. 6.7, from the measurement-in-chamber point of view, the average gain  $G_{\text{implant\_dB}}$  in horizontal polarization was  $G_{\text{aver\_h}} = -23.8\text{dBi}$ , whereas in the vertical polarization was  $G_{\text{aver\_v}} = -28.2\text{dBi}$ . These results differed from the expected simulated gain in Fig. 6.7 for the implanted antenna alone:  $G_{\text{h}} = -36.6\text{dBi}$  and  $G_{\text{v}} = -20.5\text{dBi}$ . It was interesting to notice that the feeding cable current radiation impacted in opposite ways depending on the polarization: increasing the horizontal radiation and decreasing the vertical radiation in the direction of interest. A number of nulls were also introduced.

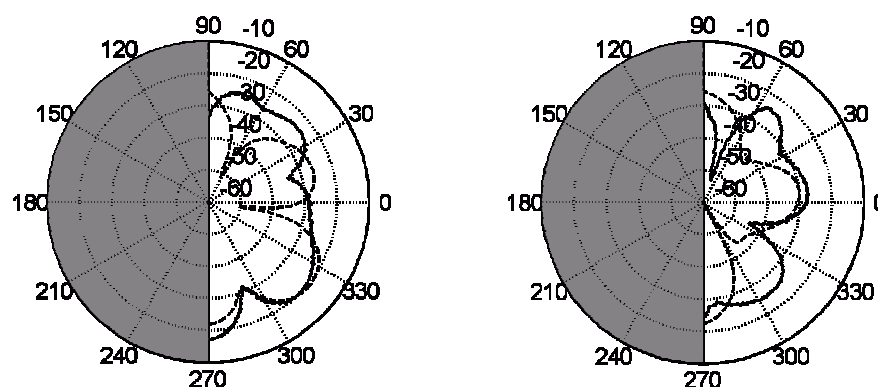


Fig. 6.9: Antenna gain comparison simulated (case (c) of Fig. 6.6, dotted) and measured (solid) at 866.5 MHz in horizontal (left) and vertical polarization (right).

### 6.1.2.3 Gain Measurement of the 3-D CVCA

The antenna radiation was evaluated in the antenna measurement facility of Ikerlan, Mondragón. The antenna was placed in the specific position within the phantom as described in section 5.3.2. Its center was

located inside the phantom at a depth of 8 cm ( $1/2$  phantom's height). The body torso section was modeled by a polystyrene tank with a footprint of 350 mm x 250 mm. With an absolute height of  $z=16$ cm the resulted fill quantity was about 14.5 l of tissue-simulating liquid.

The unit of the implant inside the phantom was placed on a plastic stand of 134 cm height for gain measurements in the horizontal plane at both polarizations (see Fig. 6.10).

The positioning of the feeding cable demands great care due to the general low gain of implanted antennas. Reflections from cables and mounts may affect the outcome. The antenna was mounted with the closest feeding cable in an upright position. As mentioned previously, three ferrite beads were clamped to the cable near the antenna (see section 5.1.2). Fig. 6.10 demonstrates that the next feeding cable was placed horizontally to prevent interferences in the vertical predominant polarization (cable 1). To suppress further radiation coming from the outer conductor, the cables running on the top (1) and the back of the phantom (2) were covered with a synthetic semi-flexible ferrite tube (Wave-X<sup>®</sup> heat shrink tube absorber WH-A750). On top of that, the feeding cables behind the phantom mount (cable 2) were enclosed with foam absorbers (not present in Fig. 6.10).

The antenna's radiation pattern of the horizontal plane over the  $360^\circ$  sweep for radiation coming from the chest are shown in Fig. 6.11 and Fig. 6.12. At 403 MHz, a VULB 9163 Log Periodic antenna by Schwarzbeck was used as a measurement antenna, and a 3146 Log Periodic antenna by EMCO was used as gain reference. At 2.45 GHz a 3160-03 horn antenna by ETS-Lindgren was used as a measurement antenna and a SAS-581 horn antenna by AH-Systems as gain reference. The measurements included both polarizations ( $\theta$  (vertical) and  $\Phi$  (horizontal) component).

Some of the attenuation dips that were observed in the measurement results, but not present in the simulation (e.g., at  $90^\circ$  in Fig. 6.11, vertical polarization), were interpreted as the scattered signal coming from cable 2 when it was no longer hidden behind the phantom, facing the measurement antenna. This effect could not be observed in simulations.

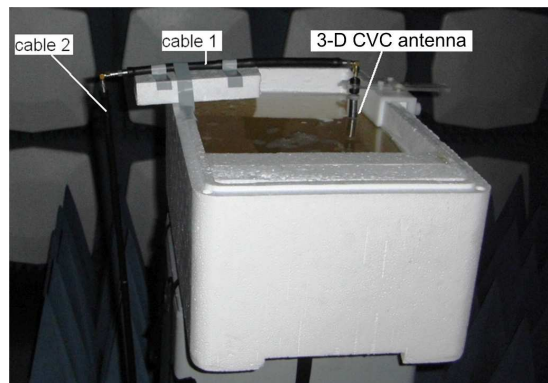


**Fig. 6.10.** Far field measurement in the anechoic chamber showing phantom with inserted 3-D CVCA (absorbers removed)

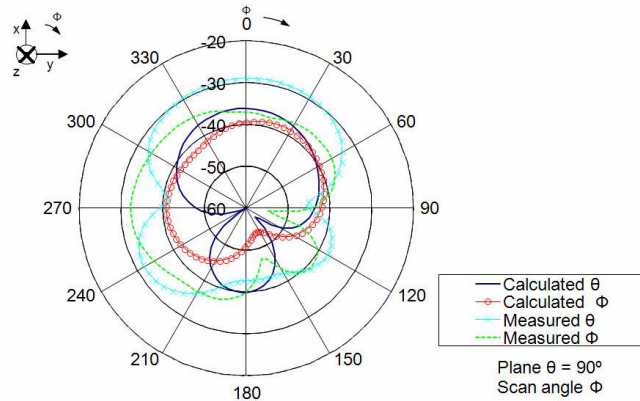


**Fig. 6.11.** Calculated vs. measured results of vertical and horizontal gain component [dBi] in the horizontal plane at 403 MHz.

The measured gain  $G_{\text{implant\_dB}}$  in vertical polarization at  $\phi=0^\circ$  and  $\theta=90^\circ$  at 403 MHz  $G_{\text{implant\_dB\_v}} = -28.95\text{dBi}$  whereas in the horizontal polarization  $G_{\text{implant\_dB\_h}} = -36.9\text{dBi}$ . Simulations revealed that theta component in  $\phi=0^\circ$   $G_{\text{implant\_dB\_v}} = -36.1\text{dBi}$  and the phi-component is  $G_{\text{implant\_dB\_h}} = -39.4\text{dBi}$ . The computed radiation efficiency was 0.017% and the maximum gain was  $-34.36\text{dBi}$ .

For the 2.45 GHz frequency, the measured gain  $G_{\text{implant\_dB}}$  in vertical polarization at  $\phi=0^\circ$  and  $\theta=90^\circ$   $G_{\text{implant\_dB\_v}} = -25.5\text{dBi}$  whereas in the horizontal polarization  $G_{\text{implant\_dB\_h}} = -19.9\text{dBi}$ . Simulations revealed that the vertical component in  $\phi=0^\circ$ ,  $G_{\text{implant\_dB\_v}} = -33.5\text{dBi}$  and the phi-component was  $G_{\text{implant\_dB\_h}} = -28.1\text{dBi}$ . The computed radiation

efficiency was 0.059% and the maximum gain was -26.14 dBi. The simulation and measurements revealed the predominant polarization changes from vertical to horizontal from 403 MHz to 2.45 GHz. Higher directivity due to the increase in electrical antenna size at this higher frequency was also observed.

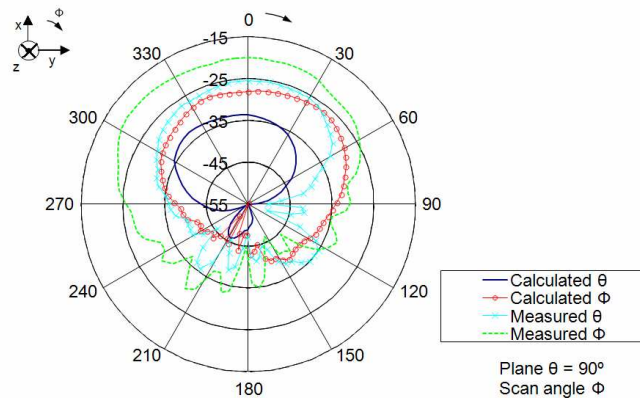


**Fig. 6.12. Calculated vs. measured results of vertical and horizontal gain component [dBi] in the horizontal plane at 2.45 GHz.**

It should be noted that the accuracy of the measurements in the anechoic chamber was limited by the performance of the absorbers and the gain of the measurement antennas. In this case, the chamber was covered with FS-400 hybrid absorbers by ETS-Lindgren (reflectivity -20 dB and -18 dB at 403 MHz and 2.45 GHz, respectively), and the gain of the measurement antennas was 6.6 dBi (Schwarzbeck VULB 9163) and 17 dBi (ETS-Lindgren 3160-03) at 403 MHz and 2.45 GHz, respectively. With these specifications, the accuracy of the measurements in the anechoic chamber was  $\pm 1.75$  dB at 403 MHz and  $\pm 0.5$  dB at 2.45 GHz. Therefore, it could not cause the differences between simulated and measured results, which were 8 dB in the theta-component and 8.2 dB in the phi component at 2.45 GHz. The main reason is the poor suppression property of the current running along the external conductors of the feeding cables presented by any choke ferrites in the GHz band. This issue is particularly sensitive for low gain implanted antennas. However, simulation gave an insight into this phenomenon, along with an impact estimate. In this case, the cable significantly increased the radiated energy. This is inevitable and should be taken into account by a read range uncertainty factor of 0.4 corresponding to the difference between simulations and measurements for 2.45 GHz.

$$10^{\frac{G_{sim}-G_{meas}}{20}} = F_{uncert} \quad (6.4)$$

Where

$G_{sim}$  [dB] is the simulated antenna gain,  
 $G_{meas}$  [dB] the measured antenna gain and  
 $F_{uncert}$  the uncertainty factor.

The equation (6.4) (after Friis) translates a variation of simulated to measured gain to a change in working range for link budget calculations.

#### 6.1.2.4 SAR Results

For the evaluation of performances and safety issues, the 1-g averaged SAR distributions were simulated and compared with ANSI/IEEE limitations [85]. The analysis was performed only at the frequency in which the implanted sensor node can transmit (i.e., MICS band [132], [133]). At 403 MHz, for 0.5 W (rms) input power, the maximum SAR at skin tissue was 59.1 W/kg, for a density of 1100 kg/m<sup>3</sup>. The transmitted power to the 3-D CVC antenna had to be decreased to 13.54 mW (11.32 dBm) in order to fulfill the SAR limit of 1.6 W/kg. For a computed maximum absolute gain at 403 MHz of -34.36 dBi, this led to an ERP of -25.19 dBm that also satisfied the -16 dBm ERP allowed by MICS standard [141].

## 6.2 LINK BUDGET ESTIMATE

The objective of the link budget calculation is to evaluate possible application scenarios and, in particular, the maximum operating distance of the system in certain positions.

At near field distances, two application areas were envisioned for passive RFID, which operates battery-less and is destined for short range. The scenario involved a reader either worn in a shirt pocket close to the body or located at a distance of up to 1 m. A third application was scheduled for longer distances employing a battery powered active implant using the MICS-ISM frequency bands. To find out the maximum range in the far field, perpendicular measurements corresponding to a furnished room were carried out.

The falsification of the gain measurement led to further studies on the transmission range of both antennas. As part of the developed methodology and based on simulations, an assumed uncertainty was introduced to the measurement results to quantify a safe transmission range.

### 6.2.1 NEAR FIELD MEASUREMENT FOR THE PLANAR CVCA

Near field measurements began with a study of transmission reliability at different reader locations on the chest. This emulated a wireless reader device located in patient's shirt pocket. The planar CVCA was submerged in the skin mimicking liquid inside the phantom in a subcutaneous position (see Fig. 6.13).

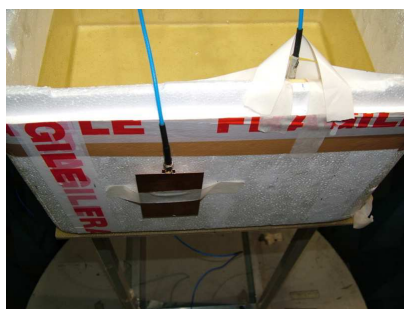
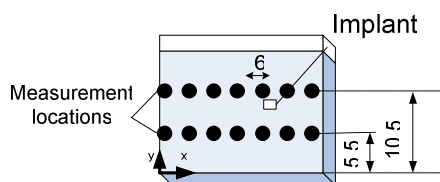


**Fig. 6.13. Measurement setup for on-chest measurement.**

As RFID reader antenna a conventional PIFA tuned to 868 MHz, employed to probe the field within a short distance from the implanted antenna, was used. The antenna was designed with a low profile (3 mm) [142]. The radiating plate had the dimensions of a portable handset (79 mm x 49 mm) over a slightly larger ground plane (106 mm x 61 mm). Antenna gain along the broadside direction was found to be 0 dBi (see Fig. 6.14 (a)).



(a)



(b)

**Fig. 6.14. (a) PIFA probe antenna and (b) the positions for on-chest measurements on phantom (dimensions in cm).**

Transmission link loss ( $S_{12}$ ) measurements were taken at the position shown in Fig. 6.14 (b), where the PIFA antenna was attached to the phantom. The PIFA antenna was moved along the  $x$  axis for two different



heights  $y$ . Vertical and horizontal PIFA orientations were considered in each case. As the PIFA antenna was placed facing the phantom, a mismatch occurred (see Fig. 6.15). Its impact is as well embedded into the calculated transmission link loss, as antenna gain in direction of the other antenna and the reflections at the phantom air interface.

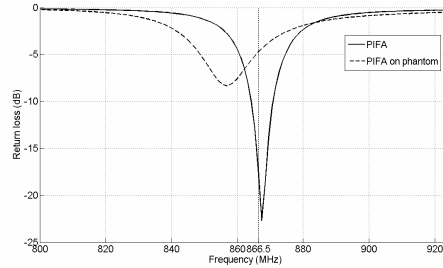


**Fig. 6.15. Return loss of the reader antenna placed on the chest phantom and in free air.**

Once the transmission link loss was obtained, the power that was received by the implant and by the reader was calculated according to the link budgets defined in equations (6.5) and (6.6) respectively. They are related to the RFID uplink and downlink budgets. The power received by the reader  $P_{reader\_dB}$  is the one backscattered by the implant within the torso. Both reader and tag antennas were matched to  $50\Omega$ . EIRP<sub>dB</sub> is 35,15 dBm due to regulation constraints.

$$P_{reader\_dB} = EIRP_{dB} - 2P_{Loss\_dB} \quad (6.5)$$

$$P_{implant\_dB} = EIRP_{dB} - P_{Loss\_dB} \quad (6.6)$$

Fig. 6.16 and Fig. 6.17 show the power received by the implant and the handset with horizontal distance  $x$  along the chest for the two different heights  $y$ , namely top and bottom. They correspond to equations (6.5) and (6.6) respectively. If no further losses are considered, the link is assured when the reader is around the chest and the received power of the implant  $P_{implant} > -20$  dBm and the received power of reader  $P_{reader} > -70$  dBm (respective minimum sensitivity levels).

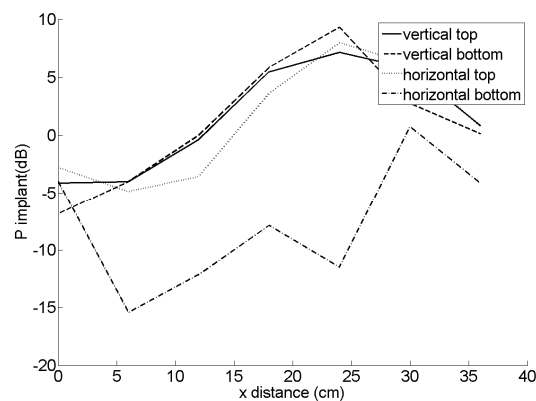


**Fig. 6.16.** Power received by the from a reader placed on the chest at positions given by Fig. 6.13 and Fig. 6.14 (b).

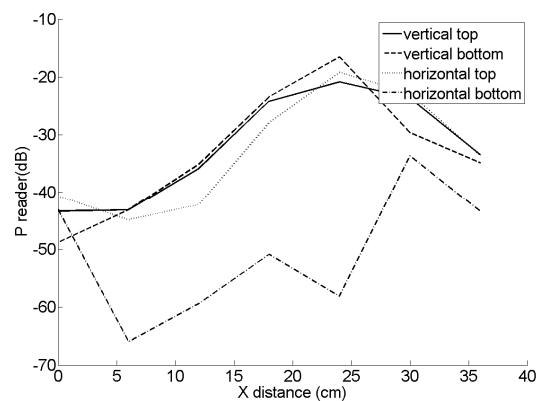


**Fig. 6.17.** Power received by the reader placed on the chest at positions given by Fig. 6.13 and Fig. 6.14 (b) from the backscattered signal by the implanted RFID tag.

### 6.2.1.1 Validation

Presumed that the implant exhibits a very low gain due to the lossy material surrounding it, it is important to check the impact of the radiation coming from the cables that could disguise the results. This was studied more closely in detailed simulations. The comparison between simulations of the whole setup (including cables) and the measurements give an estimate of uncertainty for the latter.

By using CST MWS, a detailed and realistic reproduction of the measurement environment in the anechoic chamber was generated. Models

of both antennas including their antenna feed were integrated. These feeds were represented by long ( $\approx 1.5$  m) and bent coaxial cables going down to the chamber floor.

Frequency solver simulations were performed according to the measurement setup on each position (see Fig. 6.18). Transmission link loss was represented by the logarithmic transmission coefficient  $|S_{21}|_{dB}$  at 868 MHz.

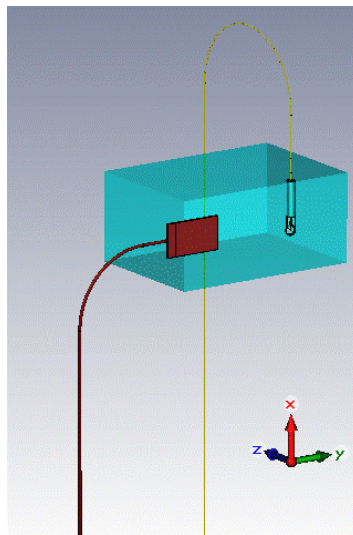


**Fig. 6.18. Simulation arrangement with long cables (main section).**

Furthermore, the simulation was repeated at every position of the reader antenna without the cables in place for comparison purposes.

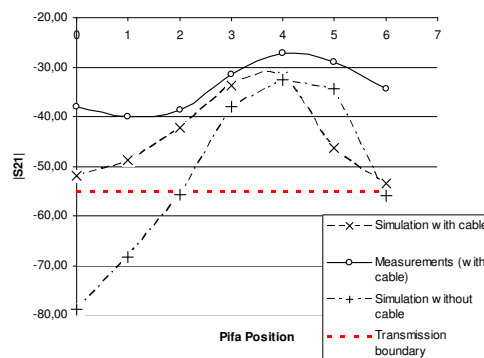


**Fig. 6.19. Comparison of the transmission coefficient for the same set of positions and horizontally oriented PIFA, top line.**

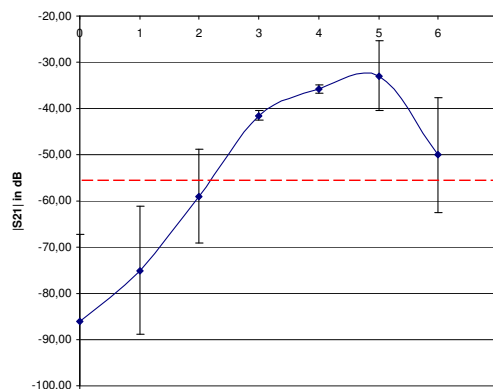
The power loss threshold  $P_{\text{Loss\_dB}}$  for reliable communication was  $P_{\text{Loss\_dB}} \leq -55.15$  dB and it was calculated from equation (6.6) (EIRP=35.15dBm and received power  $P_{\text{implant}} = -20$ dBm).

Fig. 6.19 shows the results for the top line (see Fig. 6.14 (b)) with the reader antenna in horizontal position. In the diagram, horizontal axis represents the seven registered positions along the torso. The results showed a good agreement near the implanted antenna (around position 4) when cables were considered both for simulation and measurements (inevitably in the latter). Further away from the implant, the simulated transmission coefficient dropped significantly, especially in the case of the simulation without the cables included. In the rest of cases (horizontal PIFA bottom line, vertical PIFA top and bottom lines), the results were similar and omitted for brevity.

### 6.2.1.2 Uncertainty Calculation

The simulations without cables showed a higher degradation of  $|S_{21}|$  with distance between antennas. This demonstrates the significant influence of the cables on the validity of the results.

Obviously, performing measurements without cables is as desirable as impossible. A way to get around this constraint is to add an uncertainty factor to the simulations without cable. This is shown in Fig. 6.20, Fig. 6.21, Fig. 6.22 and Fig. 6.23. An estimate of this uncertainty can be extracted by the difference between the simulations with cable and the measurements. The range of uncertainty is an estimate of the impact of the cables on the results of the measurement.



**Fig. 6.20. Simulated transmission coefficient for bottom line, measurement uncertainty included, reader antenna horizontally oriented.**

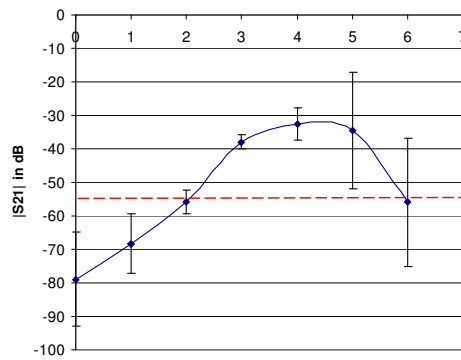


**Fig. 6.21. Simulated transmission coefficient for top line, measurement uncertainty included, reader antenna horizontally oriented.**

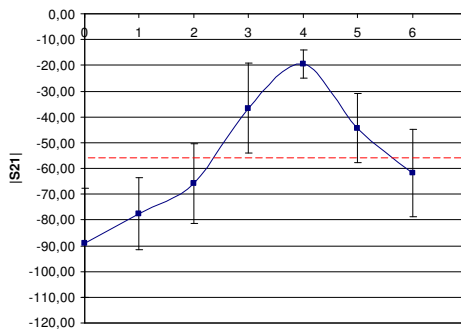


**Fig. 6.22. Simulated transmission coefficient for top line, measurement uncertainty included, reader antenna vertically oriented.**

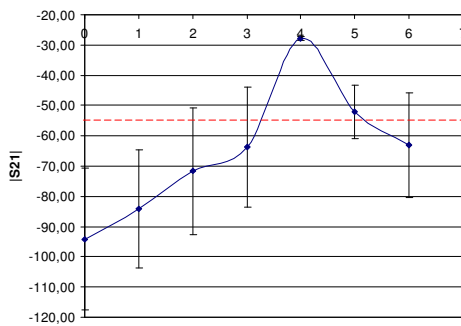


**Fig. 6.23. Simulated transmission coefficient for bottom line, measurement uncertainty included, reader antenna vertically oriented.**

The further away from the planar CVCA the reader is placed on the chest, the higher is the impact that is observed due to the small signal to noise ratio at these points.

The proposed method indicates that a communication link can only be assured within a much smaller area in comparison to the one provided only by the measurements (namely the whole torso (see Fig. 6.16 and Fig. 6.17)). Fig. 6.24 and Fig. 6.25 show three different concentric areas in the torso that represent reliable, uncertain and impossible communication respectively.

It is noteworthy, that for greater distance the polarization match of the antennas is not directly correlated with the transmission coefficient.

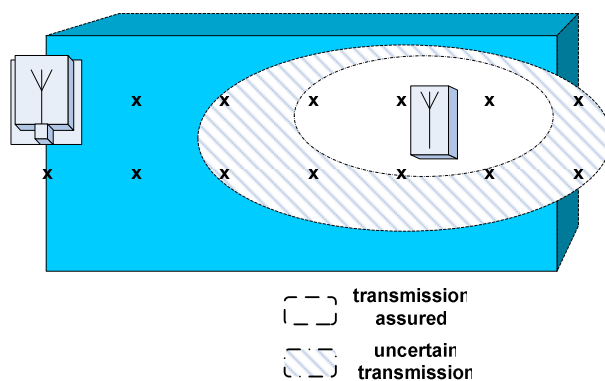


**Fig. 6.24. Characterization of zones with different transmission reliability, reader antenna PIFA vertically oriented.**

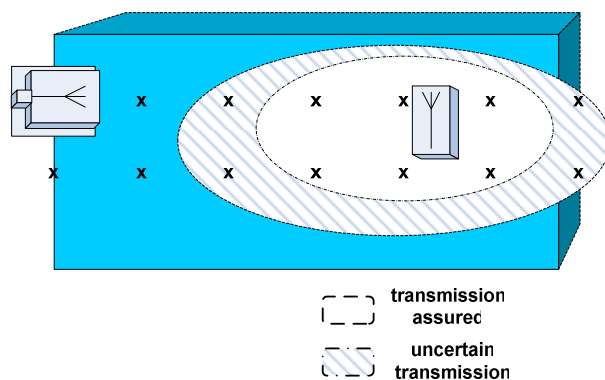


**Fig. 6.25. Characterization of zones with different transmission reliability, reader antenna PIFA horizontally oriented.**

### 6.2.2 PERPENDICULAR MEASUREMENTS OF THE PLANAR CVCA

The read range perpendicular to the chest was also measured in the antenna test chamber. The reader antenna was placed as it were worn in a shirt pocket of a standing medic and facing the implant at different distances for both PIFA orientations, vertical and horizontal. These are representative positions for vertical and horizontal polarizations for handset antennas.

The entire setup to measure path loss is shown in Fig. 6.26. The implanted antenna was placed inside a polystyrene tank filled with skin mimicking gel, 9 mm away from the phantom interface to simulate a subcutaneous insertion into a human torso. The wall thickness of the phantom is 2 cm as it represents the patient's clothing. The size of the phantom is the minimum representative for the upper part of the body (see section 5.3.1) for far field communication at the frequency of interest ( $350 \times 165 \text{ mm}^3$ ) [143].



**Fig. 6.26. Near field measurements setup for reader to implant communications.**

Path loss measurements ( $S_{12}$ ) were performed in an anechoic chamber from distance  $d=0\text{m}$  (PIFA probe antenna located on phantom surface) up to a distance of  $d=1\text{m}$ . As the PIFA was facing the phantom, a mismatch was observed, falling from free-space conditions (-17 dB) to the  $d=0\text{m}$  situation (-4.7 dB) due to the phantom proximity (see diagram for on-chest measurements Fig. 6.15 in section 6.2.1). This influence was implicitly considered in the path loss when it was measured. As the distance was kept under near field conditions, multipath and fading were not considered in the scenario's link budget. Application-oriented conditions were considered for an implanted passive RFID transceiver: minimum

power level of the implant was assumed to be  $P_{\text{implant\_dB}} = -20$  dBm and reader sensitivity  $P_{\text{reader\_dB}} = -70$  dBm.

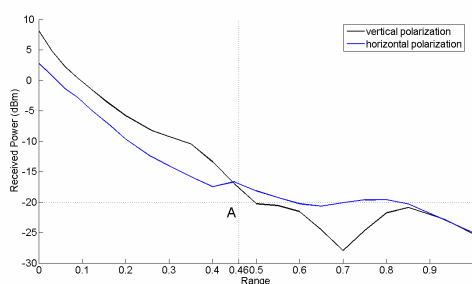


**Fig. 6.27. Power received by the implanted tag from a reader placed perpendicularly to the chest for vertical and horizontal PIFA as reader antenna (see Fig. 6.26). Point A (0.46 m, -20 dBm).**

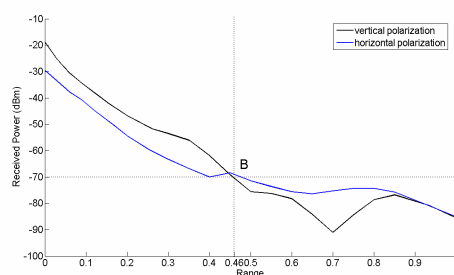


**Fig. 6.28. Power received by the reader from the implanted tag backscattered signal for vertical and horizontal PIFA as reader antenna (see Fig. 6.26). Point B (0.46 m, -70 dBm).**

As can be seen in Fig. 6.27 and Fig. 6.28, a communication link can be reliably established within a distance of 0.46 m for both polarizations.

The uncertainty introduced by the cable is not repeatable in simulations as it was in section 6.2.1.2 due to the very high simulation size to expect. But at least a maximum communication range can be justified which is further than it is possible with a passive RFID system.

### 6.2.3 FAR FIELD MEASUREMENTS OF THE 3-D CVCA

As part of the methodology to evaluate the actual working range of the implanted 3-D CVCA active measurements were launched. As the implanted device is battery-powered, longer transmission ranges are achievable beyond near field distance, compared to passive RFID systems.



### 6.2.3.1 Transmitted Power, Sensitivity and Base Station Characterization

For the measurements, two devices of the Application Development Kit (ADK) by Microsemi [138], both of them equipped with the ZL70102 transceiver chip [137], [132], [133], were employed: the implanted sensor node (SN), together with the 3-D CVCA and the external base station (BS) with its corresponding helix antenna.

Prior to the active link budget measurements, the implanted sensor node, the base station and its corresponding antenna had to be characterized. A complete communication sequence involves three consecutive operations: implant search, wake-up and data exchange. In the present system, the communication can be initiated at 2.45 GHz as well as at 403 MHz. The former is taken for energy efficiency perspective. In this manner, a search operation wakes up the sensor node from its stand-by mode. Further transmission of sensor data is accomplished exclusively at the MICS frequency of 403 MHz and not at 2.45 GHz to avoid possible interferences within the unlicensed ISM band in implanted sensitive high-end applications. During the search implant operation, the transmit power ( $P_{TX}$ ) of the base station was measured at both frequencies. For this purpose, a 3 dB hybrid coupler and a spectrum analyzer were used (see Fig. 6.29). The obtained values of the transmit power were  $P_{TX} = -12.7\text{dBm}$  at 403 MHz and  $P_{TX} = 17.5\text{dBm}$  at 2.45 GHz.

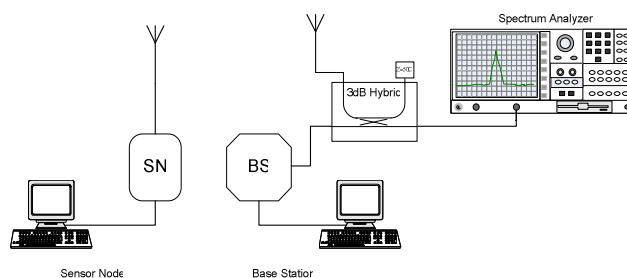


**Fig. 6.29. Principal sketch of the measurement of the transmit power  $P_{TX}$  of the base station.**

The sensitivity of the implanted sensor node was separately measured. This was accomplished by connecting the base station to the sensor node via cable and two calibrated attenuators, one of them adjustable (see Fig. 6.30). The two attenuators together with cable losses represented the total gain and free space losses of both antennas. The attenuation was slowly lowered to the point where the system went into on-session. Then, the attenuation was again increased until the communication link was lost. The obtained values reflected the sensitivity ( $P_{RXp}$ ) of the implanted sensor node

( $P_{RXp}=-99\text{dBm}$  at 403 MHz and  $P_{RXp}=-68\text{dBm}$  at 2.45 GHz). Although it was below the typical manufacturer's expectation at 2.45 GHz, the measured sensitivity was in between the expected values.

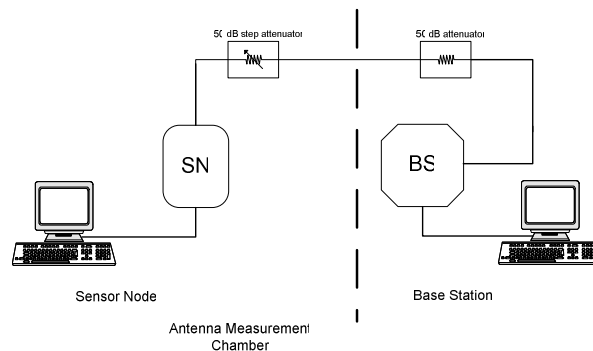


**Fig. 6.30. Principal sketch of the measurement of the maximum sensitivity  $P_{RXp}$  of the SN.**

In order to characterize the base station's low profile helical antenna (shown in Fig. 6.34), it was mounted directly in a vertical position on a ground plane, which resembled the PCB of the base station in shape and size. The respective measurements involved gains ( $G_{BS}$ ) and reflection coefficients ( $|S_{11}|_{BS\_dB}$ ) for both frequencies (see Fig. 6.32). At 403 MHz the reflection coefficient is  $|S_{11}|_{BS\_dB} = -4.42\text{dB}$  and at 2.45GHz it is  $|S_{11}|_{BS\_dB} = -5.37\text{dB}$  (see Fig. 6.32). This corresponds to mismatch losses of  $L_{BS}=1.92\text{dB}$  at 403 MHz and  $L_{BS}=1.48\text{dB}$  at 2.45 GHz. The predominant polarization of the helical antenna is vertical with  $-3.27\text{dBi}$  average gain at 403 MHz and  $-2.71\text{dBi}$  at 2.45 GHz in this horizontal plane (see Fig. 6.31 for 2.45 GHz). This is the reason why vertical polarization is considered in the link budget. The radiation pattern is omni-directional in this plane.

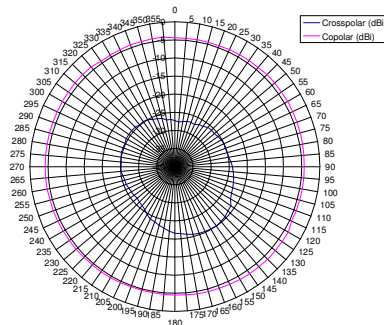


**Fig. 6.31: Measured radiation diagram of the helica BS antenna at 2.45 Ghz**

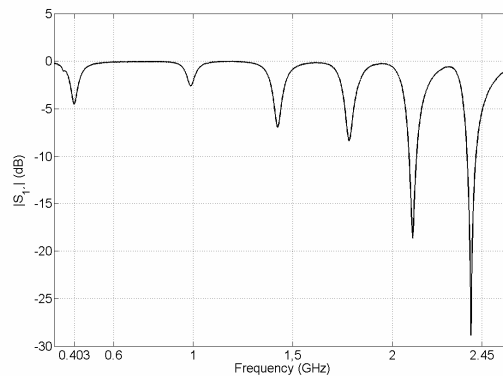


**Fig. 6.32. Measured reflection coefficient of the base station helical antenna ( $|S_{11}|_{BS}$ ).**

### 6.2.3.2 Wireless Test Bed Setup

After completing the preceding characterizations, the active wireless link budget measurements were carried out. At one end the ADK sensor node was connected to the 3-D CVC A in the phantom by using a coaxial cable. In the wireless measurements, only one variable attenuator was inserted between the sensor node and the 3-D CVC A completed at the other end by the external ADK base station with its corresponding helix antenna. The base station and sensor node were controlled by a computer via USB connection (see Fig. 6.33). This allowed the wireless link to be monitored in addition to initiating the communication process. Both antennas were positioned at 1.34 m height. The whole setup was arranged in an anechoic chamber (see Fig. 6.34).

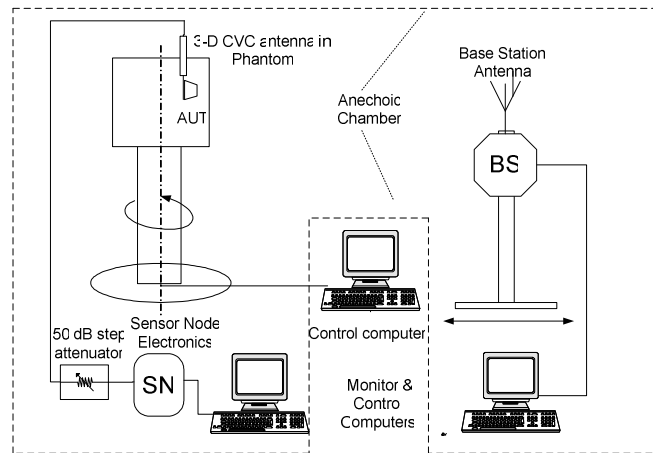


**Fig. 6.33. Principal sketch of the measurement for maximum transmission range.**

The distance between the two antennas ( $d_{\text{set}}$ ) was fixed to  $d_{\text{set}}=1.43\text{m}$  in free space. This distance was determined by approaching the base station manually to the point where the system went into on-session at the wake-up frequency of 2.45 GHz (downlink). The losses in free space ( $L_{\text{FS}}$ ) for both frequencies were calculated according to equation (6.7), derived from the free space loss expression  $(\lambda/4\pi r)^2$  after rearranging the term.

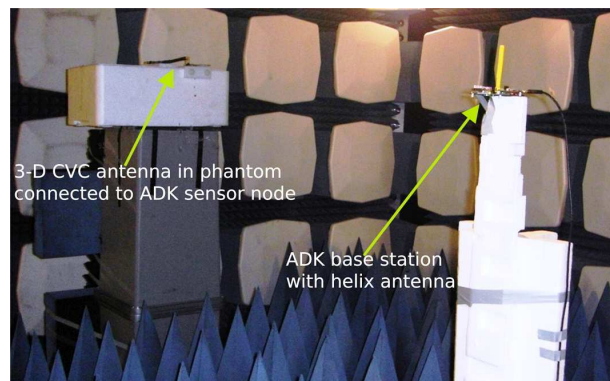


**Fig. 6.34. Measurement setup in anechoic chamber for link budget calculation in free space.**

$$L_{\text{FS}} = 20\log_{10}(d_{\text{set}}) + 20\log_{10}(f) - 27,55 \quad (6.7)$$

Where

$f$  [MHz] is center frequency of the frequency band,  
 $d_{\text{set}}$  [m] distance between the two antennas, set to 1.43 m and

$L_{FS}$  [dB]: free-space loss.

For  $f=403\text{MHz}$ , the free space loss was  $L_{FS}=27.7\text{dB}$  and for  $f=2450\text{MHz}$  it resulted in  $L_{FS}=43.3\text{dB}$  at  $d_{set}=1.43\text{m}$ .

The transmission of sensor data (uplink) was accomplished in the MICS band at 403 MHz. In order to avoid further inaccuracies in positioning, the 1.43 m separation was kept while increasing the attenuator value to emulate communication over distances longer than the chamber length. Regarding possible near-field effects, it should be noted that 1.43 m cover approximately two wavelengths at 403 MHz (free-space wavelength at 403 MHz =0.74m). The impact of the near field in this situation could be estimated by calculating the ratio between the near-field and far-field factors of a dipole antenna [144], [145]. This calculation indicated an inductive near field 22 dB below the radiated field, which implied an uncertainty of +/-0.65 dB in the measurements. This accuracy was considered sufficient for the proposed experiment.

The communication link was lost at the point where attenuation value ( $L_A$ ) reached 20 dB at the input of the sensor node. Tab. 6.1 gives a comprehensive summary of the measured results, including losses introduced by cables in the setup of Fig. 6.33.

	Frequency [MHz]	403.35	2450
Transmission (Base Station)	Transmit Power, $P_{TX}$ (dBm)	-12.7	17.5
	Gain, $G_{BS}$ (dBi)	-3.27	-2.71
	Mismatch Loss, $L_{BS}$ (dB)	1.92	1.48
	Free-space Loss, $L_{FS}$ (dB) [at Distance $d_{set}=1.43\text{m}$ ]	27.7	43.3
Receiving (Implant)	Gain, $G_{AUT}$ (dBi)	-28.95	-25.5
	Mismatch Loss, $L_{AUT}$ (dB)	0.15	0.09
	Coaxial Cable Loss, $L_{cable}$ (dB)	2.4	8.2
	Attenuation, $L_A$ (dB)	20	2

**Tab. 6.1. Link budget calculation according to the measured results for line of sight.**

Equation (6.8) [145] shows the link budget at both frequencies for the described setup.

$$P_{RX} = P_{TX} - L_{BS} + G_{BS} - L_{FS} + G_{AUT} - L_{AUT} - L_{cable} - L_A \quad (6.8)$$

Where

$P_{RX}$  [dBm] is the receiver sensitivity of the sensor node,  
 $P_{TX}$  [dBm] the transmit power of the base station,  
 $L_{BS}$  [dB] the mismatch loss of the helix antenna,  
 $G_{BS}$  [dBi] the gain of the base station antenna,  
 $L_{FS}$  [dB] the free space loss at the given  
frequency  $f$  [Hz] and  
distance  $d_{set}$  [m] (see equation (6.7),  
 $G_{AUT}$  [dBi] gain of the 3-D CVCA under test,  
 $L_{AUT}$  [dB] mismatch loss of the 3-D CVCA under test,  
 $L_{cable}$  [dB] losses of the coaxial cable and  
 $L_A$  [dB] value of the attenuator losses.

By applying equation (6.8) and the data provided in Tab. 6.1 a new value of sensitivity of the electronics was achieved for the wireless setup. The results were compared with the wired measured data of the previous section to assess the accuracy of the setup in Tab. 6.2. There is a good agreement between the sensitivity values in the conducted (wired) and wireless measurements.

	Frequency [MHz]	403-35	2450
In free space	Sensitivity, $P_{RX}$ (dBm)	-97.1	-65.8
Cable connection	Sensitivity, $P_{RXp}$ (dBm), premeasured	-99	-68

**Tab. 6.2. Resulting values of sensitivity of the electronics.**

### 6.2.3.3 Range Estimate Calculation

In this manner, equation (6.9) describes the maximum distance  $d_{max}$  that can be reached in an ideal free space scenario, where feeding cables and the attenuator are not included.

$$20\log_{10}(d_{max}) = L_{cable} + L_A + 20\log_{10}(d_{set}) \quad (6.9)$$

The losses in the cable  $L_{cable}$  and the attenuation  $L_A$  were different at the different frequencies (see Tab. 6.1). They effectively represented the respective free-space loss for a specific additional distance.

Elevated values could be noticed on account of the perfect conditions in the antenna measurement lab. Maximum operating distances of  $d_{\max\_INI}=4.72\text{m}$  for communication initiation at 2.45 GHz and  $d_{\max\_DATA}=18.95\text{m}$  for data exchange in the MICS band were reached. The value of  $d_{\max\_INI}$  is an overestimate due to the radiating effect of the feeding cable.

By applying the uncertainty factor of 0.4 (as in section 6.1.2.3 identified) for the 2.45 GHz frequency, the best estimate for  $d_{\max\_INI}$  is 1.88 m.

### 6.3 FUNCTIONAL TESTS OF THE 3-D CVCA

The objective of the reflection and transmission test was to define the read range of the communication link between the SCVC and an external base station in an indoor scenario for the future application. The base station made use of the same Z70102 transceiver chip by Zarlink, corresponding to the ADK, with a helix antenna. The range measurement was contrasted with the estimated one in the literature.

The purpose of this section is to show the measurement results of the functional performance test of the 3-D CVCA prototype with proprietary electronics in an adverse scenario (laboratory environment).

#### 6.3.1.1 *Reflection and Transmission Test*

The 3-D CVCA was placed into a phantom that modeled a human torso. The phantom was composed of a polystyrene tank of 35 cm x 25 cm cross section filled with 14.5 liters of tissue simulating liquid [116]. The antenna was placed at 9 mm from the front phantom wall and with an offset of 60 mm with respect to the vertical center axis. The reflection coefficient  $|S_{11}|$  was measured with the Agilent 8714ET Vector Analyzer.

Then, the implanted electronics was fed by a 3 V battery. The implant transceiver was programmed to transmit an emergency signal every few seconds. Both wake-up and communication signals were transmitted in the MICS band at 403 MHz to test the longest read range.

The transmitted power was -15.7 dBm, which complied with the maximum approved power according to the MICS standard (-16 dBm, 25  $\mu\text{W}$ ) [146]. This was registered in an Agilent E4402B Spectrum Analyzer connected to the output of the circuit without antenna when transmitting (see Fig. 6.35).

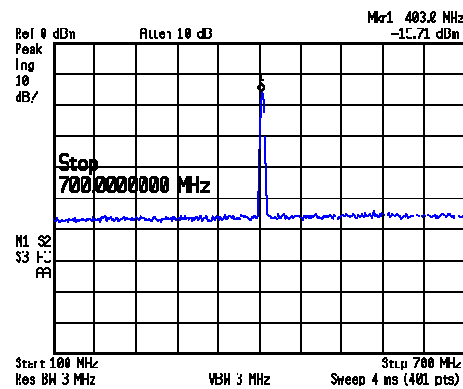


Fig. 6.35. Output signal of the CVC-implant PCB.

The measured reflection coefficient from the port 1 at the mock board (see section 5.2.1) terminal was below -15 dB for both operation frequencies, 403 MHz and 2.4 GHz, as it is illustrated in Fig. 6.36.

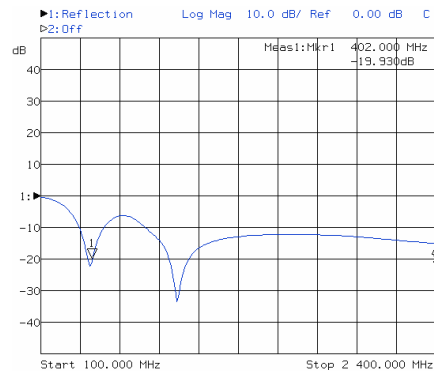
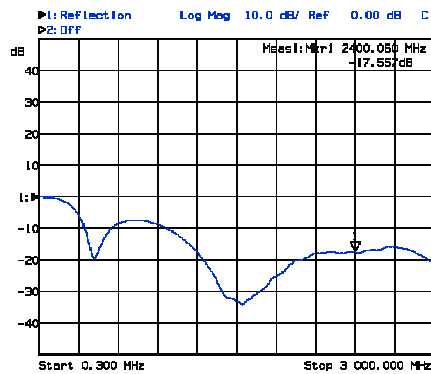


Fig. 6.36. Measured reflection coefficient for the mock board at port 1.

The antenna was set into the phantom at the same position as in the gain characterization test (9 mm from the front phantom wall). The 3-D CVCA reflection coefficient  $|S_{11}|$  was found to be below -10 dB from 345 MHz to 555 MHz and from 960 MHz to 3000 MHz, which was the limit of the analyzer (see Fig. 6.37). Therefore, it covered the expected MICS and ISM bands with broadband behavior.





**Fig. 6.37.** Reflection coefficient from the antenna placed into the phantom at the defined position.

### 6.3.1.2 Functional Test of the Implanted Antenna with Proprietary Electronics

Finally, the implanted electronics and the 3-D CVCA were assembled to form an SCVC prototype and placed into the human phantom facing the base station (see Fig. 6.38 (a)). The whole setup, including a control unit, is shown in Fig. 6.38. In a laboratory environment the base station and the SCVC were placed at 74 cm and 94 cm from the floor, respectively.

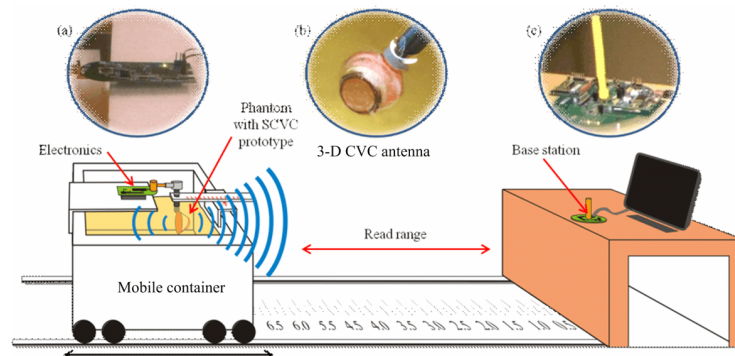


**Fig. 6.38.** (a) Electronics connected to (b) the 3-D CVCA placed into the phantom. (c) Laboratory environment with base station and control laptop at maximum operating distance.

The antenna was now connected to the proprietary electronics (see Fig. 6.39) that employed the same transceiver as the one on which previous tests had been performed.

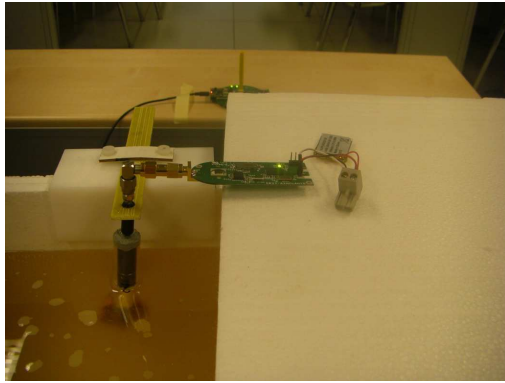


**Fig. 6.39. Implanted 3-D CVCA setup with proprietary electronics.**

The electronics is autonomous as it is fed by a 3 V battery (see Fig. 6.40). The mote was programmed to transmit an emergency signal every few seconds. Both wake up and communication signals are emitted at 403 MHz.

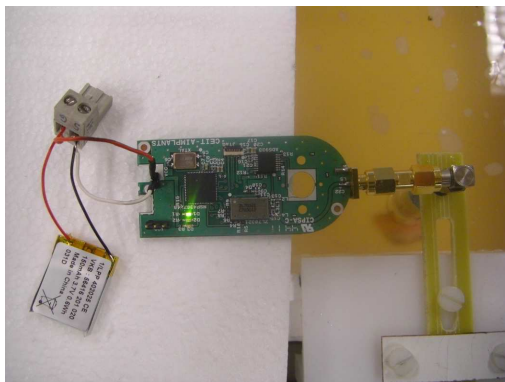


**Fig. 6.40. Implanted electronics transmitting for an emergency event.**

The whole setup (including the base station on a table and a control unit represented by a computer) is shown in Fig. 6.41.



**Fig. 6.41. Setup of the entire implanted smart system, with base station and control unit.**

The phantom was progressively separated from the base station once the session was established.



**Fig. 6.42. Separation of human phantom from base station while communication session is maintained (see green light on the computer screen).**

The average distance at which the session was lost was 6.36 m (Fig. 6.42). When approximating the phantom to the base station again, the session was restored at approximately 5.76 m.

Because in the previous test (active measurements in the anechoic chamber, see section 6.2.3) the wake up signal was transmitted at 2.45 GHz, only in the MICS band a comparison of the working range is possible. The two different measurement environments have to be taken into account.

### 6.3.1.3 Validation of Working Range in an Indoor Environment

The transmission measurements according to Fig. 6.38 showed that the communication link was lost (transition from “in session” to “session lost”) at an average distance of 6.36 m and the communication was re-established (transition from “session lost” to “in session”) at 5.76 m when bringing the phantom closer to the base station again.

In order to verify the obtained data, an indoor propagation model according to Rappaport [147] and Seidel [148] was applied for the laboratory measurements. This empirical model is based on measurements and statistical analysis, see equation (6.10).

$$PL(d)[dB] = PL(d_0)[dB] + 10n_{SF} \log\left(\frac{d}{d_0}\right) + FAF [dB] \quad (6.10)$$

Where

- $n_{SF}$  [ ] is single floor path loss exponent,
- $PL(d)[dB]$  is the average path loss,
- $FAF [dB]$  is the floor attenuation factor and
- $d_0 [m]$  is the close-in reference distance taken as free space distance from which indoor attenuation is applied.

Therefore, the resulting path loss exponent  $n_{SF}$  and the floor attenuation factor  $FAF$  represent the additional attenuation in a real indoor environment, compared to the ideal free space propagation. The equivalent value to  $n_{SF}$  for free space communications (without floor and obstacles) is 2, whereas the value for environments with obstacles between the transmitter and the receiver is higher.

In this manner,  $n_{SF}$  exponent was calculated to verify the indoor performance of the system according to equation (6.10). With equation (6.11)  $n_{SF}$  was obtained by rearranging the terms:

$$n_{SF} = \frac{PL(d)[dB] - PL(d_0)[dB]}{10 \log\left(\frac{d}{d_0}\right)} \quad (6.11)$$

The floor attenuation factor  $FAF [dB]$  was set to zero, as the measurements were performed over the same floor. By de-embedding the antenna gains and mismatch losses (see section 6.2.3.2, Tab. 6.1) from the ratio between the implanted electronics sensitivity and the measured

transmitted power of the base station ( $P_{TX} = -15.7\text{dBm}$ ), a path loss of  $PL(d) = 47.1\text{dB}$  was computed. By using the free space loss equation for the reference distance  $d_o = 1\text{m}$ , the reference path loss  $PL(d_o)$  was  $24.5\text{dB}$ . With this data, equation (6.11) led to a path loss exponent of  $n_{SF} = 2.81$  for the distance of  $d = 6.36\text{m}$  (on-off) and  $n_{SF} = 2.97$  for  $d = 5.76\text{m}$  (off-on).

According to the indoor propagation model [147] the path loss exponent  $n_{SF}$  should be close to  $3.27$  for office buildings at  $914\text{MHz}$  with a variance of  $11.2\text{dB}$ . The obtained values ( $2.81$  and  $2.97$ ) are therefore consistent. The slight difference to the expected value ( $3.27$ ) is likely due to the frequency difference effect: lower frequency ( $403\text{MHz}$  compared to  $914\text{MHz}$ ) means lower path loss and therefore lower  $n_{SF}$ .

Another indoor path loss model by Vaughn and Andersen [149] is proposed. The empirical model equation (6.12) is obtained from measurement data taken in the ISM  $433\text{MHz}$  band, therefore closer to the MICS band, in several European building types.

$$PL(\text{dB}) = -23 + 90 \log_{10}(d) \quad (6.12)$$

Where  $d$  [m] is the distance between transmitter and receiver, for  $d > 3\text{m}$ .

The equation reflects the best-case scenario calculation, i.e., only the best 1% of all measurement positions are below this low path loss. The scenario in the present experiment can be considered close to the optimal, as it is a line-of-sight transmission in a not cluttered office.

By applying  $d = 6.36\text{m}$  to equation (6.12), an indoor path loss of  $PL = 49.3\text{dB}$  is calculated, which is a quite good correlation to  $PL = 47\text{dB}$ , employed in equation (6.11). This reveals again the consistency of theoretical and measured results.

Furthermore, applying the simulated gain for  $403.5\text{MHz}$   $G_{\text{implant\_dB\_v}} = -36.1\text{dBi}$  (see section 6.1.2.3) in equation (6.10) by using the calculated single floor path loss exponent  $n_{sf}$  of  $2.81$  an indoor working range of  $3.56\text{m}$  is calculated. This range corresponds to an estimated minimum range for MICS without the antenna's testbed in an indoor environment.



# *Chapter 7*

## **Conclusions and Future Work**

---

Beside the shown methods and results in this thesis, further conclusions can be drawn. Apart from that, an outlook on promising future investigation is given, which complements the presented work.

This final Chapter 7 summarizes the research described in the previous chapters. It is divided into the three main objectives: the result description of both the antenna design process and the verification of their performance with a new measurement methodology, the conclusions and the description of future work prospects.

## 7.1 RESULT SUMMARY

### 7.1.1 DESIGN OF IMPLANTED ANTENNAS

State-of-the-art antenna topologies for implants were studied and appropriate antenna layouts chosen for the use in smart CVC implants. The given requirements, i.e., broadband capability to prevent detuning, limited use of the implant surface, low profile adjustment to the given 3-D shape of the portacath (a truncated cone) as well as the necessary access to the reservoir, make antenna type selection a challenge.

Having in mind the application of a short range battery-less implant capable of monitoring the bacterial pollution of the CVC reservoir, an antenna for the UHF-RFID frequency band was designed. Intended for a subcutaneous position, a short circular microstrip monopole design encapsulated in a ceramic substrate was proposed. With a simple modification, it was mounted on the top cap of the portacath reservoir and showed an excellent radiation performance of  $G_h = -23.8$  dBi in horizontal polarization and broadband characteristics for -10 dB bandwidth of 334 MHz together with a minimum profile of 2.54 mm. The radiation efficiency is about -25 dB and the antenna exhibits a high tolerance to tissue variations.

In the thesis the parameterization model of the printed monopole-strip antenna is also presented. A planar matching geometry was introduced to easily adapt the layout to other frequencies, tissues and substrates.



Antenna	Dimension with insulation [mm]	Body phantom			Implant depth [mm]	Gain [dBi]
		$\epsilon'_e$	$\sigma'_e$	dimension [mm] <sup>11</sup>		
Spiral based [117]	38.0 x 42.0 x 4.0 = 6384.0	49.60	0.51	50 x 40 x 20	5	-30.6
Spiral PIFA [105]	17.0 x 27.0 x 6.0 = 2754.0	42.80	0.64	50 x 40 x 20	7	-35.0
Meandered PIFA [150]	22.5 x 22.5 x 2.5 = 1265.6	46.70	0.68	103 x 103 x 8.5	3	-24.9
Stacked PIFA [151]	3.62 x $\pi$ x 0.7 = 28.5	46.70 13.1 57.4	0.69 0.09 0.74	100 95 90	$\cong$ 2	-55.6
PIFA with 3-D ground plane [152]	40 x 30 x 13.2 = 15600.0	38.10	0.53	100 x 100 x 50	4	-28.0
FIFA [153]	$\cong$ 162 x $\pi$ x 33.8 = 27184.0	57.10	0.79	90	$\cong$ 18	-29.2
Painted FIFA [153]	62 x $\pi$ x 18.2 = 2058.4	57.10	0.79	90	$\cong$ 34	-29.1
FRH [153]	17 x 17 x 18 = 5202.0	57.10	0.79	80 x 100	$\cong$ 20	-28.5
3-D CVCA	8645.7	48.0	0.34	160 x 350 x 250	9	-28.9
RFID CVCA <sup>12</sup>	797.9	40.8	0.37	160 x 350 x 250	9	-23.8

**Tab. 7.7.1. Basic performance comparison of implanted antennas for MICS based on [153].**

The second approach of an implanted antenna aimed to overcome the short range constraint by using a battery powered implant. A modified monopole over ground plane was developed as layout. For miniaturization, the bent monopole was short circuited to ground and subsequently adapted to work as dual-band antenna for MICS frequency and the ISM 2.4 GHz band. The antenna topology is very flexible and adaptable in order to take advantage of a big share of the truncated cone shell. With its very low profile, the structure integrates into the surface and the merely small elevation over the original cone trunk sustains the accessibility of the reservoir. Moreover, this solution is cost-effective, as no special material for dielectric media is mandatory

The antenna proved good performance characteristics in terms of antenna gain in the MICS band with  $G_v = -28.95$  dBi in vertical polarization

<sup>11</sup> Three values are for box geometries, two for cylindrical (diameter x height) and one for spherical (diameter).

<sup>12</sup> The RFID-CVCA is designed for UHF-RFID band and added for general comparison.

and in the ISM 2.4 GHz band with  $G_h = -19.9$  dBi in horizontal polarization. Its broadband capabilities were demonstrated with a -10 dB matching bandwidth from 345 MHz to 555 MHz and 965 MHz to 2.5 GHz. The regulation permitted ERP of -16 dBm SAR resulted in 2.9 mW/kg. The radiation efficiency is 0.059 for ISM 2.4 GHz and 0.017 for the MICS band. Further simulations suggested that the thickness of the biocompatible protection layer, which insulates the metal stripes from the body tissue, had an impact on the detuning of the input matching, radiation efficiency and therefore, the overall gain of the antenna.

Antenna	Dimension with insulation [mm]	Body phantom			Implant depth [mm]	Gain [dBi]
		$\epsilon'_e$	$\sigma'_e$	Dimension [mm] <sup>13</sup>		
Cavity slot antenna [154]	$1.6 \times 4 \times 2.8 = 17.9$	35.15	1.60	180 x 60 x 60	4	-22.3
Double helix [155]	$0.6^2 \times \pi \times 17.7 = 20.1$	38.00 5.30 52.70	1.50 0.10 1.70	180 x 60 x 60 180 x 56 x 56 180 x 48 x 48	2	-14.0
Meandered PIFA [150]	$22.5 \times 22.5 \times 2.5 = 1265.6$	38.06	1.44	$103 \times 103 \times 8.5$	3	-8.5
PIFA [156]	$\cong 5.5^2 \times \pi \times 1.7 = 161.6$	50.0	2.20	$152 \times 152 \times 20$ $80 \times 50 \times 8$	$\cong 8$	-24.8
FIFA [153]	$\cong 16^2 \times \pi \times 33.8 = 27184.0$	52.73	0.24	90	$\cong 18$	-31.7
Painted FIFA [153]	$6^2 \times \pi \times 18.2 = 2058.4$	52.73	0.24	90	$\cong 34$	-28.3
3-D CVCA	8645.7	25.0	0.5	$160 \times 350 \times 250$	9	-19.9

**Tab. 7.7.2. Basic performance comparison of implanted antennas for ISM 2.4 GHz based on [153].**

Simulations also revealed the robustness of the antenna in terms of input impedance against variations of the liquid level in the reservoir and the external tissue. The influences of battery and electronics proximity in the final device were analyzed beforehand and turned out to be not critical.

The whole design process is described in detail including all steps of input impedance matching at both frequencies. The test results proved the thickness of the outer dielectric protection layer towards the surrounding tissue to be a crucial factor in order to obtain a high efficiency and robustness against tissue property variations. Based on its flexible

<sup>13</sup> Three values are for box geometries and one for spherical (diameter).

adjustment by bending on 3D-surfaces, this antenna layout is a promising option for various types of small implants with limited space.

### 7.1.2 MEASUREMENT METHODOLOGY

The simulation and measurement methodology developed in this work covered different design aspects. A test bed was provided and its viability was secured in prior simulations. Influences of phantom size, position of the antenna in the phantom in relation to the phantom-air interface and the body tissue-simulating liquid were examined in simulations and test measurements.

In the antenna measurement laboratory, special attention was paid to the validity of simulated antenna gain and the influence of the feeding cable during the antenna gain verification. The newly developed methodology integrates the results of the antenna simulations with and without test bed and cable to calculate their uncertainty factor for the final smart implant.

For the RFID CVCA, transmission simulations validated the actual safe range for near field transmission to a transceiver worn on the chest to about 8.5 cm. By using an uncertainty calculation it was demonstrated that the area on the chest where the transmission is proved is much smaller than previously measured with the cable attached to the antenna. In broadside direction near-field measurements showed that a passive RFID link is likely to be set when the reader is within 0.46 m distance.

For the MICS CVCA, the antenna gain was measured in the antenna laboratory under ideal circumstances using a wireless test bed. Incorporating the results of the simulation and gain measurements by applying the uncertainty factor, an effective working range of 1.88 m for ISM 2.4 GHz. Then, a real-world working range was verified by applying these results to an indoor propagation model. The assembly of the final prototype and functional tests in the MICS frequency band revealed a high accordance of prediction and measurement results of about 6 meter. With this methodology applied, the obtained working range could be verified and was proved in final functional indoor tests.

## 7.2 CONCLUSIONS

Finally, the selection of the two topologies proved to be a feasible and particularly flexible solution for implanted antennas. Comparing the performance to other proposed topologies (see Tab. 7.7.1 and Tab. 7.7.2) it can be concluded that the gain is in the expected magnitude order for

implanted antennas and is even higher with a phantom size larger than any other. Many different influences of the measurement environment and the application scenario take their toll, as studies in this work revealed. Only a procedure that comprehends a combination of measurement and simulation, as introduced in this work, is a viable way to accurately characterize antenna properties despite all manipulating factors.

The link budget calculation allows the evaluation of possible application scenarios and, in particular, the maximum operating distance of the future system in certain positions prior to a working smart implant prototype.

### 7.3 FUTURE WORK

Future directions for investigations deriving from the presented work are outlined here. The low over-all efficiency of implanted antennas is a core problem to solve. It is recommendable to focus on optimizing gain, bandwidth and multiband capabilities by studying further modifications and allow still adaptability to various implant types and designs. Proposals of additional antenna layouts and variations of the given 3-D dual-band design were part of a patent proposal including topologies with meandered monopole-strip and alternating width of the monopole strip.

On account of the highly lossy properties of body tissues, the improvement of the transmission link is of major importance. The challenge of the very limited space destined to an antenna in a smart implant should focus also on approaches beyond antenna topology optimization. The implanted antenna's robustness against tissue variations is raised by active adaptation or reconfiguration to its surroundings and other frequencies for low bandwidth designs respectively, which can be accomplished by using, e.g.,  $z$ -diodes and monopole stubs. Multiband designs are promising due to their elevated transmission security and allowing further power saving implementations or the integration into BANs. The transmission range can be raised by lowering the body surface reflections using flexible patches like plasters with dedicated permittivity and directional capabilities.

Taking a step further would imply the integration of the antenna directly into the cone trunk and the continuous minimization of the design for smaller 3-D implants. Finally, further standardized phantom models would simplify the comparison with other research results and increase the predictability of measurements both in the laboratory and in real world environments.

## 7.4 ACKNOWLEDGMENT

The fundamental research on implantable antennas framing the present Ph.D. thesis was carried out in the Antenna Group of the Department of Electronics and Communications at CEIT (Centro de Estudios e Investigaciones Técnicas) in Gipuzkoa in collaboration with Tecnun. Within an interdisciplinary investigation project, further applied research was ventured together with the Medical Bioengineering Department of CEIT. This project was aimed at developing new advanced implants capable of communicating with external devices wirelessly.

In the beginning, the design and measurements of the 868 MHz antenna were kindly mentored by Queen Mary University of London. Later on, the investigation was frequently supported by the Communication Department of Ikerlan.



## **Bibliography**

---

- [1] T. Sommer, "The Business of Ageing," netcarity project, Tübingen, Germany, IST-2006-045508, 2010.
- [2] A. Arriola, "Design and Analysis of Planar and Low-Profile Antennas for Body Area Networks at 2.45 GHz," University of Navarra; Tecnun, 2011.
- [3] G.-Z. Yang and M. Yacoub, *Body sensor networks*. London, UK: Springer, 2006.
- [4] B. E. Kartsakli, A. Lalos, and M. Di Renzo, "Enhancing quality of life with wireless sensor technology," *IEEE Life Sci. Newsl.*, no. Dec., pp. 1–5, 2013.
- [5] U. Anliker, J. a Ward, P. Lukowicz, G. Tröster, F. Dolveck, M. Baer, F. Keita, E. B. Schenker, F. Catarsi, L. Coluccini, A. Belardinelli, D. Shklarski, M. Alon, E. Hirt, R. Schmid, and M. Vuskovic, "AMON: a wearable multiparameter medical monitoring and alert system.," *IEEE Trans. Inf. Technol. Biomed.*, vol. 8, no. 4, pp. 415–427, Dec. 2004.
- [6] P. S. Hall and Y. Hao, "Introduction to Body-Centric Wireless Communication," in *Antennas and Propagation for Body-Centric Wireless Communications*, 1st ed., P. Hall and Y. Hao, Eds. Norwood, MA, USA: Artech House Publisher, 2006, pp. 1–5.
- [7] K. Agarwal, "ICU infection , a common sight worldwide," *The Money Times*, 02-Dec-2009. [Online]. Available: <http://www.themoneytimes.com/featured/20091202/icu-infection-common-sight-worldwide-id-1092819.html>. [Accessed: 15-Dec-2011].

- 
- [8] L. Hall-Stoodley, J. W. Costerton, and P. Stoodley, "Bacterial biofilms: from the natural environment to infectious diseases," *Nat. Rev. Microbiol.*, vol. 2, no. 2, pp. 95–108, Feb. 2004.
- [9] D. Davies, "Understanding biofilm resistance to antibacterial agents," *Nat. Rev. Drug Discov.*, vol. 2, no. 2, pp. 114–122, Feb. 2003.
- [10] L. G. Harris and R. G. Richards, "Staphylococci and implant surfaces: a review," *Injury*, vol. 37, Suppl., no. 2, pp. S3–S14, May 2006.
- [11] P. S. Stewart, "New ways to stop biofilm infections," *Lancet*, vol. 361, no. 9352, p. 97, Jan. 2003.
- [12] R. M. Donlan, "Biofilms and device-associated infections," *Emerg. Infect. Dis.*, vol. 7, no. 2, pp. 277–281, 2001.
- [13] J. Paredes, M. Alonso-Arce, C. Schmidt, D. Valderas, B. Sedano, J. Legarda, F. Arizti, E. Gómez, A. Aguinaga, J. L. Del Pozo, and S. Arana, "Smart central venous port for early detection of bacterial biofilm related infections," *Biomed Microdevices*, vol. 1, Springer US, New York, NY, USA, pp. 1–10, Feb-2014.
- [14] R. F. Weir, P. R. Troyk, G. DeMichele, and T. Kuiken, "Implantable myoelectric sensors (IMES) for upper-extremity prosthesis control-preliminary work," in *Proceedings of the 25th Annual International Conference of the IEEE Engineering in Medicine and Biology Society (IEEE Cat. No.03CH37439)*, 2003, vol. 2, pp. 1562–1565.
- [15] J. A. Moore and H. F. B. Teagle, "An Introduction to cochlear implant technology, activation, and programming," *Lang. Speech. Hear. Serv. Sch.*, vol. 33, no. 3, pp. 153 –161, 2002.
- [16] M. S. Humayun, J. D. Weiland, and E. de Juan Jr., "Electrical Stimulation of the Human Retina," in *Retinal Degeneration Diseases and Experimental Therapy*, 1st Ed., J. G. Hollyfield, R. E. Anderson, and M. M. LaVail, Eds. New York, NY, USA: Springer US, 1999, pp. 479–485.
- [17] D. A. LaVan, T. McGuire, and R. Langer, "Small-scale systems for in vivo drug delivery," *Nat. Biotechnol.*, vol. 21, no. 10, pp. 1184–1191, Oct. 2003.



- [18] P. Cong, D. J. Young, B. Hoitl, and W. H. Ko, "Novel long-term implantable blood pressure monitoring system with reduced baseline drift," in *28th IEEE EMBS Annual International Conference*, 2006, pp. 1854–1857.
- [19] Y. Zhao, S. Li, A. Davidson, B. Yang, Q. Wang, and Q. Lin, "A MEMS viscometric sensor for continuous glucose monitoring," *J. Micromechanics Microengineering*, vol. 17, pp. 2528–2537, 2007.
- [20] M. N. Ericson, T. E. McKnight, S. F. Smith, and J. O. Hylton, "Implantable device for in-vivo intracranial and cerebrospinal fluid pressure monitoring," US6533733 B1, 18-Mar-2003.
- [21] A. Kim and T. Maleki, "A Novel Electromechanical Interrogation Scheme For Implantable Passive Transponders," in *IEEE 25th Int. Conf. Micro Electro Mechanical Systems (MEMS)*, 2012, Paris, Fra., pp. 31–34.
- [22] D. Bhatia, S. Bairagi, S. Goel, and M. Jangra, "Pacemakers charging using body energy," *J. Pharm. Bioallied Sci.*, vol. 2, no. 1, pp. 51–54, Jan. 2010.
- [23] A. Lymberis, "Microsystems and Smart Integrated Systems: A key enabling technology for AAL," European Commission, Brussels, Belgium, 2009.
- [24] B. Ismer, "Hands-on seminar - Remote Data Transmission by Active Implants," *Lecture, University of Rostock*, 2008. [Online]. Available: <http://www.herzrhythmustechnologie.med.uni-rostock.de/en/messpraktikummonitor.htm>. [Accessed: 28-Apr-2013].
- [25] J. Penders, B. Gyselinckx, R. Vullers, O. Rousseaux, M. Berekovic, M. Nil, C. Hoof, J. Ryckaert, R. Yazicioglu, P. Fiorini, and V. Leonov, "Human++: Emerging Technology for Body Area Networks," in *14th Int. Conf. Very Large Scale Integration System Chip (VLSI-SoC2006)*, 2006, 14th ed., vol. 249, pp. 175–180.
- [26] ZigBee® Alliance, "ZigBee® Health Care Standard Overview," *ZigBee Wireless Sensor Applications for Health, Wellness and Fitness*, Mar-2009. [Online]. Available:

- <http://www.zigbee.org/Standards/ZigBeeHealthCare/Overview.aspx>.  
[Accessed: 20-Nov-2012].
- [27] Bluetooth® SIG, “Specification | Bluetooth® Special Interest Group,” *Bluetooth® Core Specification 4.0*, 30-Jun-2010. [Online]. Available: <https://www.bluetooth.org/en-us/specification/adopted-specifications>. [Accessed: 11-Dec-2012].
- [28] Dynastream Innovations Inc., “THIS IS ANT,” *ANT® Message Protocol and Usage, Rev. 5.0*, 22-Feb-2013. [Online]. Available: [http://www.thisisant.com/developer/resources/downloads/#documents\\_tab](http://www.thisisant.com/developer/resources/downloads/#documents_tab). [Accessed: 04-Apr-2013].
- [29] A. Ghildiyal, B. Godara, and K. Amara, “Ultra Wideband for in and on-body medical implants: A study of the limits and new opportunities,” in *Proc. 5th European Conf. Antennas and Propagation (EUCAP)*, 2011, Rome, Ital., pp. 3941–3945.
- [30] M. S. Wegmueller, “Intra-Body Communication for Biomedical Sensor Networks,” Sc.D. dissertation, Integrated Systems Laboratory, ETH Zurich, 2007.
- [31] D. Mayhew, “Leadless pacemaker brings new hope to cardiac patients,” *Cambridge Consultants*, 14-Nov-2011. [Online]. Available: <http://www.cambridgeconsultants.com/news/pr/release/6/en>. [Accessed: 12-Feb-2012].
- [32] K. Foster and H. Schwan, “Dielectric properties of tissues,” in *The Biomedical Engineering Handbook: Second Edition*, 2th. ed., CRC Press LLC, 2000.
- [33] D. Miklavčič, N. Pavšelj, and F. Hart, “Electric properties of tissues,” *Wiley Encycl. ...*, 2006.
- [34] M. Ibrani, E. Hamiti, and L. Ahma, *The age-dependence of microwave dielectric parameters of biological tissues*. Intech, 2012, pp. 139–157.
- [35] M. Schroeder, S. Anupama, and R. Nelson, “An analysis on the role of water content and state on effective permittivity using mixing formulas,” *J. Biomech. Biomedical, ...*, vol. 2, no. 1, 2008.

- [36] J. Bakker, “Dosimetry of Exposure to Electromagnetic Fields in Daily Life and Medical Applications,” Erasmus University Rotterdam, 2012.
- [37] A. Lak, “Human Health Effects from Radiofrequency and Microwave Fields,” vol. 2, no. 12, pp. 12302–12305, 2012.
- [38] H. Matikka, “The effect of metallic implants on the RF energy absorption and temperature changes in head tissues,” Eastern Finland University of Kuopio, Kuopio, 2010.
- [39] C. Gabriel, S. Gabriel, and E. Corthout, “The dielectric properties of biological tissues: I. Literature survey.,” *Phys. Med. Biol.*, vol. 41, no. 11, pp. 2231–49, Nov. 1996.
- [40] R. Bansal, *Handbook of engineering electromagnetics*. New York, NY, USA: Marcel Dekker, 2004, p. 690.
- [41] A. Peyman, S. Holden, and C. Gabriel, “Dielectric Properties of Tissues at Microwave Frequencies,” London, UK, 2005.
- [42] S. Seewattanapon and P. Akkaraekthalin, “A Broadband Complex Permittivity Probe Using Stepped Coaxial Line,” *J. Electromagn. Anal. Appl.*, vol. 03, no. 08, pp. 312–318, 2011.
- [43] Agilent Technologies, “Agilent Basics of Measuring the Dielectric Properties of Materials,” *Measurement Techniques*. Agilent Technologies Inc., p. 32, 2006.
- [44] K. Foster, “Microwave Dispersion and Absorption in Tissues: Molecular Mechanisms,” 1987.
- [45] S. R. Smith and K. R. Foster, “Dielectric properties of low-water-content tissues,” *Phys. Med. Biol.*, vol. 30, no. 9, p. 965, 1985.
- [46] D. Light, *Cell, Tissues and Skin*. Philadelphia: Chelsea House, 2004, p. 155.
- [47] National Institute of Health, “The Visible Human Project,” 2012. [Online]. Available:

- [http://www.nlm.nih.gov/research/visible/visible\\_human.html](http://www.nlm.nih.gov/research/visible/visible_human.html).  
[Accessed: 30-Sep-2012].
- [48] University Medical Center Hamburg-Eppendorf, "Voxel-Man Project." [Online]. Available: <http://www.voxel-man.com/about/>. [Accessed: 30-Sep-2012].
- [49] University of New Mexico, "Anatomy of Skin," Aug-2013. [Online]. Available: [http://hospitals.unm.edu/burn/skin\\_anatomy.shtml](http://hospitals.unm.edu/burn/skin_anatomy.shtml). [Accessed: 12-Dec-2013].
- [50] H. A. E. Benson, "Transdermal Drug Delivery: Penetration Enhancement Techniques," *Curr. Drug Deliv.*, vol. 2, no. 1, pp. 23–33, Jan. 2005.
- [51] U. Pliquet and J. Weaver, "Feasibility of an electrode-reservoir device for transdermal drug delivery by noninvasive skin electroporation," *Biomed. Eng. IEEE ...*, vol. 54, no. 3, pp. 536–538, 2007.
- [52] A. Christ and T. Samaras, "Characterization of the electromagnetic near-field absorption in layered biological tissue in the frequency range from 30 MHz to 6000 MHz," *Phys. Med. ...*, vol. 51, no. 19, p. 4951, 2006.
- [53] Italian National Research Council - Institute for Applied Physics, "Dielectric Properties of Body Tissues in the frequency range 10 Hz - 100 GHz," *INRC*, 2012. [Online]. Available: <http://niremf.ifac.cnr.it/tissprop/>. [Accessed: 05-Mar-2012].
- [54] A. Dupont and E. Sauerbrei, "Real - time sonography to estimate muscle thickness: Comparison with MRI and CT," *J. Clin. ...*, vol. 29, no. 4, pp. 230–236, 2001.
- [55] S. Muraki, K. Fukumoto, and O. Fukuda, "Prediction of the muscle strength by the muscle thickness and hardness using ultrasound muscle hardness meter.," *Springerplus*, vol. 2, no. 1, p. 457, Jan. 2013.
- [56] C. Chou, G. Chen, A. Guy, and K. Luk, "Formulas for preparing phantom muscle tissue at various radiofrequencies," *Bioelectromagnetics*, vol. 441, no. 5, pp. 435–441, 1984.

- 
- [57] S. Gabriel, R. W. R. Lau, and C. Gabriel, "The dielectric properties of biological tissues: II. Measurements in the frequency range 10 Hz to 20 GHz," *Phys. Med. Biol.*, vol. 41, p. 20, 1996.
- [58] M. Golio, *The RF and microwave handbook*, 2th. ed. Boca Raton: CRC Press LLC, 2000, p. 1356.
- [59] A. Vander Vorst, A. Rosen, and Y. Kotsuka, *RF/Microwave Interaction with Biological Tissues*, Wiley Inte. Wiley & Sons, 2006, p. 345.
- [60] P. S. Hall and Y. Hao, *Antennas and Propagation for Body-Centric Wireless Communications*, 1st ed. Norwood, MA, USA: Artech House Publisher, 2006.
- [61] W. Callister and D. Rethwisch, *Fundamentals of materials science and engineering*. Utah: Wiley & Sons, 2013, p. 952.
- [62] W. Kuang and S. Nelson, "Low-frequency dielectric properties of biological tissues: a review with some new insights," ... *ASAE-American Soc. ...*, vol. 41, no. 1, pp. 173–184, 1998.
- [63] D. Formica and S. Silvestri, "Biological effects of exposure to magnetic resonance imaging: an overview," *Biomed. Eng. Online*, vol. 12, no. 3, 2004.
- [64] C. Gabriel, "Compilation of the Dielectric Properties of Body Tissues at RF and Microwave Frequencies.," London, 1996.
- [65] W. Skierucha, A. Szyplowska, and A. Wilczek, "Aquametry in Agrophysics," *Adv. Agrophysical Res.*, 2013.
- [66] A. De Lorenzo and A. Andreoli, "Predicting body cell mass with bioimpedance by using theoretical methods: a technological review," *J. Appl. ...*, vol. 82, pp. 1542–1558, 1997.
- [67] Francis Ashley Duck, *Physical Properties of Tissue: A Comprehensive Reference Book*. York, United Kingdom: IPFM, 1990, p. 360.
- [68] D. M. Pozar and S. M. Duffy, "A Dual-Band Circularly Polarized Aperture-Coupled Stacked Microstrip Antenna for Global Positioning

- Satellite,” *IEEE Trans. an Antennas Propag.*, vol. 45, no. 11, pp. 1618–1625, 1997.
- [69] W. Scanlon, “Analysis of tissue-coupled antennas for UHF intra-body communications,” *Source*, 2003.
- [70] A. J. Johansson, “Wireless Communication with Medical Implants: Antennas and Propagation,” Lund University, Sweden, 2004.
- [71] G. Yang, *Body sensor networks*. London: Springer London, 2006, p. 507.
- [72] C. Furse, D. Christensen, and C. Durney, *Basic Introduction to Bioelectromagnetics*, 2nd ed. Utah, 2009, p. 283.
- [73] W. P. Roach, “Radio Frequency Radiation Dosimetry Handbook,” Brooks City Base, Texas, 2009.
- [74] “SPEAG - E-field probes.” [Online]. Available: <http://www.speag.com/products/easy4-mri/probes-2/>. [Accessed: 24-Sep-2014].
- [75] P. Vecchia, R. Matthes, M. Feychting, and A. Green, “ICNIRP Guidelines for limiting exposure to time varying electric, magnetic and electromagnetic fields (up to 300 GHz),” *Health Phys.*, vol. 74, no. 4, pp. 494–523, 1998.
- [76] “Effects of the Electromagnetic Susceptibility of the human body.” [Online]. Available: <http://www.narda-sts.us/>. [Accessed: 24-Feb-2013].
- [77] World Health Organization and UN World Health Organization, “Electromagnetic fields and public health : mobile phones,” WHO, 2011.
- [78] K. Fujimoto and J. James, *Mobile Antenna Systems Handbook*, 3rd ed. Artech House, 2001, p. 790.
- [79] Medical Imaging Systems Pte. Ltd., “ATOM Dosimetry Verification Phantoms,” 2014. [Online]. Available: [http://medimsgsys.com.sg/?page\\_id=401&SingleProduct=14](http://medimsgsys.com.sg/?page_id=401&SingleProduct=14). [Accessed: 20-Apr-2014].

- [80] SPEAG, "SAM v6 Facedown Head Phantom." [Online]. Available: <http://www.speag.com/support/dasy-2/flyers-posters/>. [Accessed: 12-Apr-2014].
- [81] A. Christ, W. Kainz, E. G. Hahn, K. Honegger, M. Zefferer, E. Neufeld, W. Rascher, R. Janka, W. Bautz, J. Chen, B. Kiefer, P. Schmitt, H.-P. Hollenbach, J. Shen, M. Oberle, D. Szczerba, A. Kam, J. W. Guag, and N. Kuster, "The Virtual Family--development of surface-based anatomical models of two adults and two children for dosimetric simulations.," *Phys. Med. Biol.*, vol. 55, no. 2, pp. N23–38, Jan. 2010.
- [82] M. Clemens and T. Weiland, "Discrete Electromagnetism with the Finite Integration Technique," *Prog. Electromagn. Res.*, pp. 65–87, 2001.
- [83] D. B. Davidson, *Computational Electromagnetics for RF and Microwave Engineering*. Cambridge: Cambridge University Press, 2005, p. 433.
- [84] European Telecommunication Standardizations Institute, *ETSI EN 301 489-1 V1.9.2 - Electromagnetic compatibility and Radio spectrum Matters (ERM); ElectroMagnetic Compatibility (EMC) standard for radio equipment and services; Part 1: Common technical requirements*, vol. 2. Europe, 2011, pp. 1–45.
- [85] I. I. Committee and E. Safety, *IEEE Standard for Safety Levels With Respect to Human Exposure to Radio Frequency Electromagnetic Fields, 3 kHz to 300 GHz*, vol. 2005, no. April. 1992.
- [86] Z. Chen, *Antennas for Portable Devices*. Singapore: Wiley & Sons, 2007, p. 307.
- [87] K. Ito, "Human body phantoms for evaluation of wearable and implantable antennas," *IET Semin. Dig.*, pp. 590–590, 2007.
- [88] K. Ito, "Antennas and Propagation for Body-Centric Wireless Communications." Queen Mary University, London, UK, 2009.
- [89] SATIMO, "TWIN SAM liquid head and body phantom." [Online]. Available: [http://www.mvg-world.com/products/field\\_product\\_family/sar-38/sam-phantom](http://www.mvg-world.com/products/field_product_family/sar-38/sam-phantom). [Accessed: 12-Dec-2014].

- [90] F. Klaus, *RFID Handbook*, 2nd ed. Chichester, UK: Wiley & Sons, 2003.
- [91] International Standards Organisation, *IEC/CD 60601-1-2 Medical electrical equipment -- Part 1-2: General requirements for basic safety and essential performance -- Collateral standard: Electromagnetic disturbances -- Requirements and tests*. 2007, p. 251.
- [92] V. Corp., “VeriTeQ Corp. - Dosimeter technologies and Unique Device Identification (UDI).” [Online]. Available: <http://www.veriteqcorp.com/>. [Accessed: 28-Mar-2013].
- [93] SageData Solutions Inc., “Active RFID Tags.” [Online]. Available: [http://www.sagedata.com/learning\\_centre/active-rfid-tags.html](http://www.sagedata.com/learning_centre/active-rfid-tags.html). [Accessed: 12-Dec-2014].
- [94] F. Censi, G. Calcagnini, E. Mattei, M. Triventi, and P. Bartolini, “Electromagnetic Compatibility of Portable RF Emitters in Uniquos Health Environment : Regulatory Issues,” *Heal. (San Fr.)*, pp. 456–460, 2011.
- [95] Texas Instruments Inc., “TI Low Power RF Designer ’ s Guide to LPRF TI Low-Power RF at a glance ...,” Dallas, 2010.
- [96] “Gentag Inc.,” 2013. [Online]. Available: <http://www.gentag.com/applications.html>. [Accessed: 13-Dec-2012].
- [97] E. Strömmer, J. Kaartinen, J. Pärkkä, A. Ylisaukko-Oja, and I. Korhonen, “Application of near field communication for health monitoring in daily life.,” *Conf. Proc. IEEE Eng. Med. Biol. Soc.*, vol. 1, pp. 3246–9, Jan. 2006.
- [98] M. Alabdulhafith, R. V. Sampangi, and S. Sampalli, “NFC-enabled smartphone application for drug interaction and drug allergy detection,” *2013 5th Int. Work. Near F. Commun.*, pp. 1–6, Feb. 2013.
- [99] K. Ok, V. Coskun, M. N. Aydin, and B. Ozdenizci, “Current Benefits and Future Directions of NFC Services,” *Manag. Technol.*, pp. 334–338, 2010.



- [100] "FCC: Medical Device Radiocommunications Service - Operations Rules," 2010. [Online]. Available: [http://wireless.fcc.gov/services/index.htm?job=service\\_home&id=medical\\_implant](http://wireless.fcc.gov/services/index.htm?job=service_home&id=medical_implant). [Accessed: 21-Nov-2010].
- [101] P. Bradley, "Draft Proposal for Correction to IEEE 802-15-6 MICS MedRadio band," 2010.
- [102] REITU-R SA.1346, "Sharing between the MetAids Service and MICS operating in the mobile Service in the frequency band 401-406 MHz," 1998.
- [103] C.R. Bard Inc., "M.R.I. Implantable Port - Implantable Port Devices - Bard Access Systems," 2013. [Online]. Available: <http://www.bardaccess.com/port-mri-port.php>. [Accessed: 16-Apr-2013].
- [104] A. Mahanfar, S. Bila, M. Aubourg, and S. Verdeyme, "Design considerations for the implanted antennas," *2007 IEEE/MTT-S Int. Microw. Symp.*, pp. 1353–1356, Jun. 2007.
- [105] P. Soontornpipit, "Design of implantable microstrip antenna for communication with medical implants," *Microw. Theory ...*, vol. 52, no. 8, pp. 1944–1951, Aug. 2004.
- [106] Y. Rahmat-Samii and J. Kim, *Implanted Antennas in Medical Wireless Communications*, Synthesis., vol. 1, no. 1. Los Angeles: Morgan & Claypool, 2006, p. 82.
- [107] Y. Ahmed, Y. Hao, and C. Parini, "A 31.5 GHz Patch Antenna Design for Medical Implants," *Int. J. Antennas Propag.*, vol. 2008, pp. 1–6, 2008.
- [108] J. Volakis, C. Chen, and K. Fujimoto, *Small Antennas: Miniaturization Techniques & Applications*. 2010.
- [109] A. K. Skrivervik and F. Merli, "Design strategies for implantable antennas," in *2011 Loughborough Antennas & Propagation Conference*, 2011, pp. 1–5.

- 
- [110] R. Hansen, "Fundamental limitations in antennas," *Proc. IEEE*, vol. 69, no. 2, pp. 170–182, 1981.
- [111] S. Schenke, F. Sabath, F. Sutter, M. Clemens, and S. Dickmann, "Electromagnetic interference coupling into cardiac pacemaker electrodes," *2008 Int. Symp. Electromagn. Compat. - EMC Eur.*, no. 1, pp. 1–5, Sep. 2008.
- [112] L. Geisbusch, "Berechnungsverfahren und auf Abtastung basierende Messverfahren zur Bestimmung elektrischer HF-Störfelder und der damit verbundenen," Stuttgart University, 2006.
- [113] A. R. R. League, *The ARRL antenna book*, 18th ed. Newington, USA: ARRL Inc., 1997, p. 810.
- [114] C. A. Balanis, *Modern Antenna Handbook*, 2008th ed. Tempe, Arizona: John Wiley & Sons, 2008, p. 1700.
- [115] Telonics, "Implantable VHF Systems (IMP)," *Telonics, Inc.* [Online]. Available: <http://www.telonics.com/products/vhfImplants/>. [Accessed: 12-Mar-2012].
- [116] T. Karacolak, A. Z. Hood, and E. Topsakal, "Design of a Dual-Band Implantable Antenna and Development of Skin Mimicking Gels for Continuous Glucose Monitoring," *IEEE Trans. Microw. Theory Tech.*, vol. 56, no. 4, pp. 1001–1008, 2008.
- [117] J. Kim and Y. Rahmat-Samii, "Implanted Antennas Inside a Human Body: Simulations, Designs, and Characterizations," *IEEE Trans. Microw. Theory Tech.*, vol. 52, no. 8, pp. 1934–1943, Aug. 2004.
- [118] M. Haneishi, "Stacked microstrip antenna," *US Pat. 5,124,733*, 1992.
- [119] S. Egashira and E. Nishiyama, "Stacked microstrip antenna with wide bandwidth and high gain," *IEEE Trans. Antennas Propag.*, vol. 44, no. 11, pp. 1533–1534, 1996.
- [120] C.-M. Lee, T.-C. Yo, and C.-H. Luo, "Compact broadband stacked implantable antenna for biotelemetry with medical devices," in *IEEE*

- Annual Wireless and Microwave Technology Conference WAMICON '06*, 2006, pp. 1–4.
- [121] W. C. Liu, F. M. Yeh, and M. Ghavami, “Miniaturized implantable broadband antenna for biotelemetry communication,” *Microw. Opt. Technol. Lett.*, vol. 50, no. 9, pp. 2407–2409, 2008.
- [122] A. Skrivervik and J.-F. Zürcher, “PCS antenna design: The challenge of miniaturization,” *Antennas ...*, vol. 43, no. 4, pp. 12–27, 2001.
- [123] C. M. Lee, T. C. Yo, F. J. Huang, and C. H. Luo, “Dual-resonant  $\Pi$ -shape with double L-strips PIFA for implantable biotelemetry,” *Electron. Lett.*, vol. 44, no. 14, pp. 837–838, 2008.
- [124] J. Abadía, F. Merli, J.-F. Zürcher, J. R. Mosig, and A. K. Skrivervik, “3D-Spiral Small Antenna for Biomedical Transmission operating within the MICS band,” in *EuCAP 2009*, 2009, pp. 1845–1849.
- [125] E. C. Committee, “ERC Recommendation 70-03,” *ed. Tromso, Oct.*, no. February, p. 96, 2014.
- [126] D. Valderas, C. Schmidt, and X. Chen, “Broadband implanted UHF RFID antenna,” in *Antennas and Propagation Society International Symposium (APSURSI), 2010 IEEE*, 2010, p. 4.
- [127] F. Merli, L. Bolomey, J. Zürcher, G. Corradini, E. Meurville, and A. K. Skrivervik, “Design, Realization and Measurements of a Miniature Antenna for Implantable Wireless Communication Systems,” *IEEE Trans. Antennas Propag.*, vol. 59, no. 10, pp. 3544–3555, 2011.
- [128] M. Z. Azad and M. Ali, “A Miniature Implanted Inverted-F Antenna for GPS Application,” *IEEE Trans. Antennas Propag.*, vol. 57, no. 6, pp. 1854–1858, Jun. 2009.
- [129] B. Babu, D. Selvaraj, and R. Srinivas, “Analysis of Relative Permittivity and Tan Delta Characteristics of Silicone Rubber Based Nanocomposites,” *IJSET*, vol. 1, no. 5, pp. 201–206, 2012.

- [130] F. Merli, B. Fuchs, J. R. Mosig, and A. K. Skrivervik, "The Effect of Insulating Layers on the Performance of Implanted Antennas," *IEEE Trans. Antennas Propag.*, vol. 59, no. 1, pp. 21–31, 2011.
- [131] Varta Microbattery GmbH, "Rechargeable Lithium-Ion Pouch - Data Sheet: Varta LPP 402025 CE," *Datasheet*. Ellwangen, Germany, p. 1, 2011.
- [132] P. D. Bradley, "An Ultra Low Power, High Performance Medical Implant Communication System (MICS) Transceiver for Implantable Devices," in *IEEE Biomedical Circuits and Systems Conference BioCAS*, 2006, pp. 158–161.
- [133] B. P. D. Bradley, "Implantable ultralow-power radio chip facilitates in-body communications," *rfdesign.com*, no. June, pp. 21–23, 2007.
- [134] F. Merli and A. Skrivervik, "Design and measurement considerations for implantable antennas for telemetry applications," in *Antennas and Propagation (EuCAP), ...*, 2010, pp. 12–16.
- [135] Analog Devices, "AD5933: 1 MSPS, 12-Bit Impedance Converter, Network Analyzer," *Datasheet*. p. 40, 2013.
- [136] Texas Instruments Inc., "MSP430F24x: Mixed Signal Microcontroller," no. December. Texas Instruments, p. 92, 2012.
- [137] Microsemi Corp., "ZL70321 MICS-Band RF Standard Implant Module (SIM)," *Datasheet, Rev. 3*, vol. 3, no. February. Microsemi Corp., p. 26, 2013.
- [138] Zarlink Semiconductor Inc., "ZL70102 Medical Telemetry Application Development Kit (ADK)," *Datasheet*. Zarlink Semiconductor Inc., p. 2, 2010.
- [139] "Body Tissue Simulating Liquids - SPEAG," 2012. [Online]. Available: <http://www.speag.com/products/dasy/tissue-simulating-liquids-gels-and-solids/body-tissue-simulating-liquids-2/>. [Accessed: 03-Mar-2012].
- [140] W. L. Stutzman and G. A. Thiele, *Antenna Theory and Design*, 3rd ed. Wiley & Sons, 2012, p. 843.

- [141] ETSI, *ETSI TR 102 343 V1.1.1 - Electromagnetic compatibility and Radio spectrum Matters (ERM); Ultra Low Power Active Medical Implants (ULP-AMI) operating in the 401 MHz to 402 MHz and 405 MHz to 406 MHz bands; System Reference Document*, vol. 1. 2004, pp. 1–17.
- [142] J. Garcia, A. Arriola, G. Sasiain, and D. Valderas, “Characterization of phantom size and link budget for off-body communications,” *Proc. Fourth ...*, pp. 1–5, 2010.
- [143] D. Valderas, C. Schmidt, and X. Chen, “RF Implanted Antenna Gain Characterisation: Procedures and Challenges,” in *Electronics*, 2010, no. 1.
- [144] L. H. Hemming, *Electromagnetic Anechoic Chambers: A Fundamental Design and Specification Guide*. Hoboken, NJ; USA: Wiley IEEE Press, 2002, p. 248.
- [145] C. A. Balanis, *Antenna Theory: Analysis and Design*, 3rd ed. Hoboken, NJ; USA: Wiley-Interscience, 2005, p. 1136.
- [146] ETSI, *ETSI EN 301 839-1 - V1.3.1 - Electromagnetic compatibility and Radio spectrum Matters (ERM);...; operating in the frequency range 402 MHz to 405 MHz; Part 1: Technical characteristics and test methods*, vol. 1. ETSI, 2009.
- [147] T. S. Rappaport, *Wireless Communications: Principles and Practice*, Pearson Ed. Prentice Hall, 2nd, 2006, p. 736.
- [148] S. Y. Seidel and T. S. Rappaport, “914MHz Path Loss Prediction Models for Indoor Wireless Communications in Multifloored Buildings,” *IEEE Trans. an Antennas Propag.*, vol. 40, no. 2, pp. 207–217, 1992.
- [149] R. Vaughan, J. Bach-Anderson, and J. B. Andersen, *Channels, Propagation and Antennas for Mobile Communications*. The Institution of Engineering and Technology, 2003.
- [150] T. Karacolak, R. Cooper, and E. Topsakal, “Electrical Properties of Rat Skin and Design of Implantable Antennas for Medical Wireless Telemetry,” *IEEE Trans. Antennas Propag.*, vol. 57, no. 9, pp. 2806–2812, Sep. 2009.

- 
- [151] A. Kiourti and M. Christopoulou, "Design of a novel miniaturized implantable PIFA for biomedical telemetry," *Wirel. Mob. ...*, pp. 127–134, 2011.
- [152] T. Houzen, M. Takahashi, K. Saito, and K. Ito, "Implanted Planar Inverted F-Antenna for Cardiac Pacemaker System," in *Antenna Technology: Small Antennas and Novel Metamaterials, 2008. iWAT 2008. International Workshop on*, 2008, pp. 346–349.
- [153] F. Merli, "Implantable Antennas for Biomedical Applications," EPF Lausanne, 2011.
- [154] K. Ito, H. Usui, and M. Takahashi, "Performances of an implanted cavity slot antenna embedded in the human arm," *Antennas Propagation, ...*, no. 1, pp. 4–7, 2009.
- [155] H. Mizuno, K. Ito, M. Takahashi, and K. Saito, "A helical folded dipole antenna for implantable communication devices," in *Antennas and Propagation Society International Symposium (APSURSI), 2010 IEEE*, 2010, no. 1, pp. 1–4.
- [156] R. Warty, M.-R. Tofighi, U. Kawoos, and A. Rosen, "Characterization of Implantable Antennas for Intracranial Pressure Monitoring: Reflection by and Transmission Through a Scalp Phantom," *IEEE Trans. Microw. Theory Tech.*, vol. 56, no. 10, pp. 2366–2376, Oct. 2008.

## *Appendix A*





# **Publications**

---

The publications that came out during the Ph.D. period are summarized below. Those most related with the presented research are included in the following pages.

## *JOURNALS*

Schmidt, C., Casado, F., Arriola, A., Ortego, I., Bradley, P. D., & Valderas, D. (2014). Broadband UHF Implanted 3-D Conformal Antenna Design and Characterization for In-Off Body Wireless Links. *IEEE Transactions on Antennas and Propagation*, 62(3), 1433–1444.

Paredes, J., Alonso-Arce, M., Schmidt, C., Valderas, D., Sedano, B., Legarda, J., et.al. Arana, S. (2014, February). Smart central venous port for early detection of bacterial biofilm related infections. *Biomed Microdevices*, 1, 1–10.

Alonso-Arce, M., Bustamante, P., Schmidt, C., Legarda, J., & Sedano, B. (2014). Ultra low-power smart medical sensor node based on a central venous catheter for in-body biomonitoring. *Irbm*, 35(6), 362–369.

## *CONFERENCES*

Schmidt, C., Valderas, D., Garcia, J., Ortego, I., & Chen, X. (2011). Passive UHF RFID near field link budget for implanted sensors. In Proceedings of the 5th European Conference on Antennas and Propagation (EUCAP), (pp. 3479–3483). Rom, Italy.

Valderas, D., Schmidt, C., & Chen, X. (2010). RF Implanted Antenna Gain Characterisation: Procedures and Challenges. In Electronics. APS 2010.

Valderas, D., Schmidt, C., & Chen, X. (2010). Broadband implanted UHF RFID antenna. In 2010 IEEE Antennas and Propagation Society International Symposium (APSURSI), (p. 4). Toronto, ON, Canada.

C. Schmidt, F. Casado, A. Arriola, I. Ortego, P.D. Bradley, D. Valderas

**Broadband UHF Implanted 3-D Conformal Antenna Design and  
Characterization for In-Off Body Wireless Links**

IEEE Transactions on Antennas and Propagation

## Broadband UHF Implanted 3-D Conformal Antenna Design and Characterization for In-Off Body Wireless Links

Christoph Schmidt, Félix Casado, Aitor Arriola, Iñaki Ortego, Peter D. Bradley, and Daniel Valderas

**Abstract**—A broadband UHF antenna for implanted central venous catheters (CVC) is designed, implemented, and properly characterized. According to the requirements, the CVC antenna (CVCA) is low profile, surface integrated, and 3-D conformal to a 16 mm base radius, 10 mm upper radius, and 16 mm high truncated cone. It operates at the MedRadio band (401–406 MHz) for implant communication and at the ISM 2.45 GHz band for electronics wake up. A prototype implementation including a test-bed within a phantom that is representative of a body is introduced. The antenna exhibits  $S_{11} < -10$  dB at the bands of interest with broadband behavior. The measured gain is  $-28.95$  dBi in vertical and  $-36.9$  dBi in horizontal polarization in the MedRadio band and  $-25.5$  dBi and  $-19.9$  dBi at 2.45 GHz. The gain is corroborated by the link characterization between an implanted node with electronics and an external base station. Base station antenna, electronics sensitivity, transmitted power, and path loss are independently measured and introduced in a broken down link budget for read range estimate. This is 18.95 m for the MedRadio band in free space conditions. By using the power saving mode at 2.45 GHz, it is reduced to an estimate of 1.88 m.

**Index Terms**—Antenna measurements, biomedical communication, biomedical monitoring, biomedical telemetry, broadband antennas, implantable biomedical devices, monopole antennas.

### I. INTRODUCTION

TOO often, patients have a large number of consultations and/or spend long observation periods in hospitals to monitor the evolution of a certain pathology resulting in a delay in the appropriate therapy. Communication with low-cost, low-power, multifunctional small nodes may facilitate real time diagnosis and therapy on the spot in an autonomous way. This

Manuscript received August 02, 2012; revised November 04, 2013; accepted December 08, 2013. Date of publication January 14, 2014; date of current version February 27, 2014. This work was supported in part by the Spanish Ministry of Science and Innovation through the COSIMA project (TEC2010-19545-C04-02), in part by the Basque Department of Education, Universities and Research (PI-2008-26), and in part by the Catedra Telefónica. I. Ortego received a scholarship from the Department of Education of the Basque Government.

C. Schmidt, I. Ortego, and D. Valderas are with CEIT and Tecnun (University of Navarra), Manuel de Lardizábal 15, 20018 San Sebastián, Spain (e-mail: chschmidt1@web.es; iortego@ceit.es; dvalderas@ceit.es).

A. Arriola and F. Casado are with IK4-Ikerlan, P<sup>o</sup> J. M. Arizmendiarieta, 2, 20500 Arrasate-Mondragón, Spain (e-mail: aarriola@ikerlan.es; fcasado@ikerlan.es).

P. D. Bradley is with Microsemi, San Diego, CA 92127 USA (e-mail: peter.bradley@microsemi.com).

Color versions of one or more of the figures in this paper are available online at <http://ieeexplore.ieee.org>.

Digital Object Identifier 10.1109/TAP.2013.2295816



Fig. 1. Implanted MRI compatible CVC [8].

could offer savings to the health system via a reduced number of consultations and shorter observation periods in hospitals.

One common feature that makes this technology so attractive is the ability to be operated remotely, i.e. wirelessly, from outside the body. Possible applications include prosthesis control via myoelectric sensors [1], interaction with cochlear implants [2], artificial electrical stimulation of the surviving ganglion cells [3], automated drug delivery devices [4] etc. Additionally, the opportunities to perform in-vivo, in-real-time diagnosis are multiplied by implanted wireless telemetry, in which implanted sensor data is extracted for diagnostic purposes. The state of the art in this area over the last decade has been focused on developing new ways to monitor parameters such as blood pressure [5], glucose ratio for diabetes treatment [6] and intracranial pressure [7]. In all these applications, cables could be eliminated, procedures simplified and care made cost-effective by implanted wireless links.

This paper seeks to address wireless monitoring of microbial biofilm formation in implanted Central Venous Catheters (CVC), which are commonly used in clinical practice as drug delivery interfaces. The CVC is subcutaneously implanted in the chest with an offset of several centimeters with respect to its center. In this study, an MRI (bio)compatible silicon rubber truncated cone CVC is employed [8] with a base radius and height of 16 mm and an upper radius of 10 mm. The implant has an internal 14 mm base diameter and a 10 mm high cylindrical reservoir for drug injection from the outside. It is inserted into the upper part of the truncated cone (Fig. 1).

In the European framework in which this study is conducted, there are a number of standards on Electromagnetic Compatibility and Radio spectrum matters for wireless medical devices in different frequency ranges, particularly for ultralow-power active medical implants (ULP-AMI). There are two main standards in Europe: one at the 9–315 KHz band [9] for proximity magnetic coupling and another one at the 401–406 MHz band [10], which allows for an increased data rate over longer ranges.

ULP-AMI communication using inductive loop techniques in the Low Frequency (LF) 9–315 KHz band has found wide acceptance as it allows easy penetration into human tissue. It was the first technology used for these purposes in the early 1970's, particularly for pacemakers [11], and it is quite often the current technology of choice. However, these communication links are mainly established in a clinical setting, which limits the autonomy of the system. In addition, communication with the implant requires the external loop antenna be placed precisely over it, which again undermines the possibility of an autonomous and sustainable scenario. Some other downsides include the exhibited low data rate.

On the other hand, the MedRadio band (401–406 MHz) has the potential for long-range communications (meters) between an external peripheral ULP-AMI-P and an ULP-AMI. The limit set for transmitted power by the ULP-AMI-P (25  $\mu$ W E.R.P. =  $-16$  dBm [10]) is far below the ones required to wirelessly charge battery-less, state-of-the-art electronics including a sensor [12] if body losses are added. With battery assisted ULP-AMIs allocated in this band, the communication range is boosted relative to their LF counterparts, the data rate is increased and the number of potential applications multiplies. Given this scenario, it seemed reasonable to explore 401–406 MHz as the appropriate band for the communication for an estimated data throughput of 800 Kbps with a BER  $< 1.5e - 10$  [13]. This is compatible with the CVC application scenario, where the battery lifetime will not be a bottleneck if the CVC is implanted for several months. The implant will be inserted at a subcutaneous level, where RF body losses are kept under a certain threshold.

In this manner, the first objective of this paper is to design a MedRadio antenna that is compact, conformal to the CVC truncated cone, low profile, insulated and as efficient and directive as possible. A major requirement is that the antenna must not obstruct access to the exterior for the liquid exchange. As justified in Section II-A, the antenna should also be dual band. The radiator that meets these requirements should be chosen mainly among loop antennas [14], linear conformal antennas [15], compact multilayer helical antennas [16], stent-shape antennas [17] and microstrip antennas either in one [18] or several layers [19], [20].

The second objective of this paper is to examine a MedRadio power link budget between an ULP-AMI-P and a CVC ULP-AMI by breaking down the transmitted power, electronics sensitivity and antenna characteristics to corroborate the read range operation. Power link budgets within real human bodies are difficult to assess experimentally. Although some communication links have been studied within the body [21], [22], clear standards and procedures to define the terms at which medical implant communication tests should be standardized are still being developed. Thus, there has been little discussion about implanted antenna gain characterization. When performing radiation measurements, the feeding cables tend to mask the results due to low gain when antennas are placed in phantoms. In fact, gain measurements for implantable antennas are rare, whereas extended numerical simulations have already appeared in the literature [18], [19], [23], [24]. This makes the workflow jump, in most cases, from antenna simulation

straight to transmitting implant measurements once the antenna has been integrated [16] without having feedback on proper antenna characterization.

Furthermore, other aspects, such as the minimum required human phantom size representative of a human being [25], are not usually taken into account; this means that different antennas cannot be compared for the same application when they are in different phantoms. A representative phantom size for the patient will be included in the study as a third objective.

This paper has been divided into six sections. After the introduction, the second part deals with the implanted antenna design that includes the proper phantom size definition; the third section analyzes the robustness on the matching to several parameter variations. In the fourth part, the implementation and proper characterization of the antenna are addressed. The read range in free space communication links with a ULP-AMI-P is determined by examining the components of the link budget in section fifth. The last section describes the conclusions.

## II. ANTENNA DESIGN

### A. Requirements of the Implanted Antenna

The shape of the supporting reservoir is a truncated cone with a base radius of 16 mm and a height of 16 mm. Although the top part of the truncated cone is the surface closest to the skin, this area was discarded as the antenna locus as it must be unobstructed for liquid exchange between the implant's inner reservoir and possible external pumps, syringes, etc. As a result, the antenna was determined to be 3-D, conformal to the truncated cone, and low-profile, i.e., ideally with no extra volume added to the smart implant. The antenna required broadband behavior to avoid detuning in a changing live environment. Dual band operation in the MedRadio frequency at 401–406 MHz as well as in the global ISM band of 2.4–2.5 GHz was also required. As a basic principle, data is transferred in the MedRadio band, whereas the higher frequency is used to initiate communication and wake up the smart implant in order to enter its operating mode. A biocompatible synthetic layer made up of the same material as the CVC [8] prevents physiological interaction between the surrounding tissue and the antenna.

### B. Antenna Design Process

The constraints mentioned above were taken into account when selecting a monopole-like structure as a radiating element. Its broadband impedance bandwidth [26], unlike implanted microstrip antennas [18], [19], and low-profile extension are major advantages with respect to the antenna requirements. The design needed a convenient way to mount a monopole onto the cone. The constraint of having to accommodate the radiator on the limited surface with enough length to allow the antenna to operate in the 401–406 MHz MedRadio band is set.

In order to reduce computation time, the simulation model used a body phantom that had smaller dimensions than the phantom used in the measurements. This is considered an acceptable approximation, as the impact of phantom size on the input impedance matching is mostly negligible within certain limits. The reduced cubical phantom for the simulation had a side length of 6 cm. The position of the implant in the body

SCHMIDT *et al.*: BROADBAND UHF IMPLANTED 3-D CONFORMAL ANTENNA DESIGN

1435

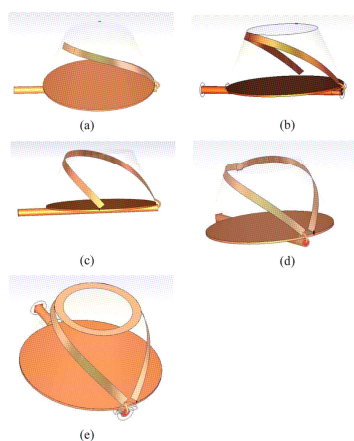


Fig. 2. Topologies used during the optimization process: (a) Short monopole. (b) Long monopole. (c) Long monopole with short circuit to ground. (d) Extended monopole with short circuit. (e) Extended monopole with short circuit and loop.

was replicated in the simulation by locating it at 9 mm from the phantom-air interface (subcutaneous position). The chosen antenna topology was designed with CST Microwave Studio electromagnetic simulation software.

Moreover, a single skin tissue phantom was considered to be accurate enough for the simulation for several reasons. Firstly, its properties are similar to general muscle tissue at 403 MHz ( $\epsilon_{r,skin} = 46.7, \epsilon_{r,muscle} = 57.1; \sigma_{skin} = 0.658, \sigma_{muscle} = 0.623$ ); secondly, it represents the volume between implant and air, through which the data transmission is studied. Simulations will show that peak SAR is more critical in this area and accurate material definition should be done accordingly. The use of a more complex three-tissue phantom (skin, fat and muscle) would not significantly alter the return loss of the antenna, and it would only increase the simulation time [16], [23], [24]. The skin mimicking liquid was elaborated according to [18] and measured with a dielectric probe 85070E by Agilent Technologies. The results were gathered and compiled in a dispersion list. Prior to simulation, the dispersion list was imported into CST Microwave Studio, which in turn calculated the missing data based on a dispersion model (2nd order Debye model).

A broadband simulation type from 0 up to 4 GHz was utilized by applying a transient solver based on the Finite Integration Method. By using the Fast Perfect Boundary Approximation (FPBA), hexahedral mesh was employed without the need to resort to the subgridding technique in most cases. The absorbing boundary condition was chosen for the computation domain around the phantom. A space in the off-body direction of  $\lambda/4$  for a precise far field computation was kept. An increased number of meshcells per wavelength of 35 was considered for

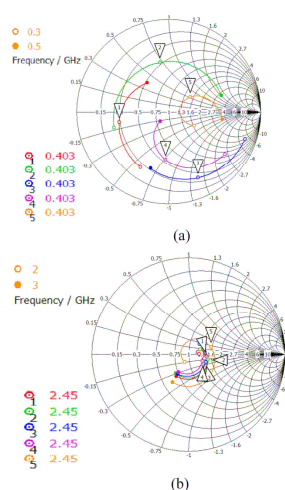


Fig. 3. Smith chart showing the complex impedance matching between (a) 0.3–0.5 GHz and (b) 2.0–3.0 GHz referring to the design steps towards the final antenna model 1) Short monopole. 2) Long monopole. 3) Long monopole with short circuit to ground. 4) Extended monopole with short circuit. 5) Extended monopole with short circuits and loop.

the upper frequency limit. The “Bend sheet” feature was employed to project the antenna over the CVC truncated cone. The feeding cable was included in the model. The design was optimized with respect to a reference impedance of  $50 \Omega$ .

The design process is illustrated through the Figs. 2 and 3, where the optimization steps in Fig. 2(a)–(e) correspond to markers 1–5 shown in Fig. 3. The simulation model includes a round ground plane that covers the bottom side of the cone. The outer conductor of the coaxial feed cable was soldered to this implant’s groundplane. The inner conductor was connected to the monopole, which, in turn, is attached to the cone shell. To describe the cone itself, the parameters of silicon rubber [8] based material were employed. Its relative permittivity was set to 3 according to [27].

The design process started with a single monopole [see Fig. 2(a)]. Marker 1 in the Smith chart in Fig. 3(a) shows its resistive properties around 403 MHz. The monopole is too short as the resonating frequencies are located above the MedRadio band. In this case, matching conditions are not optimal. By extending the monopole [see Fig. 2(b)], the frequency point of interest in Fig. 3(a), marker 2, moves clockwise towards the inductive part of the Smith chart. In order to take advantage of the cone surface, a short circuit implementation as a miniaturization technique is now applied [see Fig. 2(c)]. By adding a short circuit to this configuration, the graph is mirrored to the capacitive region of the diagram with respect to the

1436

IEEE TRANSACTIONS ON ANTENNAS AND PROPAGATION, VOL. 62, NO. 3, MARCH 2014

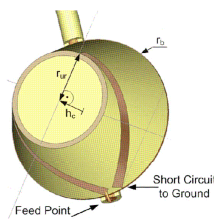


Fig. 4. Top view of the final antenna simulation model without the protection layer.

TABLE I  
FINAL GEOMETRY OF THE CVCA

Parameter	Value (mm, <sup>2</sup> )
Base radius ( $r_b$ )	16
Upper ring outside radius ( $r_u$ )	10
Cone height ( $h_c$ )	16
Copper strip length	33
Copper strip width at upper ring	1.5
Copper strip width at monopole	2
Angle between the monopole-to-ring connections	90

[Fig. 3(a), marker 3]. Even by adding a further extension of the monopole Fig. 2(d) the matching leaves room for improvement [see Fig. 3(a), marker 4]. By using a closed loop [see Fig. 2(e)], which can be seen as an additional inductance, the input impedance rotates clockwise from marker 4 to 5 and almost matches the desired  $50 \Omega$  [see Fig. 3(a), marker 5]. This loop is narrow enough to leave the top of the implant clear.

The Smith chart in Fig. 3(b) demonstrates the low influence of the abovementioned geometric changes of the antenna on the impedance matching for the 2–3 GHz range. This is due to the resistive properties of the lossy medium around the antenna. After applying further minor optimizations, the final topology was singled out, where the monopole extends over both sides of the truncated cone shell (see Fig. 4). The specific design parameters are displayed in Table I. The radiator is referred to as the CVC antenna (CVCA) hereafter.

The outside metal antenna parts have to be insulated to prevent interactions with the surrounding body tissue. As a design strategy, when the coating is made thinner, the antenna reduces its operating frequency (becoming more compact) due to the size-reduction effect introduced by the closer presence of the high permittivity media. At the same time, a large relative frequency bandwidth is achieved. This increases the robustness against implant environment variations [28], [29], including for example, variations in the proportion of body tissues over different patients or position variations of the implant itself. However, the radiation efficiency decreases due to the proximity of the same lossy media and a trade-off should be struck.

Therefore, the antenna was coated with a 0.2 mm biocompatible synthetic film made up of the same silicone rubber material

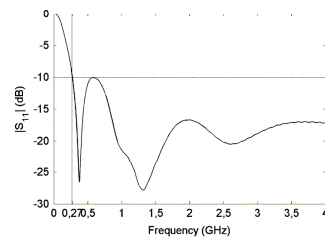


Fig. 5. Simulated  $|S_{11}|_{dB}$  versus frequency of the CVCA in a  $6 \text{ cm}^3$  skin phantom.

as the CVC. In this way, the CVCA is fully integrated. This non-conductive coating has a major impact on the electromagnetic properties, as it is placed in the near field of the antenna. Commonly used coatings for implanted planar microstrip antennas include a ceramic layer with high permittivity ( $\epsilon_r \geq 10$ ) and low loss with at least 0.6 millimeter [18]–[20]. This solution was not feasible because of the 3-D cone-like shape of the antenna topology.

Fig. 5 depicts the simulation results of the antenna's S-parameter  $|S_{11}|$  dB (reference impedance  $50 \Omega$ ) with a 0.2 mm biocompatible synthetic film isolation within the  $6 \text{ cm}^3$  cube phantom.

At the reference value of  $|S_{11}| \text{ dB} < -10 \text{ dB}$  the antenna covers the required bandwidth from 0.273 GHz to more than 4 GHz. This means that it can be operated worldwide in the MedRadio band as well as in the ISM 2.45 GHz band.

### C. Phantom Size

It is known that the amount of body tissue surrounding the implanted antenna undermines its efficiency in two ways: by affecting the losses introduced by the body, and by the variation of the reflections coming back from the body-air interface.

For the measurement setup, the antenna is placed like in a typical subcutaneous case (9 mm deep from the top part) and with an offset of 6 cm with respect to the vertical center axis of a human torso, as shown in Fig. 6.

The cross section of the torso is modeled by a polystyrene tank of  $355 \text{ mm} \times 255 \text{ mm}$  filled with skin tissue mimicking liquid composed of 56.18% Sugar, 41.49% deionized water and 2.33% NaCl salt [18]. The liquid's properties were measured by the dielectric probe, and its permittivity and its loss tangent are shown in Fig. 7 with reference to [30]. As previously mentioned, these properties are the ones that were employed in the design process (Section II-B).

A study should set the minimum phantom height that will dramatically influence the radiation properties. Since real size human-phantoms are not often practical in terms of radiation measurements and simulation time, a phantom size representative of the whole body would depend on the operation frequency and direction of interest. The latter was specified to be on the horizontal plane for the communication link.

SCHMIDT *et al.*: BROADBAND UHF IMPLANTED 3-D CONFORMAL ANTENNA DESIGN

1437

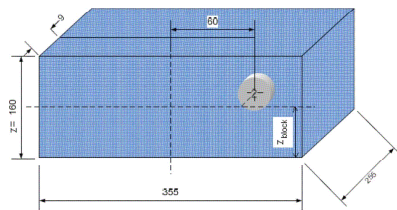


Fig. 6. Human torso-size phantom and location of the implant (dimensions in mm).

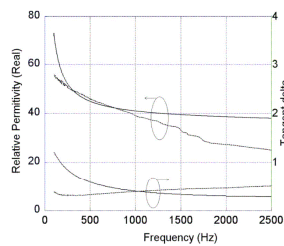


Fig. 7. Comparison of dielectric properties of dry skin and of tissue-simulating liquid (solid theory, dash experimental).

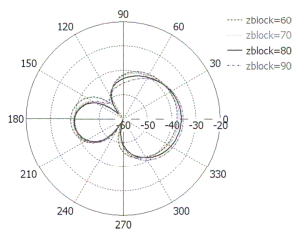


Fig. 8. Simulated antenna gain (dBi) in relation to phantom height  $z$  ( $z/2 = z_{\text{block}}$  (mm)) for 403 MHz (vertical polarization, horizontal plane).

Simulations are performed to investigate this minimum height  $z$  that the phantom should have in order to represent its impact on the gain pattern for the vertical polarization (theta-component) in the horizontal plane ( $\theta = 90^\circ$ ). Fig. 8 shows the change of the gain in relation to the phantom height  $z$  ( $z_{\text{block}}$  equals  $z/2$ ) (Fig. 6). A value of  $z = 160$  mm is estimated to be sufficient to account for body effects as the simulated gain patterns reasonably converge at 403 MHz below 109, million meshcells. For higher frequencies, the phantom will be electrically larger and, therefore, representative, as well. In this manner, the CVCA is placed at  $z_{\text{block}} = 80$  mm.

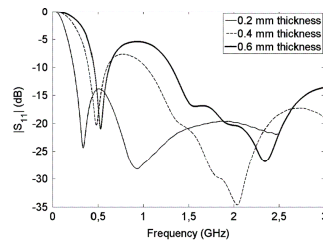


Fig. 9. Simulated  $|S_{11}|_{\text{dB}}$  versus frequency of the CVCA in representative skin phantom for different isolation layer thicknesses.

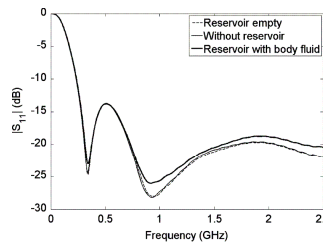


Fig. 10. Simulated  $|S_{11}|_{\text{dB}}$  versus frequency of the CVCA in representative skin phantom for different functional states.

### III. MATCHING ROBUSTNESS STUDY AGAINST PARAMETER VARIATIONS

Once the basic antenna shape and an appropriate phantom size were defined, a study of the robustness of the matching against certain functional aspects was addressed. The study was performed in the  $355 \text{ mm} \times 250 \text{ mm} \times 160 \text{ mm}$  phantom.

#### A. Biocompatible Layer Thickness

Fig. 9 shows the impact that the biocompatible layer lateral thickness has on the CVCA matching. The lowest  $|S_{11}| < -10$  dB condition recorded around the MedRadio band is given at 230 MHz, 395 MHz and 452 MHz for 0.2 mm, 0.4 mm, and 0.6 mm, respectively. It is observed that from a thickness of 0.6 mm, the matching is not accomplished in the MedRadio band. The top isolation is kept to a thickness of 1 mm and its variation does not significantly affect performance (not shown for brevity).

#### B. Functional Operation

Computed matching against reservoir status (not present, present but empty, and filled with body liquid) was studied. The body liquid [30] was selected as being representative of functional operation, and imported in CST Microwave Studio with a 2nd order Debye model fit. Fig. 10 shows that the antenna is robust against the functional variations.



1438

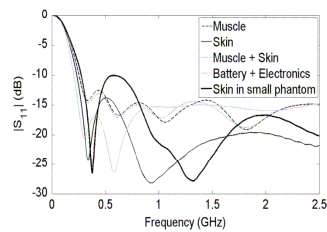


Fig. 11. Simulated  $|S_{11}|_{dB}$  versus frequency of the CVCA in representative phantom for different tissue phantoms and in the presence of battery and electronics.

### C. Tissue Variation

In order to analyze the impact of the variability of the surrounding tissue on the antenna matching, a muscle and a muscle-skin bilayer phantom were considered. In the latter case, the skin was considered to be between the top antenna part and the free space interface. Therefore, its thickness is 9 mm, which is the same as the CVCA insertion depth as described in Section II-C. The positioning of the antenna is also kept as described in that section. Muscle properties were extracted from [30] and imported by a 2nd Debye fitting into CST Microwave Studio. The selected antenna proves to have a robust  $|S_{11}| < -10$  dB condition against tissue variability (Fig. 11) from skin to other tissues (thin solid to dash and dot lines). The performance in the small phantom (Fig. 5) has been also superimposed for comparison purposes in Fig. 11. It is observed how increasing phantom size improves the matching (thick to thin dark solid).

The robustness of the antenna against dielectric environment changes can be attributed to the short-circuit at one end, which gives the CVCA a magnetic nature.

### D. Battery and Electronics Proximity

The antenna was conceived to operate in close proximity to a biofilm sensor, electronics and implanted battery Varta LPP 402025 CE [31]. The specific battery dimensions are 25.5 mm  $\times$  20.5 mm  $\times$  4.3 mm. The electronics and battery are placed alongside the truncated cone to avoid placing them beneath it and, therefore, preventing excessively long total implant height (Fig. 12). Previous cable antenna feeding running under the groundplane was substituted by a discrete port at the antenna terminals for functionality purposes.

The computed CVCA 50  $\Omega$  reflection coefficient in this situation is shown in Fig. 11 (grey solid). When the whole implant is tested with all its parts integrated—not the purpose of the present study—two matching networks in parallel should be introduced between each transceiver chip's RF ports (MICS and ISM bands) with arbitrary impedances [32], [33] and the antenna.

IEEE TRANSACTIONS ON ANTENNAS AND PROPAGATION, VOL. 62, NO. 3, MARCH 2014

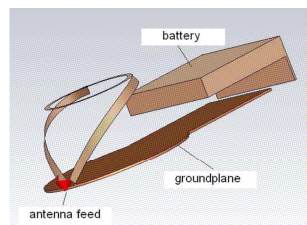


Fig. 12. CVCA along with metallic parts corresponding to the presence of the battery and electronics. The nonmetallic elements have been removed for clarity.

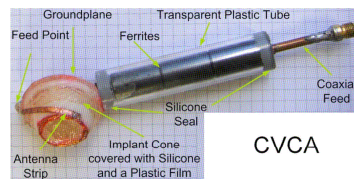


Fig. 13. Antenna prototype with detailed assembly.

## IV. ANTENNA CHARACTERIZATION

### A. Test-Bed Implementation

During the simulations a standing wave was observed in the stretch of the cable under the liquid level, as the wave undergoes a strong reflection due to the interface between very different permittivity media (air and skin mimicking liquid). To overcome this phenomenon, and inspired by [16] and [34], a test-bed is considered, where the cable was covered by a plastic tube and sealed at its edges with silicone as shown in Fig. 13. Magnetic beads were placed around the cable inside the plastic tube to minimize undesired currents along the outer conductor.

The antenna structure on the truncated cone was covered with silicone plus a thin plastic film protection layer. Due to prototyping limitations, the width is estimated to be between 0.2 mm and 0.4 mm. The core of a thin coax cable (RG 402) was soldered to the radiating element (monopole) while the outer conductor was soldered to the copper ground plane of the cone. The junction at the feed point, as well as the ground plane was sealed with glue.

Once the prototype was assembled, reflection coefficient and gain characterization was conducted.

### B. Reflection Coefficient

The CVCA measured reflection coefficient in the representative phantom at the MedRadio band (Fig. 17 and according to Fig. 6) is shown in Fig. 14. The  $|S_{11}|_{dB}$  fits very accurately between the simulations corresponding to 0.2 mm and 0.4 mm

SCHMIDT *et al.*: BROADBAND UHF IMPLANTED 3-D CONFORMAL ANTENNA DESIGN

1439

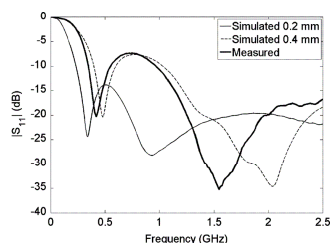


Fig. 14. Simulated with different isolation thickness and measured reflection coefficient  $|S_{11}|_{dB}$ .

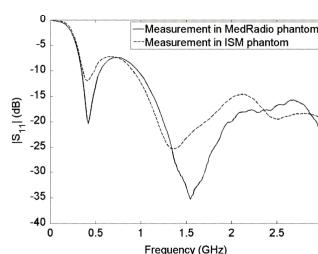


Fig. 16. Measured reflection coefficient  $|S_{11}|_{dB}$  at two experimental phantoms.

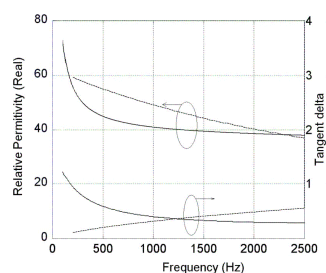


Fig. 15. Comparison of dielectric properties of dry skin and of tissue-simulating liquid at 2.45 GHz (solid theory, dash experimental).

film protection layers. It is below  $-10$  dB from 345 MHz to 555 MHz and from 965 MHz onwards.

In order to disregard possible imprecise conclusions at the higher band, a phantom of the same size is realized for ISM 2.4 GHz band with 53% sugar and 47% deionized water according to [18]. The phantom properties are measured against theoretical values [30] and shown in Fig. 15. Fig. 16 shows that the  $|S_{11}|_{dB} < -10$  dB broadband performance at this band is kept.

### C. Gain

The antenna was placed in the specific position within the phantom as described in Section II-C. The antenna's centre was placed inside the phantom at a depth of 8 cm (half the phantom's height). This body torso section was modeled by a polystyrene tank with a 350 mm  $\times$  250 mm footprint. With an absolute height of  $z = 16$  cm this resulted in 14.5 dm<sup>3</sup> of tissue-simulating liquid.

The implant within the phantom was placed in an anechoic chamber for gain measurements in the horizontal plane at both polarizations (see Fig. 17) and placed on a plastic stand 134 cm tall. Due to the general low gain of implanted antennas,

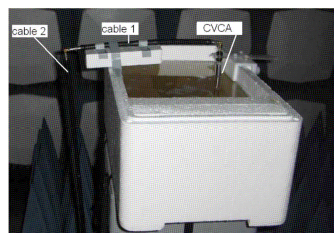


Fig. 17. Farfield measurement in the anechoic chamber showing phantom with inserted implant antenna.

reflection from cables and mounts may affect the outcome. The antenna was mounted with the closest feeding cable in an upright position. As mentioned previously, three ferrite beads were clamped to the cable near to the antenna (Fig. 13). The next feeding cable was placed horizontally to prevent interference in the vertical predominant polarization (see Fig. 17: cable 1). To suppress further radiation coming from the outer conductor, the cable running on the top (1) and the back of the phantom (2) were covered with a synthetic semi flexible ferrite tube (Wave-X® heat shrink tube absorber WH-A750). On top of that, the feeding cables behind the phantom mount were enclosed with foam absorbers (cable 2).

The gain patterns of the horizontal plane over the 360° sweep for radiation coming from the chest are shown in Figs. 18 and 19. At 403 MHz, a VULB 9163 Log Periodic antenna by Schwarzbeck was used as a measurement antenna, and a 3146 Log Periodic antenna by EMCO was used as gain reference; at 2.45 GHz, a 3160-03 horn antenna by ETS-Lindgren was used as a measurement antenna and a SAS-581 horn antenna by AH-Systems as gain reference. The measurements included both polarizations ( $\theta$  (vertical) and  $\Phi$  (horizontal) component).

The attenuation dips that are observed in the measurement results and not present in simulation (e.g., at 90° in Fig. 18, vertical polarization) are interpreted as the scattered signal coming from cable 2 when it is not longer behind the phantom and facing

1440

IEEE TRANSACTIONS ON ANTENNAS AND PROPAGATION, VOL. 62, NO. 3, MARCH 2014

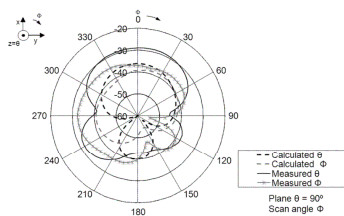


Fig. 18. Calculated versus measured results of vertical and horizontal component of gain (dBi) in the horizontal plane at 403 MHz.

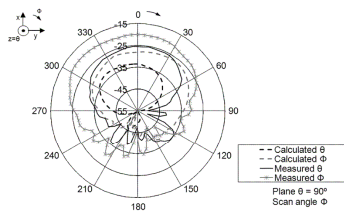


Fig. 19. Calculated versus measured results of vertical and horizontal component of gain (dBi) in the horizontal plane at 2.45 GHz.

the measurement antenna. This effect cannot be observed in simulations.

The measured gain  $G_{\text{implant\_dB}}$  in vertical polarization at  $\phi = 0^\circ$  at 403 MHz  $G_{\text{implant\_dB}_v} = -28.95$  dBi whereas in the horizontal polarization  $G_{\text{implant\_dB}_h} = -36.9$  dBi. Simulations revealed that theta component in  $\phi = 0^\circ$   $G_{\text{implant\_dB}_v} = -36.1$  dBi and the phi-component is  $G_{\text{implant\_dB}_h} = -39.4$  dBi. The computed radiation efficiency was 0.017% and the maximum gain was  $-34.36$  dBi.

For the 2.45 GHz frequency, the measured gain  $G_{\text{implant\_dB}}$  in vertical polarization at  $\phi = 0^\circ$   $G_{\text{implant\_dB}_v} = -25.5$  dBi whereas in the horizontal polarization  $G_{\text{implant\_dB}_h} = -19.9$  dBi. Simulations revealed that vertical component in  $\phi = 0^\circ$   $G_{\text{implant\_dB}_v} = -33.5$  dBi and the phi-component is  $G_{\text{implant\_dB}_h} = -28.1$  dBi. The computed radiation efficiency was 0.0599% and the maximum gain was  $-26.14$  dBi. The simulation and measurements revealed the predominant polarization changes from vertical to horizontal from 403 MHz to 2.45 GHz. Higher directivity due to the increase in electrical antenna size at this higher frequency was also observed.

It should be noted that the accuracy of the measurements in the anechoic chamber is limited by the performance of the absorbers and the gain of the measurement antennas. In this case, the chamber is covered with FS-400 hybrid absorbers by ETS-Lindgren (reflectivity  $-20$  dB and  $-18$  dB at 403 MHz and 2.45 GHz, respectively), and the gain of the measurement antennas is 6.6 dBi (Schwarzbeck VULB 9163) and 17 dBi

(ETS-Lindgren 3160-03) at 403 MHz and 2.45 GHz, respectively. With these specifications, the accuracy of the measurements in the anechoic chamber is  $\pm 1.75$  dB at 403 MHz and  $\pm 0.5$  dB at 2.45 GHz. Therefore, it cannot cause the differences between simulated and measured results, which are 8 dB in the theta-component and 8.2 dB in the phi component at 2.45 GHz. This is due to the poor suppression properties of the current running along the external conductors of the feeding cables presented by any choke ferrites in the GHz band. This issue is particularly sensitive for low gain implanted antennas. However, simulation gives insight into this phenomenon, along with an impact estimate. In this case, the cable significantly increased the radiated energy. This is inevitable and should be taken into account by a read range uncertainty factor of 0.4 corresponding to the difference between simulations and measurements.

#### D. Specific Absorption Rate (SAR)

For the evaluation of performances and safety issues, the 1-g averaged SAR distributions are simulated and compared with ANSI/IEEE limitations [35]. The analysis was performed only at the frequency in which the implanted sensor node can transmit (i.e., MICS band [32], [33]). At 403 MHz, for 0.5 W (rms) input power, the maximum SAR at skin tissue was 59.1 W/Kg, for a density of 1100 kg/m<sup>3</sup> [36]. The transmitted power to the CVCA had to be decreased to 13.54 mW (11.32 dBm) in order to fulfill the SAR limit of 1.6 W/Kg. For a computed maximum absolute gain at 403 MHz of  $-34.36$  dBi, this led to an ERP of  $-25.19$  dBm that also satisfied the  $-16$  dBm ERP allowed by MICS standard [10].

#### V. FREE SPACE LINK BUDGET

The objective of the link budget calculation is to evaluate possible application scenarios and, in particular, the maximum operating distance of the system.

##### A. Transmitted Power, Sensitivity and Base Station Characterization

For the measurements, two devices of the Application Development Kit (ADK) by Microsemi [37], both of them equipped with the ZL70102 transceiver chip [13], [32], [33], were employed: the implanted sensor node (SN), together with the CVCA, and the external base station (BS) with its corresponding helix antenna. Prior to the active link budget measurements, the implanted SN, the BS and its corresponding antenna had to be characterized.

A complete communication sequence involves three consecutive operations: implant search, wake-up and data exchange. In the present system, the communication can be initiated at 2.45 GHz as well as at 403 MHz. In this manner, a search operation wakes up the sensor node from its stand-by mode. Further transmission of sensor data is accomplished exclusively at the MedRadio frequency of 403 MHz and not at 2.45 GHz to avoid possible interference with unlicensed ISM bands in implanted sensitive high-end applications. During the search implant operation, the transmit power ( $P_{TX}$ ) of the base station was measured at both frequencies. For this purpose, a 3 dB hybrid coupler and a spectrum analyzer were used (Fig. 20).

SCHMIDT *et al.*: BROADBAND UHF IMPLANTED 3-D CONFORMAL ANTENNA DESIGN

1441

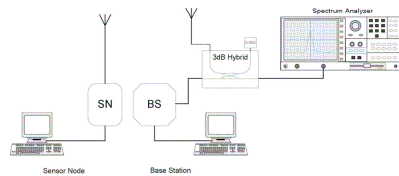


Fig. 20. Principal sketch of the measurement of the transmit power  $P_{TX}$  of the base station.

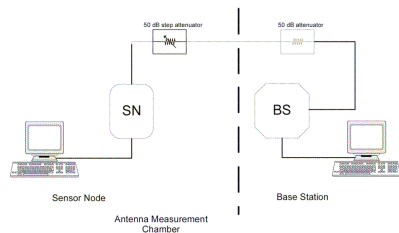


Fig. 21. Principal sketch of the measurement of the maximum sensitivity  $P_{RXp}$  of the SN.

The obtained values of the transmit power are  $P_{TX} = -12.7$  dBm at 403 MHz and  $P_{TX} = 17.5$  dBm at 2.45 GHz.

The sensitivity of the implanted sensor node was separately measured. This was accomplished by connecting the base station to the sensor node via cable and two calibrated attenuators, one of them adjustable (Fig. 21). The two attenuators together with cable losses represented the total gain and free space losses of both antennas. The attenuation was slowly lowered to the point where the system went into on-session. Then, the attenuation was again increased until the communication link was lost. The obtained values reflect the sensitivity ( $P_{RXp}$ ) of the implanted sensor node ( $P_{RXp} = -99$  dBm at 403 MHz and  $P_{RXp} = -68$  dBm at 2.45 GHz). Although it is below the typical manufacturer's expectation at 2.45 GHz, the measured sensitivity is in between the expected values.

In order to characterize the base station's low profile helical antenna (shown in Fig. 24), it was mounted directly in a vertical position on a ground plane, which resembled the PCB of the base station in shape and size. The respective measurements involved gains ( $G_{BS}$ ) and reflection coefficients ( $|S_{11}|_{BS,AB}$ ) for both frequencies (see Table II). At 403 MHz the reflection coefficient is  $|S_{11}|_{BS,AB} = -4.42$  dB and at 2.45 GHz it is  $|S_{11}|_{BS,AB} = -5.37$  dB (Fig. 22). This corresponds to mismatch losses of  $L_{BS} = 1.92$  dB at 403 MHz and  $L_{BS} = 1.48$  dB at 2.45 GHz. The predominant polarization of the helical antenna is vertical with  $-3.27$  dBi average gain at 403 MHz and  $-2.71$  dBi at 2.45 GHz in this horizontal plane. This is the reason why vertical polarization is considered in the link budget. The radiation pattern is omni-directional in this plane and it is not shown for brevity.

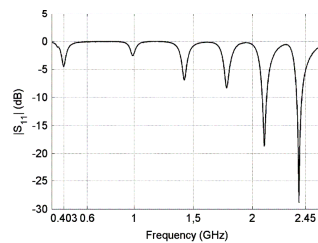


Fig. 22. Measured reflection coefficient of the base station helical antenna ( $S_{11BS}$ ).

TABLE II  
LINK BUDGET CALCULATION ACCORDING TO THE  
MEASURED RESULTS FOR LINE OF SIGHT

		Frequency (MHz)	
		403.35	2450
Transmission (Base Station)	Transmit Power, $P_{TX}$ (dBm)	-12.7	17.5
	Gain, $G_{BS}$ (dBi)	-3.27	-2.71
	Mismatch Loss, $L_{BS}$ (dB)	1.92	1.48
	Free-space Loss, $L_{FS}$ (dB) [at distance $d_{set}=1.43$ m]	27.7	43.3
	Receiving (Implant)	Gain, $G_{AUT}$ (dBi)	-28.95
	Mismatch Loss, $L_{AUT}$ (dB)	0.15	0.09
	Coaxial Cable Loss, $L_{cable}$ (dB)	2.4	8.2
	Attenuation, $L_A$ (dB)	20	2

### B. Wireless Test-Bed Setup

After completing the preceding characterizations, the active wireless link budget measurements were carried out. At one end the ADK sensor node was connected to the CVCA in the phantom by keeping the same cabling set up (Figs. 17 and 24). In the wireless measurements, only one variable attenuator was inserted between the sensor node and the CVCA. The setup was completed at the other end by the external ADK base station with its corresponding helix antenna. The base station and sensor node were controlled by a computer via USB connection (Fig. 23). This allowed the wireless link to be monitored in addition to initiating the communication process. Both antennas were positioned 1.34 m high. The whole setup was arranged in an anechoic chamber (Fig. 24).

The distance between the two antennas ( $d_{set}$ ) was fixed to  $d_{set} = 1.43$  m in free space. This distance was determined by approaching the base station manually to the point where the system went into on-session at the wake-up frequency of 2.45 GHz (downlink). The losses in free space ( $L_{FS}$ ) are calculated according to the following (1), derived from the term  $(\lambda/4\pi r)^2$  after units arrangements and dB application, for both frequencies

$$L_{FS} = 20 \log_{10}(d_{set}) + 20 \log_{10}(f) - 27.55 \quad (1)$$

1442

IEEE TRANSACTIONS ON ANTENNAS AND PROPAGATION, VOL. 62, NO. 3, MARCH 2014

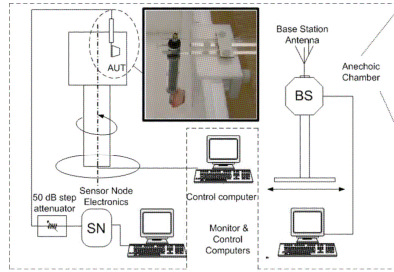


Fig. 23. Principal sketch of the measurement for maximum transmission range and detail of antenna orientation without phantom liquid.

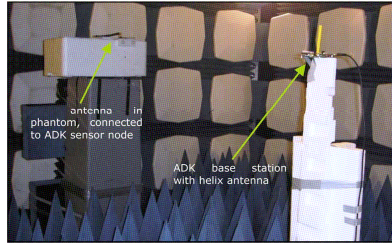


Fig. 24. Measurement setup in anechoic chamber for link budget calculation in free space.

where

- $f$  [MHz] is center frequency of the frequency band
- $d_{set}$  [m] distance between the two antennas, set to 1.43 m
- $L_{FS}$  [dB] free-space loss

For  $f = 403$  MHz free space loss resulted in  $L_{FS} = 27.7$  dB and for  $f = 2450$  MHz  $L_{FS} = 43.3$  dB at  $d_{set} = 1.43$  m.

The transmission of sensor data (uplink) is accomplished in the MedRadio band at 403 MHz. In order to avoid further inaccuracies in positioning, the 1.43 m separation was kept while increasing the attenuator value to emulate communication over distances longer than the chamber length. Regarding possible near-field effects, it should be noted that 1.43 m covers approximately two wavelengths at 403 MHz (free-space wavelength at 403 MHz = 0.74 m). The impact of the near field in this situation can be estimated by calculating the ratio between the near-field and far-field factors of a dipole antenna [38]; this calculation indicates an inductive near-field 22 dB below the radiated field, which implies an uncertainty of  $\pm 0.65$  dB in the measurements. This accuracy was considered sufficient for the proposed experiment.

The communication link was lost at the point where attenuation value ( $L_A$ ) reached 20 dB at the input of the sensor

TABLE III  
RESULTING VALUES OF SENSITIVITY OF THE ELECTRONICS

		Frequency (MHz)	
		403.35	2450
in free space	Sensitivity, $P_{RX}$ (dBm)	-97.1	-65.8
cable connection	Sensitivity, $P_{RXsp}$ (dBm), premeasured	-99	-68

node. Table II gives a comprehensive summary of the measured results, including losses introduced by cables in the setup of Fig. 23:

Equation (2) [39] shows the link budget at both frequencies for the described setup

$$P_{RX} = P_{TX} - L_{BS} + G_{BS} - L_{FS} + G_{AUT} - L_{AUT} - L_{cable} - L_A \quad (2)$$

where

- $P_{RX}$  [dBm] is the receiver sensitivity of the sensor node
- $P_{TX}$  [dBm] the transmit power of the base station
- $L_{BS}$  [dB] the mismatch loss of the helix antenna
- $G_{BS}$  [dBi] the gain of the base station antenna
- $L_{FS}$  [dB] the free space loss at the given frequency  $f$ [MHz] and distance  $d_{set}$ [m] (see (1))
- $G_{AUT}$  [dBi] gain of the CVCA under test
- $L_{AUT}$  [dB] mismatch loss of the CVCA under test
- $L_{cable}$  [dB] losses of the coaxial cable
- $L_A$  [dB] value of the attenuator losses

By applying (2) and the data provided in Table II a new value of sensitivity of the electronics is achieved, now in the wireless setup, for comparison with the conducted wired measurement in Section V-A. The results are compared in Table III. There is a good agreement between the sensitivity values in the conducted (wired) and wireless measurements.

### C. Range Estimate Calculation

In this manner, (3) describes the maximum distance  $d_{max}$  that can be reached in an ideal free-space scenario, where feeding cables and the attenuator are not included

$$20 \log_{10}(d_{max}) = L_{cable} + L_A + 20 \log_{10}(d_{set}). \quad (3)$$

The losses in the cable  $L_{cable}$  and attenuation  $L_A$  were different at the different frequencies (see Table II). They effectively represent the respective free space loss for a specific additional distance.

Therefore, in an ideal environment, such as an anechoic chamber without cables and attenuators, the system attains in free space a maximum operating distance of  $d_{max\_INI} = 4.72$  m for communication initiation at 2.45 GHz and  $d_{max\_DATA} = 18.95$  m for data exchange in the MedRadio band. The value of  $d_{max\_INI}$  is an overestimate due to the



radiating effect of the feeding cable. By applying the uncertainty factor of 0.4 for the 2.45 GHz frequency defined in Section IV-C, the best estimate for  $d_{\text{IMAX\_INT}}$  is 1.88 m.

#### VI. CONCLUSION

A low profile, broadband UHF antenna has been integrated on the surface of a Central Venous Catheter (CVC) implant with a truncated cone shape (base radius and height of 16 mm and upper radius of 10 mm) for wireless interaction with an external base station. The 3-D antenna exhibits compact and broadband features due to the application of short circuit and inductive loading techniques. It operates in the MedRadio band (401–406 MHz) for communication and the ISM 2.45 GHz band for electronic wake up. After a characterization that included proper phantom dimensioning, the antenna gain in vertical polarization is  $-28.95$  dBi and  $-25.5$  dBi at the respective frequencies. An uncertainty provided by the combination of simulation and measurements is estimated for the upper frequency, in which test-bed limitation is discussed. After thorough characterization of the base station antenna, path loss, transmitted power and sensitivity of the electronics involved in the link, a communication distance of 18.95 m is estimated for communication and 1.88 m for wake up operation in free space. This analysis sets an estimate of the limits and potentials for implanted medical application range within current regulation framework.

#### ACKNOWLEDGMENT

The authors would like to thank J. L. Moreno of R.C. Microelectrónica, S.A., and ARC Technologies, Inc., for providing samples of the Wave-X® absorber WH-A750c, as well as B. Sedano and M. Alonso for configuring the ADK.

#### REFERENCES

- [1] R. F. ff Weir, P. R. Troyk, G. De Michele, and T. Kuken, "Implantable myoelectric sensors (IMES) for upper-limb prostheses control—Preliminary work," in *Proc. 25th Annu. Int. Conf. IEEE EMBS*, Cancun, Mexico, Sep. 17–21, 2003.
- [2] J. A. Moore, "An introduction to cochlear implant technology, activation, and programming," 2002.
- [3] J. G. Hollyfield, R. E. Anderson, and M. M. LaVail, "Retinal degenerative diseases and experimental therapy," in *Electrical Stimulation of the Human Retina*. New York, NY, USA: Springer, 1999.
- [4] D. A. LaVan, T. McGuire, and R. Langer, "Small-scale systems for in vivo drug delivery," *Nat. Biotechnol.*, vol. 21, no. 10, pp. 1184–1191, Oct. 2003.
- [5] P. Cong, D. J. Young, B. Hoi1, and W. H. Ko, "Novel long-term implantable blood pressure monitoring system with reduced baseline drift," in *Proc. 28th IEEE EMBS Annu. Int. Conf.*, New York, NY, USA, Aug. 30–Sept. 3 2006.
- [6] Y. Zhao, S. Li, A. Davidson, B. Yang, Q. Wang, and Q. Lin, "A MEMS viscometric sensor for continuous glucose monitoring," *J. Micromech. Microeng.*, vol. 17, pp. 2528–2537, 2007.
- [7] M. N. Erison, T. E. McKnight, S. F. Smith, and J. O. Hylton, "Implantable Device for In-Vivo Intracranial and Cerebrospinal Fluid Pressure Monitoring," United States Patent and Trademark Office granted patent, 2003, US6533733.
- [8] [Online]. Available: <http://www.bardaccess.com/port-mri-port.php?section=FeaturesAccessed>, Apr. 16, 2013
- [9] ETSI EN 302 195-1.
- [10] ETSI TR 102 343, EN 301 839.
- [11] Magjarevic, Ratko, Ferek-Petric, Bozidar. *Implantable Cardiac Pacemakers-50 Years from the First Implantation*, 2010.
- [12] J. Yin, J. Yi, M. K. Law, Y. Ling, M. C. Lee, K. P. Ng, B. Gao, H. C. Luong, A. Bermak, U. Chan, W.-H. Ki, C.-Y. Tsui, and M. Yuen, "A system-on-chip EPC gen-2 passive UHF RFID tag with embedded temperature sensor," *IEEE J. Solid-State Circuits*, vol. 45, no. 11, pp. 2404–2419, Nov. 2010.
- [13] Zarlinc Semiconductors, ZL70102 Datasheet [Online]. Available: <http://www.microsemi.com/ultra-low-power-wireless/implantable-medical-transceivers/zl70102#docs-amp-specs> Accessed, Apr. 22, 2013
- [14] F. Po, E. De Foucauld, and J. David, "An Efficient Adaptive Antenna-Impedance Tuning Unit Designed for Wireless Pacemaker Telemetry [Online]. Available: <http://www.intechopen.com/books/modern-telemetry/an-efficient-adaptive-antenna-impedance-tuning-unit-designed-for-wireless-pacemaker-telemetry>, p. 24, 2010. Accessed, Apr. 22, 2013
- [15] A. J. Johansson, "Wireless communication with medical implants: Antennas and propagation," in *Competence Centre for Circuit Design*. Lund, Sweden: Lund Univ., 2004.
- [16] F. Merit, L. Bolomey, J.-F. Zürcher, G. Corradini, E. Meurville, and A. K. Skrivervik, "Design, realization and measurements of a miniature antenna for implantable wireless communication systems," *IEEE Trans. Antennas Propag.*, vol. 59, no. 10, pp. 3544–3555, Oct. 2011.
- [17] C. Occhiuzzi, G. Contri, and G. Marrocco, "Design of implanted RFID tags for passive sensing of human body: The STENTag," *IEEE Trans. Antennas Propag.*, vol. 60, no. 6, pp. 3146–3154, Jun. 2012.
- [18] T. Karacolak, A. Z. Hodi, and E. Topsakal, "Design of a dual-band implantable antenna and development of skin mimicking gels for continuous glucose monitoring," *IEEE Trans. Microw. Theory Tech.*, vol. 56, no. 4, pp. 1001–1008, Apr. 2008.
- [19] W. C. Liu, F. M. Yeh, and M. Ghavami, "Miniaturized implantable broadband antenna for biotelemetry communication," *Microw. Opt. Technol. Lett.*, vol. 50, no. 9, pp. 2407–2409, Sep. 2008.
- [20] C.-M. Lee, T.-C. Yo, and C.-H. Luo, "Compact broadband stacked implantable antenna for biotelemetry with medical devices," in *Proc. IEEE Annual Wireless and Microwave Technology Conf.*, Dec. 2006, pp. 1–4.
- [21] A. Aloaima and Y. Hao, "Modelling and characterisation of biotelemetry radio channel from ingested implants considering organ contents," *IEEE Trans. Antennas Propag.*, vol. 57, no. 4, pp. 999–1005, Apr. 2009, Special Issue on Body-Centric Wireless Communications.
- [22] K. Sayrahan-Pour, W.-B. Yang, J. Hagedorn, J. Terrill, and K. Y. Yazdandoost, "A statistical path loss model for medical implant communication channels," in *Proc. IEEE 20th Int. Symp. Personal, Indoor and Mobile Radio Communications*, Sep. 13–16, 2009, pp. 2995–2999.
- [23] J. Kim and Y. Rahmat-Samii, "Implanted antennas inside a human body: Simulations, designs, and characterizations," *IEEE Trans. Microw. Theory Tech.*, vol. 52, no. 8, pp. 1934–1943, Aug. 2004.
- [24] M. Z. Azad and M. Ali, "A miniature implanted inverted-F antenna for GPS application," *IEEE Trans. Antennas Propag.*, vol. 57, no. 6, pp. 1854–1858, Jun. 2009.
- [25] J. Garcia, A. Arriola, G. Sasiain, D. Valderas, J. I. Sancho, and X. Chen, "Characterization of phantom size and link budget for off-body communications," presented at the EuCAP, Barcelona, Spain, Apr. 12–16, 2010.
- [26] D. Valderas, C. Schmidt, and X. Chen, "Broadband implanted UHF RFID antenna," in *Proc. IEEE APS Int. Symp. Antennas and Propagation and CNC/USNC/URSI Radio Science Meet.*, Toronto, ON, Canada, Jul. 11–17, 2009.
- [27] B. G. Babu, D. E. Selvaraj, R. Srinivas, B. G. Prakash, R. V. Prakash, E. Muthupandi, and R. Balakumar, "Analysis of relative permittivity and tan delta characteristics of silicone rubber based nano-composites," *Int. J. Sci. Eng. Technol.*, vol. 1, no. 5, pp. 201–206.
- [28] P. S. Hall and Y. Hao, *Antennas and Propagation for Body-Centric Wireless Communications*. Norwood, MA, USA: Artech House, 2006, ch. 9.
- [29] F. Merit, B. Fuchs, J. R. Mosig, and A. K. Skrivervik, "The effect of insulating layers on the performance of implanted antennas," *IEEE Trans. Antennas Propag.*, vol. 59, no. 1, pp. 21–31, Jan. 2011.
- [30] Dielectric Properties of Body tissues in the frequency range 10 Hz–100 GHz. Institute For Applied Physics, Florence/Italy, 2010. [Online]. Available: [Online]. Available: <http://niremf.ifac.cnr.it/tissprop/>, Oct. 03, 2009
- [31] [Online]. Available: [http://www.varta-microbattery.com/applications/mb\\_data/documents/data\\_sheets/DS56416.pdf](http://www.varta-microbattery.com/applications/mb_data/documents/data_sheets/DS56416.pdf), Apr. 07, 2013

1444

IEEE TRANSACTIONS ON ANTENNAS AND PROPAGATION, VOL. 62, NO. 3, MARCH 2014

- [32] P. D. Bradley, "An ultra low power, high performance medical implant communication system (MICS) transceiver for implantable devices," in *Proc. IEEE Biomedical Circuits and Systems Conference BioCAS*, Nov. 2006, pp. 158–161.
- [33] P. D. Bradley, "Implantable ultralow-power radio chip facilitates in-body communications," *RF Design (Online Magazine)* 2007 [Online]. Available: [http://rfdesign.com/next\\_generation\\_wireless/short\\_range\\_wireless/706RDFDF1.pdf](http://rfdesign.com/next_generation_wireless/short_range_wireless/706RDFDF1.pdf)
- [34] F. Merli and A. K. Skrivervik, "Design and measurement considerations for implantable antennas for telemetry applications," presented at the 4th *Eur. Conf. Antennas and Propagation*, Barcelona, Spain, Apr. 12–16, 2010.
- [35] *IEEE Recommended Practice for Measurements and Computations of Radio Frequency Electromagnetic Fields With Respect to Human Exposure to Such Fields, 100 kHz–300 GHz*, IEEE Std. C95.3™-2002.
- [36] A. Christ, A. Kligenböck, T. Samaras, C. Goiceanu, and N. Kuster, "The dependence of electromagnetic far-field absorption on body tissue composition in the frequency range from 300 MHz to 6 GHz," *IEEE Trans. Microw. Theory Tech.*, vol. 54, no. 5, pp. 2188–2195, May 2006.
- [37] ZL70102 Application Development Kit (ADK), accessed, [Online]. Available: [http://www.zarlink.com/zarlink/hs/82\\_ZLE70102.htm](http://www.zarlink.com/zarlink/hs/82_ZLE70102.htm), Apr. 21, 2013.
- [38] L. Hemming, *Electromagnetic Anechoic Chambers: A Fundamental Design and Specification Guide*. Hoboken, NJ, USA: Wiley, 2002.
- [39] C. A. Balanis, *Antenna Theory: Analysis and Design*, 3rd ed. Hoboken, NJ, USA: Wiley, 2005.



**Aitor Arriola** received the M.S. degree in telecommunications engineering from the University of the Basque Country (UPV/EHU), Bilbao, Spain, in 1999, and the Ph.D. degree from the University of Navarra, San Sebastián, Spain, in 2011.

Since 1999, he has been with the Communications Department of IK4-IKERLAN Technological Research Center, Arrasate-Mondragón, Spain. From 2006 to 2008, he was with the RF Component Design and Modeling (RFCDM) Group of Imec, Leuven, Belgium, as visiting researcher. He has participated in several national and international research projects involving the design, measurement, and integration of planar antennas into products. His research interests include reconfigurable antennas and antennas for body area networks.



**Iñaki Ortego** received the degree in telecommunications engineering from Tecnun, University of Navarra, Spain, in 2010. He is currently pursuing the Ph.D. degree at Tecnun-CEIT (Investigaciones Técnicas de Gipuzkoa), San Sebastián, Spain, on a fellowship from the Basque Government. His Ph.D. is focused on the design, simulation, fabrication, and measurement of different implanted radiating structures.

He is with the Electronics and Communication Department, Antennas for Communication and Monitoring Systems Group, Tecnun-CEIT. He is a specialist in Inkjet Printing Technology.



**Christoph Schmidt** received the degree in electrical and electronics engineering (specialized in high frequency technology) from the University of Erlangen-Nuremberg (FAU), Germany, in 2001. He is currently pursuing the Ph.D. degree in the Electronics and Communication Department, CEIT and Tecnun (University of Navarra), San Sebastián, Spain.

He was a research and development engineer within the Department for High Frequency Electronics, Fraunhofer Institute for Integrated Circuits (IIS), Erlangen, Germany. In 2007, he joined CEIT in Donostia–San Sebastián, Spain, as a junior researcher. He has been working on projects for navigation applications like Galileo and digital satellite radio broadcasting receivers. His current research interests include ultralow power medical transceivers (smart implants), high-frequency electronics and antennas, especially compact antennas for wireless body applications, and antenna interactions with the human body.

Mr. Schmidt has published and presented many papers in a number of established international conferences.



**Peter D. Bradley** received the B.E. degree in electrical engineering with first class honors in 1987 and the M.E. degree in biomedical engineering in 1996, both from the University of New South Wales, Sydney, Australia. He received the Ph.D. degree in medical physics from the University of Wollongong, Australia, in 2000.

He has over 20 years experience in medical device design and analysis, including implantable devices such as implantable cardiac defibrillators and pacemakers. Early research work included the first extensive analysis of the effects of cosmic radiation on implantable devices. Since 2000, he has worked with Zarlink/Microsemi, San Diego, CA, USA, developing integrated circuits for medical applications and particularly ultralow power medical communications. He is currently a medical device systems consultant. He was the system architect for several of Zarlink-Microsemi's medical transceivers which dominate the implanted medical transceiver market, including the EETimes product of the year in 2008. His interest areas include low-power radio transceivers, integrated circuits for biomedical instrumentation and system analysis, semiconductor radiation detectors, microdosimetry, and the effects of ionizing radiation on implantable medical devices. He has published over 20 papers and holds six patents on low-power transceiver techniques.



**Félix Casado** received the B.Sc. degree in telecommunications engineering (electronic systems specialty) from the Universitat Autònoma de Barcelona (UAB), Spain, in 2008; the M.Sc. degree in telecommunications engineering from Universitat Autònoma de Barcelona (UAB), Spain, in 2010; and the M.Sc. degree in applied engineering from the University of Navarra, Spain, in 2012. He is currently pursuing the Ph.D. degree in antennas and microwaves at IK4-IKERLAN Technological Research Center, Arrasate-Mondragón, Spain, together with the University of Navarra.

His research interests include reconfigurable antennas and matching networks for reliable communication links.



**Daniel Valderas** received the M.Sc. and the Ph.D. degrees from Tecnun, University of Navarra, Spain, in 1998 and 2006, respectively.

He is a researcher with the Electronics and Communications Department of the Centro de Estudios e Investigaciones Técnicas de Gipuzkoa (CEIT) and a lecturer with Tecnun, University of Navarra, Spain. He was an Academic Visitor at Florida Atlantic University, Boca Raton, FL, in 2003, at Imperial College, London, U.K., in 2007, and at Queen Mary, University of London, London, U.K., in 2008. He has participated in many different research projects on antenna and electromagnetic fields. His research interests focus on UWB and broadband antennas, RFID antennas, and antennas for body applications.

J. Paredes, M. Alonso-Arce, C. Schmidt, D. Valderas, B. Sedano, J. Legarda, F. Arizti, E. Gómez, A. Aguinaga, J. L. Del Pozo, S. Arana

**Smart central venous port for early detection of bacterial biofilm related infections**

Biomed Microdevices



## Smart central venous port for early detection of bacterial biofilm related infections.

J. Paredes<sup>1,2\*</sup>, M. Alonso-Arce<sup>2</sup>, C. Schmidt<sup>1</sup>, D. Valderas<sup>1</sup>, B. Sedano<sup>1</sup>, J. Legarda<sup>1</sup>, F. Arizti<sup>1</sup>, E. Gómez<sup>1</sup>, A. Aguinaga<sup>3</sup>, J.L. Del Pozo<sup>3</sup>, S. Arana<sup>1,2</sup>

<sup>1</sup>CEIT and Tecnun (University of Navarra), Paseo de Manuel Lardizábal, nº 15, 20018 Donostia-San Sebastián, SPAIN.

<sup>2</sup>CEIT, Paseo de Manuel Lardizábal, nº 15, 20018 Donostia-San Sebastián, SPAIN.

microGUNE

<sup>3</sup>Microbiology department of the Clínica University of Navarra, Avenida Pío XII, 36, 31008 Pamplona, SPAIN.

\*Corresponding author: e-mail jparedes@ceit.es, Phone: +34 943 212 800, Fax: +34 943 213 076

### Abstract

Central venous catheters (CVC) are commonly used in clinical practice to improve the quality of life of patients. Unfortunately there is an intrinsic risk of acquiring an infection related to microbial biofilm formation inside the catheter lumen. It has been estimated that the rate of biofilm-associated infection was over the 80% of all bacterial human infections. Besides, 50% of all nosocomial infections are associated with indwelling devices. In this work we present a new design of a venous access port that allows the monitoring of the inner reservoir surface by mean of an impedimetric biosensor. An ad-hoc specific electronics has been design to manage the sensor and to allow the communication with the external receiver. A recorded historic data, stored in the device, was used as the reference value for the detection of bacterial biofilm. The RF communication system would send an alarm signal to an external receiver when a microbial colonization of the port occurs. In this work the successfully *in vitro* analysis of the biosensor, the electronics and the antenna of the new indwelling device prototype are shown. The experimental conditions were selected in each case as the closest to the clinical working conditions for the smart central venous catheter (SCVC) testing. The results of this work allow a new generation of this kind of devices that could potentially provide more efficient treatments for the catheter related infections.

**Keywords:** intravascular port, intelligent implant, catheter sepsis, *in vivo* diagnostics, bacterial biofilms.

### 1 Introduction

Microbial biofilms are responsible of a wide range of infectious diseases associated with indwelling medical devices. Intravenous catheters, prosthetic heart valves, prosthetic joints, pacemakers, etc are widely used in the healthcare attention saving millions of lives, but assuming an intrinsic risk of infection (Hall-Stoodley et al., 2004). Medical implants are the propitious environment for the development of bacterial biofilms, which will lead to an infection. The importance of biofilm-associated infection was estimated to represent over 80% of human microbial infections (Davies, 2003). Approximately, 50% of nosocomial infections per year in the US are associated with indwelling devices (Harris and Richards, 2006).

These bacterial communities are composed of microbes that irreversibly attach to a biological or to an inert surface, and generate an extracellular matrix based on polysaccharide that also mediates in the adhesion process (Donlan and Costerton, 2002). The unique physiology, the complexity and heterogeneity of this micro-bio-system provide microorganism antimicrobial resistance at levels extremely higher than planktonic or free-floating microorganisms (Davies, 2003, Stewart and William Costerton, 2001, Costerton et al., 1999).

Gram positive cocci (*Staphylococcus aureus*, *Staphylococcus epidermidis*, *Enterococcus faecalis*), *Streptococcus vidrians*, *Klebsiella pneumonia*, *Pseudomona aeruginosa*, are some of the most common bacteria isolate from infected implanted devices. These microorganisms arise from the environment, the skin of the patient, the healthcare personnel or other environmental sources (Fux et al., 2005, Donlan, 2001). Within the listed pathogens, *Staphylococcus epidermidis* is presented as the predominant microorganism related to device-associated infections (Wang et al., 2011). Many of the current persistent and chronic bacterial infections have their origin in the antimicrobial resistant characteristic of biofilms (Costerton et al., 1999).

Routine monitoring of patients is usually inefficient for detecting biofilm-related infectious pathologies (Fux et al., 2005). The detection and diagnosis before the treatment of the infectious processes caused by microbial biofilms are

not really solved. The period between the infection and the detection, the process to analyze which bacteria is growing, often results too time-consuming.

In this context the infectious process not detected on time may end up in several medical complications for which, in many cases, the only way to ensure a good outcome is removing the infected device (Stewart, 2003; Donlan, 2001). These events have a high cost on top of the high importance of the patient health risk under such medical complications. Every achievement made on improving the treatment would be a success (Rupp and Archer, 1994; Vuong and Otto, 2002; Harris and Richards, 2006). For this reason it is necessary to develop new methods to improve biofilm early detection.

Nowadays there is a wide variety of novel techniques that allow in-depth *in vitro* study of the most important aspects of the formation of bacterial biofilms, from gene expression to microscopic characterization. However, there still remains a great demand in the field of *in vivo* detection specially for indwelling devices. To achieve this purpose it would necessary to develop new intravascular catheters that provides a continuous monitoring of the content of the reservoir of the CVC and to send an alarm signal in case of bacterial colonization. The new device should have an electronic module to provide the measurement and to process the communications protocol to the external reader.

## 2 Smart central venous catheter (SCVC) prototype

The new SCVC (see Fig. 1.a) is composed of three complementary modules that provide with full functionality to this device (European Patent 11380064.3): Biosensor, electronics and antenna. The integration of these modules allows the device to detect the infection at the early stages and to transmit an alarm signal outside the body. An interdigitated microelectrode biosensor is used to drive sequentially impedance measurements. This module provides the electrical characteristics monitoring of the reservoir content of the portal. Specific electronics control the biosensor operation and sets a wireless link through the antenna and the body to an external reader. The presence of the initial stage biofilm development is detected onto the biosensors surface.

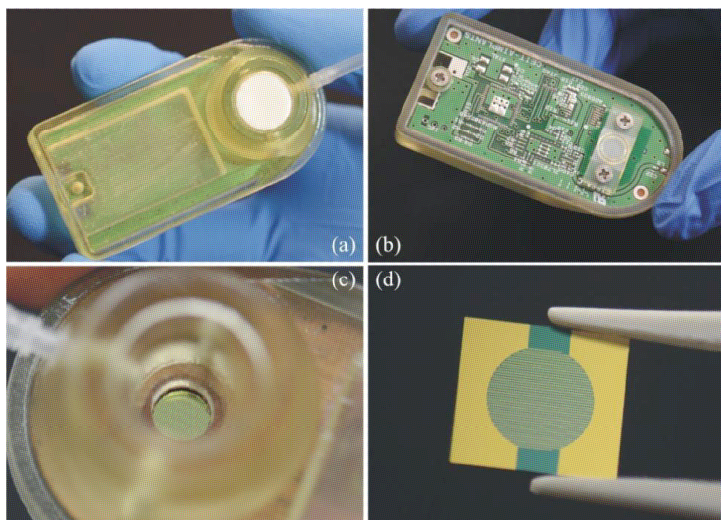


*Fig. 1 Photographs of the smart central venous catheter prototype. (a) top side of the prototype; (b) Detail of the electronics inside the implantable device; (c) Detail of the sensor inside the reservoir of the catheter; (d) Photograph of an interdigitated microelectrode biosensor.*

In this section the design of each one of the modules that compose the device is presented highlighting the most relevant characteristics.

### **2.1 Sensing module design**

Interdigitated microelectrode biosensor was proved to be a suitable solution for microbial biofilm detection and monitoring (Varshney and Li, 2008, Yang et al., 2004). Previous works (Paredes et al, 2012) presented a surface free biosensor used for impedance monitoring according to the long-term application of this. The design and fabrication of this kind of biosensors are traditionally developed by means of silicon technologies that are detailed below.

The impedance-based interdigitated microelectrode biosensor will measure the variations of electrical characteristics of the biological sample. The biosensor is placed at the bottom of the reservoir (see Fig. 1.c), ensuring a total contact between the content of the chamber (the human fluids) and the sensing surface during the operation. Its design was made according to the device geometry in the chamber as a circular area that covers the whole bottom surface with interdigitated microelectrodes. The biosensor is electrically connected with the electronics that will conduct and analyze impedance measurements. The contact pads of the biosensor shown in Figure 1.d) ensure the total electric connection of the prototype for experimental assays.

### **2.2 Electronic module design**

The SCVC electronic module is designed in compliance with the Medical Implant Communication Systems, MICS, which is the standard specification for the Ultra Low Power Active Medical Implants and Peripherals, EN301839 (ETSI EN 301 839, v1.3.1, 2009-01) and with the global Industrial Scientific and Medical (ISM) band (Loy et al., 2005).

Regarding the new device application it has to be noted two main features that may be into limited requirements: the long term application and the limited size of the implant. Both concepts are connected as the bigger space the SCVC has, the bigger battery could lodge, or rewording that affirmation: the lower available space, the less battery size and therefore the less operation time. Although the main idea is cover the energy needs by the combination of different power supply technologies, this first prototype has installed a battery.

From the electronics design point of view one of the most important concerns is the energy consumption and so provides the new device the largest operation life. For this reason the module designed, shown in Figure 2, is based in the MSP430F248 ultra low power microcontroller (Texas Instruments). On the one hand, the biosensor is measured by the AD5933 impedance converter (Analog Devices). On the other hand, the communications system is managed by the ZL70321 transceiver (Zarlink Semiconductors), which uses the ISM band to start the communication link in the MICS band, in order to save energy. These components have software selectable operation modes that enable them to put in low-power modes to save energy.

In order to manage the operation modes it has been designed specific software which controls the electronics by the microcontroller. Software reduces the energy consumption by choosing the lowest consumption mode in each case.

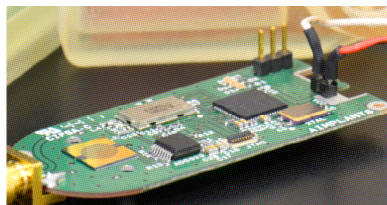


Fig. 2. Photograph of the hardware designed PCB used for electronic testing, which shows the shape of the bottom part of the implantable prototype and over which is placed an IDAM biosensor in its inverted final location for the electronic connection.

### 2.3 Antenna module design

Along with an efficient electronics, an optimal antenna design is required to achieve long range communication with low power consumption. It is required to be dual band to operate within a patient in the MICS frequency band (402-405MHz) as well as in the global ISM band (2.4-2.5GHz). The antenna also requires broadband behavior to avoid detuning when facing a changing live environment. Although the top part of the reservoir is the closest surface to the skin, this area is disregarded as the antenna locus as it is to be unobstructed for liquid exchange capability purposes between the implant inner reservoir and external catheters or syringes. As a result, the antenna is determined to be three-dimensional, conformal to the side walls of the reservoir and low-profile, i.e. with ideally no extra volume added on the SCVC. The antenna should be compact, insulated from the body and as efficient as possible.

The shape of the supporting reservoir is given to be a truncated cone with a base radius  $r_b=16\text{mm}$ , upper radius  $r_u=10\text{mm}$  and height  $h_c=16\text{mm}$  (Fig. 3.a). The constraints mentioned above are taken into account when selecting a monopole-like structure as a radiating element. A round ground plane covers the base of the cone. A short circuit between the end of the monopole and the ground plane is implemented as miniaturization technique. By using a closed loop on the top of the implant, which can be seen as an additional inductance, the input impedance matches quite accurately the desired  $50\Omega$ . This loop is narrow enough to leave clear the top of the implant. The whole radiating structure is herein after referred to as "Eye antenna" (i-antenna) (Fig. 3). The i-antenna was coated with a  $0.5\text{mm}$  biocompatible synthetic film and sealed with silicone adhesive to prevent physiological interaction with the surrounding tissue. The chosen antenna topology is designed within a single skin tissue phantom as a surrounding environment, which is considered accurate enough for the body simulation (Fig. 3.b).

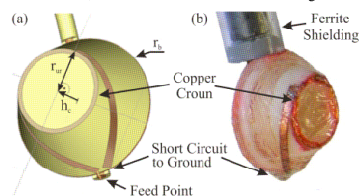


Fig. 3. (a) i-antenna layout computer design with feeding cable at the bottom part (b) Prototype of the i-antenna inside human tissue simulating liquid.

## 3 Material and methods

### 3.1 Bacterial growth impedance monitoring

#### 3.1.1 Design and fabrication of biosensors

Biosensors were fabricated and characterized under clean room environment. A  $100\text{nm}$  thin film layer of gold forms the interdigitated microelectrodes deposited by RF sputtering onto  $3''$  oxidized silicon wafers. Each sensor has a  $6\text{mm}$  diameter circle active sensitive surface composed of 210 pairs of  $30\mu\text{m}$  wide,  $3980\mu\text{m}$  of long fingers with a separation of  $30\mu\text{m}$  between them.

Before carrying out the measurements all chips were cleaned with Hellmanex dissolution in ultrasonic bath for 10 minutes. They were rinsed with deionized water again in ultrasonic bath for other 10 minutes, and finally another 10 minutes in ethanol absolute (99.5% ICT.S.L. ref: 161086.1211). Once the biosensors were set up in the chips holder the complete array was sterilized at  $121^\circ\text{C}$  for 1 hour in the autoclave.

### 3.1.2 Impedance spectroscopy (IS) measurements

IS monitoring was performed with a Solartron 1260 Impedance/Gain-phase Analyzer (Solartron Analytical) connected to an own-developed multiplexer system that sequentially connects each biosensor to the impedance analyzer. Through specific LabVIEW<sup>®</sup>-based software the impedance changes were tracked in real time during the microbial culture development. IDAM biosensors were measured every 10 minutes during the assays with the same electrical conditions. The measurement settings were: 100 mV of sinusoidal excitation signals without polarization, applying variable frequency between 10 Hz and 10 kHz. All the data were measured inside the incubator system at 37°C and 10% of CO<sub>2</sub>.

### 3.1.3 Microbiological biofilm samples

A biofilm generator strain of *Staphylococcus epidermidis* was used on this work: the ATCC 35984 obtained from the Colección Española de Cultivos Tipo (CECT). Isolation of pure cultures was carried out following the protocol reported before (Paredes et al., 2012) where an impedimetric monitoring of bacterial growth were carried out inside a modified CDC biofilm reactor system.

Diluted sample from a 0.5 McFarland vial was incubated in Tryptic Soy Broth, TSB (BBL<sup>™</sup>, ref: 211768), enriched with 5% glucose (Dextrose from Difco<sup>™</sup>, ref: 215530) for 1 hour to leave the microbes reach the exponential growth point. Two milliliters of infected broth with different bacterial concentration in each assay were injected at the initial moment in each one of the *Lab-Tester* devices.

### 3.2 Electronics Lifetime test

The objective of the lifetime test is to evaluate the operation lifetime of the device. The lifetime is evaluated by analyzing the normal use of the device, which can be summarized in three operations: sniff operation, alive request operation and measure request operation. In addition, there is one operation related to an emergency communication created by a medical event. The consumption of the operations is obtained by using the methodology exposed in (Benini et al., 1998), related to the evaluation of the power consumption by analyzing a power state machine.

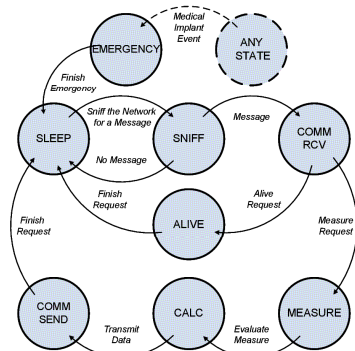


Fig. 4. Power State Machine for the SCVC. Different stages of the electronics are shown in the graph and the normal flow between them while operating normally.

In Fig. 4 the main states and the different events of the software designed are shown. The states are defined in table 1 each state is composed of different sub-states, for example the SNIFF state is composed for the wake-up of the microcontroller, the wake-up of the RF chip and the decision. The power consumption and time evaluation of the states is performed by measuring the voltage drop across a 19.6Ω resistor placed in series with the Hewlett Packard E3631A power supply unit with the Agilent 54622A oscilloscope. The Base Station Mezzanine (BSM100 rev E)

included in the ZL70101 Application Development Kit (ADK) [252 Zarlink Semiconductors] is used for the control and setting-up of the communication link. In addition to the evaluation, the node is configured with the worst case in terms of output power transmission.

Table 1: Power states machine definition

State Name	Definition
<i>SLEEP</i>	All the devices are in power-down mode or the best low power mode.
<i>SNIFF</i>	It includes all the processes/actions to poll for its code in the network in the 2.4 GHz ISM band.
<i>COMM RCV</i>	It includes all processes/actions to communicate with the external device in the 402-405 MHz band under the Listen Before Talk (LBT) and Adaptive Frequency Agility (AFA) conditions explained in more detail in [ref].
<i>COMM SEND</i>	It includes all processes/actions to start and to communicate with the external device in the 402-405 MHz band under the Listen Before Talk (LBT) and Adaptive Frequency Agility (AFA) conditions explained in more detail in (Zarlink Semiconductors, ).
<i>ALIVE</i>	It includes all processes/actions to answer to the external device that the device it is alive.
<i>MEASURE</i>	It includes all processes/actions to measure a complex EBI in the sensor through the Analog-to-Digital converter.
<i>CALC</i>	It includes all processes/actions to perform all operations required to transform data into information.
<i>EMERGENCY</i>	It includes all processes/actions to communicate with the external device by using an emergency communication caused by a Medical Implant Event, explained in more detail in (Zarlink Semiconductors, ).

### 3.3 Reflection and transmission test

The objective of the reflection and transmission test is to define the read range of the communication link between the SCVC and an external base station in an indoor scenario for the future application. The base station makes use of the same Z70102 transceiver chip by Zarlink, corresponding to the ADK, with a helix antenna. The range measurement will be contrasted with the estimated one in the literature.

The *i*-antenna is placed into a phantom that models a human torso. The phantom is composed of a polystyrene tank of 35 cm x 25 cm cross section that is filled with 14.5 litres of tissue simulating liquid (Karacolak et al., 2008). The antenna is placed at 9 mm from the front phantom wall and with an offset of 60 mm with respect to the vertical center axis. The reflection coefficient  $S_{11}$  is measured with Agilent 8714ET Vector Analyzer.

Then, the implanted electronics is fed by a 3 V battery. The implant transceiver is programmed to transmit an emergency signal every few seconds. Both wake up and communication signals are transmitted in the MICS band at 403MHz to test the longest read range. By connecting an Agilent E4402B Spectrum Analyzer to the output of the circuit without antenna, the transmitted power is found to be -15.7dBm, which is closely related to the maximum approved power according to the MICS standard (-16 dBm, 25 $\mu$ w) [ETSI EN 301 839, v1.3.1, 2009-01].

Finally, the implanted electronics and the *i*-antenna into the human phantom are assembled to form an SCVC prototype facing the base station (Fig. 5.a). The whole setup, including a control unit, is shown in Fig. 4.b. The base station and the SCVC are placed at 74 cm and 94 cm from the floor, respectively, in a laboratory environment. The phantom was progressively separated from the base station once the session had been established.

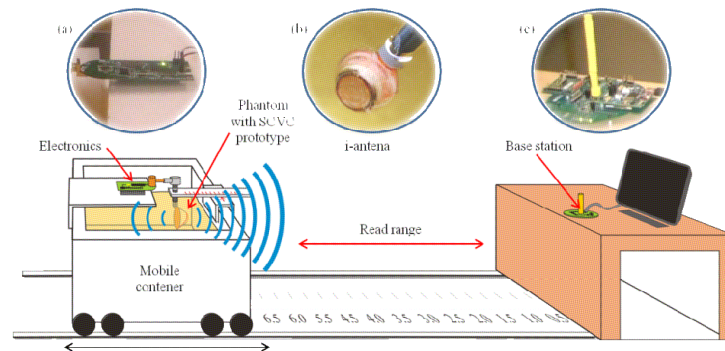


Fig. 5. (a) Electronics connected to the i-antenna placed into the phantom (b) Laboratory environment with base station and control laptop at maximum operating distance.

### 3.3.1 *Read range analytical verification*

## 4 Results and discussion

### 4.1 Bacterial growth impedance monitoring

Impedance monitoring of bacterial biofilm development principles was previously described (Paredes et al., 2012), where an equivalent electrical circuit is proposed for electric analysis. Fig. 6 represents the relative variation of the impedance magnitude in panel (a) and the equivalent serial capacitance ( $C_{Serial}$ ) in panel (b) at different frequencies, from 10 Hz to 10 kHz for the total duration of the trial. In Fig. 6.b a comparison of the impedance monitoring between two different initial concentrations is shown as the relative variations of the  $C_{Serial}$ .

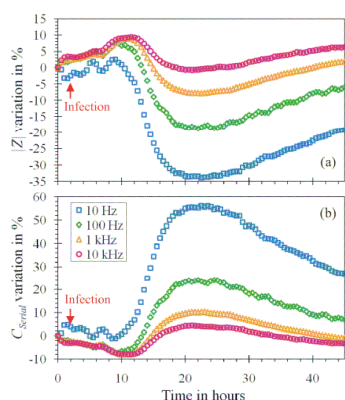


Fig. 6. (a) Relative changes at different frequencies of the serial magnitude of impedance measurements and (b) relative changes of the equivalent serial capacitance during *Staphylococcus epidermidis* ATCC 35984 biofilm development inside the lab prototype with an initial bacterial concentration of  $\sim 1.2 \times 10^5$  CFU/mL.

Microorganisms were inoculated at the first hours of the experiment, injecting the infected media through the silicon cop of the lab prototype. Approximate 10 hours after the infection the serial capacitance starts changing reaching a maximum relative variation another 10 hours later. The time that is needed until significant variations on the impedance curves were recorded, is related to the lag phase of growth. Microbes need to get used to the new culturing conditions to start multiplying exponentially. Once the microbes start to grow up, both the IZI and C<sub>Serial</sub> show the significant relative changes. After that maximum the curves slowly start to decrease regarding the death phase of the biofilm shape growth. The other electrical parameters as the magnitude, the phase or the equivalent serial resistance are not shown due to the smaller changes that present.

Bacterial culture development produces a decrease on the values of the electrical impedance characteristic due to microbe's growth in the media. Under those conditions, the low range of the frequency has been previously reported as the suitable configuration for bacterial detection in real samples (Yang et al., 2004). The changes of conductivity related with the ionic concentration result of the metabolic activity reach the maximum variation for higher frequencies (Varshney and Li, 2008).

The capacitance is the most sensitivity electrical parameter for tracking the biofilm development. This parameter is closely related with the biosensor geometry based on interdigitated microelectrodes and has been proved as effective tool for microbial detection and growth monitoring (Laczka et al., 2008). The maximum response is related to the lowest frequency of 10 Hz achieving a 55% of maximum variation. So it is clear that, the higher frequency of measurement the lower relative recorded sensitivity.

#### 4.2 Electronics Lifetime test

The states power consumption is obtained by analyzing the power profile obtained with the oscilloscope, Fig. 7 shows a capture of some states. The average results of 10 measures' average are presented in Table 2.

*Table 2: Experimental results*

	Voltage Drop mV	Current mA	Time ms	Consumption ms mA
SLEEP	0.031	0.002	-	-
SNFF	28.381	1.448	6	8.688



COMM RCV	89.547	4.569	104	475.147
COMM SEND	92.799	4.735	365	1728.275
ALIVE	-	-	-	-
MEASURE	209.092	10.668	752	8022.336
CALC	15.683	0.799	28	22.372
EMERGENCY	92.799	4.735	365	1728.275

\* The calculation is composed of 2 square roots and 2 multiplications of 16-bit float point values

The lifetime result depends on the period used for the measurements and for the alive requests. For this application the measurements are performed every hour and the device is called for an alive request operation every minute. Taking into account that a general coin-cell battery has 50mAh and the use of a normal cycle, the lifetime estimation result is around 330 days.

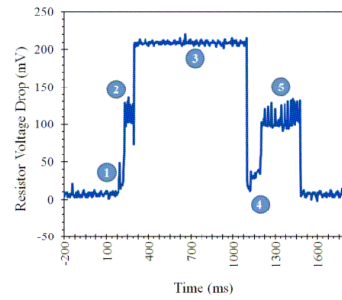


Fig. 7. Power profiles for different concatenated states: 1 corresponds to Sniff state; 2 corresponds to a Comm Rcv state and the acknowledge; 3 corresponds to Measure state; 4 corresponds to Calc state and 5 corresponds to Emergency Communication.

### 4.3 Reflection and Transmission test

#### 4.3.1 *L*-antenna reflection coefficient

The *i*-antenna reflection coefficient  $S_{11}$  is found to be below -10 dB from 345 MHz to 555 MHz and from 960 MHz to 3000 MHz that is the limit of the analyzer (Fig. 8). Therefore it covers the expected MICS and ISM bands with broadband behavior.

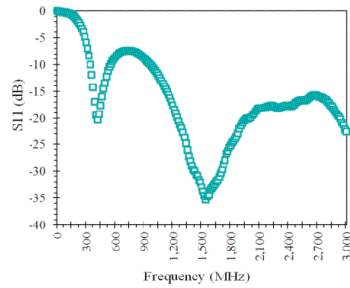


Fig. 8. Reflection coefficient (dB) vs. frequency (MHz) of the *i*-antenna into the human phantom.

The transmission measurements according to Fig. 8 showed that the communication link is lost (transition from “in session” to “session lost”) at an average distance of 6.36m and the communication is reestablished (transition from “session lost” to “in session”) at 5.76m when bringing the phantom closer to the base station again.

In order to verify the obtained data, an indoor propagation model according to (Rappaport, 1996) and (Seidel and Rappaport, 1992) is applied for the laboratory measurements. This empirical model is based on measurements and statistical analysis (Equation 1).

$$PL(d)[dB] = PL(d_0)[dB] + 10n_{sf} \log\left(\frac{d}{d_0}\right) + FAF [dB] \quad (1)$$

Where:

$n_{sf}$  [ ] is single floor path loss exponent,

$PL(d)[dB]$  average path loss

$FAF [dB]$  floor attenuation factor and

$d_0 [m]$  is the close-in reference distance, taken as free space distance from which indoor attenuation is applied.

Therefore, the resulting path loss exponent  $n_{sf}$  and the floor attenuation factor  $FAF$  represent the additional attenuation in a real indoor environment, compared to the ideal free space propagation. The equivalent value to  $n_{sf}$  for free space communications (without floor and obstacles) is 2, whereas the value for environments with obstacles between the transmitter and the receiver is much higher.

In this manner,  $n_{sf}$  exponent was calculated to verify the indoor performance of the system according to Equation (1). Equation (2) obtains  $n_{sf}$  by rearranging the terms:

$$n_{sf} = \frac{PL(d)[dB] - PL(d_0)[dB]}{10 \log\left(\frac{d}{d_0}\right)} \quad (2)$$

The floor attenuation factor  $FAF [dB]$  is set to zero, as the measurements are performed over the same floor. By de-embedding the antenna gains and mismatch losses from the ratio between the implanted electronics sensitivity and the measured transmitted power of the base station ( $P_{TX} = -15.7 \text{ dBm}$ ), a path loss of  $PL(d)=47.1 \text{ dB}$  is computed. By using the free space loss equation for the reference distance  $d_0=1 \text{ m}$ , the reference path loss  $PL(d_0)$  is  $24.5 \text{ dB}$ . With this data, equation (2) leads to a path loss exponent of  $n_{sf}=2.81$  for the distance of  $d=6.36 \text{ m}$  (on-off) and  $n_{sf}=2.97$  for  $d=5.76 \text{ m}$  (off-on).

According to the indoor propagation model (Rappaport, 1996), the path loss exponent  $n_{SF}$  should be close to 3.27 for office buildings at 914 MHz with a variance of 11.2 dB. The obtained values (2.81 and 2.97) are therefore consistent. The slight difference to the expected one (3.27) is likely due to the frequency difference effect: lower frequency (403 MHz compared to 914 MHz) means lower path loss and therefore lower  $n_{SF}$ .

Another indoor path loss model is proposed by Vaughn and Andersen (Vaughn and Andersen, 2003). The empirical model (Equation 3) is obtained from measurement data taken in the ISM 433MHz band, therefore closer to the MICS band, in several European building types.

$$PL(dB) = -23 + 90 \log_{10}(d) \quad (3)$$

Where  $d[m]$  is the distance between transmitter and receiver, for  $d > 3m$ .

The equation reflects the best case scenario calculation, i.e., only the best 1% of all measurement positions are below this low path loss. The scenario in the present experiment can be considered close to the optimal, as it is a line of sight transmission in a not cluttered office. By applying  $d=6.36m$  to Eq 3, an indoor path loss of  $PL=49.3dB$  is calculated, which is a quiet good correlation to  $PL=47.1dB$ , which is employed in Eq 2. This reveals again the consistency of theoretical and measured results.

## 5 Conclusions

A new smart central venous catheter was developed for early detection of bacterial biofilm associated infectious processes. The three complementary modules, biosensor, electronics and antenna were successfully developed and *in vitro* tested.

*S. epidermidis*, reviewed as one of the most relevant device-associated pathogens, was probed to be detected by impedance spectroscopy technique. Label-free interdigitated microelectrode biosensors are an easy and effective solution to be integrated in any kind of indwelling device. The low range of the frequency was found as the more sensitive setting to track changes related to biofilm development.

From an electronic point of view, the set designed consisting of hardware and software has been tested and evaluated. The obtained results validates as a solution with the key feature of a lifetime of more than 11 months with a coin-cell battery of 50 mAh.

A low profile, broadband UHF antenna has been integrated onto the surface of the SCVC with a truncated cone shape for wireless interaction with an external base station. The 3D antenna exhibits compact and broadband features due to the application of short circuit and inductive loading techniques. A transmission test revealed a maximum operational range of 6.36 m in a line-of-sight indoor environment using the MICS frequency band, which fits the theoretical expected results. This analysis sets the limits and read range potentials for biofilms growth monitoring in SCVC within current regulation framework.

This new medical device should provide a better knowledge of the bacterial biofilm colonization process inside a central venous catheter allowing more effective treatments and therefore improving patient's quality life during that pathology. *In vivo* assays now must be carried out to probe the real working functionality of this intelligent CVC.

Finally, we realize that the development of this prototype into a commercial one will suppose a real challenge, but the real motivation of this research is the fact of its application will enhance the quality life of the patients and we provide the physicians a new tool for saving life.

## 6 Acknowledgements

The authors also would like to thank the CECT *Universidad de Valencia* for providing the ATCC 35984 strain.

## References

- Analog Devices, AD5933 Datasheet, [http://www.zarlink.com/zarlink/hs/82\\_ZL70102.htm](http://www.zarlink.com/zarlink/hs/82_ZL70102.htm), Accessed 31 January 2013
- Benni, L., Hodgson, R., Siegel, P., System-level power estimation and optimization. *Low Power Electronics and Design, 1998. Proceedings. 1998 International Symposium on*, 173-178
- Costerton, J.W., Stewart, P.S., Greenberg, E.P., 1999. . *Science*. 284, 1318-1322

- Davies, D., 2003. . *Nat Rev Drug Discov.* 2, 114-122
- Donlan, R.M., 2001. . *Emerg Infect Dis.* 7, 277-281
- Donlan, R.M., Costerton, J.W., 2002. . *Clin. Microbiol. Rev.* 15, 167-193
- ETSI EN 301 839, v1.3.1. 2009-01
- Fux, C.A., Costerton, J.W., Stewart, P.S., Stoodley, P., 2005. . *Trends Microbiol.* 13, 34-40
- Hall-Stoodley, L., Costerton, J.W., Stoodley, P., 2004. . *Nat. Rev. Microbiol.* 2, 95-108
- Harris, L.G., Richards, R.G., 2006. . *Injury.* 37, S3-S14
- Karacolak, T., Hood, A.Z., Topsakal, E., 2008. . *Microwave Theory and Techniques, IEEE Transactions on.* 56, 1001-1008
- Laczka, O., Baldrich, E., Muñoz, F.X., del Campo, F.J., Detection of *Escherichia coli* and *Salmonella typhimurium* Using Interdigitated Microelectrode Capacitive Immunosensors: The Importance of Transducer Geometry. *Anal. Chem.* 80(19), 7239-7247
- Loy, M., Karingattil, R., Williams, L., 2005. . Application Report, Texas Instruments, SWRA048
- Paredes, J., Becerro, S., Arizti, F., Aguinaga, A., Del Pozo, J.L., Arana, S., 2012. . *Biosensors and Bioelectronics.* 38, 226-232
- Rappaport, T.S., 1996. *Wireless Communications, Principles and Practice*, in: . Pearson Ed. Prentice Hall, 2nd, pp. 641
- Seidel, S.Y., Rappaport, T.S., 1992. . *Antennas and Propagation, IEEE Transactions on.* 40, 207-217
- Stewart, P.S., 2003. . *The Lancet.* 361, 97-97
- Stewart, P.S., William Costerton, J., 2001. . *The Lancet.* 358, 135-138
- Texas Instruments, MSP430F248 Datasheet, <http://www.zarlink.com/zarlink/zl70102-shortform-datasheet-jun10.pdf>. Accessed 31 January 2013
- Varshney, M., Li, Y., 2008. . *Talanta.* 74, 518-525
- Vaughan, R., Andersen, J.B. (Eds.), 2003. *Channels, Propagation and Antennas for Mobile Communications*, The Institution of Engineering and Technology
- Wang, R., Khan, B.A., Cheung, G.Y.C., Bach, T.H.L., Jameson-Lee, M., Kong, K.F., Queck, S.Y., Otto, M., 2011. . *J. Clin. Invest.* 121, 238-248
- Yang, L., Li, Y., Griffiths, C.L., Johnson, M.G., 2004. . *Biosensors and Bioelectronics.* 19, 1139-1147
- Zarlink Semiconductors, ZL70102 Datasheet, <http://www.zarlink.com/zarlink/zl70102-shortform-datasheet-jun10.pdf>. Accessed 31 January 2013

M. Alonso-Arce, P. Bustamante, C. Schmidt, J. Legarda, B. Sedano

**Ultra low-power smart medical sensor node based on a central  
venous catheter for in-body biomonitoring**

Innovation and Research in BioMedical engineering

## ARTICLE IN PRESS

IRBM:322



Disponible en ligne sur

**ScienceDirect**  
[www.sciencedirect.com](http://www.sciencedirect.com)

Elsevier Masson France

**EM|consulte**  
[www.em-consulte.com](http://www.em-consulte.com)
**IRBM**

IRBM ●●● (●●●●) ●●●●●●●●

## Ultra low-power smart medical sensor node based on a central venous catheter for in-body biomonitoring

M. Alonso-Arce<sup>a,\*</sup>, P. Bustamante<sup>a</sup>, C. Schmidt<sup>a</sup>, J. Legarda<sup>b</sup>, B. Sedano<sup>a</sup>

<sup>a</sup> CEIT and Tecnun (University of Navarra), P<sup>o</sup> Manuel Lardizábal 15, 20018, Donostia, Spain

<sup>b</sup> Deusto Institute of Technology – DeustoTech (University of Deusto), Av. Universidades 24, 48007, Bilbao, Spain

Received 12 December 2013; received in revised form 29 May 2014; accepted 2 June 2014

### Abstract

New advances in biosensor and electronic technologies will merge in new health assistance paradigms strongly based on the remote biomonitoring. Biomedical circuit and systems have much to say on this, as for example the Central Venous Catheters (CVC). Central venous catheters are commonly used in clinical practice to improve a patient's quality of life. Nevertheless, there remains a large risk of infection associated with microbial biofilm (about 80% of all human bacterial infections). The standardization bodies, the radiofrequency devices and the biosensor technology are taking their positions, and the integration of all that effort is the work proposed in this paper.

An ultra-low power active medical implant is presented for in-body monitoring of Electrical BioImpedance (EBI) based sensors with a new 3-D antenna. Transmission test and detailed evaluation have been done based on two typical monitoring parameters: the frequency of the internal sensor measuring and the frequency of external communication requests. The results show up to 20 months lifetime powered with a 50 mA coin-cell battery.

© 2014 Elsevier Masson SAS. All rights reserved.

### 1. Introduction

Microbial biofilms are responsible of a wide range of infectious diseases associated with indwelling medical devices. Intravenous catheters, prosthetic heart valves, prosthetic joints, pacemakers, etc. are widely used in the healthcare attention saving millions of lives, but assuming an intrinsic risk of infection [1]. Medical implants are the propitious environment for the development of bacterial biofilms, which will lead to an infection. The importance of biofilm-associated infection was estimated to represent over 80% of human microbial infections [2]. On the other hand the routine monitoring of patients is usually inefficient for detecting biofilm-related infectious pathologies [3], so the detection and diagnosis before the treatment of the infectious processes caused by microbial biofilms are not really solved. Besides the period between the infection

and the detection, the process to analyze which bacteria is growing, often results too time-consuming.

In this context the infectious process not detected on time may end up in several medical complications for which, in many cases, the only way to ensure a good outcome is removing the infected device [4,5]. These events have a high cost on top of the high importance of the patient health risk under such medical complications. For this reason it is necessary to develop new devices and methods to improve biofilm early detection.

Nowadays there is a wide variety of novel techniques that allow in-depth in vitro study of the most important aspects of the formation of bacterial biofilms, from gene expression to microscopic characterization. However, there still remains a great demand in the field of in vivo detection specially for indwelling devices. To achieve this purpose it would necessary to develop new intravascular catheters that provides a continuous monitoring of the content of the reservoir of the CVC and to send an alarm signal in case of bacterial colonization. For this purpose

\* Corresponding author.

E-mail address: [maarce@ceit.es](mailto:maarce@ceit.es) (M. Alonso-Arce).

<http://dx.doi.org/10.1016/j.irbm.2014.06.001>

1959-0318/© 2014 Elsevier Masson SAS. All rights reserved.

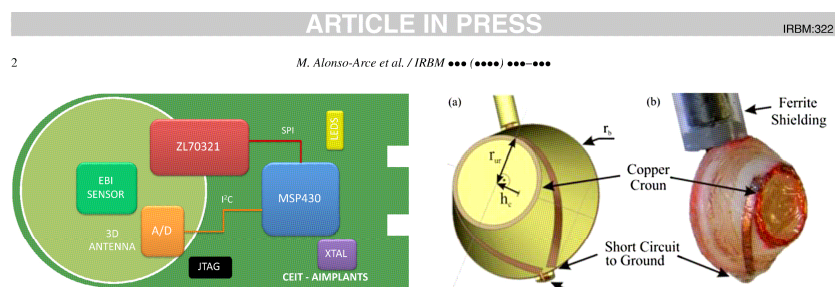


Fig. 1. Scheme of the developed platform.

a biosensor that could measure bacterial biofilm development is used [6]. This biosensor is an Electrical BioImpedance (EBI) which needs to measure its complex impedance.

There is a large amount of work oriented towards on-body medical devices using the ISM 2.4 GHz technologies [7–11] but they are not suitable for in-body medical implants, according to the European legislation [12], despite the availability of specific electronic devices specifically for standards like the EN301 839 [13]. This work tries to take a step forward from circuits to systems in implanted biosensor monitoring applications, integrating radiofrequency communications, embedded decision capabilities and EBIs, measuring them in an autonomous In-Body Sensor Node (IBSN).

This paper is organized as follows: Section 2 introduces the Hardware/Software implementation, Section 3 describes the duty cycle of the use case selected for the present work, Sections 4 and 5 show transmission test and an estimation of the lifetime of the implanted device and finally Section 6 gives the main conclusions.

## 2. In-body sensor node

This section describes the HW/SW design of a wireless IBSN for the measuring of different types of EBIs based on the AD5933 impedance converter.

### 2.1. Use case

The use case that has been considered in this work connects an IBSN located in a central venous access device with an external dedicated gateway device based on the Medical Implant Communication Service, which is the standard specification for these devices in the frequency range 402 MHz to 405 MHz. Afterwards, the dedicated gateway is connected to a Local Area Network where a Home Server manages and forwards the Personal Health Records to a remote Medical Server through the Internet. This work is only focused on the IBSN and its interaction with the external dedicated gateway.

### 2.2. Hardware implementation

The IBSN platform is composed by 4 main components: the microcontroller, the transceiver and antenna, and the sensor

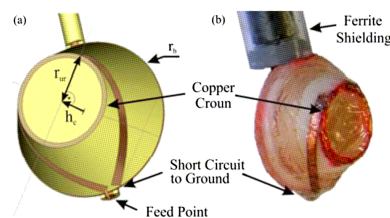


Fig. 2. SCVC-antenna showing (a) simulation model and (b) prototype.

measuring circuit and the EBI sensor. The layout on the board of these components is shown in Fig. 1.

The core of the IBSN is the ultra low power MSP430F248 microcontroller of Texas Instruments (2 KB RAM, 48 KB Flash, 256 KB EEPROM). It is a 16-bit RISC microcontroller with 4 different low power modes, between 0.1  $\mu$ A in Off mode (RAM Retention) and 0.3  $\mu$ A in Standby mode. The operation voltage is between 1.8 V and 3.6 V.

The transceiver is the ZL70321 of Zarlink Semiconductors, a complete MICS radiofrequency (RF) telemetry transceiver that meets the regulatory requirements. The main power features can be summarized as follows: 2.05 V to 3.50 V supply voltage, 5 mA in continuous average transmission and reception, 1 mA idle power mode, and 2.4 GHz ISM wake-up (290 nA at 1 s strobe period).

Along with an efficient electronics, an adequate antenna design is mandatory. A stable long range communication together with low power consumption requires the antenna to be insensitive to changing human tissue properties, which vary with age, sex and anatomy. Although the MICS frequency band is 402–405 MHz, the broader operating bandwidth is necessary.

While the top part of the liquid reservoir is close to the skin, this area is disregarded as antenna locus. That area is to be unobstructed for liquid exchange capability purposes between the implant inner reservoir and external catheters or syringes.

Therefore the antenna is determined to be three-dimensional, conformal to the side walls of the reservoir. Ideally it is low-profile as no extra volume should be added on the SCVC. The antenna is to be insulated from the body, preventing harmful physiological interaction with the surrounding tissue.

The shape of the supporting reservoir is given to be a truncated cone with a base radius  $r_b = 16$  mm, upper radius  $r_{ur} = 10$  mm and height  $h_c = 16$  mm (Fig. 2a).

Taking these constraints into account a monopole-like structure as the radiating element is selected. The base of the cone is covered by a copper film. A short circuit between the end of the monopole and this ground plane is implemented as miniaturization technique. By using a narrow, closed loop on the top of the implant the input impedance is adjusted to 50  $\Omega$  (Fig. 2). The antenna structure is coated with a thin biocompatible synthetic film and sealed with silicone adhesive. The antenna is designed within a single skin tissue phantom as a surrounding environment and simulated (Fig. 3).

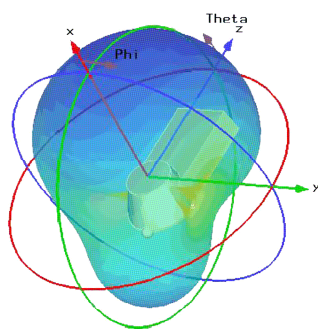


Fig. 3. SCVC-antenna model with 3D-radiation result.

The measuring circuit it needs to measure complex impedance, so a complex impedance converter it is needs. The selected one is the AD5933 of Analog Devices. It combines an on-board frequency generator with a 12-bit 1MSPS ADC and an I<sup>2</sup>C interface. AD5933 needs an external clock signal (typical 1 MHz) for proper operation. The power features can be summarized as follows: 2.7 V to 5.5 V supply voltage, 10 mA to 11 mA in normal and standby mode, and 1  $\mu$ A in power-down mode.

The printed circuit board is an FR4 2-layer board (Fig. 4). All the components are on the top layer and the size is 65 mm long and 30 mm wide, due to the packaging requirements of the central venous access device.

### 2.3. Software implementation

The software architecture has been designed in 4 different layers. The top layer is the main application and the second layer manages the power. The third layer is composed of two communication protocol stacks and an interrupt manager. Finally, the last layer groups the hardware drivers.

#### 2.3.1. Main application

The main application implements the use case represented with the flow chart of Fig. 5. The application starts in a waiting state and every  $t_{sniff}$  (configurable time from 266  $\mu$ s to 81.265 s) checks if any transmission request comes from the external gateway. If so, it starts a communication link and processes the external request actions.

There are two types of actions: *Alive Request* and *Measure Request*. The former tells the external device that the IBSN is in the ON state and working OK, while the latter measures the sensor data and sends the information to the external device.

#### 2.3.2. Power mode optimization

This layer is designed to manage all the power modes of the microcontroller, the transceiver and the impedance converter.



Fig. 4. The developed platform with an EBI sensor and a test antenna.

It puts them in the best power mode regarding the tradeoff between their functionality and the minimum power consumption.

#### 2.3.3. Communication protocol stacks and interrupt manager

The *RF comm* protocol stack allows the data exchange with the RF transceiver and has been design based on the Modbus protocol [14].

The *interface driver* protocol stack has been designed for the configuration, management and operation control of the AD5933 impedance converter through the I<sup>2</sup>C driver.

And finally, the *interrupt manager* is responsible for managing the interrupts and their priority. Interrupts are due to hardware or software triggers and the manager sets the appropriate flag according to their priority, in order to allow the *main application* to perform the required actions.

#### 2.3.4. Drivers

Five different hardware drivers have been developed: Serial Peripheral interface, the Inter-Integrated Circuit interface, the General Purpose Input Output interface, the Timer interface, and the Supply Voltage Supervisor interface.

## 3. Duty cycle definition

In any AMI, the trade-off between the duty cycle and the battery life is a key design phase. It requires an exhaustive analysis of the power consumption of each system state and the combination of those states during a specific function. The concatenation of all the functions gives the final duty cycle, and the sum of all the consumptions gives the battery life.

The basic functions required for the use case defined in Section 2 are the *Sniff*, *Alive Request*, *Measure Request* and *Emergency Communication* functions, operation states of which and the interrelation between them are shown in Fig. 6 and defined in Table 1.

### 3.1. Sniff function

The *Sniff* function starts in the SLEEP state; it polls the 2.4 GHz band each  $t_{sniff}$  looking for a connection request from an external device. If any request is detected it checks the identification code; a negative result, or a connection timeout, puts



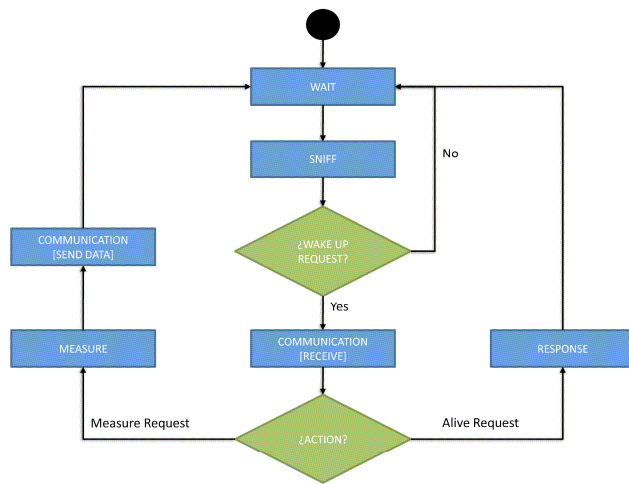


Fig. 5. Main application flow chart.

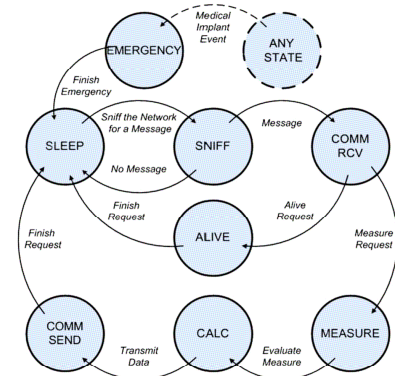


Fig. 6. Application state machine. It represents the transitions among states.

Table 1  
State definitions.

State name	Definition
SLEEP	All the devices are in power-down mode or the best low power mode.
SNIFF	It includes all the processes/actions to poll for its code in the network in the 2.4 GHz ISM band.
COMM RCV	It includes all processes/actions to communicate with the external device in the 402–405 MHz band under the Listen Before Talk (LBT) and Adaptive Frequency Agility (AFA) conditions.
COMM SEND	It includes all processes/actions to start and to communicate with the external device in the 402–405 MHz band under the Listen Before Talk and Adaptive Frequency Agility conditions.
ALIVE	It includes all processes/actions to answer to the external device that the device is alive.
MEASURE	It includes all processes/actions to measure a discrete complex EBI in the sensor through the Analog-to-Digital converter AD5933.
CALC	It includes all processes/actions to perform all operations required to transform data into information.
EMERGENCY	It includes all processes/actions to communicate with the external device by using an emergency communication caused by a Medical Implant Event.

it back into the SLEEP state, but a positive result wakes up the transceiver and sends an Interrupt to the controller, putting it into the COMM RCV state. The microcontroller configures the radio link, exchanges the information with the external device and processes the function requests: the *Alive Request* or the *Measure Request* functions.

### 3.2. *Alive Request* function

The *Alive Request* function puts the system into the ALIVE state and it answers to the external device that the IBSN is in an ON state and working OK. Finally the system is returned to the SLEEP state.

### 3.3. Measure Request function

The *Measure Request* function puts the system into a MEASURE state whereby the AD5933 impedance converter is switched on and the sensor data is measured. Immediately the CALC state is activated in order to switch off the impedance converter and process the sensor information in order to transform the data into information. This transformation is done by making 2 square roots and 2 multiplications of 16-bit float point data types. Finally, it changes into the COMM SEND state and sends the information. Once the Acknowledge is received the system is again sent into the SLEEP state.

### 3.4. Emergency Communication function

The EN301839 specification allows the definition of Emergency Medical Events in order to give priority to the radio channel. These events trigger the EMERGENCY state and execute the *Emergency Communication* function. Four sub functions are performed during this state: the transceiver is woken up and configured with the radio access parameters defined by the EN301839 specification. After that, the local oscillator of the transceiver is initialized and the information is exchanged with the external device. This process holds many acknowledged conditions in order to guarantee that the Medical Event has been properly sent. Finally, the system is again sent to the SLEEP mode.

## 4. Transmission tests

The reflection and transmission test evaluates the communication link between the SCVC and an external base station in an indoor scenario for future applications.

For the tests an external transceiver from the ADK using the Z70102 chip by Microsemi acts as a base station. It is equipped with a pre-measured helix antenna. A phantom, consisting of a polystyrene tank of 35 cm × 25 cm cross section and 14.5 liters of a tissue simulating liquid, was used to simulate a human torso. The SCVC-antenna is placed at 9 mm from the front phantom wall and with an offset of 60 mm with respect to the vertical center axis. This position is equivalent to a subcutaneous implantation in a human body's chest.

The reflection coefficient  $S_{11}$  is measured with Agilent 8714ET Vector Analyzer. The implant electronics is powered by a 3 V battery. The implant transceiver is programmed to transmit an emergency signal every few seconds. Both wake up and communication signals are transmitted in the MICS band at 403 MHz to test the read range.

Finally, the implanted electronics and the antenna (Fig. 7, a) are assembled, to form an SCVC-prototype facing the base station (Fig. 7, b). The measurements are monitored by a laptop which acts also as control unit (Fig. 7, c). The base station and the SCVC are placed at 74 cm and 94 cm over the floor, respectively, in a laboratory environment. The phantom was progressively separated from the base station once the session had been established.

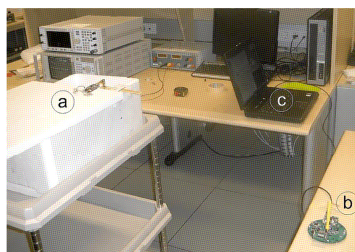


Fig. 7. Measurement setup in the stating position for the range measurements in the laboratory.

## 4.1. Results

The output power of the circuit is found to be  $-15.7$  dBm measured at the antenna connector. This complies with the maximum approved power according to the MICS standard ( $-16$  dBm,  $25 \mu\text{W}$ ) [13].

The antenna's reflection coefficient  $S_{11}$ , shown in Fig. 8 is found to be below  $-10$  dB from 345 MHz to 555 MHz. The distance between the two antennas was taken when the communication link was lost and reconnection was accomplished respectively. The monitoring laptop showed a link loss at an average distance of 6.36 m repeatedly after several trials. When bringing the phantom closer to the base station again the link was the connection was established at 5.76 m.

## 5. Lifetime evaluation

The power consumption has been measured with the Agilent 54622A oscilloscope by analyzing the voltage drop across a  $19.6 \Omega$  resistor placed in series with the power source (3 V). For the control and setting-up of the communication link the Base Station Mezzanine (BSM100 revE) included in the ZL70101 development kit is used. In addition the node is configured with the worst case in terms of output power transmission. The current consumption is obtained by applying the Ohm's law. The power consumption analysis has been done following the power state machines based methodology shown in [15].

### 5.1. Power consumption profiles analysis

#### 5.1.1. Sniff function

The voltage profile obtained during the *Sniff* function is shown in Fig. 9a. There is only 1 interval that corresponds to the SNIFF state which voltage drop average is 28.4 mV (1.448 mA) during a maximum time of 6 ms. The power consumption of this operation,  $C_{sniff}$ , is 8.688 mA ms.

#### 5.1.2. Alive Request function

The voltage profile during the *Alive Request* function is shown in Fig. 9b. There are 5 different intervals; its results are shown in Table 2.

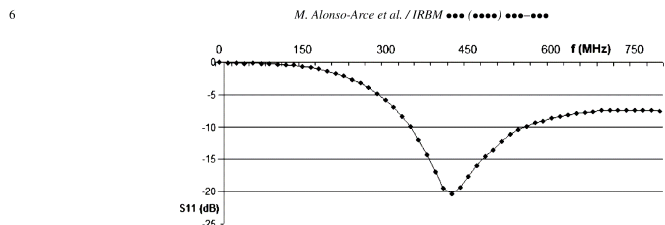


Fig. 8. Reflection coefficient (dB) vs. frequency (MHz) of the CVC-antenna in the human phantom.

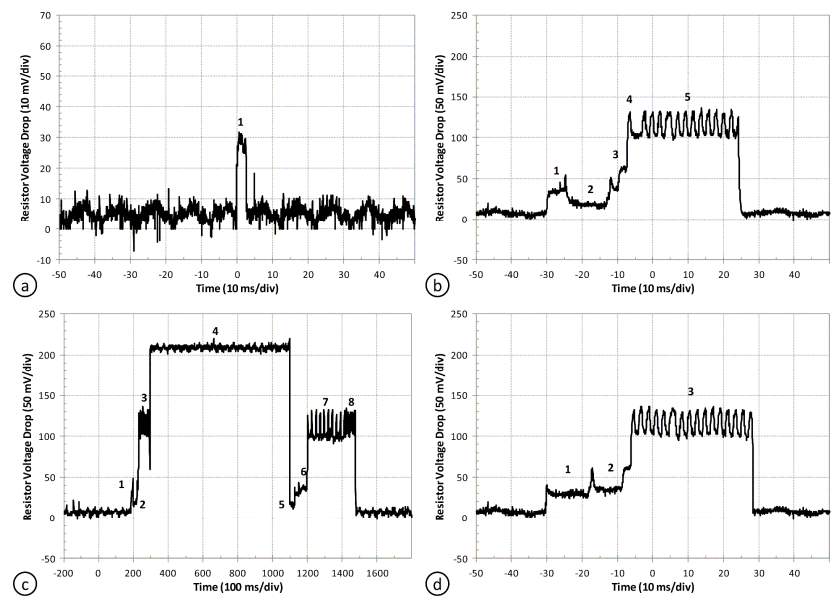


Fig. 9. Voltage profile of the different functions: (a) Sniff function, (b) Alive Request function, (c) Measure Request function (time scale is different) and (d) Emergency Communication function.

Table 2  
Alive Request function results.

Interval	State	Voltage drop (mV)	Current (mA)	Time (ms)	Consumption (ms mA)
1	SNIFF	28.4	1.448	6	8.694
2	COMM	20.6	1.051	12.05	12.662
3	RCV	47.4	2.418	5.20	12.575
4		109.1	5.566	2.75	15.307
5	ALIVE	134.6	6.867	30	206.187

The total power consumption during this function,  $C_{alive}$ , is the sum of the products of the current consumptions by the time of each state: 253.949 mA ms for 56 ms.

5.1.3. Measure Request function

The voltage profile of the Measure Request function is shown in Fig 9c: 8 different intervals can be seen; its results are summarized in Table 3.

The total power consumption of this function,  $C_{measure}$ , in the worst case is 10217.1 mA ms for 1249 ms.

## ARTICLE IN PRESS

IRBM:322

M. Alonso-Arce et al. / IRBM ••• (••••) ••••••••

7

Table 3

Measure Request function results.

Interval	State	Voltage drop (mV)	Current (mA)	Time (ms)	Consumption (ms·mA)
1	SNIFF	28.4	1.449	6	8.694
2	COMM	28.5	1.455	17.3	25.178
3	RCV	68.0	3.469	82.7	286.918
4	MEASURE	209.1	10.668	750	8000.957
5	CALC	15.7	0.800	28	22.404
6	COMM	34.9	1.780	60	106.803
7	SEND	102.1	5.209	250	1302.144
8		113.7	5.804	55	319.196

## 5.1.4. Emergency Communication function

The voltage profile during the *Emergency Communication* function is shown in Fig. 9d. It can be distinguished 3 different intervals. There could be a fourth interval if the external gateway does not send an acknowledge message, whereby extra message requests could be transmitted according to the EN301839 specification.

- Interval 1 corresponds to the wake up of the microcontroller and the configuration of the transceiver. The voltage drop average is 29.8 mV (1.523 mA) for 12 ms.
- Interval 2 is the wake up of the transceiver oscillator. The voltage drop average is 43.0 mV (2.195 mA) for 12 ms.
- Interval 3 corresponds to the communication session. The voltage drop average is 115.2 mV (5.876 mA) for 34 ms.

The total power consumption of this function,  $C_{emergency}$ , is 244.4 mA ms during a total amount of time of 58 ms.

## 5.2. Lifetime estimation

The lifetime estimation is calculated following the application flow chart shown in Fig. 5. The three most critical parameters in the lifetime estimation are:

- $t_{sniff}$ : Time between *Sniffs*.
- $t_{alive}$ : Time between *Alive Requests*.
- $t_{measure}$ : Time between *Measure Requests*.

Some assumptions have been made in order to simplify the mathematical calculation of the total power consumption, but they can be relieved for a computer calculation:

$t_{alive}$  and  $t_{measure}$  are multiples of  $t_{sniff}$ .

The maximum possible time value of  $t_{alive}$  is the maximum time value of  $t_{sniff}$  (81.265 s).

The ratio  $t_{measure} : t_{alive}$ , is 1:10.

Assuming these conditions the  $t_{alive}$  [ms] is calculated as a function of the two other parameters applying Eq. (1).

$$t_{alive} \begin{cases} \text{if } \frac{t_{measure}}{t_{sniff}} \leq 10 & t_{sniff} \\ \text{if } \frac{t_{measure}}{10} \geq 81.265 & 81.265 \\ \text{Other} & \frac{t_{measure}}{10} \end{cases} \quad (1)$$

The total power consumption is calculated as the current average of the duty cycle ( $I_{avg}$ ) multiplied by the voltage, and it is divided in two parts: the active and the inactive part.

The active power consumption is obtained by evaluating Eq. (2) using the  $t_{alive}$  values obtained in Eq. (1), and the active time is obtained by evaluating Eq. (3).

$$C_{act,cycle} = C_{sniff} \cdot \left( \frac{t_{measure}}{t_{sniff}} - \frac{t_{measure}}{t_{alive}} - 1 \right) + C_{alive} \cdot \left( \frac{t_{measure}}{t_{alive}} - 1 \right) + C_{measure} \quad (2)$$

$$t_{act,cycle} = t_{sniff} \cdot \left( \frac{t_{measure}}{t_{sniff}} - \frac{t_{measure}}{t_{alive}} - 1 \right) + t_{alive} \cdot \left( \frac{t_{measure}}{t_{alive}} - 1 \right) + t_{measure} \quad (3)$$

On the other hand the power-down consumption is obtained in Eq. (4) and the power-down time in Eq. (5). The  $I_{sleep}$  is the sum of the power-down consumption of all devices: 0.271 mA.

$$C_{inact,cycle} = I_{sleep} \cdot t_{inact,cycle} = 0.271 \cdot t_{inact,cycle} \quad (4)$$

$$t_{inact,cycle} = t_{measure} - t_{act,cycle} \quad (5)$$

The total power consumption ( $C_{total,cycle}$ ) is obtained by the sum of the results of Eqs. (2) and (4). And the total cycle time is obtained in Eq. (6) using an expansion of Eq. (7).

$$t_{total,cycle} = t_{act,cycle} + t_{inact,cycle} = t_{measure} \quad (6)$$

The current consumption average ( $I_{avg}$ ) is obtained by the division of Eq. (5) by Eq. (6):

$$I_{avg} = \frac{C_{total,cycle}}{t_{total,cycle}} \quad (7)$$

A generic coin-cell battery with 50 mAh true capacity has been selected as a power source due to the size requirement fixed by the central venous access device. Then lifetime is obtained by evaluating Eq. (8).

$$lifetime = \frac{50 \text{ mAh}}{I_{avg}} \quad (8)$$

Fig. 10 shows the results of the lifetime evaluated for different  $t_{measure}$  and  $t_{sniff}$  values for the in-body sensor node with a 50 mAh coin-cell battery.

## 6. Conclusions

The objective of the present work is to give a step forward towards a new generation of biomedical systems that are going to be required in the near future. A complete in-body sensor

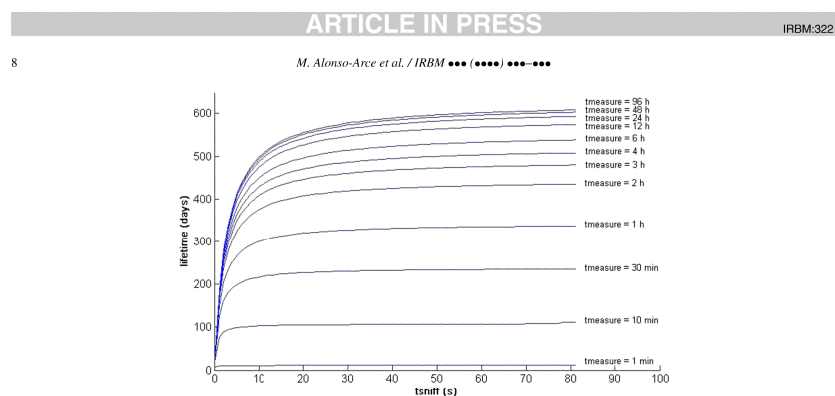


Fig. 10. Device lifetime for different  $t_{measure}$  values.

node is proposed, based on the EN301839 specification, for the biomonitoring of electrical bioimpedance sensors.

A broadband antenna has been optimally adapted to the outer shape of the reservoir of the SCVC. With a low profile and biocompatible film the design exhibits a perfect adaptation to the surrounding tissues. The compactness of that MICS-antenna is achieved by applying a short circuit to the ground plane and inductive loading techniques. Furthermore its wide band characteristic enables the application even for the new approved Medical Micro-Power Networks (MMN) [16] in the frequency range of 413–457 MHz.

In a line-of-sight indoor environment an operational range of 6.36 m has been proved.

The results of this evaluation measurement serve as a base for potential application scenarios based on the current regulation framework. According to the required transmission safety the distance between the implanted sensor node and the external gateway for the chosen application is to be adapted.

The proposed system is based on the well-known MSP430 microcontroller, the ZL70321 transceiver and the AD5933 impedance converter. Hardware and software design and implementation considerations have been shown and an exhaustive power consumption evaluation has been carried out in order to provide a practical design guide for lifetime evaluating based on two typical parameters: the frequency of the internal sensor measuring and the frequency of external communication requests.

A complete validation has been done and excellent lifetime results have been reached for many biomonitoring applications, i.e. the central venous access devices with up to 20 months powered with a 50 mAh coin-cell battery.

#### References

- [1] Hall-Stoodley L, Costerton JW, Stoodley P. Bacterial biofilms: from the natural environment to infectious diseases. *Nat Rev Microbiol* 2004;2:95–108.
- [2] Davies D. Understanding biofilm resistance to antibacterial agents. *Nat Rev Drug Discov* 2003;2:114–22. <http://dx.doi.org/10.1038/nrd1008>.
- [3] Fux CA, Costerton JW, Stewart PS, Stoodley P. Survival strategies of infectious biofilms. *Trends Microbiol* 2005;13:34–40.
- [4] Stewart PS, Costerton JW. Antibiotic resistance of bacteria in biofilms. *Lancet* 2001;358(9276):135–8.
- [5] Donlan RM. Biofilms and device-associated infections. *Emerg Infect Dis* 2001;7:277–81.
- [6] Paredes J, Becerro S, Arizti F, Aguinaga A, Del Pozo J, Arana S. Interdigitated microelectrode biosensor for bacterial biofilms growth monitoring by impedance spectroscopy technique in 96-well microtiter plates. *Sens Actuators B, Chem* 2013;178:663–70.
- [7] Bradley PD. Wireless medical implant technology – recent advances and future developments. In: *Proceedings of the ESSCIRC*. 2011. p. 37–41.
- [8] Junnila S, Kailanto H, Merilähti J, Vaino AM, Vehkaoja A, Zakrzewski M, et al. Wireless, multipurpose in-home health monitoring platform: two case trial. *IEEE Trans Inf Technol Biomed* 2010;14(2).
- [9] Rozeha AR, Sharifah SA, Mohd AR, Mohd AS, Nur HM. Home healthcare via wireless biomedical sensor network. In: *Proceedings of IEEE international RF and microwave conference*. 2008. p. 511–4.
- [10] Hui L, Wen Ding L. Low-power and portable design of bioelectrical impedance measurement system. In: *WASE international conference on information engineering*, vol. 3, 2010. p. 38–41.
- [11] Ferreira J, Seoane F, Lindcrantz K. AD5933-based electrical bioimpedance spectrometer. Towards textile-enabled applications. In: *Proceedings of annual international conference of the IEEE Engineering in Medicine and Biology Society*. 2011.
- [12] Council directive of 20 June 1990 on the approximation of the laws of the member states relating to active implantable medical devices, 90/385/EEC, October 2007.
- [13] Electromagnetic compatibility and radio spectrum matters (ERM): short range devices (SRD): ultra low power active medical implants (ULP-AMI) and peripherals (ULP-AMI-P) operating in the frequency range 402 MHz to 405 MHz; ETSI EN 301 839, v1.3.1, January 2009.
- [14] Modbus-IDA. Modbus application protocol specification v1.1b. <http://www.Modbus-IDA.org>, December 28, 2006.
- [15] Benini L, Hodgson R, Siegel P. System-level power estimation and optimization. In: *Proceedings of the 1998 international symposium on low power electronics and design*. 1998. p. 173–8.
- [16] Federal Communications Commission. FCC 11-176 – Small entity compliance guide: medical micro-power network. 2012. p. 1–5.

C. Schmidt, D. Valderas, J. Garcia, I. Ortego, X. Chen

**Passive UHF RFID near field link budget for implanted sensors**

European Conference on Antennas and Propagation (EUCAP)

## Passive UHF RFID Near Field Link Budget for Implanted Sensors

Christoph Schmidt<sup>1</sup>, Daniel Valderas<sup>1</sup>, Joseba Garcia<sup>1</sup>, Iñaki Ortego<sup>1</sup>, Xiaodong Chen<sup>2</sup>

<sup>1</sup>CEIT and Tecnun (University of Navarra), P<sup>o</sup> Manuel Lardizábal 15  
20018 San Sebastián, Spain

cschmidt@ceit.es; dvalderas@ceit.es; jgmiranda@ceit.es; iortego@ceit.es

<sup>2</sup>Dept of Electronic Eng, Queen Mary, University of London  
London E1 4NS, UK

xiaodong.chen@elec.qmul.ac.uk

**Abstract:** The precise estimation of the communication range for a passive wireless implanted sensor is an essential system design parameter in medical telemetry research. Path loss measurements between an RFID reader antenna and an implanted biosensor at UHF band were performed in an anechoic chamber representing two scenarios: depending on whether the reader is worn by a medic within 1 meter distance from the implant or by the patient in a shirt pocket.

Near-field measurements in the first scenario proved that a passive RFID communication link can be established within 0.46 m for the considered subcutaneous implant. As the gain of the implanted antenna is quite low, the impact of the feeding cables on the results of the second scenario have been estimated by simulations of the measurement set up embedded. This uncertainty is due to the radiation and reflection coming from the feeding cables and it increases with the distance between the two antennas. A methodology is presented to estimate this uncertainty for a proper link-budget estimate.

### I. INTRODUCTION

Researchers have recently shown an increased interest in short range telemetry networks which are placed directly on or near the human body [1]. In order to include implanted sensors in this so called Personal Area Network (PAN) it is necessary to have a communication link between a transceiver located in the human body and another outside but near it. This requires antennas which have a broadside radiation pattern and operate near or into the human body. Particularly, passive or semi passive sensors rely on a good estimate of the link budget.

This paper is aimed at studying the reliability of the wireless link between an implanted chip and a UHF-RFID reader near the human body. Special interest will be focused on the uncertainty introduced by the set up, respectively feeding cables, for a RFID-UHF 865-868MHz near field link measurements.

### II. RANGE MEASUREMENTS

#### A. Implanted and base station antennas employed

The implanted antenna consists of a broadband monopole-like structure in a circular arrangement. A specific designed structure helps to match the small monopole to the desired

frequency [2]. A ground plane and short circuits are avoided to improve radiation efficiency. The complete antenna is sealed by a high permittivity substrate and superstrate made out of Rogers RO3210 ( $\epsilon_r=10$ ) laminate for compact design. The whole radiator is bounded by a circumference of 20 mm diameter.

Fig. 1 shows the top view of the layout along with the feeding set up. The reflection coefficient is below -10 dB at the frequency of interest [2].

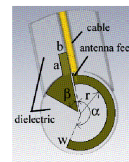


Fig. 1 Implant test antenna

As RFID reader antenna we utilized a conventional PIFA that is employed to probe the field within a short distance from the implanted antenna. The antenna is designed with a low profile (3 mm) [3]. The radiating plate has the dimensions of a portable handset (79 mm x 49 mm) over a slightly larger ground plane (106 mm x 61 mm). Antenna gain along the broadside direction was found to be 0 dBi (Fig. 2).



Fig. 2 Probe antenna – PIFA



### B. Read range perpendicularly to the chest

The reader antenna is placed as it were worn in a shirt pocket of a standing medic and facing the implant at different distances for both PIFA orientations, vertical and horizontal. These are representative positions for vertical and horizontal polarizations for handset antennas.

The entire setup to measure path loss is shown in Fig. 3. The implanted antenna is placed inside a polystyrene tank filled with skin mimicking gel, 9 mm away from the phantom interface to simulate a subcutaneous insertion into a human torso. The wall thickness of the phantom is 2 cm as it represents the patient's clothing. The size of the phantom is the minimum representative for the whole body for far field communication at the frequency of interest (350 x 250 x 165 mm) [4].

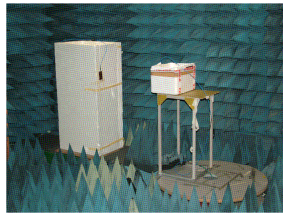


Fig. 3 Near-field measurements set up for reader to implant communications

Path loss measurements ( $S_{12}$ ) were performed in anechoic chamber from distance  $d=0\text{m}$  (PIFA probe antenna located on phantom surface) up to a distance of  $d=1\text{m}$ . As the PIFA is facing the phantom, a mismatch is observed, falling from free-space conditions (-17 dB) to the  $d=0\text{m}$  situation (-4.7 dB) due to the phantom proximity (Fig. 4). This influence is implicitly considered in the path loss when it is measured. As the distance is kept under near field conditions, multipath and fading are not considered in the scenario's link budget.

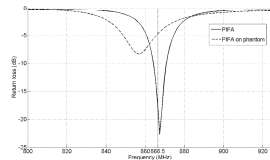


Fig. 4 return loss of the reader antenna placed on the chest phantom and in free air

Once path loss is obtained, the power that is received by the implant and by the reader is calculated according to the link budgets defined in (1) and (2) respectively. They are related to the RFID uplink and downlink budgets. The power received by the reader  $P_{\text{reader\_dB}}$  is the one backscattered by the implant within the torso. Both reader and tag antennas are matched to 50Ω.  $EIRP_{\text{dB}}$  is 35,15 dBm due to regulation constraints.

$$P_{\text{reader\_dB}} = EIRP_{\text{dB}} - 2P_{\text{Loss\_dB}} \quad (1)$$

$$P_{\text{implant\_dB}} = EIRP_{\text{dB}} - P_{\text{Loss\_dB}} \quad (2)$$

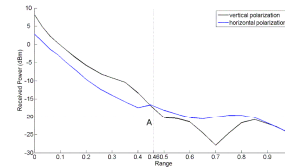


Fig. 5 Power received by the implanted tag from a reader placed perpendicularly to the chest for vertical and horizontal PIFA as reader antenna (ref. (Fig. 3)). Point A (0.46 m, -20 dBm)

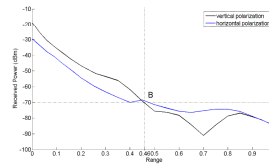


Fig. 6 Power received by the reader from the implanted-tag backscattered signal for vertical and horizontal PIFA as reader antenna (ref. (Fig. 3)). Point B (0.46 m, -70 dBm)

Application-oriented conditions are considered for an implanted passive RFID transceiver: power consumption is assumed to be  $P_{\text{implant\_dB}}=-20\text{ dBm}$  and reader sensitivity  $P_{\text{reader\_dB}}=-70\text{ dBm}$ . As can be seen in Fig. 5 and Fig. 6, a communication link can be reliably established within distance of 0.46 m for both polarizations.

### C. On-chest measurement

Once passive communication has been validated in a broadside link, the case of different reader locations on the chest is contemplated. This is the case, e.g., of a reader located in patient's shirt pocket.

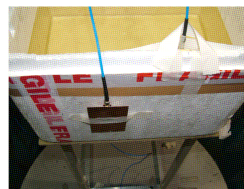


Fig. 7 Measurement set up for on-chest measurement

Path loss ( $S_{12}$ ) measurements were taken at the position showed in Fig. 8, where the PIFA antenna is attached to the phantom. The PIFA antenna is moved along the  $x$  axis for two different heights  $y$ . Vertical and horizontal PIFA orientations



are considered in each case. As the PIFA antenna is placed facing the phantom, a mismatch occurs (Fig. 4). Its impact is again embedded into the path loss measurements.

Fig. 9 and Fig. 10 show the power received by the implant and the handset with horizontal distance  $x$  along the chest for the two different heights  $y$ , namely top and bottom. They correspond again to expression (1) and (2) respectively. If no further losses are considered, the link is assured when the reader is around the chest as in all cases ( $P_{\text{implant}} > -20$  dBm and  $P_{\text{reader}} > -70$  dBm).

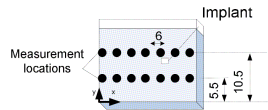


Fig. 8 Positions for on-chest measurements on phantom (dimensions in cm)

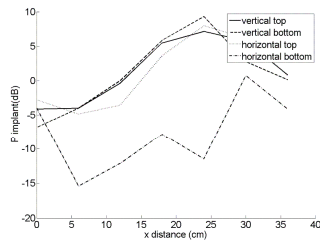


Fig. 9 Power received by the implanted-tag from a reader placed on the chest at positions given by Fig. 7 and Fig. 8

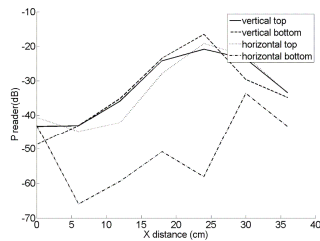


Fig. 10 Power received by the reader placed on the chest at positions given by Fig. 7 & Fig. 8 from the back scattered signal by the implanted-tag

### III. VALIDATION

Presumed that the implant exhibits a very low gain due to the lossy material surrounding it, it is important to check the impact of the radiation coming from the cables that could mask the results. This impact has been studied closer in detailed simulations. The comparison between simulations of the whole set up (including cables) with the measurements will give an estimate of uncertainty for the latter.

### A. Simulation

By using CST Microwave Studio 2010, a detailed and realistic reproduction of the measurement environment in the anechoic chamber has been modelled. Models of both antennas, including their antenna feed, were integrated. These feeds were represented by long ( $\approx 1,5$  m) and bent coaxial cables going down to the chamber floor.

Frequency Solver simulations have been performed according to the measurement set up on each position (Fig. 11). Path loss is in this fashion represented by the logarithmic transmission coefficient  $|S_{21}|$  dB at 868 MHz.

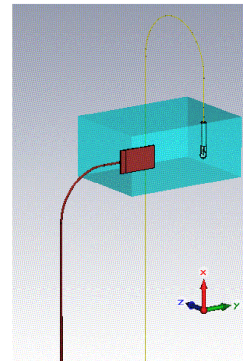


Fig. 11 Simulation arrangement with long cables (main section)

Furthermore, the simulation has been repeated at every position of the reader antenna without the cables in place for comparison purposes.

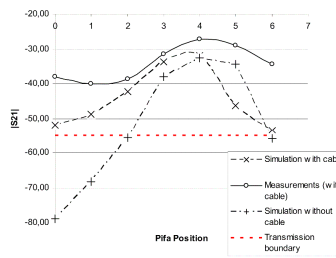


Fig. 12 Comparison of the transmission coefficient for the same set of positions and horizontally oriented PIFA, top line

The  $P_{\text{Loss}}$  dB threshold for reliable communication is  $P_{\text{Loss, dB}} \leq -55,15$  dB and it is calculated from formula (2) ( $\text{EIRP} = 35,15$  dBm and  $P_{\text{tag}} = -20$  dBm).

Fig. 12 shows the results for the top line (Fig. 8) with the reader antenna in horizontal position. In the diagram, horizontal axis represents the 7 registered positions along the torso. The results show a good agreement only near the implanted antenna (position 3-5) when cables are considered

both for simulation and measurements (inevitably in the latter). Further away from the implant, the simulated transmission coefficient drops significantly, especially in the case of the simulation without the cables included. In the rest of cases (horizontal PIFA bottom line, vertical PIFA top and bottom lines), the results are similar and omitted for brevity.

*B. Uncertainty calculation*

The simulations without cables have shown a higher degradation of  $|S_{21}|$  with distance between antennas. This demonstrates the significant influence of the cables on the validity of the results. Please notice that the position of the cables are not exactly the same in both measurement and simulated set ups.

Obviously, performing measurements without cables is as desirable as impossible. A way to get around this constraint is to add an uncertainty value to the simulations without cable. This is shown in Fig. 13, Fig. 14, Fig. 15 and Fig. 16. An estimate of this uncertainty can be extracted by the difference between the simulations with cable and measurements. The range of uncertainty is an estimate of the impact of the cables on the results of the measurement.

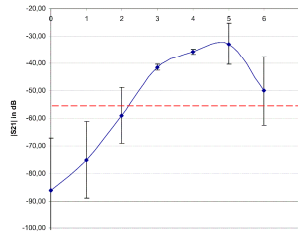


Fig. 13 Simulated transmission coefficient for bottom line, measurement uncertainty included, reader antenna horizontally oriented

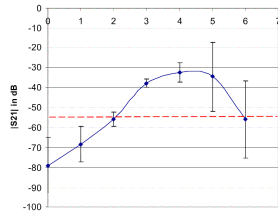


Fig. 14 Simulated transmission coefficient for top line, measurement uncertainty included, reader antenna horizontally oriented

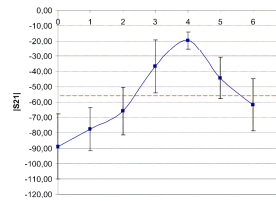


Fig. 15 Simulated transmission coefficient for top line, measurement uncertainty included, reader antenna vertically oriented

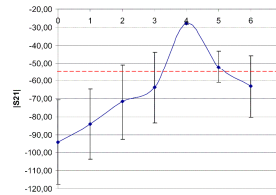


Fig. 16 Simulated transmission coefficient for bottom line, measurement uncertainty included, reader antenna vertically oriented

The further away the reader is placed on the chest, the higher is the impact that is observed due to the small signal to noise ratio at these points.

The proposed method indicates that a communication link can only be assured within a much smaller area in comparison to the one provided only by the measurements (namely the whole torso (Fig. 9 and Fig. 10)). Fig 17 and 18 show three different concentric areas in the torso that represent reliable, uncertain, and impossible communication respectively.

It is noteworthy, that for greater distance the polarisation match of the antennas is not directly correlated with the transmission coefficient.

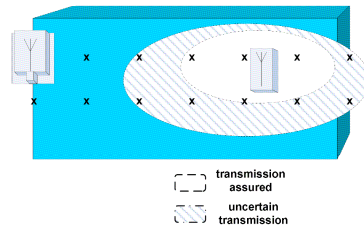


Fig. 17 Characterization of zones with different transmission reliability, reader antenna PIFA vertically oriented

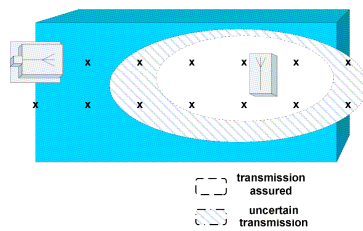


Fig. 18 Characterization of zones with different transmission reliability, reader antenna PIFA horizontally oriented

#### IV. CONCLUSION

Near-field measurements have shown that an RFID passive link is likely to be set when the reader is within 0.46 m from the torso with an implanted antenna inside at UHF band in broadside direction.

Furthermore the results demonstrate that an UHF terminal worn on the chest can surely communicate with the implant within a decent region. A method that defines this region has been presented. It includes measurement set up uncertainties. Those are due to the radiation and reflection coming from the feeding cables. The uncertainty increases with the distance between the two antennas. The results show that the suppression of leakage current of the cable is a key parameter to precise link-budget estimation for antennas worn on the chest. Further investigations are directed to practical solutions for wireless transmission measurements.

#### ACKNOWLEDGMENT

This work was supported in part by the Cátedra Telefónica of the University of Navarra and by the Spanish Ministry of Science and Innovation through the COSIMA project (TEC2010-19545-C04-02). The authors appreciate the University agreement with CST that has enabled the fulfilment of this project.

#### REFERENCES

- [1] P.S. Hall and Y. Hao, eds. *Antennas and Propagation for Body-Centric Wireless Communications*, London, UK: Artech House, 2006
- [2] D. Valderas, C. Schmidt, X. Chen, "Broadband implanted RFID antenna", IEEE APS/URSI Radio Science Meeting, Toronto 2010
- [3] J. Garcia, A. Arriola, G. Sasiain, D. Valderas, JI. Sancho, X.Chen, "Characterization of phantom size and link budget for off-body communications", *Antennas and Propagation (EuCAP)*, Barcelona, 2010
- [4] D. Valderas, C. Schmidt, X. Chen, "RF Implanted Antenna Gain Characterization: Procedures and Challenges", IEEE APS/URSI Radio Science Meeting, Toronto 2010

D. Valderas, C. Schmidt, X. Chen

**RF Implanted Antenna Gain Characterisation: Procedures and  
Challenges**

IEEE APS International Symposium on Antennas and Propagation

### RF Implanted Antenna Gain Characterization: Procedures and Challenges

D. Valderas\*<sup>(1)</sup>, C. Schmidt<sup>(1)</sup>, and X. Chen<sup>(2)</sup>

(1) CEIT and Tecnun (University of Navarra), Manuel de Lardizábal 15, 20018 San Sebastián, Spain.

(2) Queen Mary, University of London, Mile End Road, London E1 4NS, UK  
E-mail: dvalderas@ceit.es

#### Introduction

Implanted biosensors and actuators constitute an essential area for present and future telemetry research. Alongside the actual sensor or actuator, they require a communication transceiver with an antenna to establish the wireless link to the outside of the body. At RF frequencies, the major problem with this kind of applications is due to the losses introduced by the body tissues, which increase considerably at this part of the spectrum and beyond and hinder the communication link. However, they present quite promising features when they are subcutaneously implanted compared to magnetic-coupled based systems, such as higher data rates, longer ranges once the signal is outside the body and robustness to misalignment between the two ends of the link. Therefore, quite a few applications have recently emerged based on this technology, such as blood pressure monitoring, prostheses control by myoelectric sensors, cochlea implants etc. The parallel development of RFID technology presents a promising synergy that is worth exploring.

Nonetheless, characterization of implanted subcutaneous antennas is a quite challenging issue. The radiating element is no longer the conventional antenna but also includes the corresponding part of the body. Thus, antenna matching should be approached once it is placed within the body. In terms of return loss, the impact of the phantom size is virtually negligible [1]. Once the antenna is matched to a frequency band, e.g. 865 MHz 868 MHz, antenna gain in the plane of interest is the key issue to obtain reliable link budgets. Antenna efficiency is strongly dependent on implant location and phantom size and both of them must be properly defined. However, despite some preliminary research has been carried out to compare different antennas on same conditions [2] there is much to be done in this regard. For example, only in a few cases antenna efficiency is related to the size of the human model [3]. Although it is known intuitively that the bigger the phantom the lower the radiation efficiency, in many cases the phantom size is not specified for the provided efficiency of the implanted antenna [4]. Thereby, when the terms for comparison are not agreed, it is very hard to assure that one particular antenna is more efficient than others. Besides, the size of the phantom not only affects the losses by the amount of tissue, but also by the reflections from the boundaries according to phantom geometry, which produce standing waves depending on the implant location and undermine the radiation efficiency.

In the present study, a procedure to characterize implanted antenna gain is addressed. The implant will be placed asymmetrically in a human-torso whose representative minimum size will be defined so that measurements may not be significantly affected by it. Furthermore, the influence of cables on implanted antenna gain measurements will be

---

<sup>1</sup> Daniel Valderas's contract is partially supported by the Spanish Ministry of Education within the framework of the Torres Quevedo Program, and cofinanced by the European Social Fund.

addressed to explore the limitations of standard antenna characterization on implanted radiators.

#### Appropriate phantom size for suitable implant gain characterization

An implanted antenna is placed within a human torso at 9 mm from the interface, as a typical subcutaneous case, and with an offset of 60 mm respect to the center for lungs or heart monitoring. Since entire human phantoms are not often practical in terms of radiation measurements and simulation time, a study should set the minimum phantom size that will dramatically influence the radiation properties according to the working frequency and direction of interest. The horizontal plane is chosen for the 866.5 MHz radio link to a base station outside the body. For that reason, the torso cross section dimensions in this plane should be as realistic as possible, to replicate reflections caused by the change of media. This is modeled by a polystyrene tank with a 35 cm x 25 cm base, filled with tissue simulating liquid [5]. Simulations are performed with CST Microwave Studio to investigate the minimum height  $z$  (Figure 1 (a)) that the phantom should have in order to represent its impact on the horizontal plane gain patterns. Figure 1 (b) shows the convergence of the gain patterns for different phantom heights  $z$ . The antenna shown in Figure 2 (a) is used [1]. A value of  $z=160$  mm is estimated to be enough to account for body effects as the simulated gain patterns converge.

#### Discussion about cable influence on implant gain characterization

As the overall gain is very low (around -20 dBi), it is convenient to further investigate the influence from feeding cable radiation before taking gain measurements. Three setups for simulation are considered and shown in Figure 2: (a) implanted antenna, (b) antenna with testbed and (c) antenna with testbed and feeding cable placed in a similar position to the anechoic chamber's one. Figure 3 show the gain comparison for the three cases in both polarizations (vertical and horizontal). It is clear that the chamber cable has a deep impact on both polarizations and the testbed influence is below a reasonable threshold on vertical polarization.

To check this assumption, a polystyrene tank is filled with 14.5 l ( $z=165$  mm) of tissue simulating liquid [5]. The antenna is placed 90 mm deep via the testbed and 9 mm from the interface. The implant within the phantom is placed in an anechoic chamber for gain measurements. The gain patterns of the horizontal plane over the  $180^\circ$  sweep for front radiation coming from the chest are shown in Figure 4. Even if the comparison between simulated and measured results are not made in the same conditions (for one hand static cable in simulation; on the other hand rotating and arbitrarily-positioned cable in the process of measurement) some similarities can be found. This leads to the conclusion that the impact of the radiation coming from the cable currents eclipses the radiation from the implanted antenna. According to Figure 4, from the measurement-in-chamber point of view, the average gain  $G_{\text{implant, dB}}$  in horizontal polarization is  $G_{\text{aver, H}}=-23.8$  dBi, whereas in the vertical polarization is  $G_{\text{aver, V}}=-28.2$  dBi. These results differ from the expected simulated gain in Figure 3 for the implanted antenna alone:  $G_{\text{H}}=-36.6$  dBi and  $G_{\text{V}}=-20.5$  dBi. It is interesting to notice that the feeding cable current radiation impacts in opposite ways depending on polarization: increasing the horizontal radiation and decreasing the vertical in the direction of interest. A number of nulls are also introduced.

### Conclusions

Preliminary research shows that implanted antenna gain characterization is a complicated issue and common measurement procedures in anechoic chambers are not directly applicable. Finding appropriate phantom size depends upon the part of the body involved, location of the implant, frequency of operation and plane of propagation of the communication link. A procedure to define the correct size has been proposed for horizontal plane transmission by a subcutaneous implant in the human torso. In addition, due to the particular low implanted antenna gain and unbalanced currents, the impact of feeding cable is decisive in the final results. Baluns, attenuators and/or optical feeding are required in this kind of measurement set-ups.

### References

- [1] D. Valderas, C. Schmidt, X. Chen, "Broadband implanted RFID antenna", 2010 IEEE APS/URSI Radio Science Meeting, Toronto (Canada) (submitted)
- [2] P. Soontornpipit, C.M. Furse, You Chung Chung, "Design of implantable microstrip antenna for communication with medical implants" *Trans. On Microwave Theory and Techniques*, vol. 52, no. 8, pp 1944-1951, August 2004.
- [3] J. Kim and Y. Rahmat-Samii, "Implanted Antennas inside a Human Body: Simulations, Designs, and Characterizations", *IEEE Transactions on Microwave Theory and Techniques*, vol. 52, no. 8, pp.1934-1943, August 2004.
- [4] C.-M. Lee, T.-C. Yo, F.-J. Huang, C.-H. Luo, "Dual-resonant  $\pi$ -shape with double L-strips PIFA for implantable biotelemetry", *Electronic Letters*, volume 44, n<sup>o</sup> 14, pp 837 – 838, July 3 2008.
- [5] T. Karacolak, A. Z. Hood and E. Topsakal, "Design of a Dual-Band Implantable Antenna and Development of Skin Mimicking Gels for Continuous Glucose Monitoring". *IEEE Transactions on Microwave Theory and Techniques*, vol. 56, no. 4, , pp 1001-1008, April 2008.

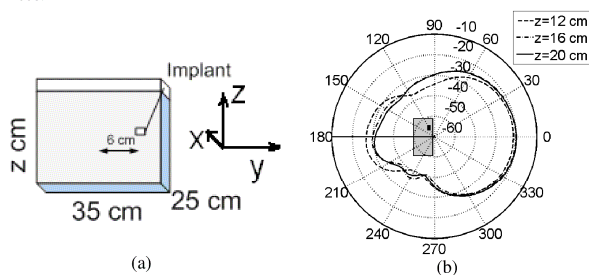


Figure 1. (a) Phantom for torso modeling, implant location and height  $z$  under consideration. (b) Simulated antenna gain patterns in the XY plane at 866.5 MHz for three  $z$  phantom heights

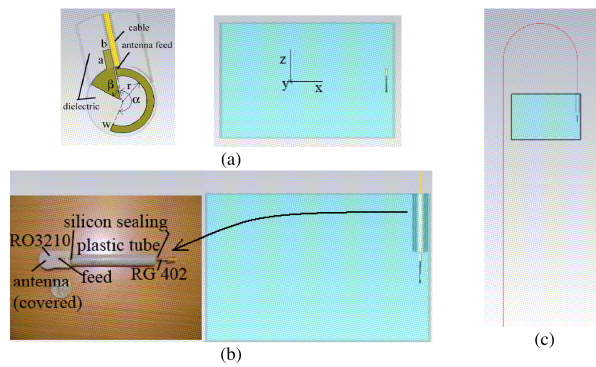


Figure 2. Antenna gain simulation models depending on the measurement set-up (side view). Phantom size is identical in the three cases (350x250x165 mm<sup>3</sup>). (a) Implanted antenna (r=8 mm, w=2 mm,  $\alpha=215^\circ$ ,  $\beta=50^\circ$ , a=5 mm, b=2 mm) (b) Implanted antenna with test bed (c) Implanted antenna with anechoic chamber feeding cable.

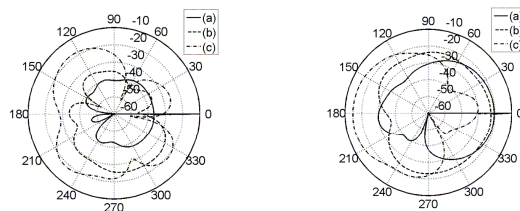


Figure 3. Antenna gain simulation comparison at 866.5 MHz depending on the measurement set-up (a), (b) or (c) in horizontal (left) and vertical polarization (right).

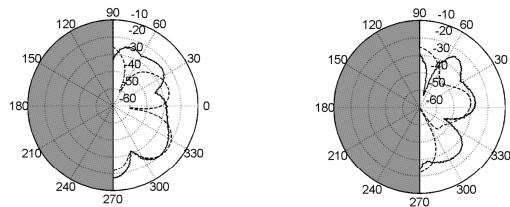


Figure 4. Antenna gain comparison simulated (case (c), dotted) and measured (solid) at 866.5 MHz in horizontal (left) and vertical polarization (right).



D. Valderas, C. Schmidt, X. Chen

**Broadband implanted UHF RFID antenna**

IEEE APSURSI Antennas and Propagation Society International  
Symposium

### Broadband Implanted UHF RFID Antenna

D. Valderas\*<sup>(1)</sup>, C. Schmidt<sup>(1)</sup>, and X. Chen<sup>(2)</sup>

(1) CEIT and Tecnun (University of Navarra), Manuel de Lardizábal 15, 20018 San Sebastián, Spain.

(2) Queen Mary, University of London, Mile End Road, London E1 4NS, UK  
E-mail: dvalderas@ceit.es

#### Introduction

One of the priorities for sustaining high standards of medium to long term health care is to provide an effective monitoring system thus reducing the need for multiple consultations and hospital visits. In this connection, implanted biosensors, equipped with a transceiver with an antenna to establish the wireless link either to an external wearable station or to a computer placed in the care unit or household, constitute an essential area for telemetry research. The major problem with this kind of application is due to the losses introduced by the body, which is very high at RF frequencies and beyond. For this reason the research today has tended to favor in magnetic coils. However, the magnetic coils have three major shortcomings: their intrinsic short range, the critical positioning required for the two coils (inside and outside the body), and the exhibited low data rate. Therefore, it is reasonable to conduct a further study on radiators based on electromagnetic coupling for subcutaneous wireless biosensors, where the distance between the implant and the interface body-air is below a few millimeters. This would be the case of certain applications such as glucose analysis for diabetes treatment, intracranial pressure characterization etc. The combination of biosensors with RFID, a well developed EM coupling technology, can offer a practical platform for a sustainable health care.

In recent years, the research in this field has tended to focus on patch-like antennas, often stacked [1], which allow for miniaturization by shorting pins. However, although the typical impedance bandwidth is around 12% [1][2], this may well not be enough in an environment which is very sensitive to intrinsic features of body tissue, e.g., differences on amount of fat or skin among patients, location shifting of the implant, time, depth into the body according to application, isolation thickness, blood circulation in the surroundings etc; or even differences among patients in whom the antenna is implanted in terms of race, age, gender etc. As these variations act as a global detuning factor, broadband matching should be pursued more likely among monopole like antennas than in narrowband patch-like antennas. Furthermore, the presence of skin and muscle tissue makes matching to a certain operation frequency not that difficult for a very compact antenna into the body, as the body itself acts as a high dielectric constant load and miniaturization is no longer an issue. In fact, the thinner the implant coating, the more compact the antenna gets for the same operational frequency [1]. Thus, typical miniaturization techniques employed in patch-like antennas, such as short-circuit to ground plane, do not seem to be really needed whereas, on top of that, decrease radiation

<sup>1</sup> Daniel Valderas's contract is partially supported by the Spanish Ministry of Education within the framework of the Torres Quevedo Program, and cofinanced by the European Social Fund.

efficiency. The aim of this paper is to provide a broadband monopole-like antenna for a subcutaneous implant: broadband enough to be patient-independent.

#### Antenna Design

Round-shaped antennas are preferred in this study to square-shaped ones so as to avoid vertices that could be harmful for the tissues. Due to space constraints, the antenna is designed so that it is bounded by a circumference of 20 mm diameter. The distance to the interface skin-air is fixed to 9 mm.

Figure 1 illustrates the top view monopole like implanted antenna along with the feeding set up. The superstrate of the antenna has been removed for clarity. The antenna is simulated in CST Microwave Studio. The simulation is performed in a 63 mm x 63 mm x 63 mm phantom. The fluid properties are the same ones as the skin simulating liquid [3]. Table 1 shows parameters that allow worldwide RFID operation (865 MHz-956MHz) in these conditions. The antenna can be easily characterized by two angles: the one which defines the radiating element ( $\alpha$ ) and the one that defines the ground plane ( $\beta$ ). The angle  $\alpha$  defines the resonant frequency. The ground plane via high values of the angle  $\beta$  can be used to add a capacity load in the open end and modify the matching. The antenna can be easily reconfigured over the same space boundary for different frequencies and isolation thickness by the adjusting of  $\alpha$  and  $\beta$ . The auxiliary parameters  $a$  and  $b$  define the area to solder the cable outer conductor. In the present case, the substrate and superstrate is made out of Rogers RO3210 laminate ( $\epsilon_r=10$ ) 1.27 mm thick each.

#### Impedance Bandwidth Measurement

A testbed is designed to measure the impedance bandwidth in the tissue simulating liquid. The cable is covered by a plastic tube and sealed at the top and bottom parts as illustrated in Figure 2. Magnetic beads are placed around the RG 402 cable inside the plastic tube to minimize undesired currents along the outer conductor.

Figure 3 shows the VSWR (reference impedance 50  $\Omega$ ) where the antenna with testbed is measured in two phantoms of different size filled with the skin fluid: a cup and a tank of 14.5 litre both made out of polystyrene. The antenna in the tank was placed close to the interface (9 mm). It can be observed that the measurement in a phantom with a reduced volume is a very acceptable approximation in terms of matching. Additionally, employing a more complex three-tissue phantom for measurement (skin, fat, muscle) does not alter significantly the return loss of a subcutaneous implant when compared with one tissue-skin phantom measurement [3]. In the simulation, neither the testbed nor the magnetic beads have been included. Besides, the critical antenna feed point cannot be perfectly modelled. However, even with these approximations, it provides the final prototype dimensions. The antenna covers the required spectrum with  $\Gamma_{11} < -10$  dB from 866.5 MHz to 1.2 GHz (32.3%) and can operate in the RFID bands worldwide.

In order to corroborate the robustness of the matching when the insertion of implant varies, the antenna matching is measured at different distances from the interface phantom-air. In this case, a phantom of dimensions 220 mm x 220 mm x 110 mm is filled with a body simulating liquid [4] as representative of the body when the antenna is inserted deep in it. Figure 4 (a) illustrates the set up and the positions where the measurements were conducted. Figure 4 (b) shows that there

is virtually no variation in reflection coefficient in those different positions. Furthermore, the result is quite similar to the one obtained in the case of skin fluid [3] in the 14.5 litre tank, what means that the implanted antenna is quite tolerant to tissue and insertion variation.

#### Conclusions

A broadband monopole-like antenna has been designed and tested for RFID subcutaneous implanted applications. The size of the phantom is irrelevant in terms of matching variation in the design process. The antenna can be easily tuned by changing two parameters within the same size and keeping its round shape. The broadband design does not employ short-circuits for miniaturization, what is beneficial for radiation efficiency, and is still quite compact (20 mm diameter section with 3.54 mm thickness). The robustness of the matching to insertion depth and tissue variations shows its versatility to changes in the conditions of the implantation. As a result, the antenna can be used in worldwide UHF RFID subcutaneous implanted systems and poses a quite promising solution for the sharply variable environments with time, location and patient.

#### References

- [1] C.-M. Lee, T.-C. Yo, and C.-H. Luo "Compact broadband stacked implantable antenna for biotelemetry with medical devices", *Electronics Letters*, vol. 43, no. 12, pp 660-662, 7<sup>th</sup> June 2007.
- [2] W.-C. Liu, F.-M. Yeh, and M. Ghavami, "Miniaturized Implantable Broadband Antenna for Biotelemetry Communication", *Microwave and Optical Technology Letters*, vol. 50, no. 9, pp 2407-2409, September 2008.
- [3] T. Karacolak, A. Z. Hood and E. Topsakal, "Design of a Dual-Band Implantable Antenna and Development of Skin Mimicking Gels for Continuous Glucose Monitoring". *IEEE Transactions on Microwave Theory and Techniques*, vol. 56, no. 4, pp 1001-1008, April 2008.
- [4] <http://www.speag.com/measurement/liquids/>: accessed January 11<sup>th</sup>, 2010.

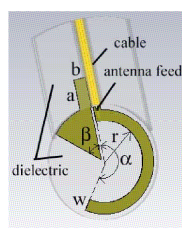


TABLE I  
ANTENNA PARAMETERS

Parameter	Value(mm,°)
r	8
w	2
$\alpha$	215
$\beta$	50
a	5
b	2

Figure 1. Top view of the monopole implanted antenna with parameter values (Table I).

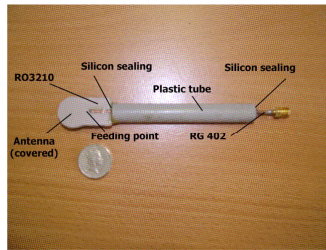


Figure 2. Monopole antenna and testbed.

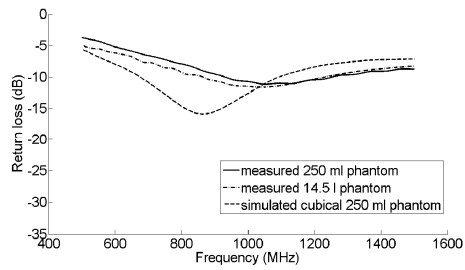


Figure 3. Return Loss for the implanted antenna in different phantoms.

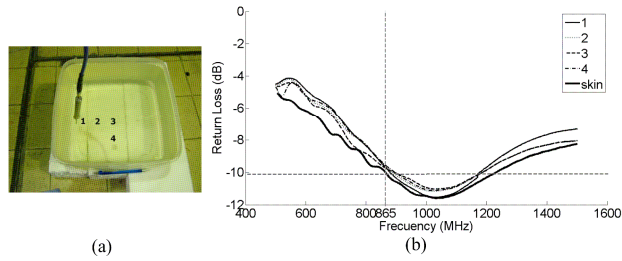


Figure 4. (a) Measurement locations for matching robustness study on the implanted antenna in testbed. (b) Return loss of the implanted antenna for the corresponding positions in the muscle case phantom compared to the skin case (Figure 3, 14.5 l phantom)



## *Appendix B*

# **Patent**

---

A patent application for the subcutaneous venous access smart implant and the associated biofilm detection procedure was submitted. Although it was assessed as promising and patentable, ultimately the patent could not be pursued for budget reasons.

*SOLICITUD DE PATENTE EUROPEA NO. 11380064.3 POR  
"IMPLANTE INTELIGENTE SUBCUTÁNEO DE ACCESO  
VENOSO Y PROCEDIMIENTO DE DETECCIÓN DE BIOCAPAS  
EMPLEANDO DICHO IMPLANTE"*

- Prior Art Search Report
- Notice of Receipt of the Patent Application of the European Patent Office



GRUPO ASESOR INDUSTRIAL

**AGENCIA OFICIAL DE  
PATENTES Y MARCAS**

FOREIGN DEPARTMENT  
P.O. BOX: 20.017  
48080 - SPAIN  
TEL: 34 94 475 33 32  
FAX: 34 94 474 54 06  
www.abgrupo.com  
patents@abgrupo.com

**LUIS BUCETA FACORRO**  
European Patent Attorney  
Agente Oficial Colegiado  
Abogado

**MIKEL VEIGA SERRANO**  
Agente Oficial Colegiado  
Abogado

**CENTRO DE ESTUDIOS E  
INVESTIGACIONES  
TECNICAS (CEIT)**  
Pº de Manuel Lardizabal, 15  
20018 SAN SEBASTIAN  
(GUIPUZCOA)

O - N/Ref.: E2183

Y - S/Ref.:

Fecha: 19/06/2012

**ASUNTO: SOLICITUD DE PATENTE EUROPEA NO. 11380064.3 POR "IMPLANTE INTELIGENTE SUBCUTÁNEO DE ACCESO VENOSO Y PROCEDIMIENTO DE DETECCIÓN DE BIOCAPAS EMPLEANDO DICHO IMPLANTE".-**

**INFORME DE BÚSQUEDA DE ANTECEDENTES**

Muy Sres. nuestros:

En relación con el trámite de su solicitud de Patente Europea arriba referenciada, les informamos que la Oficina Europea de Patentes ha emitido el Informe de Búsqueda de Antecedentes que les adjuntamos a la presente como Anexo-1.

Como podrán comprobar, se han identificado seis documentos antecedentes de categoría "A", es decir, documentos que reflejan únicamente el estado de la técnica y que según el criterio del Examinador no comprometen la patentabilidad de la invención de Uds.

Adjuntamos como Anexo-2 una copia de cada uno de los documentos citados, que son los siguientes:

- US 2007049806 A1
- US 2001053535 A1
- US 2008306454 A1
- US 2007078391 A1
- US 2008262374 A1
- WO 2008008845 A2

Sin embargo, en la Opinión Escrita que acompaña al Informe de Búsqueda de Antecedentes, el Examinador presenta una serie de objeciones en relación con diferentes aspectos de las reivindicaciones de la Patente de Uds.

Balmes 180-4º 2º  
Tel. 932322143  
Fax. 932373299  
08006 BARCELONA

Avenida Leñ. Aguirre, 44  
Tel. 944757139  
Fax. 944760753  
48014 BILBAO

Pujada Pont de Pedra, 3-2º  
Tel. 972223764  
Fax. 972223764  
17004 GIRONA


Angel 24-1ª  
Tel. 958239438  
Fax. 958265368  
18002 GRANADA

Avenida Gran Vía, 52 entp. OC2  
Tel. 941273042  
Fax. 941273041  
26005 LOGROÑO

Bravo Murillo, 219-1ºB  
Tel. 915712272  
Fax. 915702172  
28020 MADRID

Padre Calatayud, 1-3ºE  
Tel. 948291607  
Fax. 948291628  
31003 PAMPLONA



 <p>Europäisches Patentamt European Patent Office Office européen des brevets</p>	<p><b>Empfangsbescheinigung</b> <b>Receipt for documents</b> <b>Réçépissé de documents</b></p>	<p>Liste der diesem Antrag beigelagerten Unterlagen – Hiermit wird der Empfang der unten bezeichneten Dokumente bescheinigt. Wird im Falle der Einreichung der europäischen Patentanmeldung bei einer nationalen Behörde diese Empfangsbescheinigung vom Europäischen Patentamt übersandt, so ist sie als Mitteilung gemäß Regel 35(4) anzusehen (siehe FELD RENA).</p> <p>Checklist of enclosed documents – Receipt of the documents indicated below is hereby acknowledged. If this receipt is issued by the European Patent Office and the European patent application was filed with a national authority, it serves as a communication under Rule 35(4) (see Section RENA).</p> <p>Liste des documents annexés à la présente requête – Nous attestons le dépôt des documents indiqués ci-dessous. Si, en cas de dépôt de la demande de brevet européen auprès d'un service national, l'Office européen des brevets délivre le présent réçépissé de documents, ce réçépissé est réputé être la notification visée à la règle 35(4) (cf. rubrique RENA).</p>
		<p>Nur für amtlichen Gebrauch / For official use only / Cadre réservé à l'administration</p>
<p>Tag des Eingangs (Regel 35 (2)) / Date of receipt (Rule 35(2)) / Date de réception (règle 35(2))</p> <p style="text-align: right;">DREC</p>		<p>Amtsstempel / Official stamp / Cachet officiel</p> <p style="text-align: center;">- 1 ABO 2011</p>
<p>Anmeldenummer für den Schriftverkehr mit dem EPA; Aktenzeichen für Prioritäts- erklärungen / Application No. to be used in correspondence with the EPO; file No. to be used for priority declarations / N° de la demande à utiliser dans la cor- respondance avec l'OEB; n° de dépôt à utiliser pour la déclaration de priorité</p>		<p>11380064.3 / EP11380064</p>
<p>Tag des Eingangs beim EPA (Regel 35 (4)) / Date of receipt at EPO (Rule 35(4)) / Date de réception à l'OEB (règle 35(4))</p> <p style="text-align: right;">RENA</p>		

**47 A. Anmeldungsunterlagen und Prioritätsbeleg(e) / Application and priority documents / Pièces de la demande et document(s) de priorité**

1. Beschreibung (ohne Sequenzprotokollteil) / Description (excluding sequence listing part) / Description (sauf partie réservée au listage des séquences)	<input checked="" type="checkbox"/>	Blattzahl* / Number of sheets* / Nombre de feuilles* 13	Gesamtzahl der Abbildungen* / Total number of figures* / Nombre total de figures* 6
2. Patentansprüche / Claims / Revendications	<input checked="" type="checkbox"/>	4	
3. Zeichnung(en) / Drawing(s) / Dessin(s)	<input checked="" type="checkbox"/>	5	
4. Sequenzprotokollteil der Beschreibung / Sequence listing part of description / Partie de la description réservée au listage des séquences	<input type="checkbox"/>		
5. Zusammenfassung / Abstract / Abrégé	<input checked="" type="checkbox"/>	1	
6. Früher eingereichte Anmeldung / Previously filed application / Demande déposée antérieurement	<input type="checkbox"/>		
7. Übersetzung der Anmeldungsunterlagen / Translation of the application documents / Traduction des pièces de la demande	<input type="checkbox"/>		
8. Übersetzung der früher eingereichten Anmeldung / Translation of the previously filed application / Traduction de la demande déposée antérieurement	<input type="checkbox"/>		
9. Prioritätsbeleg(e) / Priority document(s) / Document(s) de priorité	<input type="checkbox"/>	Anzahl / Number / Nombre* [ ]	
10. Übersetzung des (der) Prioritätsbeleg(s)/beleg(e) / Translation of priority document(s) / Traduction du (des) document(s) de priorité	<input type="checkbox"/>		

**48 B. Der Anmeldung in der eingereichten Fassung liegen folgende Unterlagen bei: / This application as filed is accompanied by the items below: / Les pièces ci-après sont annexes à la présente demande :**

1. Vollmacht / Authorisation / Pouvoir	<input checked="" type="checkbox"/>
2. Allgemeine Vollmacht / General authorisation / Pouvoir général	<input type="checkbox"/>
3. Erfindernennung / Designation of inventor / Désignation de l'inventeur	<input checked="" type="checkbox"/>
4. Recherchenergebnisse nach Regel 141 (1) / Search results under Rule 141(1) / Résultats de la recherche conformément à la règle 141(1)	<input type="checkbox"/>
5. Gebührenzahlungsordr (EPA Form 1010) / Voucher for the settlement of fees (EPO Form 1010) / Bordereau de règlement de taxes (OEB Form 1010)	<input checked="" type="checkbox"/>
6. Elektronischer Datenträger für Sequenzprotokoll / Electronic data carrier for sequence listing / Support électronique de données pour listage des séquences	<input type="checkbox"/>
7. Zusatzblatt / Additional sheet / Feuille supplémentaire	<input type="checkbox"/>
8. Sonstige Unterlagen (bitte hier spezifizieren) / Other documents (please specify here) / Autres documents (veuillez préciser)	<input type="checkbox"/>

AREF  
E2183

**49 C. Exemplare dieser Empfangsbescheinigung (bitte zutreffende Zahl ankreuzen) / Copies of this receipt for documents (please mark appropriate number with a cross) / Exemplaires du présent réçépissé de documents (veuillez cocher le chiffre correspondant)**

<input type="checkbox"/> 2	Einreichung direkt beim EPA / Direct filing with the EPO / Dépôt direct auprès de l'OEB
<input checked="" type="checkbox"/> 4	Einreichung bei einer nationalen Behörde / Filing with a national authority / Dépôt auprès d'un service national

EPA/EPO/OEB 1001.8 01.11

10	Staat des Wohnsitzes oder Sitzes / State of residence or of principal place of business / Etat du domicile ou du siege	Spain
11	Staatsangehörigkeit / Nationality / Nationalité	Spanish
12	Telefon / Telephone / Téléphone	---
13	Fax / Teletax	-----
14	Weitere(r) Anmelder auf Zusatzblatt / Additional applicant(s) on additional sheet / Autre(s) demandeur(s) sur feuille supplémentaire	<input type="checkbox"/>
<b>Vertreter / Representative / Mandataire</b>		
<input type="checkbox"/> <b>FREP</b>		
15	Name / Nom (Nur einen Vertreter oder zwei Namen des Zusammenschlusses angeben - der in das Europäische Erfindungsregister eingetragen ist und an dem zugewiesen wird) / (Name only one representative or association of representatives, to be listed in the Register of European Patents and to whom communications are to be notified) / (N'indiquer qu'un seul mandataire ou le nom du groupement de mandataires qui sera inscrit au Registre européen des brevets et auxquelles les significations seront faites)	LUIS BUCETA FACORRO 53710
<input type="checkbox"/> et <input type="checkbox"/>		
16	Geschäftsanschrift / Address of place of business / Adresse professionnelle	A&B GRUPO ASESOR INDUSTRIAL S.L. Bravo Murillo, 219-1ºB 28020 MADRID (SPAIN)
17	Telefon / Telephone / Téléphone	902195616
18	Fax / Teletax	944760753 / patents@abgrupo.com
19	Weitere(r) Vertreter auf Zusatzblatt / Additional representative(s) on additional sheet / Autre(s) mandataire(s) sur feuille supplémentaire	<input type="checkbox"/>
<b>Vollmacht / Authorisation / Pouvoir</b>		
<input type="checkbox"/> <b>GENA</b>		
20	ist beigefügt / is enclosed / joint	<input checked="" type="checkbox"/>
21	Allgemeine Vollmacht ist registriert unter Nummer / General authorisation has been registered under No. / Un pouvoir général a été enregistré sous le numéro	
<b>Erfinder / Inventor / Inventeur</b>		
<input type="checkbox"/> <b>INVT 20</b>		
22	Der (die) Anmelder ist (sind) alleinige(r) Erfinder / The applicant(s) is (are) the sole inventor(s) / L(e)s demandeur(s) est (sont) le(s) seul(s) inventeur(s)	<input type="checkbox"/>
23	Erfindernennung in beigefügtem Schriftstück / Designation of inventor attached / Vor la désignation de l'inventeur ci-jointe	<input checked="" type="checkbox"/>
24	<b>Bezeichnung der Erfindung / Title of invention / Titre de l'invention</b>	<div style="text-align: right;"><input type="checkbox"/> <b>TIDE</b>   <input type="checkbox"/> <b>TIEN</b>   <input type="checkbox"/> <b>TIFR</b></div> IMPLANTE INTELIGENTE SUBCUTANEO DE ACCESO VENOSO Y PROCEDIMIENTO DE DETECCIÓN DE BIOCAPAS EMPLEANDO DICHO IMPLANTE
		Zeichen des Anmelders / Applicant's reference / Référence du demandeur <b>E2183</b>



**Erfindernennung**  
**Designation of inventor**  
**Désignation de l'inventeur**

(falls Anmelder nicht oder nicht allein der Erfinder ist) /  
 (where the applicant is not the inventor or is not the sole inventor) /  
 (si le demandeur n'est pas l'inventeur ou l'unique inventeur)

Zeichen des Anmelders / Applicant's reference /  
 Référence du demandeur  
(max. 15 Buchstaben / max. 15 characters au maximum)

E2183

Anmeldenummer oder, falls noch nicht bekannt, Bezeichnung der Erfindung /  
 Application No. or, if not yet known, title of the invention /  
 N° de la demande ou, s'il n'est pas encore connu, titre de l'invention

IMPLANTE INTELIGENTE SUBCUTANEO  
 DE ACCESO VENOSO Y PRODEDIMIENTO  
 DE DETECCION DE BIOCAPAS EMPLEANDO  
 DICHO IMPLANTE.

In Sachen der oben bezeichneten europäischen Patentanmeldung nennst (nennen) der (die) Unterzeichnete(n) / In respect of the above European patent application  
 I (we), the undersigned / En ce qui concerne la demande de brevet européen susmentionnée, la(s) soussigné(s)

CENTRO DE ESTUDIOS E INVESTIGACIONES TECNICAS (CEIT)

als Erfinder / I do hereby designate as inventor(s) / désigne(nt) en tant qu'inventeur(s) :

1) Jacobo Paredes Puente, Spanish nationality, addressed at c/Xabier Lizardi nº 9 2º B 20018 San Sebastian (Guipuzcoa) Spain

Weitere Erfinder sind auf einem gesonderten Blatt angegeben / Additional inventors are indicated on a supplementary sheet /  
 D'autres inventeurs sont mentionnés sur une feuille supplémentaire

Der (Die) Anmelder hat (haben) das Recht auf das europäische Patent erlangt? / The applicant(s) has (have) acquired the right to the European patent? /  
 Le(s) demandeur(s) a (ont) acquis le droit au brevet européen?

gemäß Vertrag vom /  
 by an agreement dated /  
 en vertu du contrat passé le

als Arbeitgeber /  
 as employer(s) /  
 en qualité d'employeur(s)

durch Erbfolge /  
 as successor(s) in title /  
 par succession

Ort / Place / Lieu

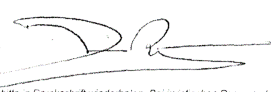
Madrid, Spain

Datum / Date

July 28, 2011

Unterschrift des (der) Anmelders (s) oder Vertreters (s) /  
 Signature(s) of applicant(s) or representative(s) /  
 Signature(s) du (des) demandeur(s) ou du (des) mandataire(s)

Luis BUCETA FACORRO  
 53710



Name des (der) Unterzeichneten bitte in Druckschrift wiederholen. Bei juristischen Personen bitte die Stellung des (der) Unterzeichneten innerhalb der Gesellschaft in Druckschrift angeben. / Please print name(s) under signature(s). In the case of legal persons, the position of the signatory within the company should also be printed. / Le ou les noms des signataires doivent être indiqués en caractères d'imprimerie. Si il s'agit d'une personne morale, la position occupée au sein de celle-ci par le ou les signataires doit également être indiquée en caractères d'imprimerie.

bitte wenden / P.T.O. / T.S.V.P.



**Erfindernennung**  
**Designation of inventor**  
**Désignation de l'inventeur**

(falls Anmelder nicht oder nicht allein der Erfinder ist) /  
 (where the applicant is not the inventor or is not the sole inventor) /  
 (si le demandeur n'est pas l'inventeur ou l'unique inventeur)

Zeichen des Anmelders / Applicant's reference /  
 Référence du demandeur  
(max. 15 Zeichen/lett. / 15 spaces / 15 caractères au maximum)

E2183

Anmeldenummer oder, falls noch nicht bekannt, Bezeichnung der Erfindung /  
 Application No. or, if not yet known, title of the invention /  
 N° de la demande ou, s'il n'est pas encore connu, titre de l'invention

IMPLANTE INTELIGENTE SUBCUTANEO  
 DE ACCESO VENOSO Y PROCEDIMIENTO  
 DE DETECCION DE BIOCAPAS  
 EMPLEANDO DICHO IMPLANTE.

In Sachen der oben bezeichneten europäischen Patentanmeldung nennt (nennen) der (die) Unterzeichnete(n) / In respect of the above European patent application  
 I (we), the undersigned / En ce qui concerne la demande de brevet européen susmentionnée, le(s) soussigné(s)

CENTRO DE ESTUDIOS E INVESTIGACIONES TECNICAS (CEIT)

als Erfinder? / I do hereby designate as inventor(s) / désigné(r) en tant qu'inventeur(s)?

2) Sergio Arana Alonso, Spanish nationality, addressed at c/Jose Antonio Loidi 17 2ºA 20304  
 Irún (Guipuzcoa) Spain

Weitere Erfinder sind auf einem gesonderten Blatt angegeben. / Additional inventors are indicated on a supplementary sheet. /  
 D'autres inventeurs sont mentionnés sur une feuille supplémentaire.

Der (Die) Anmelder hat (haben) das Recht auf das europäische Patent erlangt? / The applicant(s) has (have) acquired the right to the European patent? /  
 Le(s) demandeur(s) a (ont) acquis le droit au brevet européen?

gemäß Vertrag vom /  
 by an agreement dated /  
 en vertu du contrat passé le

als Arbeitgeber /  
 as employer(s) /  
 en qualité d'employeur(s)

durch Erbfolge /  
 as successor(s) in title /  
 par succession

Ort / Place / Lieu

Madrid, Spain

Datum / Date

July 28, 2011

Unterschrift(en) des (der) Anmelders(s) oder Vertreter(s) /  
 Signature(s) of applicant(s) or representative(s) /  
 Signature(s) du (des) demandeur(s) ou du (des) mandataire(s)

Luis BUCETA FACORRO  
 53710

Name des (der) Unterzeichneten bitte in Druckschrift wiederholen. Bei juristischen Personen bitte die Stellung des (der) Unterzeichneten innerhalb der  
 Gesellschaft in Druckschrift angeben. / Please print name(s) under signature(s). In the case of legal persons, the position of the signatory within the company  
 should also be printed. / Le ou les noms des signataires doivent être indiqués en caractères d'imprimerie. S'il s'agit d'une personne morale, la position occupée  
 au sein de celle-ci par le ou les signataires doit également être indiquée en caractères d'imprimerie.

bitte wenden / P-10 / TS-V.P.



**Erfindernennung  
Designation of inventor  
Désignation de l'inventeur**

(falls Anmelder nicht oder nicht allein der Erfinder ist) /  
(where the applicant is not the inventor or is not the sole inventor) /  
(si le demandeur n'est pas l'inventeur ou l'unique inventeur)

Zeichen des Anmelders / Applicant's reference /  
Référence du demandeur  
(max. 15 Personen / max. 15 spaces / 15 caractères au maximum)

E2183

Anmeldenummer oder, falls noch nicht bekannt, Bezeichnung der Erfindung /  
Application No. or, if not yet known, title of the invention /  
N° de la demande ou, s'il n'est pas encore connu, titre de l'invention :

IMPLANTE INTELIGENTE SUBCUTANEO  
DE ACCESO VENOSO Y PROCEDIMIENTO  
DE DETECCIÓN DE BIOCAPAS  
EMPLEANDO DICHO IMPLANTE.

In Sachen der oben bezeichneten europäischen Patentanmeldung nennst (nennen) der (die) Unterzeichnete(n) / In respect of the above European patent application  
(we), the undersigned / En ce qui concerne la demande de brevet européen susmentionnée, le(s) soussigné(s)

CENTRO DE ESTUDIOS E INVESTIGACIONES TECNICAS (CEIT)

als Erfinder / I do hereby designate as inventor(s) / désigne(nt) en tant qu'inventeur(s) :

3) Fernando Jose Arizti Urquijo, Spanish nationality, addressed at Avenida de Navarra 50, 1<sup>o</sup>  
dcha. 20013 San Sebastian (Guipuzcoa) Spain

Weitere Erfinder sind auf einem gesonderten Blatt angegeben / Additional inventors are indicated on a supplementary sheet /  
D'autres inventeurs sont mentionnés sur une feuille supplémentaire

Der (Die) Anmelder hat (haben) das Recht auf das europäische Patent erlangt / The applicant(s) has (have) acquired the right to the European patent /  
Le(s) demandeur(s) a (ont) acquis le droit au brevet européen

gemäß Vertrag vom /  
by an agreement dated /  
en vertu du contrat passé le

als Arbeitgeber /  
as employer(s) /  
en qualité d'employeur(s)

durch Erbfolge /  
as succession(s) in title /  
par succession

Ort / Place / Lieu

Madrid, Spain

Datum / Date

July 28, 2011

Unterschrift(en) des (der) Anmelder(s) oder Vertreter(s) /  
Signature(s) of applicant(s) or representative(s) /  
Signature(s) du (des) demandeur(s) ou du (des) mandataire(s)

Luis BUCETA FACORRO  
53710

Name des (der) Unterzeichneten bitte in Druckschrift wiederholen. Bei juristischen Personen bitte die Stellung des (der) Unterzeichneten innerhalb der  
Gesellschaft in Druckschrift angeben. / Please print name(s) under signature(s). In the case of legal persons, the position of the signatory within the company  
should also be printed. / Le ou les noms des signataires doivent être indiqués en caractères d'imprimerie. S'il s'agit d'une personne morale, la position occupée  
au sein de celle-ci par le ou les signataires doit également être indiquée en caractères d'imprimerie.

bitte wenden / P.T.O. / T.S.V.P.



Europäisches  
Patentamt  
European  
Patent Office  
Office européen  
des brevets

**Erfindernennung**  
**Designation of inventor**  
**Désignation de l'inventeur**

(falls Anmelder nicht oder nicht allein der Erfinder ist) /  
(where the applicant is not the inventor or is not the sole inventor) /  
(si le demandeur n'est pas l'inventeur ou l'unique inventeur)

Zeichen des Anmelders / Applicant's reference /  
Reference du demandeur  
(max. 15 Buchstaben / max. 15 spaces / 15 caractères au maximum)

E2183

Anmeldenummer oder, falls noch nicht bekannt, Bezeichnung der Erfindung /  
Application No. or, if not yet known, title of the invention /  
N° de la demande ou, s'il n'est pas encore connu, titre de l'invention :

IMPLANTE INTELIGENTE SUBCUTANEO  
DE ACCESO VENOSO Y PROCEDIMIENTO  
DE DETECCION DE BIOCAPAS  
EMPLEANDO DICHO IMPLANTE.

In Sachen der oben bezeichneten europäischen Patentanmeldung nennst (nennen) der (die) Unterzeichnete(n) / In respect of the above European patent application  
(we), the undersigned / En ce qui concerne la demande de brevet européen susmentionnée, le(s) soussigné(s)

CENTRO DE ESTUDIOS E INVESTIGACIONES TECNICAS (CEIT)

als Erfinder? / do hereby designate as inventor(s)? / désigne(nt) en tant qu'inventeur(s)?

4) Lutz Christoph Schmidt, German nationality, addressed at Pº de Manuel Lardizabal, 15  
20018 San Sebastian (Guipuzcoa) Spain

Weitere Erfinder sind auf einem gesonderten Blatt angegeben / Additional inventors are indicated on a supplementary sheet /  
D'autres inventeurs sont mentionnés sur une feuille supplémentaire.

Der (Die) Anmelder hat (haben) das Recht auf das europäische Patent erlangt / The applicant(s) has (have) acquired the right to the European patent /  
Le(s) demandeur(s) a (ont) acquis le droit au brevet européen

gemäß Vertrag vom /  
by an agreement dated /  
en vertu du contrat passé le

als Arbeitgeber /  
as employer(s) /  
en qualité d'employeur(s)

durch Erbfolge /  
as successor(s) in title /  
par succession

Ort / Place / Lieu

Madrid, Spain

Datum / Date

July 28, 2011

Unterschrift(en) des (der) Anmelders (s) oder Vertreters (s) /  
Signature(s) of applicant(s) or representative(s) /  
Signature(s) du (des) demandeur(s) ou du (des) mandataire(s)

Luis BUCETA FACORRO  
53710

Name des (der) Unterzeichneten bitte in Druckschrift wiederholen. Bei juristischen Personen bitte die Stellung des (der) Unterzeichneten innerhalb der  
Gesellschaft in Druckschrift angeben. / Please print name(s) under signature(s). In the case of legal persons, the position of the signatory within the company  
should also be printed. / Le ou les noms des signataires doivent être indiqués en caractères d'imprimerie. S'il s'agit d'une personne morale, la position occupée  
au sein de celle-ci par le ou les signataires doit également être indiquée en caractères d'imprimerie.

bitte wenden / P.T.O. / T.S.V.P.



**Erfindernennung  
Designation of inventor  
Désignation de l'inventeur**

(falls Anmelder nicht oder nicht allein der Erfinder ist) /  
(where the applicant is not the inventor or is not the sole inventor) /  
(si le demandeur n'est pas l'inventeur ou l'unique inventeur)

Zeichen des Anmelders / Applicant's reference /  
Référence du demandeur  
(max. 15 Positionen / max. 15 spaces / 15 caractères au maximum)

E2183

Anmeldenummer oder, falls noch nicht bekannt, Bezeichnung der Erfindung /  
Application No. or, if not yet known, title of the invention /  
N° de la demande ou, s'il n'est pas encore connu, titre de l'invention

IMPLANTE INTELIGENTE SUBCUTANEO  
DE ACCESO VENOSO Y PROCEDIMIENTO  
DE DETECCION DE BIOCAPAS  
EMPLEANDO DICHO IMPLANTE.

In Sachen der oben bezeichneten europäischen Patentanmeldung nennt (nennen) der (die) Unterzeichnete(n)<sup>1)</sup> in respect of the above European patent application  
(we), the undersigned<sup>1)</sup> En ce qui concerne la demande de brevet européen susmentionnée, le(s) soussigné(s)<sup>1)</sup>

CENTRO DE ESTUDIOS E INVESTIGACIONES TECNICAS (CEIT)

als Erfinder<sup>2)</sup> / do hereby designate as inventor(s)<sup>2)</sup> / désigne(n)t en tant qu'inventeur(s)<sup>2)</sup>.

5) Daniel Valderas Gazquez, Spanish nationality, addressed at Jose M<sup>a</sup> Salaberria, 31-1<sup>o</sup>A  
20010 San Sebastian (Guipuzcoa) Spain

Weitere Erfinder sind auf einem gesonderten Blatt angegeben. / Additional inventors are indicated on a supplementary sheet. /  
D'autres inventeurs sont mentionnés sur une feuille supplémentaire.

Der (Die) Anmelder hat (haben) das Recht auf das europäische Patent erlangt<sup>3)</sup> / The applicant(s) has (have) acquired the right to the European patent<sup>3)</sup> /  
Le(s) demandeur(s) a (ont) acquis le droit au brevet européen<sup>3)</sup>

gemäß Vertrag vom / by an agreement dated / en vertu du contrat passé le   als Arbeitnehmer / as employee(s) / en qualité d'employeur(s)  durch Erbfolge / as successor(s) in title / par succession

Ort / Place / Lieu

Madrid, Spain

Datum / Date

July 28, 2011

Unterschrift(en) des (der) Anmelders (s) oder Vertreters (s) /  
Signature(s) of applicant(s) or representative(s) /  
Signature(s) du (des) demandeur(s) ou du (des) mandataire(s)

Luis BUCETA FACORRO  
53710

Name des (der) Unterzeichnert bitte in Druckschrift wiederholen. Bei juristischen Personen bitte die Stellung des (der) Unterzeichnert innerhalb der  
Gesellschaft in Druckschrift angeben. / Please print name(s) under signature(s). In the case of legal persons, the position of the signatory within the company  
should also be printed. / Le ou les noms des signataires doivent être indiqués en caractères d'imprimerie. Si il s'agit d'une personne morale, la position occupée  
au sein de celle-ci par le ou les signataires doit également être indiquée en caractères d'imprimerie.

EP/PEO/DEB 1002 12.07

Bitte wenden / P.T.O. / T.S.V.P